Synchronization and Waves in Confined Complex Active Media

vorgelegt von
Jan Frederik Totz
Master of Science (M. Sc.)
geb. in Berlin

von der Fakultät II – Mathematik und Naturwissenschaften
der Technischen Universität Berlin
zur Erlangung des akademischen Grades

Doktor der Naturwissenschaften
— Dr. rer. nat. —

genehmigte Dissertation

Promotionsausschuss:

Vorsitzender: Prof. Dr. Dieter Breitschwerdt
Gutachter: Prof. Dr. Harald Engel
Gutachterin: Prof. Dr. Katharina Krischer
Gutachter: Prof. Dr. Dr. h.c. Eckehard Schöll, PhD

Tag der wissenschaftlichen Aussprache: 22. Dezember 2017

Berlin 2018

Acknowledgements

Prof. Harald Engel
Prof. Oliver Steinbock, Prof. Kenneth Showalter,
Prof. Vladimir K. Vanag, Prof. Jörn Dunkel

AG Engel (Berlin)
Steffen Martens, Julian Rode, Dumitru Calugaru, Jakob Löber, Markus Radszuweit,
Dirk Kulawiak, Florian Buchholz, Christopher Mikolajzak, Leander Self, Fabian Paul,
Franziska Böhme, Ingeborg Gerdes, Hermann Brandtstädter, Grigory Bordyugov,
Jan Schlesner, Andrea Schulze, Julia Eckert, Yulia Jagodszinski, Peter Orlowski

AG Steinbock (Florida)
Zulma Jiménez, Sumana Dutta, Laszlo Roszol, Rabih Makki

AG Showalter (West Virginia)
Darrell Collison, Desmond Yengi, Razan Snari, Simba Nkomo, Mark Tinsley

AG Vanag (Kaliningrad)
Pavel Smelov, Ivan Proskurkin, Dmitry Safonov

Special Thanks
Georg Engelhardt, Enrico Dietz, Norbert Zielinski, Rinaldo August, Sven-Uwe Urban,
Jörn Six, Fabian Sielaff, Chris Scharfenorth, Sascha Gerloff, Anna Zakharova,
Madeleine Nuck, Annette Taylor, Delora Gaskins, Valentin Flunkert, Christian Hennig,
Franz-Josef Schmitt, Philipp Strasberg, Alice Schwarze, Fachreddin Tabataba-Vakili,
Farsane Tabataba-Vakili, Ramona Rothfischer, Julien Olck, Sophie Seidenbecher,
Sophie Ernst, Pirmin Kustin

Funding
Prof. Holger Stark (GRK 1558) and Prof. Eckehard Schöll (SFB 910)

Flora high school (South Carolina)
Physics teacher Mr. Tom Sunday

Family
Cordula & Claus-Dieter & Carl Hendrik & Erika & Werner

Dedicated to my loving wife: Sonja

Abstract

The aim of this thesis is the study and characterization of a number of self-organized patterns with potential relevance to biological systems and beyond. To this end we utilize the well-established oscillating Belousov-Zhabotinsky (BZ) reaction in chemical experiments as well as numerical simulations of the underlying model equations on graphics cards.

The first part of this thesis features experiments on spiral-shaped excitation waves in a three-dimensional oscillatory medium. Their spatiotemporal evolution is governed by a circular line singularity around which the waves rotate. In the absence of medium boundaries, the singularity would contract and eventually vanish. Due to the interaction with the boundary, the singularity may stabilize, such that it acts far beyond its theoretical life time as an autonomous pacemaker. The influence can be taken into account in a semi-analytical kinematic model, which is in good agreement with experiments and simulations. Related patterns of electrical activity play a critical role in ventricular tachycardia, a life-threatening heart arrhythmia.

A small network of discrete BZ oscillators can support periodically spreading excitation waves. For a small distribution of natural oscillation frequencies, the waves propagate along the permutation symmetries. It is known, that comparable electric waves in neuronal networks control rhythmic muscle contraction.

In the final part of the thesis, we verify the spiral wave chimera state, that was predicted by Yoshiki Kuramoto in 2002. This particular state exhibits a coherent spiral wave rotating around a core that consists of incoherent oscillators. Such patterns might play a role in nonlocally coupled cardiac and cortical tissue as well as in the photoelectrodissociation on doped silicon wafers and arrays of superconducting quantum interference devices and opto-mechanical oscillators. The experimental setup, that we developed for this purpose, furthermore allows for reproducible experiments under laboratory conditions on networks with $N > 2000$ oscillators. It facilitates the free choice of network topology, coupling function as well as its strength, range and time delay, which can even be chosen as time-dependent.

Zusammenfassung

Die Zielsetzung dieser Arbeit ist die Untersuchung selbstorganisierter Muster, die potentielle Relevanz für biologische Systeme und darüber hinaus aufweisen.
Zu diesem Zweck werden chemische Experimente auf Basis der oszillierenden Belousov-Zhabotinsky (BZ) Reaktion und numerische Simulation der zugrundeliegenden Modellgleichungen auf Grafikkarten durchgeführt.

Im ersten Teil der Arbeit werden spiralförmige Erregungswellen in einem dreidimensionalen oszillatorischen Medium untersucht, die periodisch um eine kreisförmige Singularität rotieren und dabei Wellenzüge aussenden. Ohne Wechselwirkung mit der Berandung des aktiven Mediums, würde die Singularität kontrahieren und nach endlicher Zeit verschwinden. Unter Einfluss der Randwechselwirkung lässt sich die Singularität stabilisieren, so dass sie weit über ihre theoretische Lebenszeit hinaus als autonomer Schrittmacher fungiert. Der Effekt des Randes lässt sich in einem semi-analytischen kinematischen Modell berücksichtigen, welches gut mit den Ergebnissen der Experimente und Simulationen übereinstimmt. Verwandte Muster elektrischer Aktivität spielen insbesondere auf dem Herzmuskel eine kritische Rolle bei der ventrikulären Tachykardie, einer lebensbedrohlichen Herzrhythmusstörung.

Auf einem kleinen Netzwerk aus diskreten BZ Oszillatoren können sich periodisch Erregungswellen ausbreiten. Bei enger Verteilung der natürlichen Oszillationsfrequenzen breiten sich die Wellen entlang der Permutationssymmetrien aus. Es ist bekannt, dass vergleichbare elektrische Wellen in neuronalen Netzwerken rhythmische Muskelkontraktion steuern.

Im letzten Teil der Arbeit weisen wir den von Yoshiki Kuramoto in 2002 vorhergesagten Spiralwellen-Chimären Zustand nach. Dabei rotiert eine kohärente Spiralwelle um einen Kern aus inkohärenten Oszillatoren. Dieses Muster könnte eine Rolle in nichtlokal gekoppeltem Herz- und Nervengewebe spielen, in der Photoelektrodissoziation auf dotierten Silizumscheiben, sowie auf Gittern aus supraleitenden Quanteninterferenzeinheiten und optomechanischen Oszillatoren. Der zu diesem Zweck entwickelte experimentelle Aufbau erlaubt es darüber hinaus, Muster auf Netzwerken mit $N > 2000$ Oszillatoren unter reproduzierbaren Laborbedingungen zu untersuchen. Dabei lassen sich nach Bedarf Netzwerktopologie, Art der Kopplungsfunktion sowie ihre Stärke, Reichweite und Zeitverzögerung einstellen, die darüber hinaus auch zeitabhängig sein können.

Table of contents

Chapter 1

Introduction

"... on the shoulders of giants"
– Bernard of Chartres

The second law of thermodynamics[1] states, that during an irreversible process the total entropy S in an isolated system always grows:

$$\frac{d_i S}{dt} > 0. \tag{1.1}$$

As time passes, matter will decay from an ordered, but improbable state to a disordered and more probable state. Yet structures of high order, namely life forms, exist and very successfully so: From the microscopic bacterium Pelagibacter ubique[2] that measures just about 5 µm but makes up for the largest cumulated species biomass worldwide to the orders of magnitude larger blue whale (Balaenoptera musculus) reaching about 30 m in size[3]. Life prevails despite inhospitable environments that are devoid of oxygen[4], below freezing at $-20\,^{\circ}\mathrm{C}$[5] or close to boiling temperatures[6], to just give a few examples.
This paradox was addressed from the perspective of statistical physics by Erwin Schrödinger, one of the pioneers of quantum mechanics, in his book "What Is Life?"[7]. He not only argues for the existence of a biomolecular "asymmetric crystal" as a carrier of hereditary information, which inspired Crick and Watts to search for the DNA double helix molecule[8], but also he makes the case that living matter attains an ordered state and remains in it, due to consuming "negative entropy" from its environment,

$$\frac{d_i S}{dt} + \frac{d_e S}{dt} > 0. \tag{1.2}$$

Put differently, a living being is an open system, which maintains a non-equilibrium state by entropy exchange d_eS with its surroundings via nutrients and waste products. This notion was formalized mathematically by Ilya Prigogine[9,10] as a "dissipative structure", that exists far from equilibrium and bifurcates off the equilibrium state.
Meanwhile, the dynamics of self-organized structures were elucidated from a macroscopic viewpoint by Alan Turing and Arthur Winfree who had laid out in their respective seminal papers the basis for spatial pattern formation[11] and temporal synchronization of oscillators[12].
Self-organized structures are not only restricted to life. Shortly after the first working laser[13] was built, Hermann Haken successfully proposed a theory for its operation based on non-equilibrium dynamics[14]. He and Werner Ebeling went on to found and popularize the new field of "synergetics"[15,16] in divided Germany and throughout the scientific world.
The common thread in all these endeavors is *self-organization*. Its defining feature is a structure of high, life-like order that is attained due to its own internal, nonlinear dynamics. No detailed, external control on the structure is required.
Its continuing success was underscored with two Nobel prizes. One in chemistry was received by Gerhard Ertl in 2007 for developing the methods of surface chemistry in general and for observing pattern formation on catalytic platinum surfaces during CO oxidation in particular[17]. The other was awarded as recently as 2017, when the Nobel Prize in Physiology or Medicine was shared by Jeffrey Hall, Michael Rosbash and Michael Young for revealing the basic biomolecular machinery of chronobiology in virtually all living things, from bacteria, fungi to plants and animals[18,19].
It was recently proposed[20,21], that far away from equilibrium the second law needs to be adapted

$$\frac{d_eS}{dt}\Big|_{a\to b} + \frac{d}{dt}\ln\left(\frac{p_{a\to b}}{p_{b\to a}}\right) + \frac{d_iS}{dt} > 0 \tag{1.3}$$

to account for transition probabilities in and out of a given non-equilibrium state. This means that the more irreversible a process is, $p_{a\to b} \gg p_{b\to a}$, the larger its associated internal entropy production will be. Furthermore this allows for an engineered dissipative adaptation, by placing suitable driving forces on the system, that will enable it to reach desired non-equilibrium states, but not escape from them[22].
Future developments in the field of self-organization can be expected to give insight into life-like non-equlibrium phenomena as well as lead to new applications in smart materials[23] and soft robotics[24] founded on neuromorphic[25,26] and biomimetic materials[27], ultimately opening the door to artificial life forms[28,29] and new forms of medical therapies[30,31].

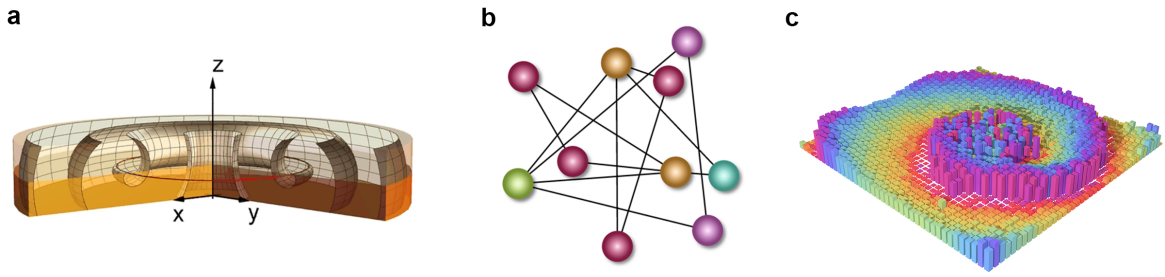

Figure 1.1 | Excitation wave patterns in different topologies. (a) Scroll ring in a 3d continuous domain (b) target wave on a network with symmetry clusters (c) spiral wave chimera on a discrete 2d grid.

An accessible test bed for predictions in the field of self-organization is the prototypical chemical oscillator, the Belousov-Zhabotinsky reaction[32]. Its popularity is due to it giving rise to concentration traces that are strikingly similiar to the biochemical activity of neurons[33]. In spatially continuous systems it supports chemical patterns similar to electrical activity patterns on the heart muscle that usurp its mechanical contraction before sudden cardiac failure[34–36].

In this thesis the overarching theme is elucidating the peculiar behavior of excitation waves as stable temporally periodic patterns on different topologies. Unlike waves in a fluid or conservative solitons[37], excitation waves require an active medium, that shows excitability[38] and is kept far from equilibrium due to energy influx like the gain medium in a laser[15]. The excitable character manifests itself in the all-or-nothing response to an external perturbation: Small perturbations below a threshold have a negligible consequence, whereas large superthreshold perturbations lead to an extensive and unique response. This definition is inspired by biological neurons[39,40], that remain quiescent in response to small current fluctuations, but emit a voltage spike once sufficiently perturbed. Before another perturbation can successfully trigger an excursion, the system must pass through its refractory stage and return to its rest state. Such elements, connected in a chain, support the sequential propagation of a spike from one end to the other: an excitation wave.
Chapter 2 is focused on the formation of a metastable pacemaker, a structure that acts as a periodic wave source in three dimensions. For parameters where stable pacemakers were previously thought impossible, it is shown that they can exist due to interaction with inherent spatial boundaries that occur in any real system like the myocardium.
In chapter 3, the focus shifts to excitation waves on networks. It is found that underlying network symmetries are intertwined with the way an excitation wave propagates over the

network. During propagation, the nodes in each symmetry cluster synchronize, such that they fire concurrently.

Finally in chapter 4, a large grid of discrete oscillators that are nonlocally coupled to each other gives rise to a structure that was predicted 15 years ago by Yoshiki Kuramoto theoretically[41], but never verified experimentally: the spiral wave chimera. The distinguishing feature is that a coherent excitation wave rotates around a central region that consists of seemingly incoherent oscillators even though all oscillators are coupled identically. This is the first experimental example for the co-existence of ordered and disordered phases in a robust and reproducible real setting without sensitive dependence on initial conditions.

Chapter 2

Confined Scroll Rings

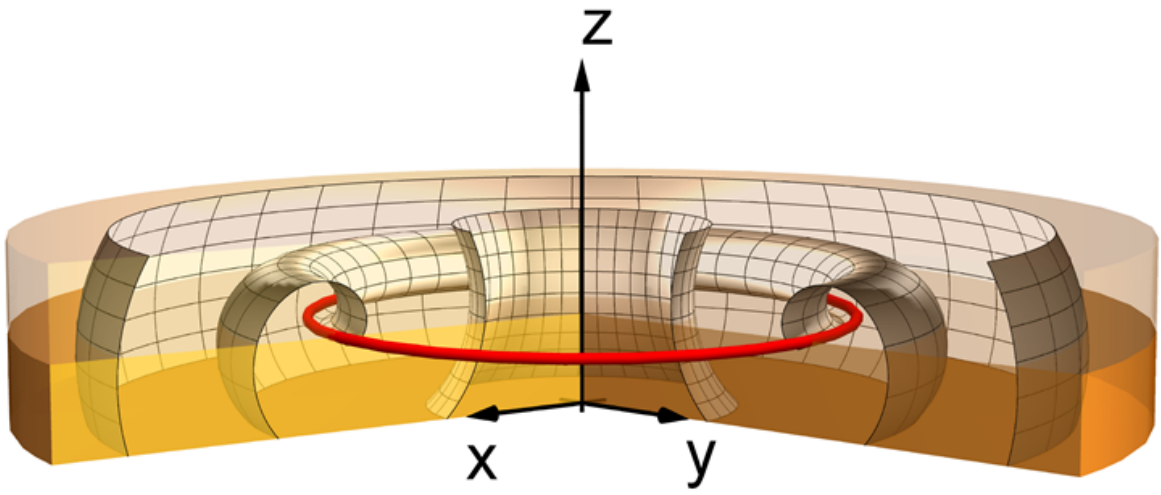

Figure 2.1 | Model for spiral wave formation. A forest consisting of trees that can catch fire, burn and regrow (unnaturally) fast is a minimal model for an excitable medium. (a) An excitation wave in the form of a planar flame front travels from left to right. In the back of the flame front, new trees are already growing. A rain cloud located in the center of the medium prevents flames from spreading in the top half, which breaks the front and creates an open end. (b) While the flame front propagates in the bottom half, the rain cloud vanishes. The broken flame front continues onward to the right and now also spreads in the upward direction. This is the genesis of the spiral wave. (c) After a sufficient number of rotations, the full-fledged spiral wave pattern is observable. This cellular automaton-like simulation was realized with the Star Craft II map editor[42].

Among the different spatio-temporal patterns of propagating excitation waves, rotating spiral-shaped waves are very common. This suggests, that their emergence must depend on general rules, that transcend microscopic details. As depicted in Figure 2.1, an initially planar wave front can break up due to interaction with inhomogeneities in an active medium. The resulting wave features an open end far from any boundaries. Still, the excitation (fire) will spread from the current excited region to any surroundings that are not in their refractory, unexcitable (burnt) state. This means that the main front will continue forward, but at the wave tip the excitation can spread upwards in addition. While the tip continues on its pirouette-like motion, it becomes the source of the excitation waves, that are periodically emitted into the medium. In this sense, the tip is the localized organizing center[43] of the delocalized spiral wave, that has a wavelength λ and rotation period T. Note that the oscillations at each location outside the spiral core are entrained to the rotation period of the spiral wave. Here, the non-equilibrium character manifests itself in the influx of external energy, that is required to return oscillators to their rest state (unburnt) so a neighboring excitation can restart the oscillation cycle.

Apart from this simple example, spiral waves have been observed in an astonishing variety of biological, chemical and physical systems [a] : myocardium[62–66], cardiac cell monolayers[67,68], optogenetically engineered cell layers[69–71], giant honey bee colonies[72], mammalian cortex[73],

[a] Some vortex patterns in nature have spiral shape, but there is no underlying excitable medium. Some examples range from Bose Einstein condensates[44], spin spirals[45], spiral crystal growth[46–48], drop-induced airflows[49], fluid mixing[50], Bernard convection in gas mixture[51,52], Faraday experiments with vertically vibrated viscous fluid and sand[53,54], Kármán vortex street[55], hurricanes[56], extraterrestrial storms, such as the Great Red Spot[57] and polar vortices[58] on Jupiter, galaxy formation[59] and the recent binary black hole as well as neutron star mergers, which emitted double spiral gravitation waves[60,61].

calcium waves in frog eggs[74], chicken retina[75], single cells and conglomerates of the social amoeba Dictyostelium discoideum[76,77], geographical tongue inflammation[78], migratory erythematous lesions[79], human crowds[80], synthetic somatic cell sheets[81], uterus during labor[82,83], yeast glycolysis[84], Min proteins[85] and actin-proteins in electro-fused cell membranes[76,86], lichen growth[87], cilia arrays[88], Belousov-Zhabotinsky (BZ) reaction medium[89], BZ-surfactant mixtures[90], BZ-infused Langmuir monolayers[91], precipitation reactions[92], CO oxidation on Pt-110 surface[93], electrodeposition of a binary alloy[94], corrosion[95], lasers[96–98], combustion[99], liquid crystals[100,101], plasma[102], dielectric barrier gas-discharge[103], trapped ultracold ion arrays[104], optomechanical oscillator arrays[105], coupled map lattices[106], and Josephson junction arrays[107].

Among the most striking examples are spiral waves on the heart muscle, where they are also called rotors or reentry. During the healthy operation of the heart, the sinoatrial node entrains the beating rhythms of all cells in the myocardium by emitting a propagating electric excitation wave. Upon arrival at a heart cell, it expands and shortly after contracts again. This synchronized, collective mechanical deformation underlies the vital heart beat that pumps blood through the body[108]. Due to e.g. unexcitable[109] or highly excitable[110] obstacles, spiral waves may nucleate. Since they are periodic wave sources, they directly compete with the sinoatrial node for the entrainment of the myocardium. If multiple spiral waves form, the ensuing wave chaos compromises the synchronized, collective deformation and leads to life-threatening fibrillation[36,65].

Due to the three-dimensional nature of the heart, the rotating patterns are actually scroll waves, which are made up of spiral waves stacked up on each other. Accordingly, the center of the spiral core is extended to a line first identified by Winfree as organizing center of the scroll wave and named filament[87,111–114].

One of the first reported experimental observations of a filament in the cardiac muscle, had a ring-shaped form[115]. Indeed, connecting both ends of the filament and bending it into a ring, leads to a simple structure called the scroll ring[87,116] (see figure 2.2a). Curiously, the periodic wave pattern of scroll rings was exploited in oil-immersed BZ drops to drive autonomous periodic motion via changes in the surface tension[117].

The dynamics of this structure in the presence of boundaries are the focus of this chapter.

2.1 Theoretical Background

The equations of motion for filaments were first derived in a mathematically rigorous way by James Keener in 1988 employing techniques from singular perturbation analysis[118]. His approach is reviewed briefly in appendix A.2 together with recent developments.

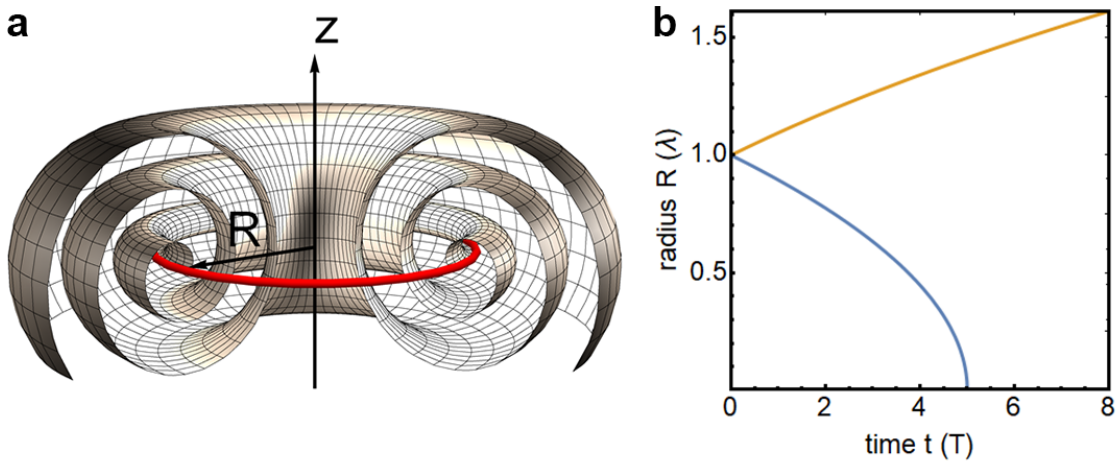

Figure 2.2 | Unperturbed dynamics of an axisymmetric, untwisted scroll ring. (a) A scroll ring is a toroid formed from a spiral wave. The tip of each spiral wave is attached to a ring with radius R, called the filament (red). For clarity, here only a single isosurface of the continuous concentration pattern is shown. (b) Without perturbations the scroll ring will either decay for filament tension $\alpha > 0$ (blue) or grow for $\alpha < 0$ (yellow), see (2.1). Time and space are scaled relative to the rotation period T and wavelength λ of the waves emitted from the ring.

In the case of a closed filament loop, a scroll ring, the equations of motion simplify to

$$\frac{dR}{dt} = -\alpha\kappa, \tag{2.1}$$

$$\frac{dz}{dt} = \beta\kappa. \tag{2.2}$$

While the ring drifts along its symmetry axis in z-direction, the radius R of the ring changes depending on the ring curvature $\kappa = 1/R$ [b] . It will either contract and vanish or expand depending on the sign of the filament tension α, see Fig. 2.2b. In its later stages a growing ring will undergo the negative line-tension instability [120]. This means it will break apart and develop into a highly disorganized pattern known as Winfree turbulence [121]. The analytical solution to the radius dynamics (2.1) is given by

$$R^2(t) = R_0^2 - 2\alpha t. \tag{2.3}$$

Thus unlike its two-dimensional counterpart, the spiral wave, a scroll ring is not a stationary pattern. Intuitively the non-stationarity is clear: In two dimensions, a spiral wave will drift under an external perturbation. This can be realized in the form of a time-periodic external parameter field [122], a parameter gradient [123], an applied electric field [124], feedback control [125]

[b] Note that this is a special case of an arbitrary closed curve $\boldsymbol{r}$ moving under mean curvature flow: $\boldsymbol{r}_t = -\alpha\kappa\boldsymbol{N}$, where $\boldsymbol{N}$ is the normal vector at each point of the curve $\boldsymbol{r}$ [119].

or a Neumann boundary[126,127]. These perturbations lead to a periodic modulation of the excitability in the core region. However, in three dimensions no external field is necessary, since the periodic perturbation is due to the pattern itself. During one rotation period, the filament loop will cycle between a large and a small radius, which have a small and large curvature, respectively. In the same way the eikonal equation,

$$c_n = c_0 - D\kappa, \tag{2.4}$$

dictates how non-planar excitation waves in two dimensions straighten out[128–130], the rotation speed of the filament increases when it goes from a large circumference to a small one and decreases on its way back[131]. This periodic curvature-induced self-modulation forbids stationary scroll ring patterns.

However, the dynamics of the unperturbed scroll ring can be complemented by considering external perturbations, specifically the effect of Neumann boundaries that naturally limit the spatial extent in a realistic setting.

To this end it is important to first understand how two-dimensional spiral waves interact with Neumann boundaries. One approach is based on the convolution of perturbations with spiral wave response functions[132–134] (appendix A.2). While it is highly successful for weak perturbations, such as spatiotemporal parametric inhomogeneities, it is not applicable to the interaction with Neumann boundaries. Boundaries break the symmetries of the Euclidean plane strongly and thus the Goldstone modes, whose adjoints are the response functions, do not exist.

An alternative data-driven approach is described in the next section.

2.2 Chemical Experiments

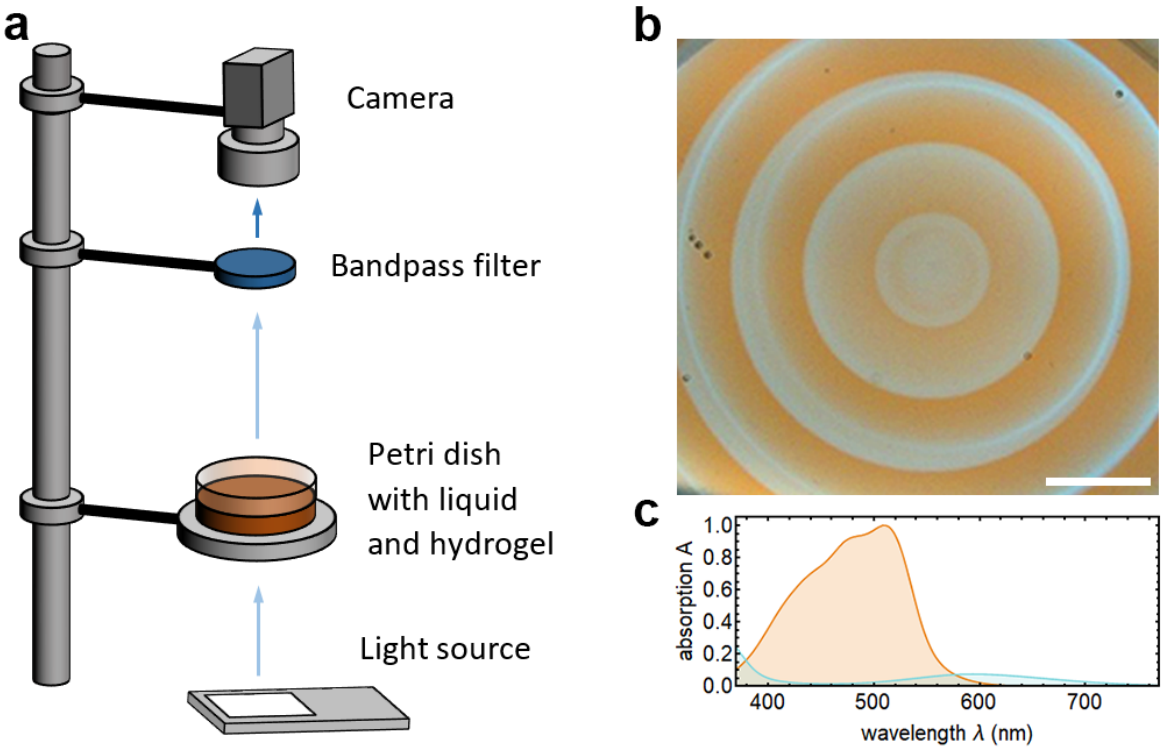

Figure 2.3 | Experimental setup for boundary stabilized scroll rings. (a) Pattern formation in the active medium is monitored spectrophotometrically. Excitation waves of oxidized catalyst absorb less light than the domains with reduced catalyst and thus the concentric waves of a scroll ring appear in bright blue on an orange background, see photograph in (b). The white bar corresponds to 1 cm. (c) Absorption spectra of the reduced form of the catalyst (Fe^{3+}) in orange and the oxidized form (Fe^{4+}) in blue.

While the Belousov-Zhabotinsky reaction has been utilized to study chemical oscillations in time, it is also readily employed to study propagating patterns in a continuous medium in time as well as space (see appendix C.1.3). The applicability of this approach is well-established by a large body of experiments on scroll rings in BZ media, testing their existence [116], formation [135], dynamics for positive and negative filament tension [136,137], behavior influenced by each other [138], temperature and electrical gradients [139,140] as well as defect sites [141–143]. However, their interaction with medium boundaries is less well explored.

Here, chemical waves in the active medium are observed with a simple spectrophotometric setup [144] (see Fig. 2.3a). Excitation waves manifest themselves as narrow, propagating domains of oxidized catalyst surrounded by large regions of reduced catalyst. Since the absorption spectrum of the ferroin catalyst, $Fe(o-phen)_3$, depends on the oxidation state of the Fe-ion (Fe^{3+}/Fe^{4+}), it is possible to optically record the concentration waves with a CCD

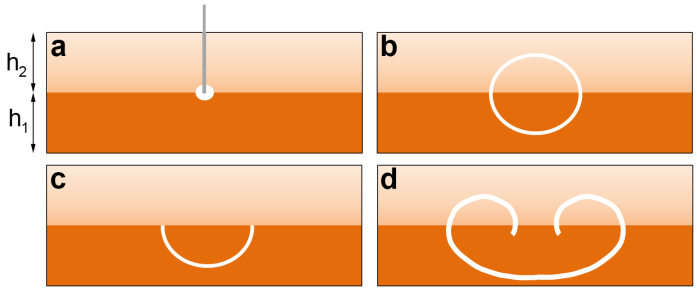

Figure 2.4 | Scroll ring nucleation. Reproducible initialization of scroll rings consists of four stages; (a) A silver wire is introduced at the liquid-gel interface of the active medium to (b) initiate a spherical wave. (c) By shaking the medium strongly enough to erase any structures in the upper liquid layer, (d) the spherical wave is converted into a scroll ring.

camera. Waves appear as bright blue on an orange background (Fig. 2.3b), because the reduced catalyst strongly absorbs blue and green parts of the VIS spectrum ($\lambda = 380 - 560\,\text{nm}$), whereas the oxidized form is nearly transparent to all wavelengths, except for a weak absorption of red wavelengths with $\lambda = 580 - 620\,\text{nm}$ (Fig. 2.3c). The optical contrast is further enhanced with a bandpass filter that only transmits light into the camera with a wavelength of $\lambda = 400 - 500\,\text{nm}$. Further details on the experiment instrumentation are given in appendix B.1.1.

The chemical medium consists of two layers to allow for a reproducible nucleation protocol of scroll rings[141] (Fig. 2.4). On the solid BZ reagent-infused hydrogel layer rests another layer of liquid BZ solution. The agarose hydrogel is solid enough to prevent convective instabilities and also sufficiently porous, such that the diffusion of chemical species in both layers is approximately identical. The first step of the initiation procedure is placing the clean end of a pure silver wire (99 % Ag) at the gel-liquid interface for about 15 s. Adding silver to the BZ solution allows for the formation of small amounts of AgBr[145]. This locally perturbs the chemical balance due to the removal of the inhibitor Br^-. Thus shortly after the silver wire is removed, a spherical wave starts to expand from the former location of the wire end. Similar to the initiation of a spiral wave (Fig. 2.1), a spherical wave is cut by strongly shaking the Petri dish, which holds the chemical medium. This removes any pattern in the upper liquid layer. The structure in the bottom solid part remains intact. After the liquid returns to rest, the wave resumes its propagation into the upper layer and forms the scroll ring.

The behavior of scroll rings is analyzed via space-time plots also known as kymographs. They are generated by plotting the intensity values of pixels taken along a line through the ring center from each image of the camera image sequence collected during the experiment. The space-time plots are processed further with a gradient filter to extract a parametrization

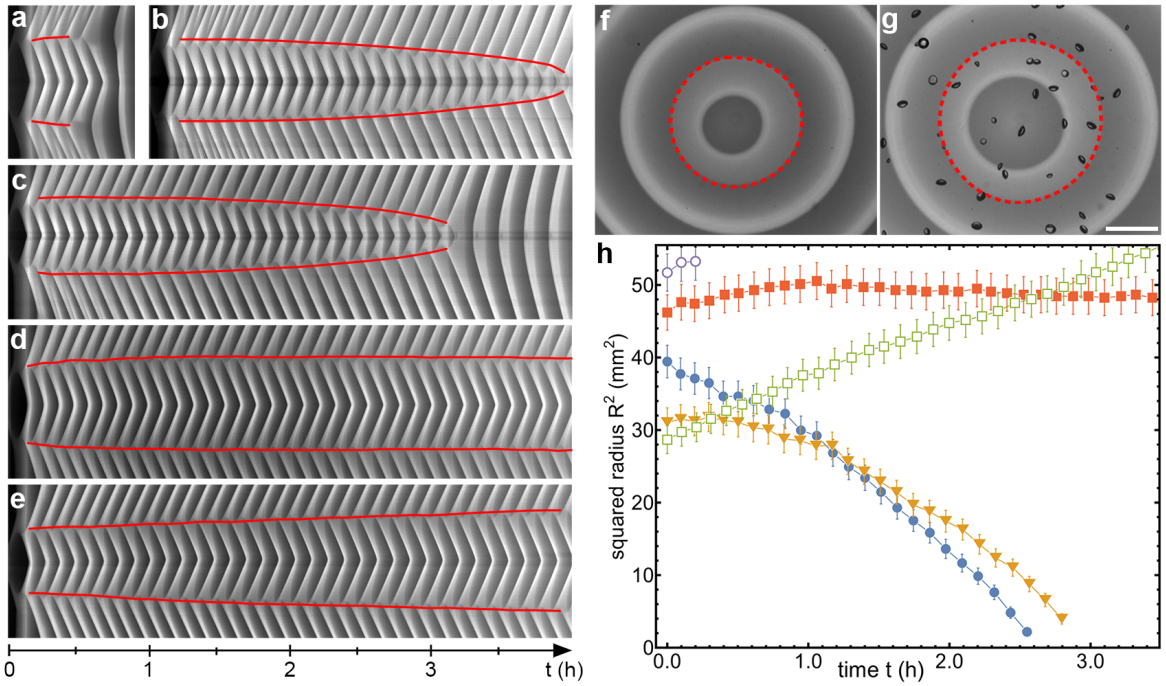

Figure 2.5 | Experiments on boundary-influenced scroll ring dynamics. Space-time plots extracted from a horizontal line through the center of each ring show excitation waves (grayscale) and filament dynamics (red) of representative cases: (a) collision of the scroll ring with the bottom boundary, (b) contracting free scroll ring outside the interaction range of the boundaries, (c) contracting, boundary-influenced scroll ring with reduced contraction rate, (d) quasi-stationary scroll ring, (e) expanding scroll ring. The vertical space axis corresponds to 2.3 cm in all cases. The horizontal time axis spans (a) 50 min, (b) 3 h, (c)–(e) 4 h. The heights of the solid layer h_1 and of the liquid layer h_2 were (a) 3 mm and 4 mm, (b) 4 mm and 4 mm, (c) 4 mm and 3 mm, (d) 4 mm and 2.5 mm, (e) 4 mm and 1.25 mm. (f) - (g) Two camera images show the expansion of the circular filament from (e) over the course of 3 h. The length of the white bar corresponds to 5 mm. (h) Radius dynamics extracted from space-time plots (a)-(e). Open circles: (a), full circles: (b), triangles: (c), full squares: (d) and open squares: (e). Error bars result from the measurement error of the spatial filament location.

for all wave trains. The intersection points of consecutive inward and outward traveling waves allow for the calculation of the filament radius over time $R(t)$. While a manual variant of this procedure was used in the past [146], it has been automatized for this thesis to analyze a large body of experiments in a short time.

The experiments reveal that the bottom Neumann boundary has a profound impact on the dynamics. Before summarizing the results of the experiments, note that in all presented examples, special caution has been given as to detect any occasions of filaments pinning to CO_2 bubbles. Experimental runs where this occurred were discarded, as pinning is known to lead to an increase in lifetime as well as stabilize filaments [141,147]. Successful experiments

without defect interactions can be subdivided into five qualitatively different categories based on their dynamics.

In the extreme case of initiating a scroll ring close to a boundary, the ring vanishes after few periods (Fig. 2.5a). Instead of contracting, the ring collides with the boundary. The collision does not happen concurrently along the filament: First a small fraction of the line singularity disappears and one rotation later the rest follows. Note that the filament grows slightly before colliding (Fig. 2.5h).

Sufficiently far away from any boundaries, $d = 0.7\,\lambda$, rings with positive filament tension α simply contract following equation (2.1), see figure 2.5b. In this case the squared radius decreases approximately linear with time in agreement with equation (2.3), as can be seen in Figure 2.5h. The measurement of the filament tension yields $\alpha = 0.026\,\lambda^2\mathrm{T}^{-1}$, which is in good agreement with previous experiments[148]. As can be expected its measured lifespan (2.6 hours) is in good agreement with its predicted lifetime

$$t_L = \frac{R_0^2}{2\alpha} \approx 2.5 \text{ hours}. \tag{2.5}$$

At a distance of $d = 0.5\,\lambda$, the boundary influence already impedes the natural contraction (Fig. 2.5c). This leads to a larger lifespan (2.8 hours) in comparison to what would have been expected (2.0 hours) based on the initial radius R_0 of the ring. Even though its initial radius is smaller, it lives significantly longer than the unperturbed ring (see yellow and blue markers in Fig. 2.5h).

In a small interval of boundary distances d, the contraction rate of rings effectively vanishes (Fig. 2.5d). The radius R barely changed for 55 periods, lasting over 5 hours. Longer measurements were inconclusive due to widespread nucleation of CO_2 bubbles throughout the active medium. However, given that the ring was expected to disappear after 2.9 hours due to contraction in the absence of boundaries, its persistence distinguishes it as a self-organized pacemaker.

Unexpectedly, scroll rings with positive filament tension, $\alpha > 0$, may also expand under the influence of a Neumann boundary (Fig. 2.5e-g). This behavior was previously assigned to negative filament tension, $\alpha < 0$, exclusively[149]. Expected to vanish after 1.8 hours, the ring radius is at 7.2 mm after 3.0 hours and continues to expand with $0.5\,\mathrm{mm\,h^{-1}}$. During this time the ring radius expanded by 40 %. Also, the ring does not show angular deformations during the expansion (Fig. 2.5f-g). Regular and deformed black circles correspond to CO_2 bubbles that nucleated in the liquid and gel part, respectively. However, no pinning interaction between bubbles and filament was observed.

The last two cases strikingly illustrate that a Neumann boundary does not lead to a small alteration of the contraction, but dramatically changes the expected behavior.

2.3 Numerical simulations and a kinematical model

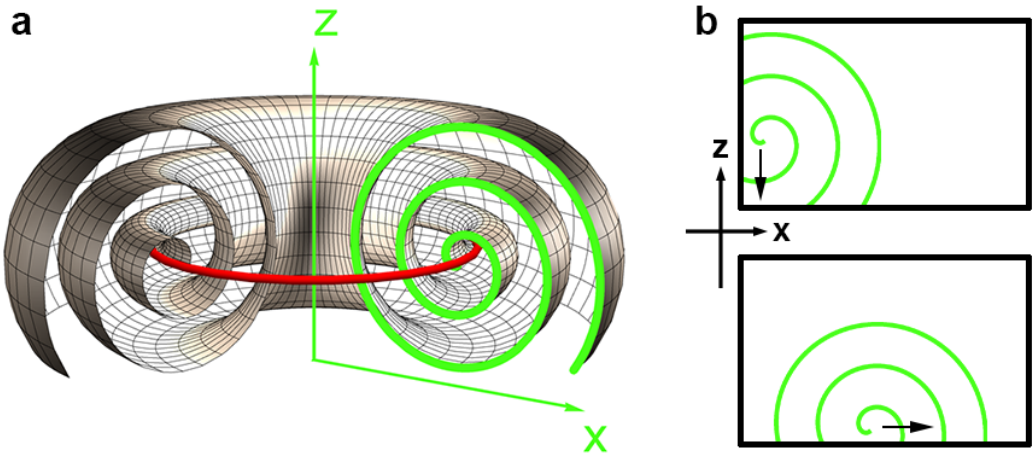

Figure 2.6 | Perturbations to confined small scroll rings. (a) One half of a cross section through a scroll ring is a spiral wave. (b) For a small scroll ring radius R, the spiral wave on the opposite site of the ring induces a perturbation that is equivalent to one from a Neumann boundary at the symmetry axis of the ring. Likewise when the scroll ring is close to a real bottom Neumann boundary, the constituting spiral waves are perturbed by it. In both situations the boundary causes spiral wave drift.

How exactly the observed surprising dynamics (Fig. 2.5) emerge is investigated further in numerical simulations. Especially the apparent contradiction of an expanding ring despite positive filament tension is resolved by constructing a detailed, kinematical model that accounts for Neumann boundaries.

From numerical simulations of three-dimensional excitable media, it is expected that boundaries may stabilize vortex patterns in systems with negative line tension $\alpha < 0$ [150,151]. This was also recently confirmed experimentally with setup II [152] (see appendix B.1.2). Intuitively this behavior is clear. An inspection of the spatial setting of the bounded scroll ring reveals, that it is equivalent to a two-dimensional spiral wave drifting at a Neumann boundary, since one half of a cross section through the ring is a spiral wave (see Fig. 2.6). Furthermore, it is well-established theoretically and experimentally that Neumann boundaries in two dimensions cause a stable spiral wave drift at a fixed distance in parallel to the boundary with a constant velocity $c_{\parallel}$ due to resonant perturbations [126,132,153]. A simple dynamical system for the behavior of a scroll ring in boundary proximity takes this drift attractor into account.

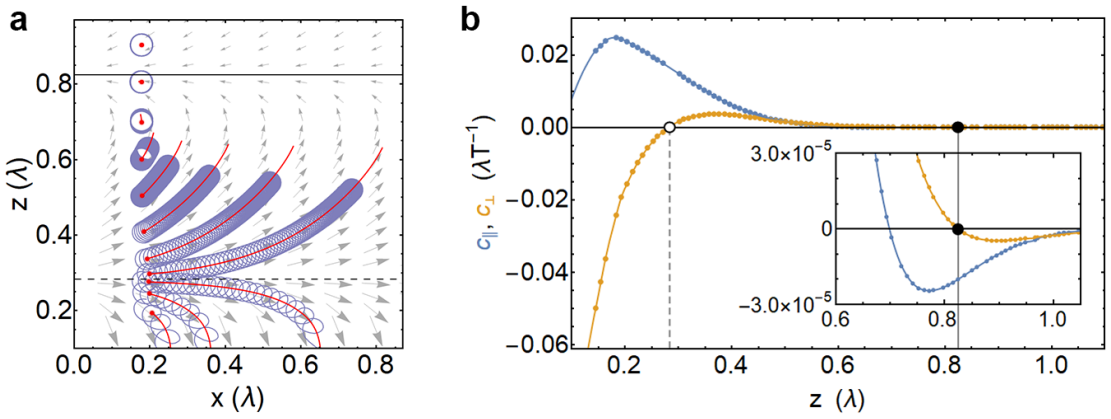

Figure 2.7 | Numerically determined drift-velocity field components. (a) Trajectories of spiral waves in the Neumann boundary-induced drift velocity field. The trajectories of the core centers (red) are extracted from averaging over the spiral tip trajectories (blue). The size of the gray arrows is scaled monotonically to visualize the direction and modulus of the vector field across different orders of magnitude. (b) Both velocity components are plotted over distance. The normal component has two fixed points. The velocity at the stable fixed point far from the boundary, $z_{att} \approx 0.824605\,\lambda$, is too small to cancel ring contraction. The unstable fixed point at $z_{rep} \approx 0.2834785\,\lambda$, is close enough to the boundary to exert a potential influence on ring dynamics. The solid lines through the measurement points are high-order spline interpolating functions.

Augmenting equation (2.1) leads to

$$\frac{dR}{dt} = -\alpha/R + c_{\parallel}\,. \tag{2.6}$$

The fixed point exists if the intrinsic radius dynamics and drift motion cancel each other. For the case of negative line tension $\alpha < 0$ this fixed point is stable. However, linear stability analysis for positive line tension reveals an unstable fixed point, so the stationary dynamics observed in the experiment (Fig. 2.3d) was not thought to be possible for $\alpha > 0$.
To resolve this conundrum, a more detailed measurement of the boundary-induced drift velocity field $\boldsymbol{c}(z)$ outside of the stable drift attractor is required. Numerical simulations can be employed to easily exclude any unwarranted perturbations on the spiral wave but the boundary. The chemical kinetics of the ferroin-catalyzed BZ reaction are well-described by the Rovinsky model[154] (see appendix C.2):

$$\frac{\partial u}{\partial \tau} = \frac{1}{\varepsilon}\left[u(1-u) - \left(2qa\frac{v}{1-v} + b\right)\frac{u-\mu}{u+\mu}\right] + D_u\nabla^2 u, \tag{2.7}$$

$$\frac{\partial v}{\partial \tau} = u - a\frac{v}{1-v} + D_v\nabla^2 v. \tag{2.8}$$

Table 2.1 | Vortex properties. Comparison of characteristic properties of experimentally and numerically observed vortex patterns.

property	experiment	simulation
wavelength λ	5.8 mm	5.6 mm
rotation period T	390 s	372 s
filament tension α	$0.026\,\lambda^2\mathrm{T}^{-1}$	$0.024\,\lambda^2\mathrm{T}^{-1}$

The parameters of this reaction diffusion system are derived from concentrations used in the chemical experiments (see table C.4). Resulting pattern characteristics from numerical simulations, such as wavelength, rotation period and filament tension, are in excellent agreement with the experiments. A comparison of the characteristic properties is given in table 2.1.

The drift velocity field induced by a planar Neumann boundary $\boldsymbol{c} = (c_\parallel, c_\perp)$ is measured in simulations of a spiral wave in a two-dimensional domain, see Fig. 2.7. The spiral tip trajectory is evaluated in such a way, that the tip rotation is averaged out and only the trajectory of the core center remains. After a transient these trajectories are analyzed to reconstruct the drift velocity field in dependence of the distance to the boundary. As can be seen in figure 2.7a, the stable drift attractor is so far away from the Neumann boundary, $z_{att} \approx 0.82\,\lambda$, that the spiral wave motion is barely affected. All shown trajectories are integrated over the same time duration of 300 unperturbed rotation periods. There is also another attractor at $z_{rep} \approx 0.28\,\lambda$, but it is unstable. Any spirals that start very close to it, will either be repelled away from the boundary or pushed into it. Due to the translation symmetry of the drift field, $\boldsymbol{c}(x,z) = \boldsymbol{c}(z)$, its components can be plotted over the distance z from the boundary (Fig. 2.7b).

Now that the complete boundary-induced drift field is known, we can construct a detailed kinematic model. To this end we will take into account the real bottom Neumann boundary as well as the symmetry axis. Unless the ring is very large, each spiral wave feels its opposite counterpart. Since the configuration is mirror symmetric about the z-axis, the concentration gradient across the axis vanishes: $\nabla u = \nabla v = \mathbf{0}$. The same condition holds true at a Neumann boundary (see Fig. 2.6b). Incorporating both boundaries into the kinematical model of a free ring, (2.1) and (2.2), results in a semi-analytic model that accounts for the boundary

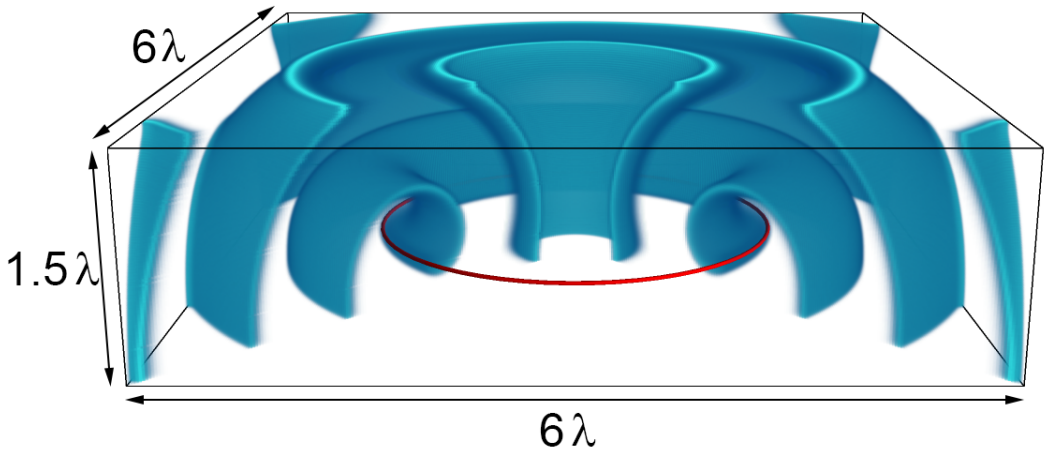

Figure 2.8 | Visualization of a simulated scroll ring. All parts of the concentration field $u(x,y,z)$ are colorized in blue whose values are larger than 0.35. The red ring highlights the position of the filament, which is the organizing center of the entire ring. A fraction of the ring is transparent to visualize the inner parts.

influences:

$$\frac{dR}{dt} = -\alpha/R + c_{\parallel}(z) + c_{\perp}(R), \tag{2.9}$$

$$\frac{dz}{dt} = \beta/R + c_{\perp}(z) - c_{\parallel}(R). \tag{2.10}$$

Variables R and z still describe the radius of the ring and its position along the symmetry axis. The influences of a horizontal Neumann boundary at $z = 0$ and a virtual vertical Neumann boundary at $R = 0$ (see Fig. 2.6) are introduced as additive perturbations. The perturbations are the previously measured boundary-induced drift velocity fields in two dimensions $\boldsymbol{c}(z)$. The minus sign in front of $c_{\parallel}(R)$ accounts for the z-axis being oriented in the opposite direction in comparison to the setting it was measured in (Fig. 2.7a). The distance to the boundary is not affected by the flip, so $c_{\perp}(R)$ is included with a positive sign.
The validity of the modified kinematical model is checked by comparing solutions of the two-component ODE (2.9) with the filament dynamics extracted from the time evolution of a full three dimensional partial differential equations, (2.7) and (2.8), that faithfully reproduces the chemical dynamics in the Petri dish (see section 2.2). [c]

[c]Note that the azimuthal symmetry of the scroll ring could be exploited for fast simulations in a two-dimensional domain of reduced cylindrical coordinates[155]. However, this approach would also suppress potential instabilities along the azimuthal direction. For example, it is known, that an inclined orientation of the filament plane relative to the Neumann boundary induces twist waves along the filament[156,157].

The reaction diffusion equations are solved on a three-dimensional Cartesian grid employing a finite-difference explicit Euler scheme[158] for speed reasons with a time step of $\Delta t = 0.05\,s$. The diffusion operator is evaluated over a 7-point Laplacian stencil with $\Delta x = 0.001\,cm$. The instantaneous filament location is determined as the set of points, which form the intersection of two level sets of the activator variable $u(x,y,z) = 0.2$ from subsequent time steps. The simulation domain is a large cuboid with length and width of $6\,\lambda$ and height of $1.5\,\lambda$. The bulk volume is bounded by Neumann boundaries. The spiral wave length λ is measured in advance to compute the required lengths. The scroll rings in the simulations are initiated in a similar manner to the experiments: They nucleate from an initial cylindrical wave whose upper fraction is removed at the start of the simulation. The size of the deleted upper fraction determines the initial distance $z(t=0)$ to the interacting, bottom Neumann boundary. The top and lateral boundaries are placed sufficiently far away to neglect their influence on the ring. A fully developed scroll ring is shown in figure 2.8. The three-dimensional numerical simulations are parallelized for fast computation and are performed on a graphical processing unit (Nvidia GTX 970), more implementation details and a speed comparison are in the appendix B.2.

As can be seen in figure 2.9a, the observed filament dynamics of the PDE, (2.7) and (2.8), in three spatial dimensions are in excellent agreement with the solutions of the semi-analytical kinematical ODE model (2.9). Thus the influence of the boundaries is correctly incorporated in the reduced ODE model (2.9). To facilitate the comparison with the experimental results, distinctive numerical trajectories are labeled (A-E) corresponding to the subfigure labels (a-e) in figure 2.5. All cases observed in the chemical experiments were reproduced in numerical simulations of the underlying reaction diffusion equations and accounted for in the modified kinematical model (2.9).

As in two dimensions (Fig. 2.7a), rings starting at a distance of $z > 0.5\,\lambda$ are barely affected by the bottom Neumann boundary (case B) and contract according to the unperturbed dynamics (2.1). Only towards the end of their lifetime t_L, when they reach a radius of $R < 0.5\,\lambda$ they are slightly pushed downwards, which is due to the mirror symmetry of the ring.

The repelling line in the drift velocity field at $z \approx 0.28\,\lambda$ still plays an important role. It separates rings that vanish by collision with the Neumann boundary at $z = 0\,\lambda$ (A) from those that contract $R \to 0\,\lambda$ (C). The contraction rate of repelled rings is impeded initially by the antagonistic influence of the boundary-induced drift $c_{\parallel}(z)$. However, due to the repulsion, the impeding influence of the boundary lessens with increased distance from it (Fig. 2.7b).

Within the framework of the kinematic model (2.9) it is also possible to explain the unexpected observation of persistent and expanding scroll rings in the experiment (Fig. 2.5d,e).

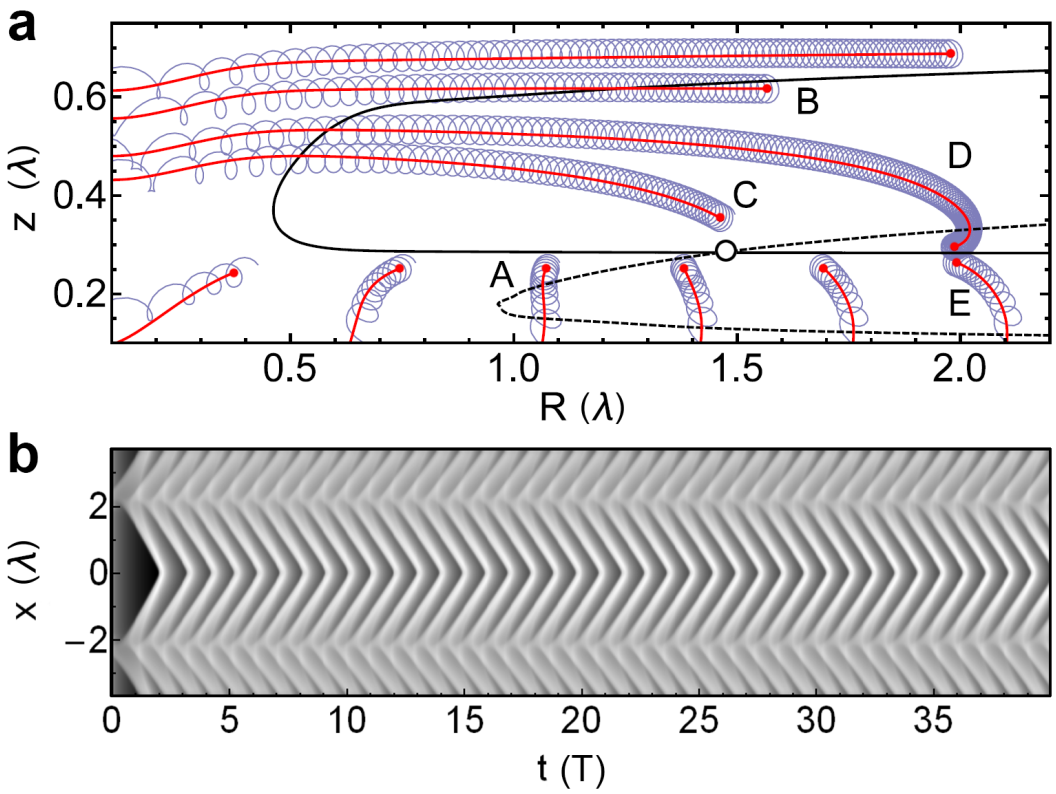

Figure 2.9 | Agreement between full three-dimensional simulations and kinematical model. (a) Radius R and boundary distance z of the three-dimensional filament evolution (blue) are extracted to compare with the solutions (red) of the kinematical model (2.9). Trajectories highlighted with capital letters (A-E) correspond to the five distinct cases observed in the experiment, which are summarized in figure 2.5 (a-e). At the intersection of the R- and z-nullclines (dashed and solid) is an unstable fixed point, which is marked by an unfilled circle. (b) A space time plot of the quasi-stationary solution (D) shows the long-time stable behavior of the transient. Parameters for the reaction diffusion system are as before and in the kinematic model $\alpha = 0.0245\,\lambda^2\mathrm{T}^{-1}$ and $\beta = -0.0004\,\lambda$.

Expanding scroll rings (E) are a special case of rings that annihilate at the boundary (A). However, they start closer to the repelling line and thus grow for a longer time before ultimately colliding with the boundary as well. Note that the dashed R-nullcline in Figure 2.9a reveals that expanding rings require a minimum initial radius R_0.

Surprisingly, the fixed point in the modified kinematic model (2.9) is unstable, even though experimental observation (Fig. 2.5d) suggests otherwise. This contradiction is resolved by analyzing the behaviors of scroll rings that originate in a small region enclosed by the R-nullcline from above and the z-nullcline from below at large radii (D). Before entering the contraction phase, these rings undergo a long-lasting transient during which their radius barely changes. An exemplary evolution of such a ring during its first 40 periods is depicted in the space-time plot shown in figure 2.9b.

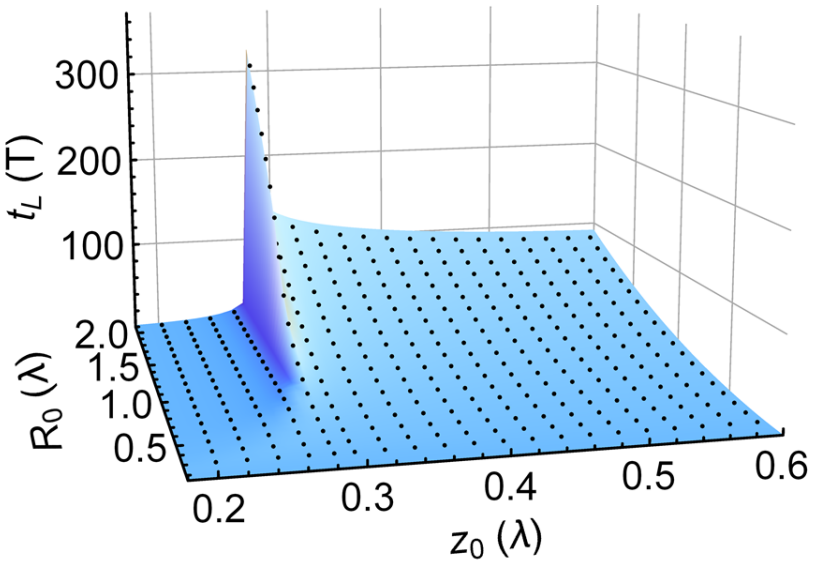

Figure 2.10 | Scroll ring lifetimes. For different initial values of radius R_0 and boundary distance z_0 the lifetime of the contracting scroll ring is determined via the modified kinematical model (2.9). The peak in the lifetime plane corresponds to the quasi-stationary solution. The saturation of the lifetime for large z_0 corresponds to the lifetime of a free ring. The flat plateau for small z_0 corresponds to rings that collide with the boundary.

Having validated the modified kinematical model (2.9), it is now possible to run a large number of simulations in a very short amount of time to determine the lifetime t_L of scroll rings starting at different initial conditions (R_0, z_0). For a fixed initial distance from the boundary z_0, larger rings outlast smaller rings. Rings that start at a sufficient distance of $z_0 > 0.5\,\lambda$ are not affected by the boundary. Their lifetime shows the expected quadratic dependence (2.5) on the initial ring radius R_0. Initial distances z_0 closer to the repelling line at z_{rep} lead to rings with diminished ring contraction rates that live slightly longer. Expanding and quasi-stationary rings contribute to the peak in figure 2.10. There, lifetimes are more than tripled. If rings start too close to the boundary, their lifetimes are an order of magnitude smaller in comparison to their unperturbed counterparts. This is in agreement with previous explicit simulations [155] of the reaction diffusion system.

The use of the modified kinematical model (2.9) is not limited to an accelerated exploration of parameter space. It can also be used for a bifurcation analysis depending on the filament tension α and drift coefficient β. Note that the right hand-sides of the dynamical system (2.9), $f_R(R,z)$ and $f_z(R,z)$ are not known explicitly. Instead they are defined by spline interpolation applied to the numerical measurements of the spiral wave drift velocity field $\boldsymbol{c}(z)$ (Fig. 2.7b). The fixed points are found numerically as the roots of (2.9) using Newton's method [158]. To accelerate their detection, the initial estimate for each parameter set is based on the roots

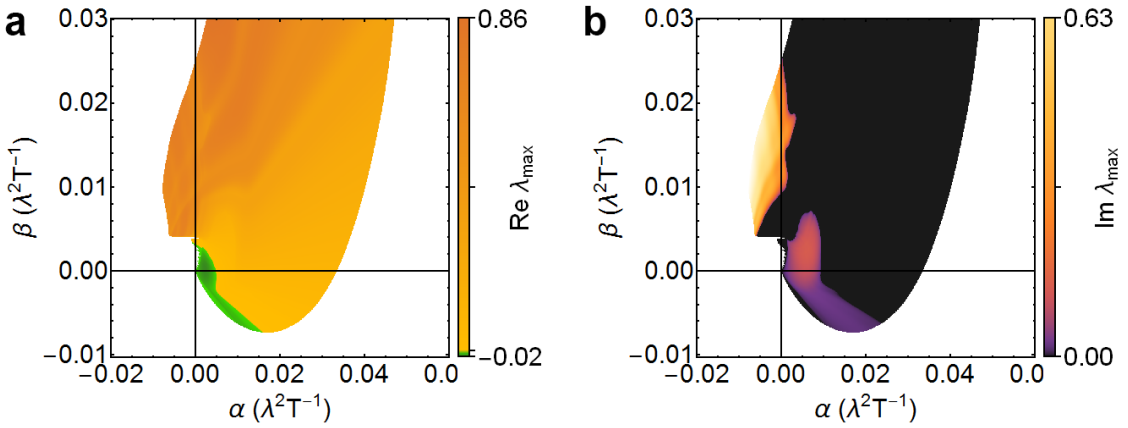

Figure 2.11 | Bifurcation analysis of the semi-analytical model. The fixed points of (2.9) and their linear stability are evaluated numerically, since analytic expressions are not available. The approximated right hand sides $f_R(R,z)$ and $f_z(R,z)$ of (2.9) are constructed from the interpolated functions shown in figure 2.7b. The bifurcation dividing unstable from stable rings is revealed to be a Hopf bifurcation, due to the non-vanishing imaginary part (b), while the real part (a) of the largest eigenvalue changes its sign.

found previously. In figure 2.11 only fixed points with $R_0 \in [0.1, 2.0]\,\lambda$ and $z_0 \in [0.1, 1.0]\,\lambda$ are taken into account. Values smaller than $0.1\,\lambda$ are unrealistic, since the spiral core, the area around which the spiral tip rotates, has a radius of about $0.1\,\lambda$. At larger distances than $z_0 = 1.0\,\lambda$, the boundary interaction vanishes. Also it is not feasible to initiate scroll rings with radii larger than $2.0\,\lambda$ using the setup described in section 2.2.

In the next step, the linear stability of the detected fixed points is analyzed via their eigenvalues. The required Jacobian $\underline{\underline{D\boldsymbol{f}}}$ is evaluated numerically using central differences:

$$\underline{\underline{D\boldsymbol{f}}} = \begin{pmatrix} \frac{f_R(R_0+\Delta R,z_0)-f_R(R_0-\Delta R,z_0)}{2\Delta R} & \frac{f_R(R_0,z_0+\Delta z)-f_R(R_0,z_0-\Delta z)}{2\Delta z} \\ \frac{f_z(R_0+\Delta R,z_0)-f_z(R_0-\Delta R,z_0)}{2\Delta R} & \frac{f_z(R_0,z_0+\Delta z)-f_z(R_0,z_0-\Delta z)}{2\Delta z} \end{pmatrix} \tag{2.11}$$

The analysis shows that the majority of parameter combinations (α, β) yield unstable fixed points (Fig. 2.11). However, there is a small region, which features stable fixed points for very small values of positive filament tension α and drift coefficient β. Previously this behavior was purely associated with negative line tension. Both domains are connected via a Hopf bifurcation, since the imaginary part of the largest eigenvalue does not vanish during the transition.

The attracting fixed point in the R-z phase space is due to a cusp in the R-nullcline (Fig. 2.12a). In the back of the cusp the R-nullcline has a negative slope and the z-nullcline has a positive slope allowing for a stable fixed point. The time series (Fig. 2.12b) shows that the transient

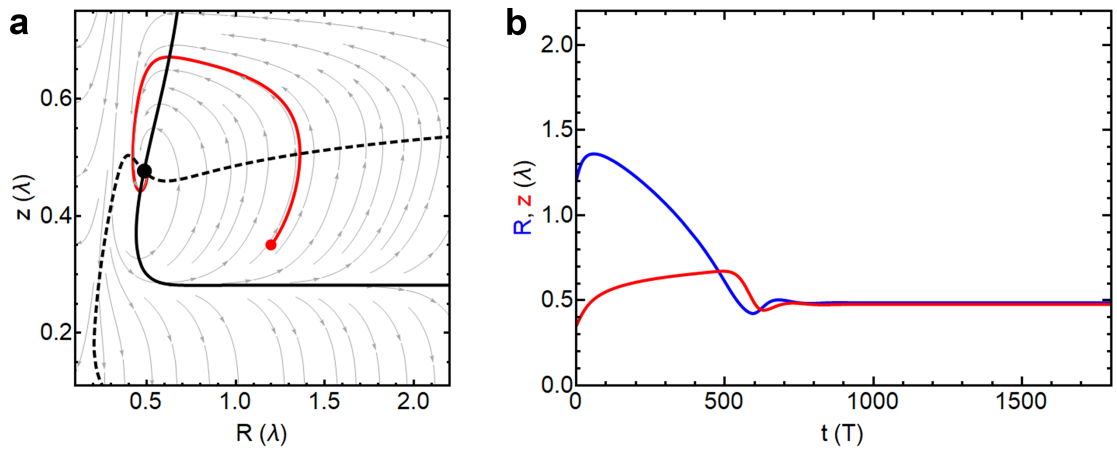

Figure 2.12 | Time evolution of stable scroll ring. (a) Filament dynamics of a stable ring in the R-z phase space. Shown in red is the solution of (2.9) for $\alpha = 0.002\,\lambda$ and $\beta = 0\,\lambda$. The trajectory starts at $(R_0, z_0) = (1.2, 0.35)\,\lambda$ (red dot) and ends in the stable fixed point (black dot) located behind a cusp in the dashed R-nullcline. (b) The radius R (blue) and boundary distance z (red) as a function of time t show the long transient period before reaching the stable fixed point at $(R, z) \approx (0.49, 0.48)\,\lambda$.

is very long: It takes 800 rotation periods before reaching the fixed point. For the purpose of an experimental confirmation it would be advantageous to start closer to the fixed point.

This transition also plays a role in the dynamics of scroll rings, simulated with the Oregonator model (C.2). Close to the bifurcation, breathing filaments exist, whose radius is a periodic function of time[152].

The interaction across the symmetry axis alone can also lead to stabilization of the scroll ring (Fig. 2.13). After a transient of about 50 periods, the self-stabilized ring exhibits a constant radius at $R = 0.38\,\lambda$ and drifts with constant speed of $v_z = 0.13\,\lambda\,\mathrm{T}^{-1}$ along its symmetry axis. While there are previous studies of this object[134,159–161], so far none confirmed its existence in full three-dimensional simulations over a long period of time. Here, the simulation was performed with the three-component Oregonator model (C.2) in a cuboid with periodic boundary conditions on all sides. Lateral boundaries are placed at sufficient distance to exclude their influence. New initial conditions are required, as the cut cylinder used before would give rise to a scroll ring pair due to the periodic boundary conditions. For this purpose, we start from a planar excitation wave traveling in the z-direction. Then a circular hole of the desired initial radius R_0 is cut out of the planar wave. Along the open edge waves start to curl in and give rise to the scroll ring.

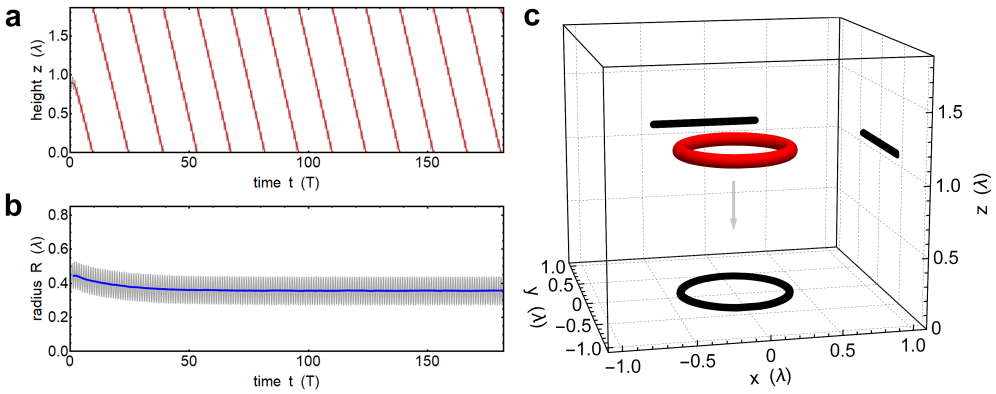

Figure 2.13 | Self-stabilized scroll ring. (a) The ring periodically traverses the simulation box with constant velocity due to the periodic boundaries. (b) After a transient, the ring reaches its stable radius of $R = 0.38\,\lambda$. The blue and red curves are the result of averaging over the fast filament oscillations during each rotation period. (c) A snapshot of the planar filament (red) in the three-dimensional simulation volume. The current position of the filament is highlighted by black projections on the box faces. The model parameters of the simulation are: $\varepsilon_1 = 1/8, \varepsilon_2 = 1/720, q = 0.002, f = 1.16$, $\phi = 0.0117$ with $\Delta x = \Delta y = \Delta z = 0.3$ and $\Delta t = 0.001$. The filament was detected as the intersection of the isoconcentration level sets $u(x,y,z) = 0.3$ and $v(x,y,z) = 0.2$.

2.4 Chapter summary

Neumann boundaries transform transient scroll rings into autonomous pacemakers in a homogeneous medium. As such they act as a self-organized source of periodic excitation waves. Unexpectedly, this is possible even for rings with positive filament tension, that would contract and vanish far from any boundaries. Beyond stabilizing - if only for a long transient - Neumann boundaries can invert the radial contraction, such that rings expand. This case was previously associated with negative filament tension exclusively.

All these distinct scenarios of scroll ring evolution observed in the experiment (Fig. 2.5) could be successfully reproduced with numerical simulations of the underlying reaction diffusion equations (Fig. 2.9a) that are in excellent agreement with a kinematical model (2.9) which is augmented to correctly account for boundary effects [162].

With the semi-analytical, data-driven model (2.9) very fast explorations of parameter space are possible (Fig. 2.10). In addition bifurcation analysis can be performed, even though the explicit formulas for boundary influenced scroll ring evolution are unknown (Fig. 2.11). This reveals the possibility of stable boundary-stabilized rings with positive filament tension (Fig. 2.12). Last but not least, the existence of self-stabilized rings in the absence of boundaries is also confirmed (Fig. 2.13).

Given that three-dimensional unperturbed scroll rings disappear on their own, the number of different scenarios under which persistent rings may appear is remarkable.

2.5 Future directions

Alternative strategies for the stabilization of scroll rings were previously investigated numerically, but never verified experimentally. This includes parametric spatiotemporal fluctuations [163] or periodic forcing [121,164,165]. Feedback methods based on the readout of localized detectors [166,167] have not been used so far to stabilize rings. Due to the inherent difficulties of applying a spatiotemporal parametric field in three dimensions, a more elegant method might be to select the shape of boundaries in such a way that they stabilize rings at a predetermined radius.

Measuring the boundary-induced drift velocity field in an experiment is difficult. The first problem is a reliable detection of the spiral wave tip. Instead of detecting it by the intersection of grayvalue-isolines from consecutive images, another more accurate option is to train image recognition software on the shape of the spiral tip. The other problem is measuring the velocity reliably. Even in simulations it is difficult to extract valid data points close to the boundary, since the spiral wave will collide with it. To circumvent this problem, one could apply an electric field. Spiral wave are known to drift in a voltage gradient [124] with constant velocity $\boldsymbol{c}^E = (c_x^E, c_z^E)$. Together with the boundary induced drift field, the equation of motion for the spiral core are:

$$\frac{dx}{dt} = c_{\parallel}(z) + c_x^E \tag{2.12}$$

$$\frac{dz}{dt} = c_{\perp}(z) + c_z^E \tag{2.13}$$

After measuring the constant drift due to the electric field $\boldsymbol{c}^E$, it can be aligned to counteract the component of the boundary-induced drift velocity field $c_{\perp}(z)$ that pushes spiral waves away or into the boundary, such that:

$$\frac{dz}{dt} = c_{\perp}(z) + c_z^E = 0 \tag{2.14}$$

While the spiral wave drifts slowly in parallel to the attractor, its drift speed $c_{\parallel}(z) + c_x^E$ can be measured reliably. This measurement can be repeated for different amplitudes or orientations of the electric field, in order to counteract different strengths of the perpendicular component $c_{\perp}(z)$. After subtracting the contribution from the electric field, one can reconstruct the boundary-induced drift velocity field for both components $c_{\parallel}(z)$ and $c_{\perp}(z)$ with precision.

To further improve upon the modified kinematical model (2.9), it is necessary to take into account drift velocity functions $\boldsymbol{c}(z;\boldsymbol{p})$ that depend on system parameters $\boldsymbol{p}$, as does the filament tension $\alpha(\boldsymbol{p})$ and the drift coefficient $\beta(\boldsymbol{p})$.

The strategy of stancing shapes out of a planar wave to nucleate a filament, can be developed further. The approach is not limited to circular filaments. It is also possible to create initially elliptic, square or heart-shaped filaments. The evolution of the latter case is interesting since its curvature varies from $\kappa \to -\infty$ to $\kappa \to +\infty$ while traversing from one cusp to the other. Another interesting case are yin-yang patterns, that keep their shape while rotating under curvature flow[119,168]. The simulations can be validated in auto-completion experiments with a photosensitive BZ reaction[169], where the top layer of an active medium is uniformly irradiated with light except at the edges of the desired shape.

Chapter 3

Target Wave Synchronization on a Network

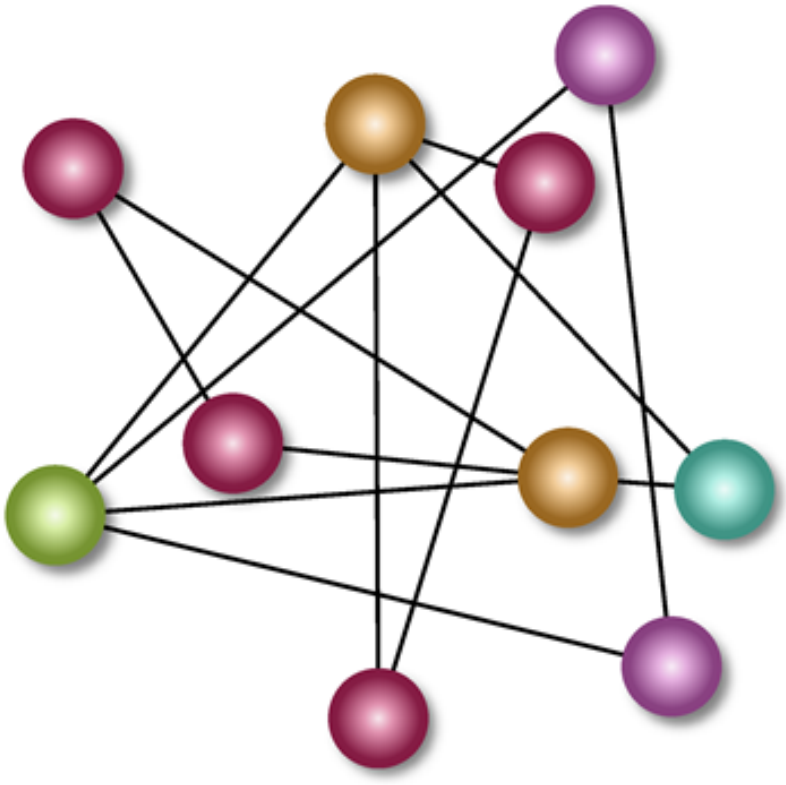

Human brain activity is an enigma. There is no chance in the near future to unravel the network of billions of neurons and trillions of connections between them[170]. To make matters worse, this is only a static snapshot of a single instant in time. Discovered more than a century ago by one of the pioneers of neurobiology, Santiago Ramón y Cajal, the brain connectome is not static, but dynamic[171,172]. This plasticity allows for learning[173–175], memorization[176,177] and encompasses regeneration[178,179].
One of the currently unsolved puzzles of inner brain mechanisms regards synchronization[180]. Experiments showed its relevance in perception processing and motor control[181,182], while pathological enhanced synchronization underlies symptoms in Parkinson's disease[183], Tinnitus[184,185] and epilepsy[186,187]. In a very simplified description, each neuron can be regarded as an oscillator. Since the pioneering work of Norbert Wiener[188] electroencephalographic measurements revealed the occurrence of synchronization among nerve cells in the brain. Further observations reveal that neurons tend to synchronize without a time-lag or in-phase $\Delta\phi = 0$[189], even though they are far apart and communication speed is finite[190]. One approach is, that in-phase synchronization can be relayed via an intermediate[191,192], other options are lag synchronization[193] and remote synchronization[194].
This chapter features experimental results on lag synchronization with neuromorphic chemical micro-oscillators. The notion of a target wave in a continuous medium is extended to networks via an analysis of the underlying symmetries.

3.1 Theoretical Background

The last decade saw an increased theoretical interest in generalizing continuous pattern formation terminology to discrete networks. The groups of Mikhailov and Schöll for example generalized Turing[195,196] and Benjamin-Feir[197] instabilities as well as the eikonal equation and propagation failure of excitation waves[198,199] to networks. Likewise lag-synchronization on a network is deeply connected to propagating excitation waves in an active medium. Once the excitation threshold is crossed due to coupling to the surrounding medium or neighboring oscillators, an oscillator emits a spike[38]. The spatial profile of these waves is determined by initial conditions. In two dimensions the basic examples encompass planar, spiral and circular waves, the last of which are known as target patterns[38]. In the same sequence, the wave propagation of these patterns accumulates translation, rotation and reflection symmetries. The target wave is special, because it conforms to all symmetries in the system, which together form the Euclidean symmetry group E(2). Also note that in a suitable co-moving reference frame, the concentration waves are stationary in time, $\boldsymbol{c}(\boldsymbol{r},t) = \boldsymbol{c}(\boldsymbol{r} - \boldsymbol{v}t)$.

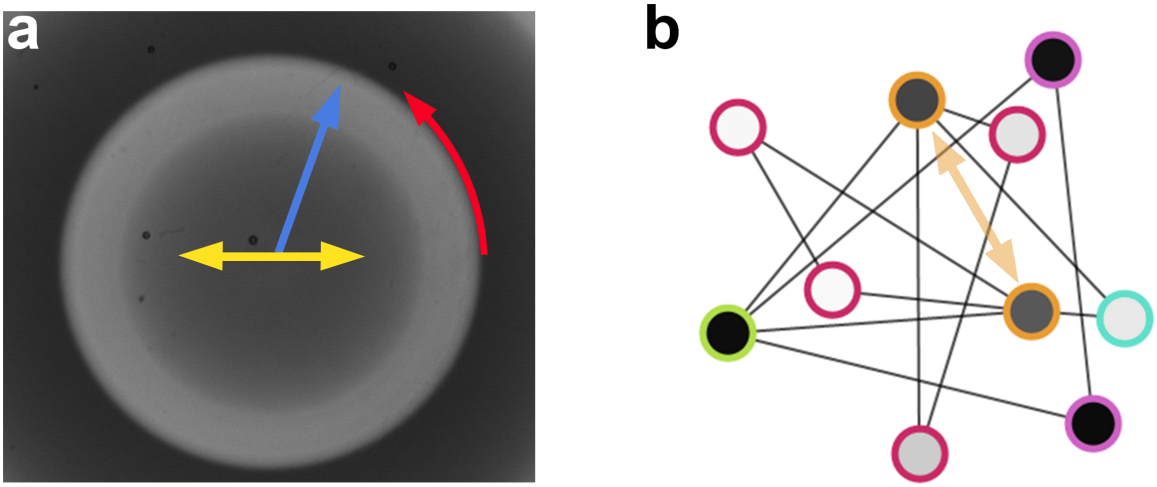

Figure 3.1 | Symmetries in continuous media and discrete networks. (a) A target pattern in a continuous BZ medium propagates, while preserving rotation (red), reflection (yellow) and translation (blue) symmetry. (b) The symmetries on a network are permutation automorphisms highlighted by identical edge colors. Under application of any of the corresponding permutation operators the pattern stays invariant throughout its evolution. On a network, a target wave is harder to naively detect, since the position of the drawn nodes does not necessarily reflect their distance form a pacemaker site. In both subfigures symmetry operations are depicted as arrows.

On a network of discrete nodes[200] the generalization of the target wave is not straightforward, because the Euclidean symmetry group is not applicable. Instead, a network of identical nodes features discrete permutation symmetries[201]. Permutation operations, defined by the permutation matrix $\underline{\underline{P}}$, exchange up to N nodes of a network. The connections between the nodes are given by the adjacency matrix $\underline{\underline{A}}$, whose elements follow:

$$A_{ij} = \begin{cases} 1 & \text{, node } i \text{ is connected to node } j \\ 0 & \text{, node } i \text{ is not connected to node } j. \end{cases} \tag{3.1}$$

A given permutation operation is a symmetry or automorphism of the network, if it obeys[194]:

$$\underline{\underline{A}}\,\underline{\underline{P}} - \underline{\underline{P}}\,\underline{\underline{A}} = [\underline{\underline{P}}, \underline{\underline{A}}] = 0. \tag{3.2}$$

This means, that the adjacency matrix $\underline{\underline{A}}$ is invariant under the given permutation operation. Furthermore, every network can be completely partitioned into symmetry clusters, which are defined as sets of nodes, whose exchange leaves the network connectivity unaltered. A symmetry cluster that contains only a single node is called a trivial symmetry cluster. The only applicable permutation operation in this case is the identity operation: It can only be exchanged with itself without changing the connectivity.

Recently Lou Pecora and coworkers[202] were able to generalize their Master Stability Function (MSF) formalism[203,204] exploiting network symmetries. Their formalism applies to a network, whose N nodes are oscillators, that communicate along the edges of the network:

$$\frac{d\boldsymbol{c}_i}{dt} = \boldsymbol{f}(\boldsymbol{c}_i) + K \sum_{j=1}^{N} A_{ij} \boldsymbol{H}(\boldsymbol{c}_i, \boldsymbol{c}_j) \tag{3.3}$$

The n_c dynamical variables of each oscillator i evolve according to the local dynamics $\boldsymbol{f} : \mathbb{R}^{n_c} \to \mathbb{R}^{n_c}$. The coupling to the network consists of two parts: The adjacency matrix $\underline{\underline{A}} \in \mathbb{R}^{N \times N}$ encodes what the neighbors of node i are and the coupling function $\boldsymbol{H} : \mathbb{R}^{n_c} \to \mathbb{R}^{n_c}$ determines how node i is coupled to its neighbors, for example diffusively or pulse-coupled[205]. The accumulated signals of the neighbors are scaled with the coupling strength K.
In this setting, the MSF allows for calculating the linear stability of the fully in-phase synchronized state, where $\boldsymbol{c}_i(t) = \boldsymbol{c}_{sync}(t)$ for all N oscillators in the network. This is achieved by calculating the Lyapunov exponents of transversal perturbations to the synchronization manifold. The longitudinal perturbation as the Goldstone mode has neutral stability[206]. However, this analysis was only applicable to the complete network, but not subnetworks. Furthermore the connectivity of all nodes is required to be identical, otherwise the synchronization manifold is not stable: Once all nodes reach the synchronized state $\boldsymbol{c}_{sync}(t)$, they need to receive the same input from their neighbors to remain synchronized.
Incorporating symmetries allows for decoupling the nodes, such that the synchronization manifolds of the decoupled symmetry clusters can be investigated independently. Intuitively, this approach works, because nodes in the same symmetry cluster can be exchanged without alteration of the network. This implies that the nodes in a symmetry cluster are all coupled identically to the rest of the network and vice versa. As an example, the evolution equations for the two orange nodes in figure 3.1b, here in keeping with later notation labeled as $i = 2, 3$, are

$$\frac{d\boldsymbol{c}_2}{dt} = \boldsymbol{f}(\boldsymbol{c}_2) + K\left(2\boldsymbol{c}_{\text{magenta}} + \boldsymbol{c}_{\text{green}} + \boldsymbol{c}_{\text{cyan}} - 4\boldsymbol{c}_2\right), \tag{3.4}$$

$$\frac{d\boldsymbol{c}_3}{dt} = \boldsymbol{f}(\boldsymbol{c}_3) + K\left(2\boldsymbol{c}_{\text{magenta}} + \boldsymbol{c}_{\text{green}} + \boldsymbol{c}_{\text{cyan}} - 4\boldsymbol{c}_3\right). \tag{3.5}$$

In the above example, the coupling function was taken as the concentration difference between two coupled oscillators, $\boldsymbol{H}(\boldsymbol{c}_i, \boldsymbol{c}_j) = \boldsymbol{c}_j - \boldsymbol{c}_i$. The coupling term for both oscillators consists of identical contributions from the other symmetry clusters. Given that the other nodes are synchronized in their respective symmetry clusters, all orange nodes receive the same input from the rest of the network and thus can be treated as an independent

subnetwork. While previously, the applicability of the MSF was limited to the stability of global synchronization of identically coupled nodes, the symmetry decomposition allows for evaluating the stability of symmetric subnetworks, such as those found in power grids[202]. Even introducing small parameter mismatches in the oscillators still allows for the successful application of the MSF[207]. However, at sufficiently large parameter mismatches in-phase synchronization ceases to exist. Instead one node will have the highest frequency in the network. This node acts as the pacemaker and over time entrains the rest of the network. Thus wave-like synchronization emerges, where all oscillators have the same frequency but varying phases ϕ, following:

$$\phi(i,t) = \phi\left(d(i,i_0) - \Delta\phi \cdot t\right) \tag{3.6}$$

where $d(i,i_0)$ is the discrete network distance between nodes i and i_0 as given by the commonly employed shortest distance algorithm by Dijkstra[208]. Node i_0 is the fastest node in the network and thus the source of the wave. Phases $\phi(t)$ can be calculated from concentration time series $\boldsymbol{c}(t)$ as described in appendix A.1. $\Delta\phi$ is the constant phase difference between neighboring oscillators with unequal distance to the source node i_0. Furthermore the phase difference is identical to the slope of the wave $m = \Delta\phi/\Delta d$, since the distance measure is discrete, $\Delta d = 1$.
This discrete wave is well-established in biological settings. There it emanates from a central pattern generator (CPG) in neural networks, which controls locomotion[209]. One neuron after another in a chain fires and periodically initiates muscle movement. This leads to swimming in case of eels or walking gaits in hexapods. The CPG architecture has also been successfully applied to construct robots that mimic the motion of animals, such as snakes[210] or roaches[211].

3.2 Experimental Results

In the experiment (Fig. 3.2), the network is realized with chemical micro-oscillators[212] that measure about 300 µm. Each oscillator consists of a porous cation-exchange bead that is loaded with ruthenium-tris-bipyridine ($Ru(bipy)_3$), the catalyst in the oscillating Belousov-Zhabotinsky (BZ) reaction. A review of the chemical mechanism of the BZ reaction is given in Appendix C. To enable chemical oscillations, the particles are immersed in a catalyst-free BZ solution. Since the concentration oscillations require the presence of the catalyst, they are confined in space to the locations of the beads (Fig. 3.2b). Thus in contrast to the experiment

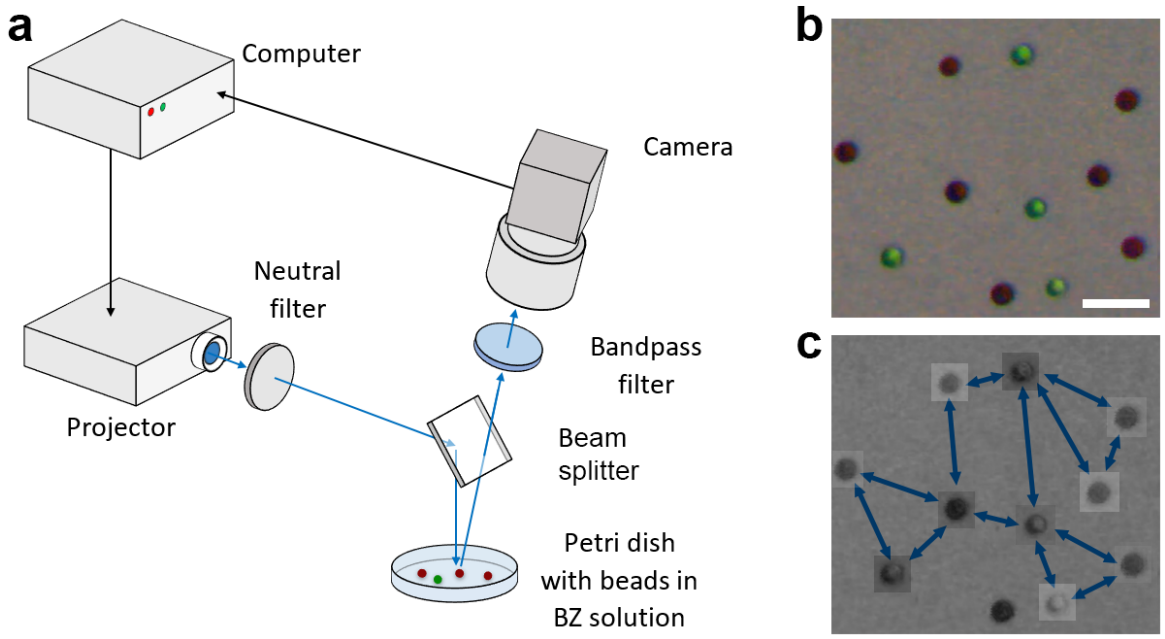

Figure 3.2 | Setup for network experiments with chemical micro-oscillators. (a) The chemical oscillators are monitored with a camera. Based on the measured state of the oscillators they are illuminated individually with light from a spatial light modulator. For completeness, the experimental setup is shown here, but is given in more detail in appendix B.1.3. (b) The oscillation cycle is conveniently tracked optically, because the absorption spectrum of the catalyst depends on its oxidation state. In this snapshot the beads appear red (Ru^{2+}) and green (Ru^{3+}) due to contrast enhancement with the bandpass filter (440 –460 nm) and a software filter. The length of the white bar corresponds to 1 cm. (c) The network (blue arrows) is established via light perturbations that depend on the state of the selected neighbors.

in a spatially extended medium (chapter 2), the beads allow for discrete reaction sites that serve as the oscillatory nodes in network experiments.

The oscillators are spaced at least 400 µm apart. This distance suffices to exclude diffusive coupling. Instead the coupling between oscillators is mediated via light (Fig. 3.2c). For this purpose, the catalyst in the reaction has two additional roles: Its visible color changes allow for optically tracking the chemical oscillation cycle. Secondly, the catalyst is photosensitive. Increased light application accelerates the oscillation, while a decrease slows the oscillation cycle down. Thus, the catalyst can be employed to realize an autonomous network experiment (Fig. 3.2a). The critical components are a camera that measures the oscillation state in the form of grayvalues v_i and a spatial light modulator that applies variable illumination levels I_i on individual beads. Here grayvalue v_i is short for the spatially averaged grayvalues across an entire bead i. One complication is that the oscillators are not fixated spatially, so they can move freely through the Petri dish. To measure at the right position and target the correct location with light, each oscillator is tracked continuously throughout the experiment.

The experiment proceeds in four stages. During the initial and last stage, the oscillators are uncoupled. All individual illumination intensities are identical to the background illumination level I_0,

$$I_i = I_0. \tag{3.7}$$

This allows for the measurement of their free oscillation period T_0 before and after the experiment. In the second stage, the experiment is initialized to start from a state of in-phase synchronization. This initial condition is enforced by exploiting the Kuramoto transition[213], where globally coupled oscillators synchronize in phase for a large enough coupling strength. The corresponding illumination protocol is:

$$I_i(t) = I_0 + K \sum_{j=1}^{N} \big(v_j(t) - v_i(t)\big). \tag{3.8}$$

Here every component in the adjacency matrix $\underline{\underline{A}}$ equals 1 (compare (3.3)). After about 5 periods, the phases of all oscillators obey the initial condition. Directly after successfully enforcing the initial condition, the coupling stage starts. The network coupling is given by:

$$I_i(t) = I_0 + \frac{K}{k_i} \sum_{j=1}^{N} A_{ij} \left(v_j(t) - v_i(t)\right). \tag{3.9}$$

Each node i receives a feedback I_i, that is based on the grayvalue differences between neighboring nodes j and node i itself. The accumulated differences are weighted with the coupling strength K that is normalized by the node degree k_i. Real-world constraints motivate the introduction of the illumination offset I_0 and node degree k_i. The intensity output range of the spatial light modulator is bounded. Feedback values outside the bounds are clipped to the minimum and maximum intensities. Clearly the minimum intensity is zero. This is problematic in the case node i fires before its neighbors, because the sum in (3.9) yields a negative value that would be clipped to zero. However, with an offset I_0, this case still leads to a non-vanishing feedback. Since it is smaller than the default value, it will decelerate the oscillation. In the case of an oscillator with a high degree k_i and not too small coupling strength K, it may be constantly exposed to a large feedback value that is clipped to the maximum intensity. Instead of being coupled to its neighboring oscillators via time-varying perturbations, this oscillator just receives an increased, time-independent intensity offset. Thus it is effectively decoupled from the rest of the network. The elevated offset might even change the dynamic behavior of the node from oscillatory to excitable. Introducing normalization by node degree k_i prevents this scenario.

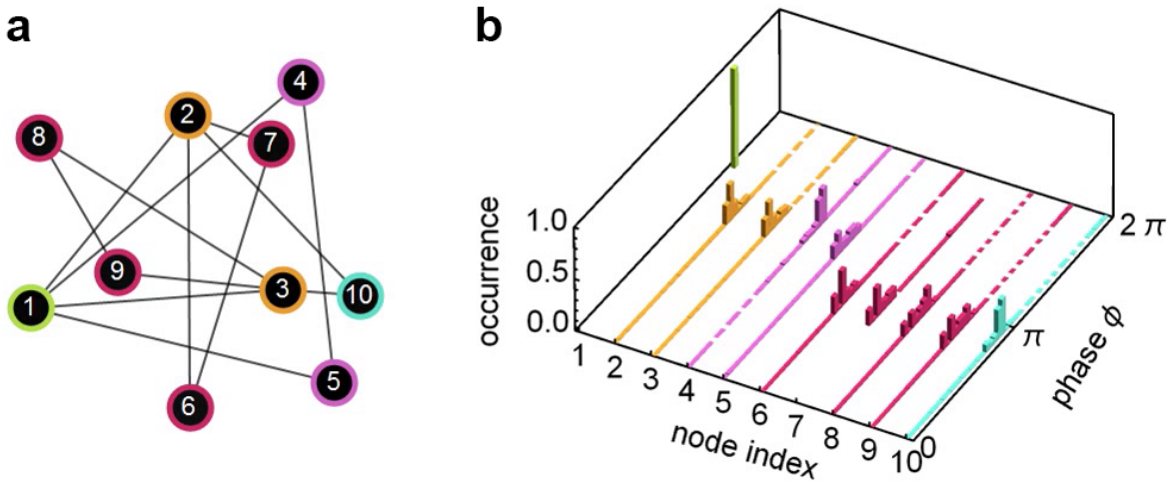

Figure 3.3 | Wave synchronization via symmetry clusters. (a) Nodes of the network are colored by their symmetry cluster affiliation. The numbering follows the path of the wave through the network, starting from the pacemaker at node $i = 1$. (b) In a co-rotating phase plot with $\phi - \omega_1 t$, the wave structure becomes apparent, as the wave travels from one shell, consisting of complete symmetry clusters, to the next. Close to the end of the experiment, at $t = 1423.0\,\mathrm{s}$, the histogram of the accumulated relative phases reveals stable phase-locking.

After the network is coupled together and for sufficient coupling strengths K, it takes a few periods for the fastest oscillator in the network to entrain[38] the other oscillators. Once the entrained nodes also oscillate with the frequency of the fastest oscillator, they in turn also entrain their neighbors until the whole network is frequency-synchronized to the frequency of the fastest oscillator (Fig. 3.3 and Fig. 3.4).

Nodes with the same network distance to the pacemaker node, also called shells[198] (Fig. 3.4a), are in-phase synchronized. This is similar to a target wave on a two-dimensional plane, where all points with the same distance to the target center are in-phase synchronized as well (Fig. 3.1a). Regarding the symmetry properties of the network, it turns out, that the wave starts from one symmetry cluster and propagates further into the others. Each shell consists of one or more complete symmetry clusters. The nodes of one symmetry cluster are not distributed over different shells (Fig. 3.3 and Fig. 3.4).

The experimental results in figure 3.3 depict this ordered sequence. The pacemaker is labeled as node 1. Node 1 occupies an entire symmetry cluster, colored in green (Fig. 3.3a). The wave propagates from node 1 to its next neighbors which are nodes 2 and 3 as well as nodes 4 and 5, which constitute the orange and violet symmetry clusters, respectively. Then the wave is relayed to the third and last shell, which consists of the complete magenta and cyan symmetry clusters. This behavior repeats itself with the period of the pacemaker oscillator $T_1 = 32.0\,\mathrm{s}$.

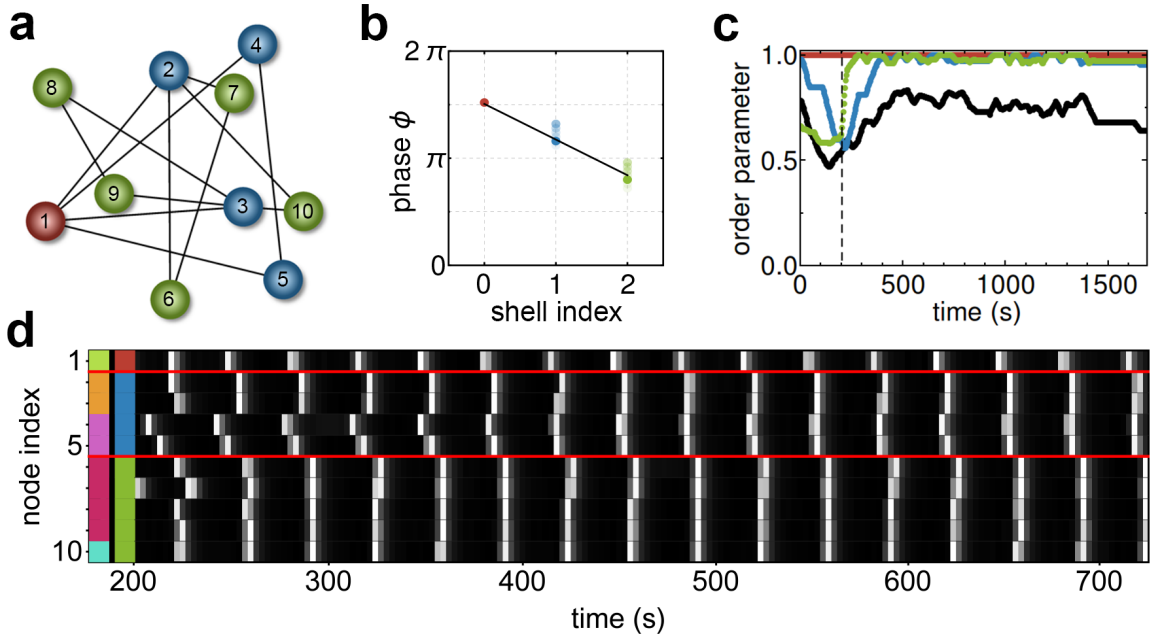

Figure 3.4 | Target wave on a network. (a) The shells of the target wave on the network are highlighted in red, blue and green. (b) In a frame co-rotating with ω_1 the constant phase relationship between the constituents of the shells over the course of the experiment becomes apparent. The occurrence of each phase is proportional to its opacity. (c) Once the network coupling is activated at $t = 200\,\mathrm{s}$, the shells (red, blue, green) quickly approach in-phase synchronization while the total network (black) does not, as quantified by the Kuramoto order parameter (3.12). (d) The color in the node-time plot shows the measured grayscale values over time for each node. After a transient all nodes oscillate with the same frequency but a phase difference depending on their shell (separated by red lines). The colorbars on the left reveal the alignment between shells and symmetry clusters. Coupling strength: $K = 2.0$.

The phase ϕ is calculated from linear interpolation between consecutive peaks at times t_i in the grayvalue time series (Fig. 3.4d):

$$\phi(t) = 2\pi \frac{t - t_i}{t_{i+1} - t_i}. \tag{3.10}$$

Since the calculation of the phase ϕ during the interval $t \in [t_i, t_{i+1}]$ requires the time points of the most recent peak at t_i and the upcoming one at t_{i+1}, the phase is evaluated after the completion of the experiment. The phase difference between consecutive shells, $\Delta\phi = 0.67\pi$, is constant (Fig. 3.3b and Fig. 3.4b).

Figure 3.4 shows the node dynamics with a focus on the shells. The nodes are colored by their distance to the pacemaker and are numbered identically as in figure 3.3. A stationary phase relationship between the shells is revealed (Fig. 3.4b) by plotting all phases of the

constituent nodes during the experiment in a co-rotating frame:

$$\phi = md + \phi_0. \tag{3.11}$$

Here $d \in \mathbb{N}$ is the distance to the pacemaker node as well as the shell index. Thus the slope $m = \Delta\phi/\Delta d$ simplifies to the locked phase difference $\Delta\phi = 0.67\pi$, since $\Delta d = 1$ between consecutive shells. The parameter ϕ_0 is an arbitrary phase offset in the co-rotating frame. This observed linear dependence of the phase on the distance is a strong indicator for one dominating excitation wave spreading on the network.

Another way to reliably detect target wave induced synchronization employs the Kuramoto order parameter[213]. Once the target wave is established, for each shell, consisting of a set of nodes S indexed by a variable s, the Kuramoto order parameter,

$$R_S = \frac{1}{|S|}\left|\sum_{s\in S} e^{\mathrm{i}\phi_s}\right|, \tag{3.12}$$

should approach unity to verify shell-wide in-phase synchronization. At the same time, the global Kuramoto order parameter R for all nodes must not reach one. Otherwise the whole network is in-phase synchronized with $\Delta\phi = 0$ between shells and does not show wave synchronization with $\Delta\phi \neq 0$. Both conditions are fulfilled in the experiment (Fig. 3.4c).

The space time plot analogue for a network (Fig. 3.4d) shows that the wave pattern quickly develops after a short transient of five periods lasting $\Delta t = 150\,\mathrm{s}$ and remains phase-locked afterwards. The colorbars on the left indicate for each node the affiliated symmetry cluster and shell. The nodes in each shell are in-phase synchronized and adjacent shells have constant phase differences. Also each shell consists exclusively of complete symmetry clusters.

The emergence of a target wave on a network is conditional on the successful entrainment between any two connected nodes in the network. However, complete entrainment is only possible for a sufficiently high coupling strength K[213]. For coupling strengths K below a critical coupling strength K_c, wave propagation breaks down. Indeed, experiments with a too small coupling strength $K < K_c$ confirm that the pacemaker node can not entrain the whole network (Fig. 3.5). In this case nodes affiliated with the same symmetry cluster lose in-phase synchronization and thus the network-wide target wave disappears.

While lowering the coupling strength K below K_c, frequency synchronization gradually fails. Entrainment first breaks down between those pairs of connected nodes, whose frequency difference $\Delta\omega_{ij}$ is large. Furthermore the difference is amplified by the larger degree of both nodes, $\max(k_i,k_j)\Delta\omega_{ij}$, due to the node degree dependence in the coupling scheme (3.9). This is similar to the pairwise synchronization transition of two coupled phase oscillators[213].

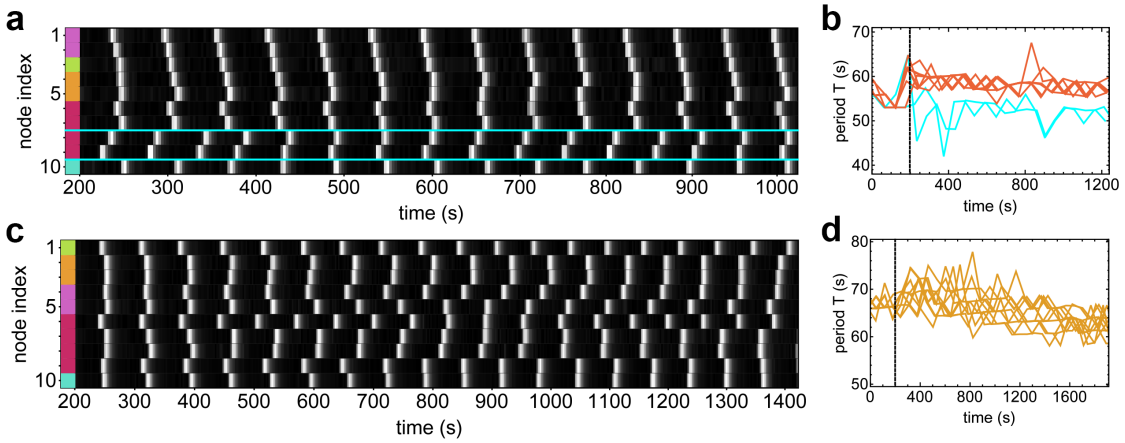

Figure 3.5 | Entrainment failure. (a) This experiment has a coupling strength of $K = 0.6$, which is slightly below the critical coupling strength guaranteeing global entrainment. Nodes 1 and 9 coexist as pacemakers in the network. Even though node 9 has the larger frequency, it can not entrain the network, because the neighboring node 5 does not follow it. The rest of the network is entrained by the node with the second highest frequency. (b) The oscillator frequencies are divided into two groups with frequencies $\omega_9 = 19\,\text{mHz}$ or $\omega_1 = 17\,\text{mHz}$. (c) At small coupling strength, $K = 0.05$, no lasting entrainment occurs and aligned phases are only temporary. (d) The oscillators exhibit no lasting frequency synchronization, but a collective parameter drift to higher frequencies.

After the first of these entrainment failures occurs, the network is divided into separate hemispheres. Each domain is under the influence of its own respective pacemaker, nodes 1 and 9 (Fig. 3.5a). Interestingly, two pacemakers coexist, even though their frequencies are different, $\omega_9 > \omega_1$ (Fig. 3.5b). In continuous media as well as on networks, this is due to oscillators at the boundaries of the influence sphere of each pacemaker being less excitable and spending more time in their refractory states. Thus, they neither respond to nor relay the wave that originates at the pacemaker.

At very low coupling strengths K, no pairs of connected oscillators are entrained to each other. The space time plot of an experiment regarding this case shows how the initially in-phase synchronized oscillators slowly lose their phase alignment over time (Fig. 3.5c). They do not oscillate with their natural periods, as they are still weakly coupled to each other. Interestingly, the frequency of an oscillator is not constant over time. Whenever its phase aligns with a neighbor it slows down until the phase alignment breaks up again. So there is temporary frequency-locking between oscillators, but it is only transient. Overall the frequencies are desynchronized and over time increase slightly (Fig. 3.5d) due to leakage of the catalyst in the chemical experiment.

To determine the robustness of the wave pattern, a large number of numerical simulations are performed with the ZBKE model of the photosensitive BZ reaction (C.5). The evolution

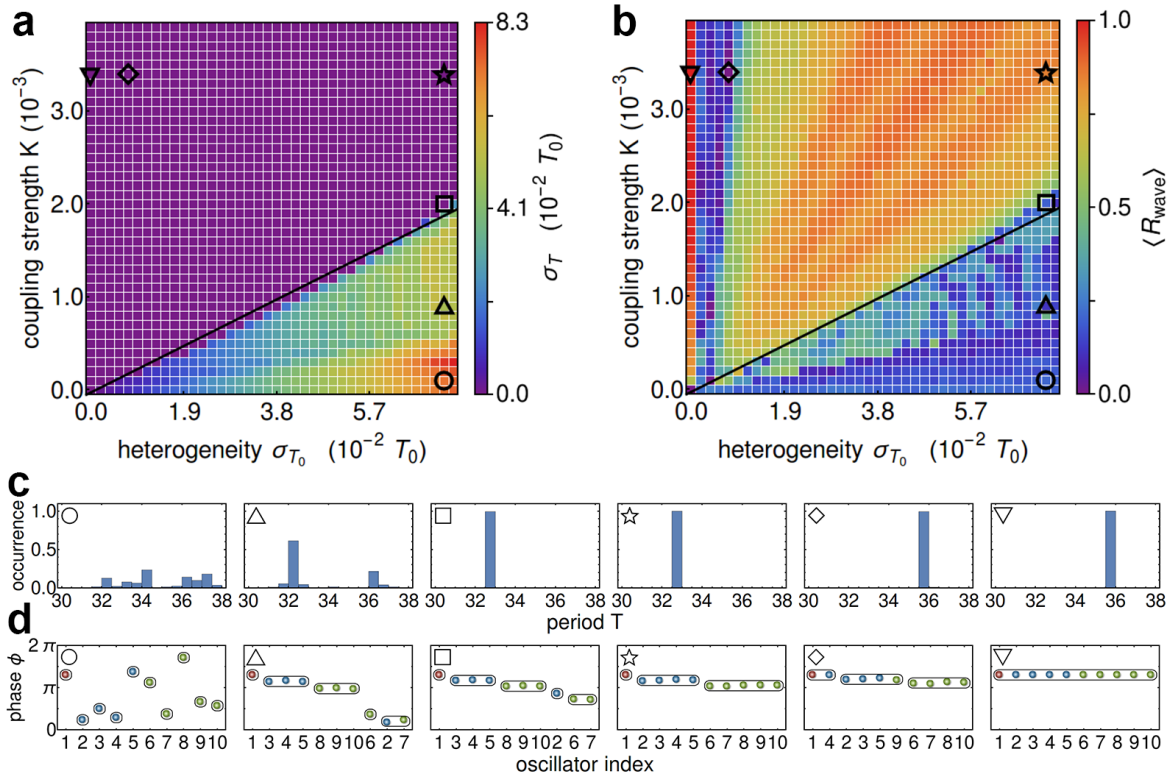

Figure 3.6 | Arnold tongue for target wave synchronization. (a) Numerical simulations with (C.5) for a range of coupling strengths K and node heterogeneities as quantified by the standard deviation σ_{T_0} of the natural period distribution relative to its mean T_0. They reveal the existence region for synchronization by a target pattern. The standard deviation of the periods σ_T during the coupled stage, shows frequency-locking (purple domain) for sufficient coupling strength regardless of heterogeneities. The transition line is highlighted in black as a guide for the eye. Each simulation started from a slightly perturbed in-phase initial condition and lasted for 200 periods. (b) The time-averaged wave order parameter (3.14) reveals that only a subset of the frequency-locked states is due to a target wave (orange), once the heterogeneity is large enough. (c) Histograms and (d) phase distributions marked in subplots a,b show representative cases. Node coloring and indices are the same as in figure 3.4.

equation for the network is:

$$\frac{d\boldsymbol{c}_i}{dt} = \boldsymbol{f}(\boldsymbol{c}_i) + \begin{pmatrix} K_u \\ K_v \end{pmatrix} \frac{K}{k_i} \sum_{j=1}^{N} A_{ij} \left(v_j - v_i \right) \tag{3.13}$$

The two-component nonlinear node dynamics $\boldsymbol{f}(\boldsymbol{c}_i)$ supply the oscillations. Since the light intensity I_i is an additive parameter in both components, the light-mediated coupling term can be separated from the nonlinear kinetics $\boldsymbol{f}$. Note that the dynamical equations (3.13) apart from the nonlinear dynamics $\boldsymbol{f}$ are in a similar form to the consensus protocol, which is a well-established model of distributed computing in computer science[214]. The dynamical variables $\boldsymbol{c} = (u, v)$ are related to the bromous acid $HBrO_2$ and the oxidized catalyst

$Ru(bipy)_3^{3+}$ concentrations. In the coupling term, only variable v plays a role, since only the catalyst is observable in the experiment (Fig. 3.2). The coupling term feeds back into both components u and v via the vector of species-dependent susceptibilities (K_u, K_v).
The parameter space of the simulations is spanned by coupling strength K and oscillator heterogeneity. A quantitative measure of the heterogeneity is given by the standard deviation σ_{T_0} of the natural period distribution relative to the distribution mean T_0. The period distribution in the simulation fits to the distribution in the experiment by drawing random samples from a suitable interval of values for parameter $q \in [0.5, 0.9]$.
The results of the numerical survey are shown in figure 3.6. The standard deviation of oscillator periods during coupling σ_T is a good measure for evaluating frequency synchronization. A vanishing σ_T requires the periods of all oscillators T_i to be identical, which is the case during frequency synchronization. As can be clearly seen in subfigure 3.6a, there exists a transition point from a desynchronized state to a synchronized state, whose critical coupling strength grows approximately linear with oscillator heterogeneity. As such this is the generalization of an Arnold tongue[189] for a network of coupled oscillators. While this structure is usually observed in the parameter space of oscillators, which are entrained to an external periodic forcing, here we have the case of a fast oscillator which entrains the rest of the network as a pacemaker.
Frequency-locking does not offer information about the phase alignment between the oscillators. As such a vanishing σ_T does not differentiate between global in-phase synchronization, phase clusters[189] or target waves (Fig. 3.4). To solve this problem, a modified Kuramoto order parameter is introduced, that detects wave synchronization in a network of N oscillators:

$$R_{\text{wave}} = \frac{1}{N} \left| \sum_{k=1}^{N} e^{\mathrm{i} \frac{2\pi}{m} \phi_k} \right| . \tag{3.14}$$

As in figure 3.4b, the slope of the wave $m = \Delta\phi$ must be determined from a linear regression of the stationary phase pattern beforehand. Intuitively, this order parameter multiplies the phase of each oscillator in such a way, that all phases converge to the same point if they are synchronized in a wave with slope m. This is possible due to the 2π-periodicity of the complex phase argument. However, the wave order parameter is not very robust against noise and gives ambivalent results for too large noise levels. With the additional constraint, that the shells of the wave align with the symmetry clusters (Fig. 3.4d), this order parameter can be utilized to detect target waves on networks.
The simulations are all prepared in such a way, that the pacemaker occupies a complete symmetry cluster (node 1 in figure 3.4a). This guarantees, that a wave propagating across the entire network must be a target wave for sufficiently high coupling strengths K. Evaluating

the wave order parameter (3.14) reveals, that target waves are the prevalent synchronization mode in the network of heterogeneous ZBKE oscillators (Fig. 3.6b). A snapshot of its period distribution and phase alignment is shown in the subplots of figure 3.6c,d) marked with a star: The frequencies are identical and there are three shells, which are aligned with the symmetry clusters (compare Fig. 3.1).

At the edges of the frequency-synchronized region, wave synchronization fails. For very small heterogeneity, at the transition to in-phase synchronization at $\sigma_{T_0} = 0$ (marked with an upside-down triangle), the wave pattern breaks apart. As can be seen in the subplot marked with a diamond in figure 3.6d, there are still three separate shells as in the fully-developed target wave. The difference to that case is, that fast oscillators join a shell that is ahead of the one they should be in, based on the network distance (nodes 4 and 9). The opposite scenario occurs for large heterogeneity (square marker). Here oscillators fire in a later shell. The reason for this is that the wave does not follow the shortest path through the network, since some links have too large a frequency heterogeneity $\Delta\omega_{ij}$. Oscillators firing in the wrong shell lead in both cases to an incorrect slope determination. This in turn results in a very small order parameter R_{wave}, which correctly indicates the absence of wave synchronization through shells.

As observed in the experiment (Fig. 3.5), the desynchronized domain is reproduced for low coupling strengths K. Before complete desynchronization (circular marker) there is partial synchronization (upright triangle). Here nodes 2 and 7 oscillate with a slower period than the period of the pacemaker, node 1.

The findings on target waves in networks are not limited to the network examined so far. Figure 3.7 shows target waves for additional network topologies: random densely-connected[202], scale-free[215,216], random sparsely-connected[217] and tree networks[218]. The scale-free network shown in figure 3.7c,d) features a large number of trivial symmetry clusters, which consist of just a single node. Thus target wave propagation on such networks, given a random pacemaker location is highly probable.

Note that, if the wave does not originate from a complete symmetry cluster, the shells and symmetry clusters will not align. This is the case when the pacemaker node is not a trivial symmetry cluster or the pacemaker site consists of equally fast nodes that only form a subset of a symmetry cluster. However, in the presence of a bottleneck node, whose removal would separate the network into two disjoint networks, wave propagation through symmetry clusters can recover. The necessary condition for this recovery is, that the bottleneck node is a trivial symmetry cluster. In this way, once the wave is relayed via the bottleneck node it acts as a pacemaker node for the remaining part of the network. This scenario is depicted in figure 3.7e,f). Node 1 is only a subset of the magenta symmetry cluster. So, wave

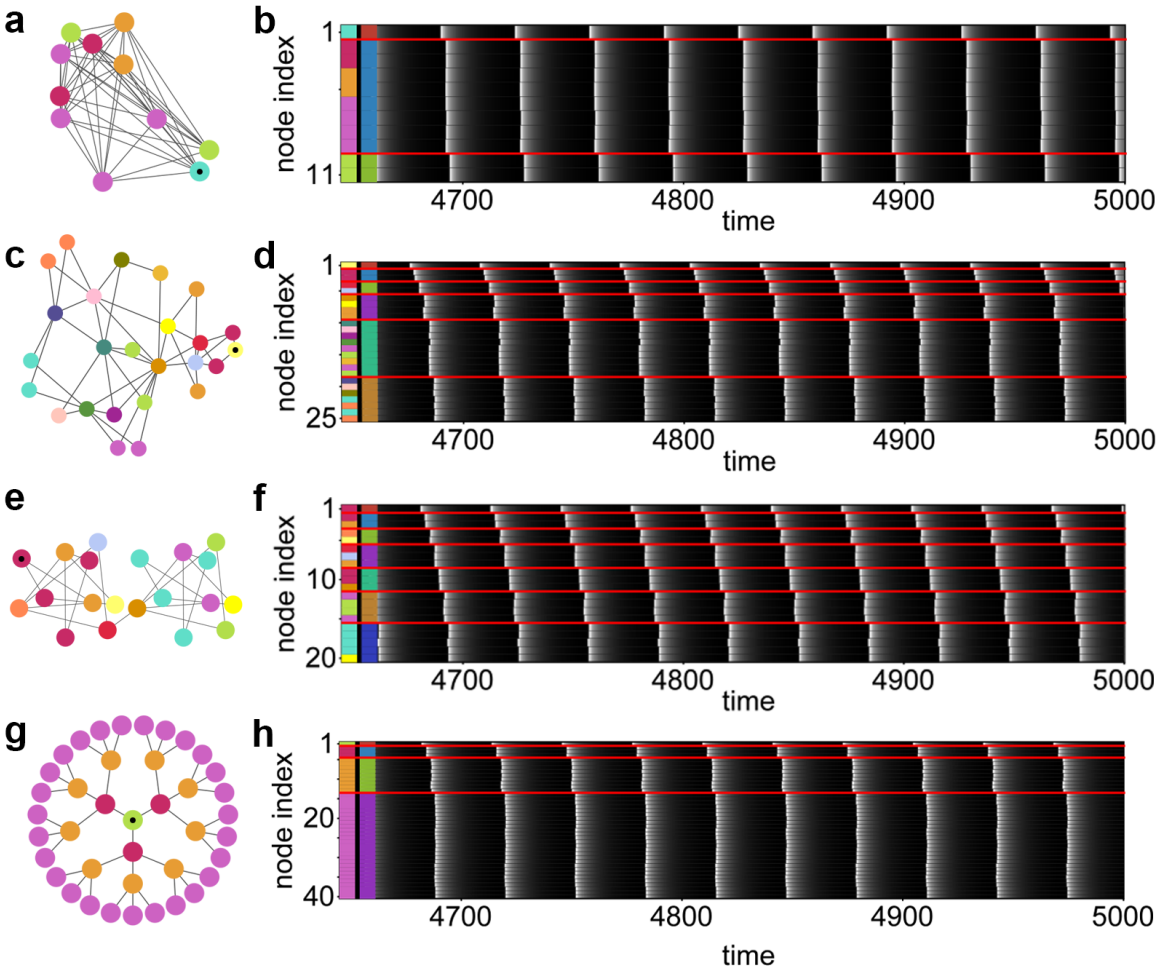

Figure 3.7 | Prevalence of target wave synchronization. Target wave synchronization was observed on (a,b) random densely-connected network with $N = 10$, (c,d) scale-free network with $N = 25$, (e,f) random sparsely-connected network with $N = 20$ nodes. (g,h) tree network with $N = 40$ nodes. The left column shows the network and its symmetry clusters. The pacemaker node is highlighted with a black dot. On the right are space-time plots of $v_i(t)$ for the last 10 periods.

propagation on the left part of the network is not a target wave. However, once it passes the brown bottleneck node in the center it is relayed symmetrically, so it regains its target wave character: The subsequent shells of the wave coincide with the symmetry clusters.

In experiments and simulations, it is striking that wave propagation follows the symmetry clusters (Fig. 3.4 and Fig. 3.6). The reason for that is that all nodes of a symmetry cluster have the same distance to all nodes of any other symmetry cluster. This is illustrated in figure 3.8.

A wave on a network spreads from its source to the neighboring nodes and in the next step continues on to their neighbors. At each step the wave front increases its distance[208] to the source node by $\Delta d = 1$, since the network is discrete.

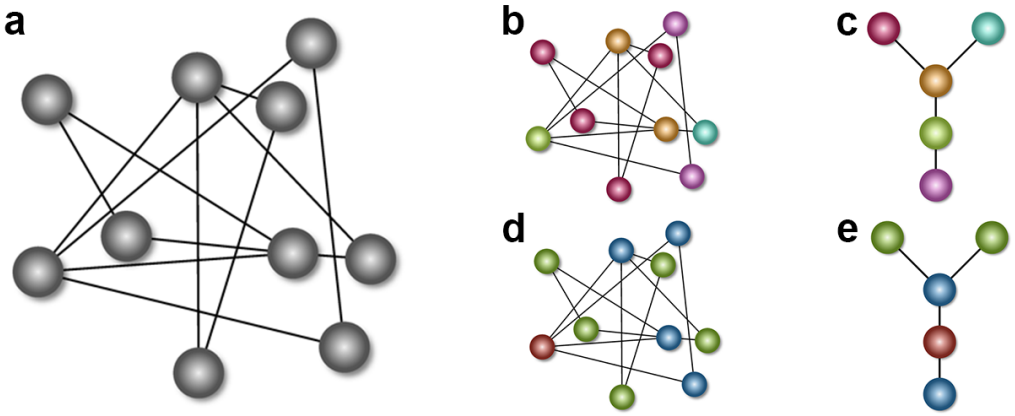

Figure 3.8 | Relationship between symmetry clusters and shells. (a) Any network is given by a set of nodes connected by a set of links. All nodes are assumed to be identical. (b) Every network can be completely decomposed into symmetry clusters. (c) The quotient network is obtained by replacing all nodes of a symmetry cluster with a single one. (d) Shells are defined by the shortest distance to a reference node (red). Nodes with distance $d = 1$ are blue, with $d = 2$ are green. (e) Coloring the nodes of the quotient network by distance to the reference node (red), reveals the same arrangement of shells as in c).

The path of the wave coincides with the symmetry clusters, if the wave originates from all nodes of a complete symmetry cluster. This can either be a single node of a trivial symmetry cluster or more (e.g. the green node or the orange nodes in figure 3.8b). In continuing forward the wave spreads to all neighboring nodes of that initial symmetry cluster. All of these neighbors must also be complete symmetry clusters, because all nodes of the original symmetry cluster are connected identically to the rest of the network. Otherwise the original nodes would not constitute a complete symmetry cluster. Note that identical connectivity is not implied to mean that all nodes have exactly the same neighbors. Instead they have the same number of neighbors from the same symmetry clusters.

The above point is further clarified by eliminating the redundancy due to the symmetry clusters. To this end, all nodes of a symmetry cluster are replaced by a single node with the same connectivity resulting in a quotient network[219] (Fig. 3.8c). Coloring the nodes in the quotient graph by their distance to the green node (Fig. 3.8e), which is also the reference node in figure 3.8d, reveals the same shell affiliations of nodes as in the full network. Thus all nodes of any symmetry clusters will fire in unison in the case of target wave synchronization.

3.3 Short summary

This chapter generalizes the notion of target waves from continuous media to discrete networks utilizing symmetries. Target waves on the two-dimensional Euclidean plane spread while adhering to all members of the Euclidean symmetry group E(2): translation, rotation and reflection. Likewise target waves on networks obey all permutation symmetries underlying the network topology. The source of the target wave is the pacemaker, a location or node, which features the largest frequency in the entire system. After a sufficiently long time, each element is entrained to the frequency ω_1 of the pacemaker.

Target waves on networks are studied in an experiment with discrete photochemical oscillators (Fig. 3.4) and reproduced in numerical simulations (Fig. 3.6)[217]. For this purpose, a wave order parameter was developed (3.12) to reliably detect and distinguish target waves from other synchronization modes. Experimentally and numerically the transition from networks, which are frequency-locked by the target wave, to desynchronization is verified to occur by entrainment failure along connected nodes i, j whose frequency difference $\Delta\omega_{ij}$ is too large. An analysis of the network symmetries further reveals their intrinsic connection to the network distance. This allows for the prediction of wave propagation using symmetry clusters.

The existence of travelling cortical excitation waves was recently observed in the motor cortex of monkeys (Macaca mulatta)[220]. Here, the findings with neuromorphic chemical oscillators reveal that target wave-induced synchronization may be responsible for robust in-phase synchronization of distant nodes in a cortical network without a delayed transmission node[180].

3.4 Future directions

With the experimental setup presented in this chapter it was only possible to study the transition from desynchronization to target waves at large heterogeneity. To study the transition from in-phase to wave synchronization (Fig. 3.6) experimentally, it is necessary to have precise control over the period distribution. For this purpose it is required to have large reservoir of $N > 2000$ oscillators, which are available in the setup described in the next chapter. Before the experiment runs, it is possible to select $N = 10$ oscillators with a desired period distribution. Furthermore, the large reservoir allows for more than 200 experiments to run in parallel. Thus a survey of the synchronization modes in the K-σ_{T_0} parameter space can be completed quickly.

It would be interesting to employ weakly coupled oscillators as a first approximation of the critical coupling strength $K_c(\sigma_{T_0})$ at which a network transitions from the desynchronized to

the synchronized state (Fig. 3.6). In the case of two mutually coupled oscillators, the critical coupling strength K_c at which they frequency-lock is given by[213]

$$K_c = \frac{\Delta\omega}{\max \mathrm{IF}(\Delta\phi)}. \tag{3.15}$$

The critical coupling strength depends on the frequency difference $\Delta\omega = \omega_1 - \omega_2$ between both oscillators and the maximum of the interaction function $\mathrm{IF}(\Delta\phi)$, which is defined as the odd part of the phase response curve of an oscillator (see appendix A.1).
The case of a pacemaker sequentially entraining one oscillator after another, can be simplified to two oscillators. One is entrained by the pacemaker and oscillates with its frequency ω_1. The other is not entrained yet and has a frequency ω_i. Thus, accounting for the degree normalization in (3.9), the critical coupling strength K_c at which every oscillator in the network is entrained follows

$$K_c = \frac{\Delta\omega_{\max}}{\max\left(\mathrm{IF}(\Delta\phi)\right)}, \text{ with} \tag{3.16}$$

$$\Delta\omega_{\max} = \max_i \left(k_i \left(\omega_1 - \omega_i\right)\right). \tag{3.17}$$

Even though, this approximation neglects the influence of neighboring oscillators j, which would alter ω_i, it might still yield reasonable results. However, its applicability to ZBKE oscillators might be limited, since their phase response curve depends nonlinearly on the coupling strength (see appendix C.2).

Chapter 4

Spiral Wave Chimera

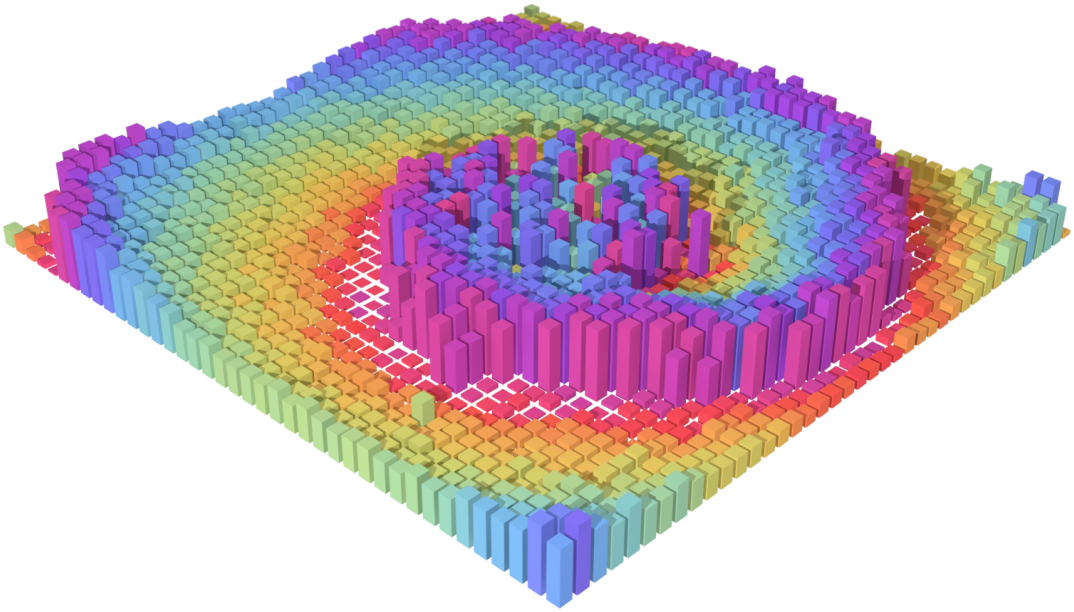

A spiral wave chimera is the union of spiral waves[87] and chimeras states[221] - two paradigms in spatial pattern formation and temporal synchronization[222]. Spiral waves have been researched extensively in simulations as well as experiments during the last 70 years[62] in excitable media due to their spontaneous formation in a plethora of natural systems (see the introduction of chapter 2 for examples). A spiral wave nucleates from the open end of an excitation wave. The open end curls in and becomes the center of the spiral wave from which waves are periodically emitted. The chimera state was numerically found by Yoshiki Kuramoto about 15 years ago [a] , when he extended his model for synchronization in networks from globally to nonlocally coupled oscillators. While dissipative oscillators with identical frequencies in a globally coupled system trivially synchronize, this is not the case for nonlocal coupling. Two groups emerge: One coherent group, which is frequency-synchronized and another incoherent one, which is desynchronized.

Chimera states are theorized to play a role in cardiac tissue, where mechanical contraction leads to an effective nonlocal coupling[225], opinion formation in social groups[226], beam shaping in laser arrays[227], computers based on arrays of optomechanical resonators[228–230], blackouts in power grids[231], SQUID metamaterials[232–234] and arrays of spin-torque oscillators for miniaturized antennae[235,236], quantum systems of ultracold atoms in a Bose-Einstein condensate[237], cortical networks, where they might play a role in bump states[238,239] and epileptic seizures[240–242], as well as hydrodynamically coupled cilia carpets[88]. The latter control for example the flow of nutrients in the brain to sustain neuronal activity[243].

Recently chimera states have been found in a variety of chemical, physical and biological experiments with: coupled photochemical[244,245] and electrochemical [246] oscillators, photo-electrodissolution of a doped silicon layer[247–249], mercury-beating heart[250], electro-optical coupled map lattices[251,252], mechanical pendula[253–255], time-delayed lasers[256,257], field-programmable gate arrays[258], electronic circuits[259,260] and cilia chains[261]. Even before there was an experimental focus on finding chimera states, there were already experiments which exhibited coexistence of coherent and incoherent behavior, e.g. in a globally coupled photosensitive Belousov-Zhabotinsky (BZ) medium[262] and in ferrofluidics[263]. However, the spiral wave chimera remained elusive so far.

In this chapter, I will present the experimental verification of a spiral wave chimera in a network of photocoupled chemical oscillators. Beyond the observation, a number of unanticipated behaviors are discovered as well.

[a] In 2001 Kuramoto presented his findings on nonlocally coupled systems, that already encompassed one- and two-dimensional problems, at a meeting named "Nonlinear Dynamics and Chaos: Where do we go from here?" in Bristol, United Kingdom. Subsequently his work, on what later became known as chimera state[223], was published as a chapter[41] in the accompanying conference monograph[224].

4.1 Theoretical Background

Inspired by bacterial biofilms[264] as well as living cells in a body[87], that instead of communicating directly, do so via exchange of biochemical species with their surroundings, Kuramoto analyzed the following model[41]:

$$\frac{du}{dt} = f_1(u,v) + K(w-u), \tag{4.1}$$

$$\frac{dv}{dt} = f_2(u,v), \tag{4.2}$$

$$\frac{dw}{dt} = \frac{1}{\varepsilon}\left(u - w + D_w \Delta w\right). \tag{4.3}$$

The first two equations form a subsystem that exhibits a stable limit cycle. The third variable w is the only species that may diffuse with diffusion coefficient D_w and couples linearly into u (4.2). Adiabatically eliminating ($\varepsilon \to 0$) the dynamics of the diffusing variable (4.3) leads to an inhomogeneous ordinary differential equation in space for w,

$$D_w \Delta w - w = u \tag{4.4}$$

that may be solved with the Green's function method[265]. The solution is a nonlocal integral operator,

$$w(\boldsymbol{r},t) = \int_{-\infty}^{+\infty} d^2\tilde{\boldsymbol{r}}\; G\left(|\boldsymbol{r}-\tilde{\boldsymbol{r}}|\right) u(\tilde{\boldsymbol{r}},t), \tag{4.5}$$

whose exact form depends on the topology of the system[41,266]. For a one-dimensional ring, the kernel G is a decaying exponential[41],

$$G(r) = \frac{1}{2\kappa} e^{-r/\kappa}, \tag{4.6}$$

while for an infinite two-dimensional plane with Neumann boundaries, it is the zeroth modified Bessel function of the second kind K_0[267],

$$G(r) = \frac{1}{2\pi\kappa^2} K_0\left(r/\kappa\right), \tag{4.7}$$

whose behavior resembles an exponential decay similar to (4.6). The characteristic coupling length κ depends on the diffusion coefficient, $\kappa = \sqrt{D_w}$. Inserting the nonlocal operator (4.5) with the Green's function (4.7) into the original reaction-diffusion equation (4.1-4.2), leads

to an equation for oscillators with nonlocal coupling[266,267]:

$$\frac{du}{dt} = f_1(u,v) + K \int_{-\infty}^{+\infty} d^2\tilde{\boldsymbol{r}}\, \frac{1}{2\pi\kappa^2} K_0\left(\frac{|\boldsymbol{r}-\tilde{\boldsymbol{r}}|}{\kappa}\right)\Big(u(\tilde{\boldsymbol{r}}) - u(\boldsymbol{r})\Big), \tag{4.8}$$

$$\frac{dv}{dt} = f_2(u,v). \tag{4.9}$$

Depending on the interaction length κ, equation 4.8 can describe systems ranging from local to global coupling. This point becomes clear[268] by considering the nonlocal coupling in a one-dimensional system:

$$\frac{du}{dt} = f_1(u,v) + \frac{K}{2\kappa} \int_{-\infty}^{+\infty} d\tilde{x}\, \exp\left(\frac{|x-\tilde{x}|}{\kappa}\right)\Big(u(\tilde{x}) - u(x)\Big). \tag{4.10}$$

To see how local coupling arises in the case of $\kappa \to 0$, we expand $u(\tilde{x})$ in the neighborhood of x as a Taylor series,

$$u(\tilde{x}) = u(x) + \sum_{n=1}^{\infty} \frac{1}{n!} \frac{\partial^n u}{\partial x^n}\bigg|_{\tilde{x}=x} (\tilde{x}-x)^n, \tag{4.11}$$

and plug it into (4.10). While the zeroth order cancels, the remaining terms lead to an integral of the form

$$\frac{1}{n!} \int_{-\infty}^{+\infty} dy\, y^n \exp\left(-\frac{|y|}{\kappa}\right) = \begin{cases} \frac{\kappa^{n+1}}{n!} & \text{n even} \\ 0 & \text{n odd.} \end{cases} \tag{4.12}$$

Since κ is small, it is possible to truncate the series after the second order. This approximation reveals local diffusive coupling:

$$\frac{du}{dt} = f_1(u,v) + K\kappa^2 \frac{\partial^2 u}{\partial x^2}. \tag{4.13}$$

Conversely the kernel function assumes identity as the coupling range grows, $G \xrightarrow{\kappa\to\infty} 1$. Since each element is weighted identically, the coupling (4.10) is global:

$$\frac{du}{dt} = f_1(u,v) + \lim_{\kappa\to\infty} \frac{K}{2\kappa} \int_{-\infty}^{+\infty} d\tilde{x}\ \Big(u(\tilde{x}) - u(x)\Big). \tag{4.14}$$

In this case, κ acts as a normalization constant for the diverging integral, such that the coupling term results in a finite value.
Remarkably, nonlocal coupling with finite coupling range $\kappa < \infty$ (4.10) is well approximated by local diffusion (4.13). The approximation is valid for small κ or equivalently for systems, which exhibit patterns that vary on a length scale λ_p being much larger than the coupling range[41]:

$$\lambda_p \gg \kappa. \tag{4.15}$$

Put differently, the pattern is spatially smooth. The length scale λ_p of a smooth pattern described by diffusive coupling (4.13) is related to the effective diffusion coefficient:

$$\lambda_p \sim \sqrt{K}\kappa. \tag{4.16}$$

Combining the preceeding arguments (4.15) and (4.16) leads to a consistency condition for the local-coupling approximation:

$$\sqrt{K}\kappa \gg \kappa. \tag{4.17}$$

Thus, for large coupling strength K the approximation is valid. Both equations, (4.10) and (4.13), describe smooth patterns. However, for sufficiently small K the peculiar effects of nonlocal coupling dominate as non-smooth patterns emerge. These patterns break the diffeomorphism[269] between physical and phase space. Intuitively this means that two infinitesimally close points in physical space exhibit states, which are not close in phase space[41].
An intuitive explanation of the underlying mechanism generating non-smooth, discontinuous patterns is revealed during the analysis of nonlocally coupled oscillators. The limit cycle dynamics of equations (4.1) and (4.2) can be simplified by introducing a scalar phase variable φ via a phase reduction technique[213] (see appendix A.1):

$$\frac{d\varphi}{dt} = \omega + \frac{K}{2\kappa}\int_{-\infty}^{+\infty} d\tilde{x}\, \exp\left(\frac{|x-\tilde{x}|}{\kappa}\right) \sin\Big(\varphi(\tilde{x}) - \varphi(x) - \alpha\Big) \tag{4.18}$$

Due to the phase reduction, the magnitude of the nonlocal coupling (4.18) does not depend anymore on the difference of variables (4.10), but on the model-dependent 2π-periodic interaction function. For weakly coupled prototypical Stuart Landau[266] and FitzHugh-Nagumo[267] oscillators the interaction function closely resembles a simple harmonic. Taking

one further step, Kuramoto's mean field approach[213] for studying the synchronization of globally coupled networks of oscillators (A.32) can be extended to the nonlocal case. As a result, the corresponding single-oscillator equation, which describes the interaction between a single oscillator and the mean field via its modulus R and phase Ψ, becomes spatially dependent[266,267]:

$$\frac{d\varphi(x,t)}{dt} = \omega + KR(x)\sin\Big(\Psi(x,t) - \varphi(\boldsymbol{r},t) - \alpha\Big). \tag{4.19}$$

This shows that in the nonlocal case, coupling strength K is modulated by the local coherence. The level of coherence is quantified by the spatially varying modulus $R(x)$ of the order parameter. This modulus is equivalent to a localized Kuramoto order parameter, which can be approximated by

$$R(x) = \frac{1}{|\Omega(x)|}\left|\int_{\Omega(x)} d\tilde{x}\, e^{\mathrm{i}\varphi(\tilde{x})}\right|, \tag{4.20}$$

measuring the level of in-phase synchronization[189] in a nonlocal neighborhood of position x

$$\Omega(x) = \{x, \tilde{x} \in \mathbb{R} \;\big|\; |x-\tilde{x}| \leq \ell_R\}. \tag{4.21}$$

The parameter $\ell_R \in \mathbb{R}^+$ is chosen as to cover a sufficiently small neighborhood, such that the localized order parameter is not smoothed out. If all oscillators move in unison, the effective coupling strength $KR(\boldsymbol{r})$ will be large. In turn this will recruit further neighboring oscillators for near zero-lag synchronization. However, in an area with greatly varying phases, the coupling $KR(\boldsymbol{r})$ vanishes, leading to even lower synchronization levels (Fig. 4.1).
This also explains the robust structure of the spiral wave chimera. In the wave that rotates around the core, there is only a small and smooth phase gradient. This leads to a large order parameter and re-enforces the high synchronization level. In the core region, all phases ranging from 0 to 2π occur simultaneously due to the phase singularity [b] . The order parameter nearly vanishes here and the resulting coupling is so weak, that frequency-entrainment fails. Thus, a spiral-shaped phase pattern naturally gives rise to incoherent region under nonlocal coupling. Consequently, there is no sensitive dependence on initial conditions, as is the case for the chimera state on a network with two subpopulations[270] or a ring[271].
In one dimension the mechanism is qualitatively different: Attractive difference coupling (4.18) always leads to in-phase synchronization as it removes phase differences (appendix A.1). A

[b] Since the pattern is discontinuous, the phase singularity is not localized at a single point, as for regular spiral waves with a continuous concentration field. Instead the singularity is spread out over the entire core region.

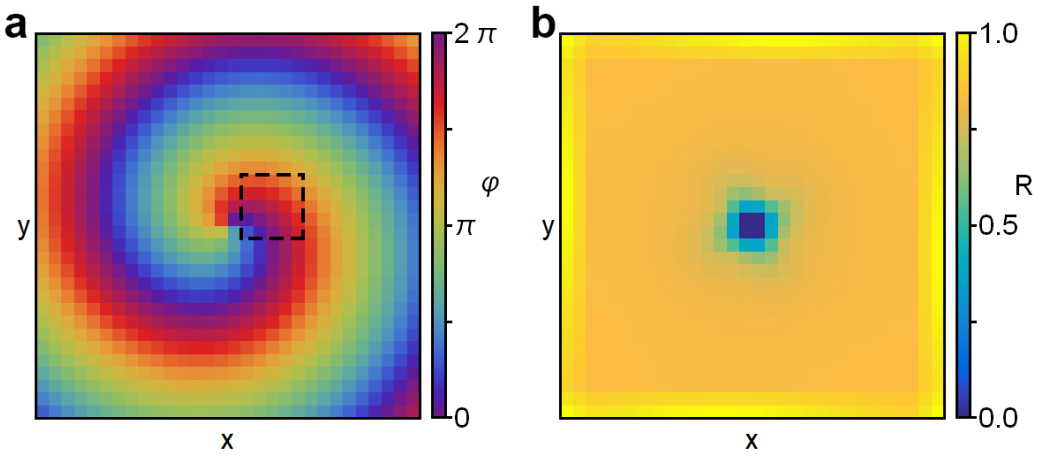

Figure 4.1 | Order in the phase field of a spiral wave. (a) A snapshot of the phase field for a rotating spiral wave. In the center is the phase singularity, where all phases φ ranging from 0 to 2π meet. The dashed square with sidelength $2\ell_R + 1$ and $\ell_R = 2$ is the nonlocal neighborhood of an oscillator close to the phase singularity over which the localized Kuramoto order parameter (4.20) is evaluated. (b) The resultant localized Kuramoto order parameter shows low order $(R < 0.2)$ inside the core and high order $(R > 0.6)$ outside.

phase singularity, which might counteract this tendency, requires two spatial dimensions, so it does not occur on a one-dimensional ring. In order to oppose eventual in-phase synchronization the phase-frustration parameter α in the coupling function is utilized. Exploiting trigonometric identities, the interaction function decomposes into two antagonistic parts, that promote $(\sin(\Delta\varphi))$ and oppose $(\cos(\Delta\varphi))$ in-phase synchronization:

$$\sin(\Delta\varphi - \alpha) = \cos(\alpha)\sin(\Delta\varphi) - \sin(\alpha)\cos(\Delta\varphi) \tag{4.22}$$

$$\approx \varepsilon \sin(\Delta\varphi) - \cos(\Delta\varphi). \tag{4.23}$$

Approximating both parts (4.22) for $\alpha = \pi/2 - \varepsilon$, with ε small, leads to (4.23). In this range chimera patterns are likely to be observed[41]. Comparing the coefficients of (4.23), reveals that in-phase synchronization $(\Delta\varphi = 0)$ is heavily penalized (1) and only weakly encouraged (ε). In summary the desynchronized domains of the one-dimensional chimera are re-enforced not due to a topological cause, as in two dimensions, but via suppression of in-phase synchronization in the coupling.

Due to large theoretical interest over the last years in states of partial synchronization in general and chimera states in particular, there is now a large body of research. Chimera states were observed numerically in one[271–276], two[60,271,277–281] and three[282–284] dimensions as well as different network topologies[285–289]. They occur in a variety of discrete and continuous dynamical systems exhibiting bistability[290], oscillations[41,291], excitability[292]

and chaos[293,294]. In addition they also persist under detrimental influences such as time delay[295–297], noise[298–300] and time-varying network topologies[301]. Beyond that the position and lifetime of chimera states are amenable to control[302–305]. Consequently, the growing variety of chimera states prompted the development of a classification scheme[306]. A more detailed summary of endeavors in this direction also recently appeared[221]. The experimental verification of these findings is often limited by the large number of oscillators required.
In regards to spiral wave chimeras, their existence and stability properties in a continuous system were analyzed by Carlo Laing[307,308]. Utilizing the Ott-Antonsen ansatz[309] allows for calculating the evolution equation of the order parameter $R(x)$ in the continuum limit, where it was found that spiral wave chimeras persisted. Thus, they are not artifacts of numerical discretization schemes.
Furthermore, Steven Strogatz and coworkers were able to calculate the size of the incoherent core as well as the rotation frequency of the rotating wave in the case of Kuramoto phase oscillators. They combined the known spiral phase field description[310] and simplified the nonlocal kernel operator to a Gaussian, which allowed for the analytic treatment of the coupling integral[311]. They concluded their article by posing the following challenge:

> The possibility of observing spiral wave chimeras in physical systems naturally arises. [...] We leave the experimental observation of chimera states as a challenge to others.

4.2 Experimental Setup

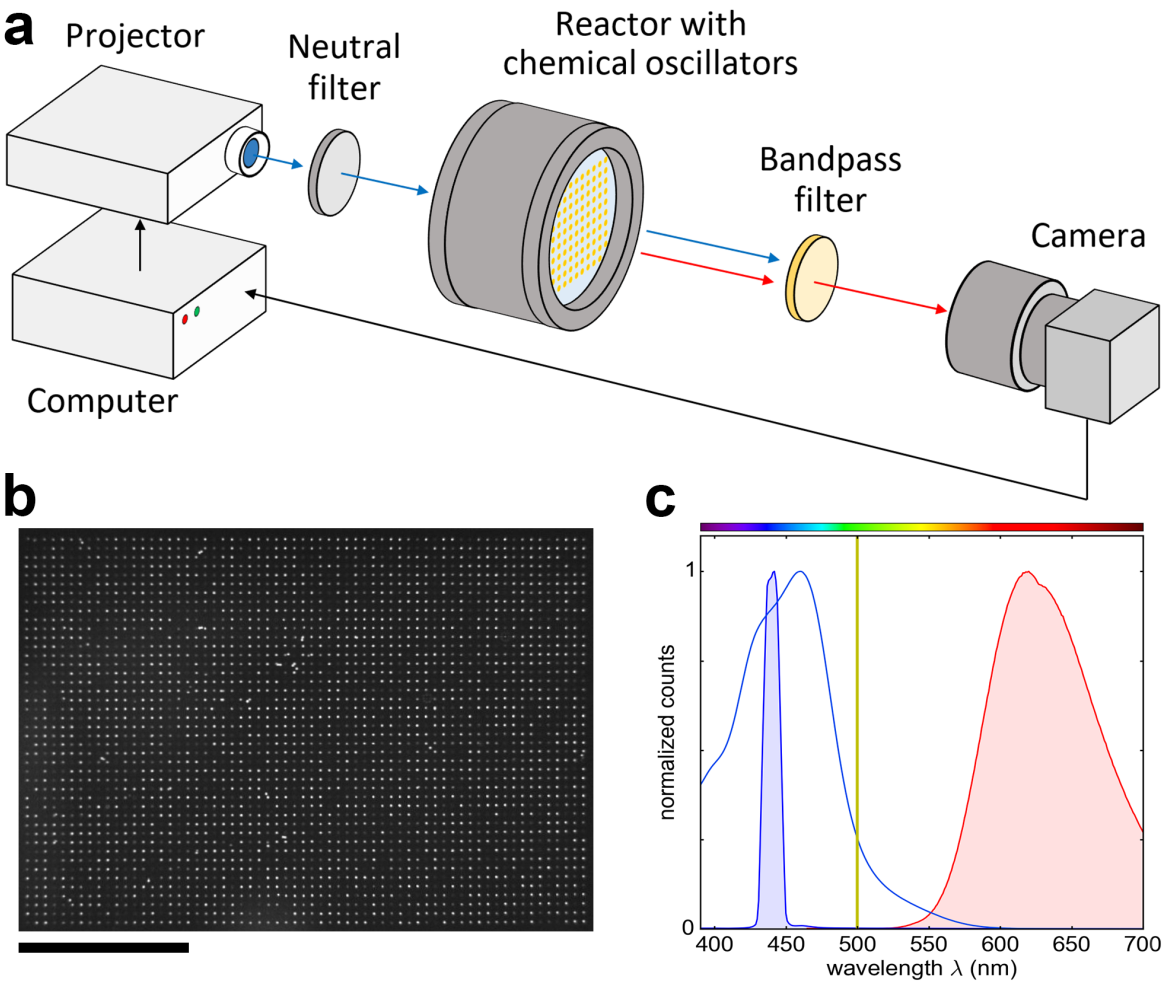

Figure 4.2 | Experimental Setup. (a) A reservoir of chemical micro-oscillators is fixated on an acrylic glass plate in a thermostatted reactor[126]. During their oscillation cycles they emit fluorescence photons, which are recorded with a CMOS camera as grayvalues v_i of each oscillator i. The values are sent to a computer to determine the projected light intensity I_i according to (4.25). This feedback is applied to the oscillators with a projector. (b) A camera snapshot of the reservoir of 2816 oscillators. Each white dot corresponds to a single chemical oscillator. The black bar represents 1 cm and the image is to scale at 1:2.2 (c) Spectral observation: The projector emits a spatiotemporal pattern at a wavelength of 440 nm (filled blue curve); the light is absorbed (blue curve) and excites the photosensitive catalyst, which leads to the emission of fluorescence light above 550 nm (red filled curve). The light from the projector is filtered by a bandpass filter with a cut-off wavelength at 500 nm (yellow line). Further details on the experimental setup can be found in appendix B.1.5.

The difficulties associated with the experimental verification of the spiral wave chimera and how they are resolved is the content of this section. The main challenge is to overcome the oscillator number limit. In addition it is required, that each oscillator can be controlled and

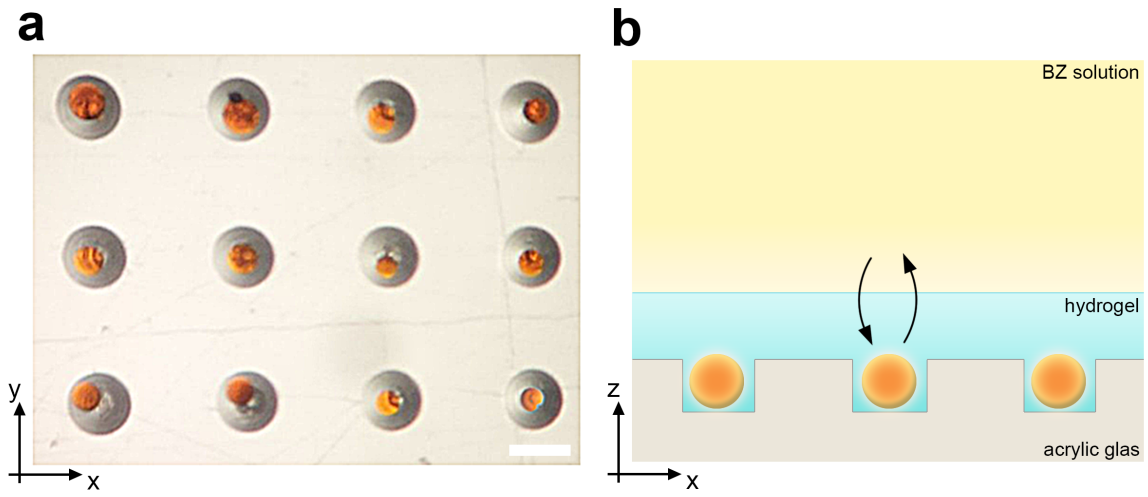

Figure 4.3 | Fixation of chemical micro-oscillator. (a) A top-view photograph of an early prototype of the acrylic glas plate with drilled wells. Each cylindrical well holds a spherical bead, that is loaded with catalyst. The white bar corresponds to 200 µm. (b) A schematic side view of chemical beads during the experiment. The BZ reagents required for the oscillatory reaction are exchanged through the hydrogel layer (indicated by black arrows).

monitored individually. Setups used for previous experiments on synchronization focused on small populations[217,228,244,253,258,312–316]. Scaling up the size of the network beyond $N > 1000$ oscillators, is often unfeasible. However, numerical simulations indicate (see next section 4.3), that an array of oscillators spanning $N = 32 \times 32 = 1024$ nodes is required to resolve the incoherent core and coherent rotating arm.

In principle, the catalyst-loaded cation-exchange beads previously utilized for studying synchronization on small networks (chapter 3) are a good candidate. The problem with the naive approach of simply increasing their number from $N = 10$ to $N > 1000$ in a Petri dish (see Fig. 3.2) is that each bead is mobile. Tracking each oscillator location is not a remedy anymore, since over time all beads will stick to each other after colliding and form a continuous medium[317].

The solution is to place each bead within the confines of a small cavity (Figs. 4.2 and 4.3). For this purpose we utilize an acrylic glas plate that has 64×44 cylindrical wells drilled into it (Fig. 4.2b). All wells have a depth of 150 µm, a diameter of 200 µm and are separated from their respective next neighbors by 400 µm. Each well holds a cation-exchange bead that is loaded with the photosensitive catalyst of the BZ-reaction (appendix C.1.3). Furthermore, the wells are sealed off with a 200 µm high layer of silica hydrogel (Fig. 4.3b). Since the hydrogel is microporous[318], it allows for the passage of BZ reagents, such as hydrogen ions H^+, bromate BrO_3^- and malonic acid MA. They are required for the oscillatory reaction to occur

at the bead sites. In addition, we employ a variant of the photosensitive catalyst, $Ru(dmbipy)_3$, with additional dimethylene ligands[126]. This sterically fixates the catalyst molecules inside the bead polymer matrix, such that they can not escape. As a consequence, chemical aging effects are greatly reduced, which extends the potential runtime of experiments to beyond 24 hours.

Another challenge is measuring the current state of the oscillation cycle. The traditional method of absorption spectrophotometry[144], where the optical contrast originates from the difference in absorption spectra at varying oxidation states of the catalyst (chapter 2.2), is not applicable here. There is only a vanishingly small contrast, because the amount of catalyst on each oscillator is too miniscule. While the lacking contrast could be improved using specialized image software, there is a better alternative. Instead of relying on absorption, a highly enhanced optical contrast is obtained exploiting the fluorescence of the catalyst (Fig. 4.2c). In the reduced form, $Ru(dmbipy)_3^{2+}$, the catalyst emits fluorescence photons with a wavelength of $\lambda > 550\,\mathrm{nm}$ whereas in the oxidized form, $Ru(dmbipy)_3^{3+}$, it does not. During the oscillation cycle, the catalyst will periodically switch between both oxidation states. This allows for the direct observation of chemical oscillations with a grayscale camera that records the fluorescence photons with spatial resolution.

Due to its photosensitivity, the catalyst can not only be exploited for observation of the oscillation cycle, but also for its perturbation. Additional light intensity accelerates the oscillation, while less decelerates it. These are the prerequisites for experiments on synchronization. While the simplest cases of frequency-locking in periodic forcing and mutual coupling can be successfully reproduced, the experimental possibilities are far from exhausted. The light interaction opens the possibility for a very general coupling scheme involving N oscillators:

$$I_i(t) = I_0 + \sum_{j=1}^{N} \left(W_{ij}(t)\, H_{ij}\Big(v_i(t,\tau), v_j(t,\tau), t\Big) \right) + D_i(t)\xi_i. \tag{4.24}$$

There is a background intensity I_0, which enables cumulated perturbations from the network that reduce the applied light intensity. The topology of the system is defined by the weighted adjacency matrix $\underline{\underline{W}}$. In addition to encoding the connectivity of the network, it also holds information on the strength of each link. For identical coupling strength K across all links, $\underline{\underline{W}}$ simplifies to $\underline{\underline{W}} = K\underline{\underline{A}}$, where $\underline{\underline{A}}$ is the adjacency matrix. Possible topologies include one-, two- and three-dimensional grid networks as well as prototypical and real-world networks, such as scale-free[216], small-world[319], sparsely and densely random networks with symmetries[202,217] as well as power grids[320] and the complete connectome of the nematode C. Elegans[321,322]. The coupling function H_{ij} may be different for each edge $i \to j$, but always depends on the measured grayvalues v_i at a current $v_i(t)$ or past time $v_j(t-\tau)$. Furthermore

the coupling strength and type are not stationary, but can be time-dependent and thus allow for the implementation of control schemes. Last but not least it is also possible to include additive noise, where each node has an individual noise intensity D_i and white or colored noise spectrum[323,324] determining ξ_i .
The general coupling (4.24) includes as a special case the nonlocal coupling (4.8) required for the verification of spiral wave chimeras. In a concise notation, the nonlocal coupling on a two-dimensional grid network is given by

$$I_{\boldsymbol{i}}(t) = I_0 + K \sum_{\boldsymbol{j} \in \Omega_{\boldsymbol{i}}} e^{-r(\boldsymbol{i},\boldsymbol{j})/\kappa} \Big(v_{\boldsymbol{j}}(t-\tau) - v_{\boldsymbol{i}}(t) \Big), \tag{4.25}$$

with a characteristic coupling range κ, a vector-valued node index,

$$\boldsymbol{i} = (i_x, i_y), \tag{4.26}$$

that accounts for two dimensions and a corresponding Euclidean distance function

$$r(\boldsymbol{i},\boldsymbol{j}) = \|\boldsymbol{i}-\boldsymbol{j}\|_2 = \sqrt{(i_x-j_x)^2 + (i_y-j_y)^2}. \tag{4.27}$$

The square area Ω_i on which the discrete coupling integral is evaluated stems from the maximum norm

$$\Omega_{\boldsymbol{i}} = \Big\{ \boldsymbol{i},\boldsymbol{j} \in \mathbb{Z}^2 \;\Big|\; \|\boldsymbol{j}-\boldsymbol{i}\|_{\max} \leq \ell \Big\} = [i_x-\ell, i_x+\ell] \times [i_y-\ell, i_y+\ell], \tag{4.28}$$

where $2\ell+1$ is the side length of the square as in (4.21). Furthermore a variety of initial conditions are accessible, because each oscillator can be manipulated individually. Employing periodic forcing close to the unperturbed oscillation period $T_{\text{forcing}} \approx T_{0,\boldsymbol{i}}$, it is possible to entrain a node i, such that it oscillates according to

$$\frac{d\varphi_{\boldsymbol{i}}}{dt} = \omega_{\text{forcing}} + \varphi_{0,\boldsymbol{i}} \tag{4.29}$$

with an oscillator-dependent phase offset $\varphi_{0,\boldsymbol{i}}$. This allows for global in-phase synchronization, phase gradients, chimera states and more as initial conditions using light.
Still, the photosensitivity brings to the forefront yet another predicament: The heterogeneity of the oscillators. Preliminary experiments with coupled oscillators revealed, that the distribution of unperturbed periods $T_{0,\boldsymbol{i}}$ was too broad, as to allow for frequency synchronization. Without it, chimera states are unobservable, because they coexist with the globally in-phase synchronized state[270]. A measurement of the bead diameters reveals that the bead sizes

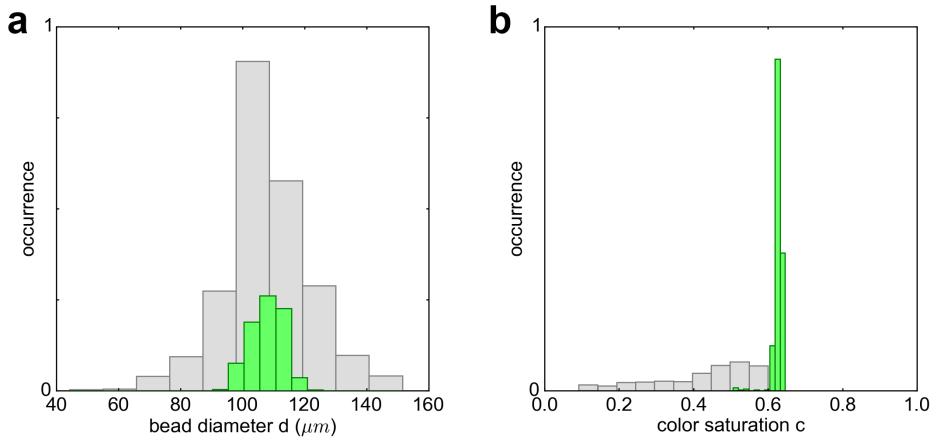

Figure 4.4 | Oscillator heterogeneity. (a) Comparison of oscillator bead diameters before (gray) and after sieving procedure (green). (b) Comparison of catalyst loading for manual mixing (gray) and by a vortex mixer (green). In both cases the occurrence is normalized to the initial size of the distribution.

are not monodisperse (Fig. 4.4a). The bead diameters approximately follow a Gaussian distribution ranging from 75 –150 µm centered at 110 µm. Previously the size distribution of beads was identified as a source of period heterogeneity[325]. The reason is that larger beads feature a larger surface area allowing for a greater reactant flux. This influences the resulting periods. In addition each bead – even of identical size – may hold different amounts of catalyst (Fig. 4.4b).

With the root causes of the period heterogeneity identified, it is possible to rectify them. To homogenize the size distribution, we built our own sieving machine. It consists of a frequency generator, a car amplifier stage, a subwoofer speaker, different fine sieves and tape. A detailed description of the sieve machine is in the appendix B.1.5. The mesh sizes of the three stacked sieves are: 106 µm, 112 µm and 125 µm. The bead throughput is greatly enhanced when adding tiny glas spheres with a diameter of 1 mm to each sieve, because their kinetic energy pushes the beads through the holes. After the sieving procedure is finished, the remaining beads are collected between sieves with meshes 106 µm and 112 µm.

Homogeneous catalyst loading of these beads is achieved by slowly adding the catalyst to a vial of beads in water solution. It is critical that this is done while the vial is continuously shaken by a vortex mixer.

The final result of this procedure is quantified under a light microscope. Utilizing image recognition software to detect the beads as circles on a camera snapshot, it is possible to subsequently extract their diameters d and average color saturation c (Fig. 4.4). In this way their quality is automatically and quickly assessed. This reveals, that the beads have a very narrow size distribution (100 –120 µm) and are loaded nearly identically with catalyst, such that they are suitable for experiments on spiral wave chimeras.

Taken together each immobile bead is a node in the reservoir of chemical oscillators. Depending on properties such as their natural period T_0 and their phase response curve, all beads are filtered. Suitable candidates are utilized as nodes in a network experiment that is connected to its neighbors via light. Exploiting the fluorescence properties of the catalyst allows for a simple yet compact experimental setup (Fig. 4.2).

4.3 Numerical Simulations

In order to guide the search for the spiral wave chimera in the experiments, a large number of numerical simulations were performed to explore the space of coupling parameters.
The dynamics of the catalyst loaded beads can be reproduced qualitatively with the ZBKE model[326]. It was originally devised by Zhabotinsky and Epstein in 1993 and later enhanced[244,262,327] to account for the excitatory effect of light illumination[328] (see appendix C.1.3 for a brief review of the derivation). Here, the model is adapted to describe the local dynamics of an oscillator $\boldsymbol{i} = (i_x, i_y)$ in a network:

$$\begin{aligned}
\frac{du_i}{dt} &= \frac{1}{\varepsilon_1}\left(I_i + \frac{\mu - u_i}{\mu + u_i}\left(\beta + q_i \frac{\alpha v_i}{\varepsilon_3 + 1 - v_i}\right) + \gamma\varepsilon_2 w_{ss,i}^2 + (1 - v_i) w_{ss,i} - u_i^2 - u_i\right), \\
\frac{dv_i}{dt} &= 2I_i + (1 - v_i) w_{ss,i} - \frac{\alpha v_i}{\varepsilon_3 + 1 - v_i}, \\
w_{ss,i}(u_i, v_i) &= \frac{1}{4\gamma\varepsilon_2}\left(\sqrt{16\gamma u_i \varepsilon_2 + v_i^2 - 2v_i + 1} + v_i - 1\right).
\end{aligned} \tag{4.30}$$

In this model the variables u_i, v_i and $w_{ss,i}$ represent the dimensionless concentrations of bromous acid [$HBrO_2$], oxidized catalyst [$Ru(dmbipy)_3^{3+}$] and bromous acid radical in equilibrium [$HBrO_2^+$]$_{ss}$, respectively. Chemical model parameters and their values are listed in table 4.1 together with parameters of the coupling.
Two parameters stand out due to their special role: The period heterogeneity is introduced heuristically[244] by drawing the stoichiometric parameter q_i of each bead from a uniform distribution $q_i \in [0.5, 1.0]$, which leads to a distribution of natural periods $T_0(q_i)$ between 30.2 and 45.9. In relation to the reference period $T_0 = 34.4$ at $q = 0.7$, the limits are $0.88\,T_0$ and $1.33\,T_0$. Note that, since the model is dimensionless, absolute time durations are given without units. The resulting spread of periods in the simulations agrees well with the experiments. Parameter I_i represents the light intensity applied on oscillator $\boldsymbol{i}$. This is the most important parameter, because it plays the central role of introducing nonlocal coupling.

In the simulations the oscillators on a two-dimensional grid of $n_x \times n_y$ nodes are coupled according to

$$I_i(t) = I_0 + K \sum_{j \in \Omega_i} e^{-r(i,j)/\kappa} \Big(v_j(t-\tau) - v_i(t) \Big). \tag{4.31}$$

This is the same coupling formula as used earlier for the experiments (4.25), since the light interaction introduced via I_i is additive in the local dynamics (4.30). The time-delayed differences in grayvalues between the oscillator i and its nonlocal neighbor j are weighted with an exponential kernel, that decreases with the Euclidean distance r (4.27). The parameter κ is the characteristic coupling length. For small κ the coupling is very localized, while for large κ it encompasses distant nonlocal neighbors. The neighbors are taken from a square region Ω_i with side length $2\ell+1$ centered on oscillator i (4.28).

Table 4.1 | ZBKE model. For a derivation of the values based on the reagent concentrations in the experiment, see appendix C.2. Note that the stiff dynamics of the ZBKE model require the use of the double precision datatype. Simulations with single precision floating point values develop numerical artifacts, that lead to strong deviations from the original limit cycle.

variable / parameter	value	description
$u_i(t)$		dimensionless [$HBrO_2$] on node i
$v_i(t)$		dimensionless [$Ru(dmbipy)_3^{3+}$] on node i
$w_{ss,i}(u_i, v_i)$		dimensionless steady state [$HBrO_2^+$] on node i
$i = (i_x, i_y)$		two-dimensional index
I_i		light intensity projected on node i
τ		time delay
K	5.25×10^{-4}	coupling strength
κ	2.5	coupling range parameter
ℓ	4	maximum coupling distance
Δt	1.0×10^{-4}	integration time step
I_0	5.25×10^{-4}	background light intensity
q_i	0.5-1.0	stoichiometric parameter of node i
ε_1	0.11	time scale parameters
ε_2	1.7×10^{-5}	
ε_3	1.6×10^{-3}	
α	0.1	kinetic parameters
β	1.7×10^{-5}	
γ	1.2	
μ	2.4×10^{-4}	

Different types of nonlocal kernels, such as a constant[277] or Gaussian[311] did not show qualitatively different results. For simplicity the employed kernel is not normalized as in previous work[267]. Here, a possible normalization factor just rescales the coupling strength K. Since the grid is finite, it is important to account for boundary effects. Generalizing the nonlocal coupling in (4.31) by replacing the time-delayed grayvalue difference with a coupling function $H(v_i, v_j)$ leads to

$$I_i(t) = I_0 + K \sum_{j \in \Omega_i}^{N} e^{-r(i,j)/\kappa} H(v_i, v_j). \tag{4.32}$$

At the boundary, the general coupling function H is modified as,

$$H(v_i, v_j) = \begin{cases} v_j(t-\tau) - v_i(t) & , 1 \leq j_x \leq n_x \wedge 1 \leq j_y \leq n_y \\ 0 & , \text{else} \end{cases}, \tag{4.33}$$

in order to omit non-existent nodes beyond the grid. This procedure is similar to Neumann boundary conditions[158]. Whereas for periodic boundary conditions the modifications are:

$$H(v_i, v_j) = v_{j_{\text{bc}}}(t-\tau) - v_i(t) \tag{4.34}$$

with the components of $\boldsymbol{j}_{\text{bc}}$ obeying the grid periodicity,

$$j_{x,\text{bc}} = \big((j_x - 1) \bmod n_x\big) + 1, \tag{4.35}$$

$$j_{y,\text{bc}} = \big((j_y - 1) \bmod n_y\big) + 1. \tag{4.36}$$

Additive shifts are included in the cyclic modulo function to account for the row and column indices starting at a node index of 1 instead of 0. Preliminary simulations with either boundary conditions, (4.33) or (4.34), show the same patterns in the bulk area. This excludes the possibility of spiral wave chimeras being a boundary induced artifact.

Note that instead of a phase frustration parameter α, as in the Kuramoto phase oscillator model[213], we employ time delay[245,295,329]. It can be shown, that small time delay τ plays a similar role as α in coupled phase oscillators[221]. While α offsets the phase difference in the sinusoidal interaction function,

$$\sin\Big(\varphi_j(t) - \varphi_i(t) - \alpha\Big), \tag{4.37}$$

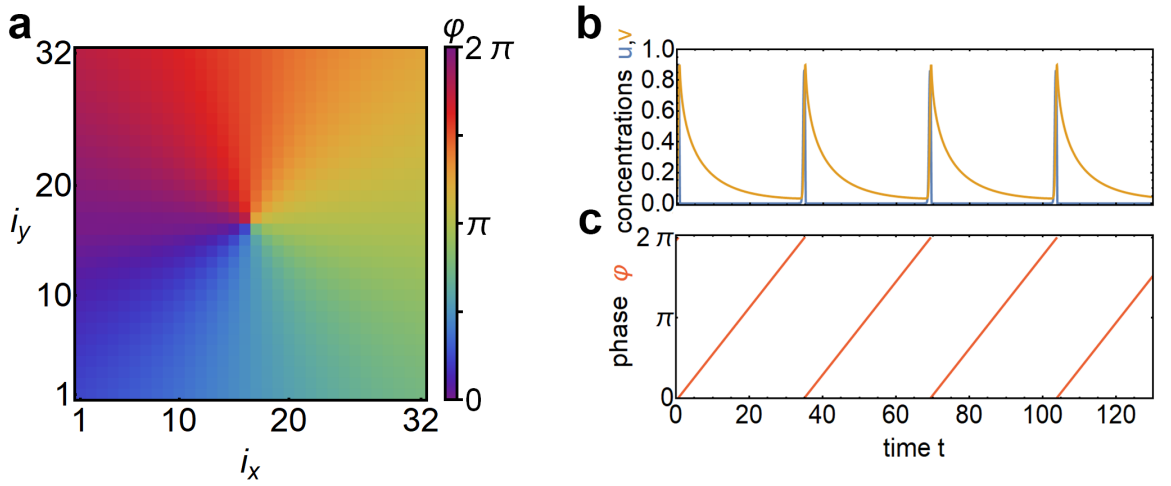

Figure 4.5 | Initial condition for spiral wave chimeras. (a) The initial phase distribution contains a topological defect in the form of a phase singularity[87] at its center. At this point, all phases coincide. (b) From the periodic behavior in the time series of concentrations v (yellow) it is possible to (c) calculate a phase variable φ, that increases linearly from 0 to 2π between consecutive peaks.

the time delayed phase $\varphi_j(t-\tau)$ can be linearized around vanishing delay $\tau \approx 0$, such that is also leads to a phase offset:

$$\sin\left(\varphi_j(t-\tau) - \varphi_i(t)\right), \tag{4.38}$$

$$= \sin\left(\varphi_j(t) - \varphi_i(t) - \tau\frac{d\varphi_j(t)}{dt}\right). \tag{4.39}$$

Comparing (4.37) and (4.39) reveals $\alpha = \tau\omega_j(t)$. Thus, in the time-delayed case the offset depends on the rotation frequency $\omega_j(t)$. In both cases the offset makes it more difficult to attain stable in-phase synchronization, because the interaction does not vanish in this state. Even though it has been demonstrated that it is also possible to encode phase frustration in the coupling coefficient matrix[330], using time delay τ is a more intuitive option, as it naturally arises due to finite propagation speeds. Besides changing the chemical reaction kinetics, the coupling coefficients $C_{v\to v} = 2$ and $C_{v\to u} = 1/\varepsilon$, which are the prefactors of the light intensity I_i in (4.30), are not independently accessible.

Chimera states are known to depend very sensitively on initial conditions[272]. However, it turns out that the spiral wave variant can be initiated very reliably. Inspired by the traditional way of initializing spiral waves, an earlier approach[245] required a meticulous protocol that started with breaking a planar wave in a reaction-diffusion system. Subsequently the interaction type was morphed incrementally from local diffusion to nonlocal coupling by

slowly increasing the maximum coupling range l and time delay τ. Since this procedure depends crucially on the occurrence of a planar wave and furthermore on the right duration of each incremental stage, its success rate is not very high. Another approach[282] requires no specialized external interference: Spiral wave chimeras develop by chance from a random initial condition. Testing this procedure in simulations with the ZBKE model (4.30) revealed, that the probability for a successful spiral initiation was not high enough, in order to be applied in the chemical experiment. The final and most reliable procedure applies a non-vanishing topological charge $Q \neq 0$ that is a feature of spiral waves[38]. Instead of concentrations u_i and v_i, the initial condition is encoded in phases[311],

$$\varphi_{ic}(i_x, i_y) = \arctan\left(\frac{i_y - i_{y,0}}{i_x - i_{x,0}}\right), \tag{4.40}$$

and contains a phase singularity at its center $(i_{x,0}, i_{y,0})$ (Fig. 4.5a). The function arctan is the four-quadrant inverse of the tangent function tan. It produces a smooth gradient from 0 to 2π while traversing a unit circle along the azimuthal direction. For its successful application in the numerical simulation, the mapping $\varphi \to (u, v)$ is required, such that (4.40) can be utilized for limit cycle oscillators. Because there is no analytic parametrization of the limit cycle in the ZBKE model (4.30), the alternative is to measure the concentrations during a full oscillation cycle and assign a phase variable to them, that increases linearly with time (Fig. 4.5b,c). In the chemical experiment the initial phases can be set by utilizing individual periodic forcing as described before (4.29). Even with modest amounts of heterogeneity or noise, a spiral wave chimera always develops from initial condition (4.40) for suitable parameter combinations.

The simulations reveal the existence of spiral wave chimeras over a large range of coupling parameters K and τ (Fig. 4.6). A spiral wave chimera is reliably detectable by evaluating the global topological charge $Q = \sum_i Q_i$, where the local charge Q_i is calculated via a discretized line integral[331]:

$$Q_i = \sum_k \mathrm{mod}(\Delta\phi_k, 2\pi). \tag{4.41}$$

The indexed phase differences $\Delta\phi_k$ are evaluated along a discretized loop enclosing oscillator i. Measured far from the core region, a spiral wave as well as a spiral wave chimera exhibits a topological charge of $Q = \pm 1$ depending on the direction of rotation.
The detection of a spiral wave chimera is indicated in figure 4.6 with colored squares. If the standard deviation of the topological charge fluctuates ($\sigma_Q > 0.01$), no stable spiral wave

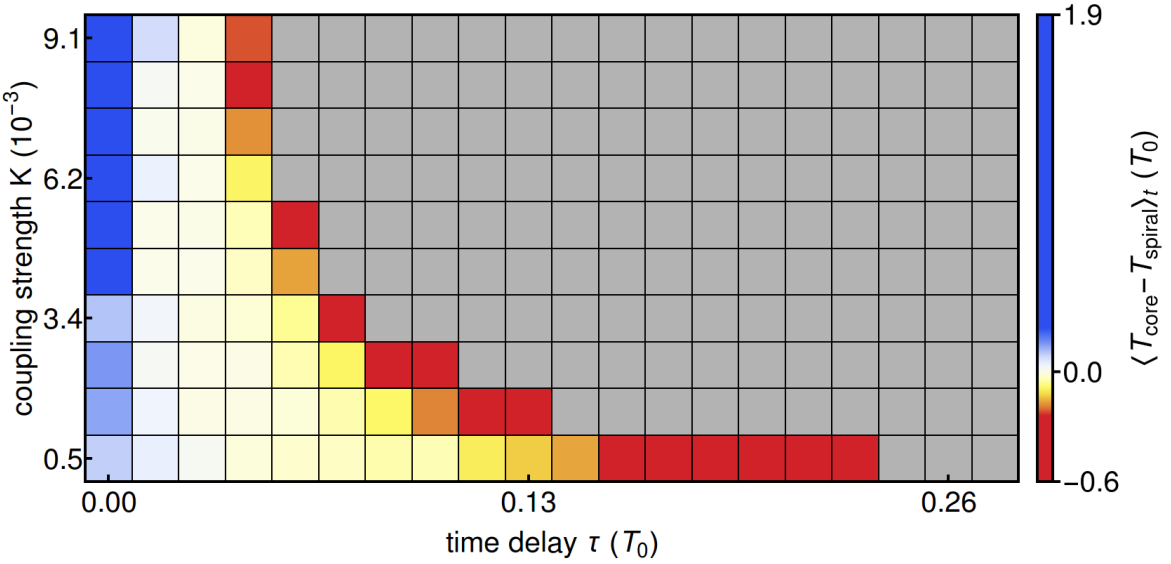

Figure 4.6 | Numerical phase diagram in the K-τ plane. Spiral wave chimeras are detected if the topological charge (4.41) follows $|Q| = 1$ and its standard deviation is $\sigma_Q < 0.01$. Parameter combinations which lead to spiral wave chimeras are colored from red to blue depending on the time-averaged difference between the mean periods of oscillators inside, T_{core}, and outside the core, T_{spiral}. Gray squares indicate the absence of a spiral wave chimera. Fixed parameter values as in table 4.1.

pattern exists and the square is colored gray. Otherwise, the square is colored according to the difference of the averaged periods inside the core, T_{core}, and outside of it, T_{spiral}. This serves to highlight the period difference of oscillators in the coherent and incoherent parts, which is characteristic for chimera states[332]. It turns out that in contrast to phase oscillators[311], spiral wave chimeras in the ZBKE model (4.30) feature a core region with slower as well as faster oscillators than its surroundings. In agreement with previous findings for phase oscillators[311] the overall existence region for spiral wave chimeras extends from zero to small values $\tau < 0.25\,T_0$ of time delay τ. Furthermore, the interval of delay values in which chimeras are observable shrinks for larger coupling strength K.

As a consequence, further exploration of parameter space is focused on a small value of coupling strength K. Keeping K fixed at $K = 5.25 \times 10^{-4}$, the impact of time delay τ is explored for values spanning the natural rotation period from $\tau = 0$ to $\tau = T_0$ (Fig. 4.7). As the time delay τ is increased, a sequence of spiral wave chimeras, antiphase clusters, global in-phase synchronization and eventually spiral wave chimeras again is observed on the nonlocally coupled array of ZBKE oscillators (4.30). Representative samples from this numerical phase diagram will later be plotted and compared to their experimental counterparts shown in the next section (Figs. 4.10 and 4.11).

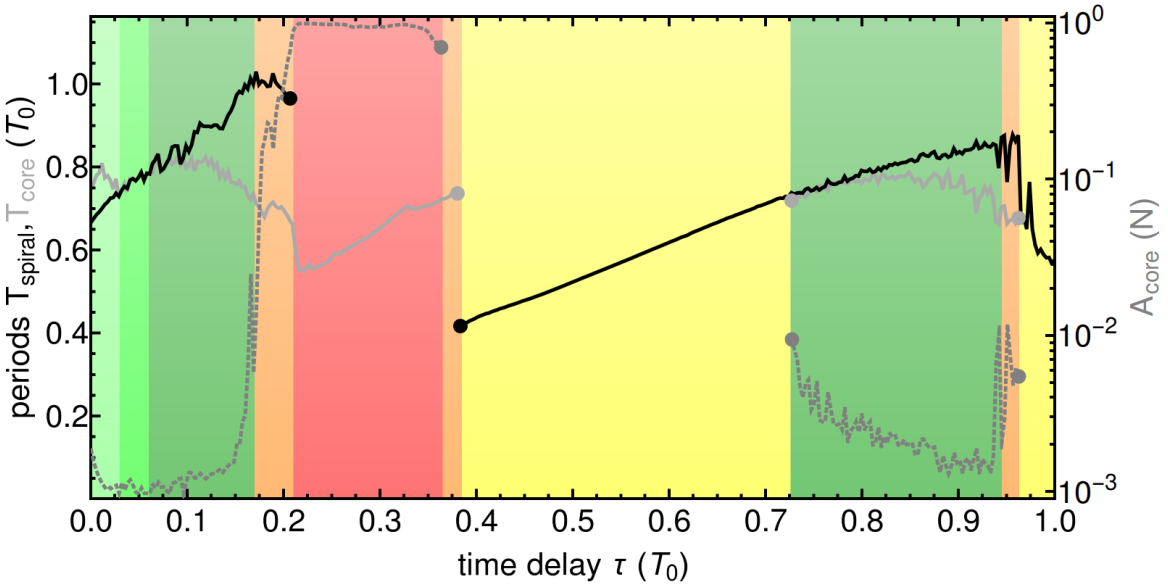

Figure 4.7 | Numerical phase diagram for time delay τ. The sequence of patterns on the delay-coupled nonlocal grid comprises: Spiral wave chimera with slow core (bright green), ordinary spiral waves with no core (medium green), spiral wave chimera with fast core (dark green), core splitting and fleeting coherence as discussed in the next section (orange), antiphase clusters (red), coexistence of in-phase and antiphase clusters (orange), in-phase synchronization (yellow), spiral wave chimera (dark green), core synchronization, as described in the next section (orange) and in-phase synchronization again (yellow). The periods outside T_{spiral} and inside the core T_{core} are given as solid black lines and solid gray lines, respectively. In cluster regions only one of both periods is shown, because the other is irrelevant. The dashed gray line represents the number of oscillators far from zero-lag synchronization. Time delay τ and periods T_{spiral}, T_{core} are normalized by the reference period T_0 and the size A_{core} is normalized by the total number of oscillators in the array N. Time delay range is resolved in 350 steps. Fixed parameter values as in table 4.1.

At each value of time delay τ the stability of the spiral and cluster patterns is evaluated by starting from three suitable initial conditions. For spiral wave chimeras the initial condition is given by a phase distribution with a phase singularity (4.40), whereas the d-clusters with $d = 1,2$ are started from d-clusters overlayed with a small amount of noise. The case $d = 1$ corresponds to in-phase and $d = 2$ to antiphase synchronization. After 60 periods the perseverance of an initial state is evaluated by checking if the topological charge fulfills $Q = \pm 1$ for spiral wave chimeras or whether the generalized Kuramoto order parameter[333],

$$R_d = \frac{1}{N}\left|\sum_{j=1}^{N} e^{\mathrm{i}d\varphi_j}\right|, \tag{4.42}$$

satisfies $R_d > 0.7$ for d-clusters. The total number of oscillators in the grid is given by $N = n_x \times n_y$. This analysis reveals (Fig. 4.7), that the global in-phase synchronized state is

stable for the entire range of time delay values (yellow, green, orange shading), except for a small window $\tau \in [0.21, 0.35]\, T_0$. In this interval only antiphase-synchronized states prevail (red shading). Finally, in green regions the in-phase synchronized state coexists with the different variants of the spiral wave chimera, as is typical for chimera states[272].
Further details of the chimera states are revealed by evaluating the mean period inside T_{core} and outside the core T_{spiral} as well as its size A_{core}. Depending on a discretized local Kuramoto order parameter,

$$R_{\boldsymbol{i}} = \frac{1}{|\Omega_{R,\boldsymbol{i}}|} \left| \sum_{\boldsymbol{j} \in \Omega_{R,\boldsymbol{i}}} e^{\mathrm{i}\varphi_{\boldsymbol{j}}} \right|, \tag{4.43}$$

oscillators are declared as elements of the core $R_{\boldsymbol{i}} < 0.4$ or of the spiral $R_{\boldsymbol{i}} > 0.6$. The set of oscillators $\Omega_{R,\boldsymbol{i}}$ are defined similar to the square domain in equation 4.28,

$$\Omega_{R,\boldsymbol{i}} = \left\{ \boldsymbol{i}, \boldsymbol{j} \in \mathbb{Z}^2 \;\middle|\; \|\boldsymbol{j} - \boldsymbol{i}\|_{\max} \leq \ell_R \right\}, \tag{4.44}$$

with $\ell_R = 2$. Comparing both periods T_{core} and T_{spiral} shows (Fig. 4.6), that spiral wave chimeras existing for small time delay τ can be divided into three qualitatively distinct subclasses, where the core oscillators have a slower $T_{\text{core}} > T_{\text{spiral}}$, approximately equal $T_{\text{core}} \approx T_{\text{spiral}}$ or faster period $T_{\text{core}} < T_{\text{spiral}}$. Similar to previous results for phase oscillators[311], the core size of fast core spirals grows with increasing time delay for $\tau \in [0.05, 0.18]\, T_0$. The growth continues throughout the orange transition domain until the core fills the entire grid (red domain). Here, $\tau \in [0.21, 0.35]\, T_0$, the oscillators are not incoherent, but instead cover the grid with a random arrangement of oscillators in antiphase. For larger time delay, $\tau \in [0.39, 0.72]\, T_0$, antiphase clusters are superseded by global in-phase synchronization, where all oscillators share the same phase (yellow domain). Remarkably, for large time delay, $\tau \in [0.72, 0.935]\, T_0$, there is a resurgence of spiral wave chimeras with a fast core (green domain). Note that the dynamical behavior does not repeat itself at a delay value of the full natural period $\tau = T_0$, because spiral wave chimeras transition into in-phase synchronization (yellow domain) around $\tau \approx 0.94$.
The preceeding numerical evidence (Figs. 4.6 and 4.7) strongly suggests the possibility of finding spiral wave chimera states in the chemical experiment with initial condition (4.40) for suitable coupling parameters. Furthermore it will be shown in the next section how the numerical findings on cluster states can be rationalized with the peculiar shape that the phase response curve assumes for strong coupling.

4.4 Results

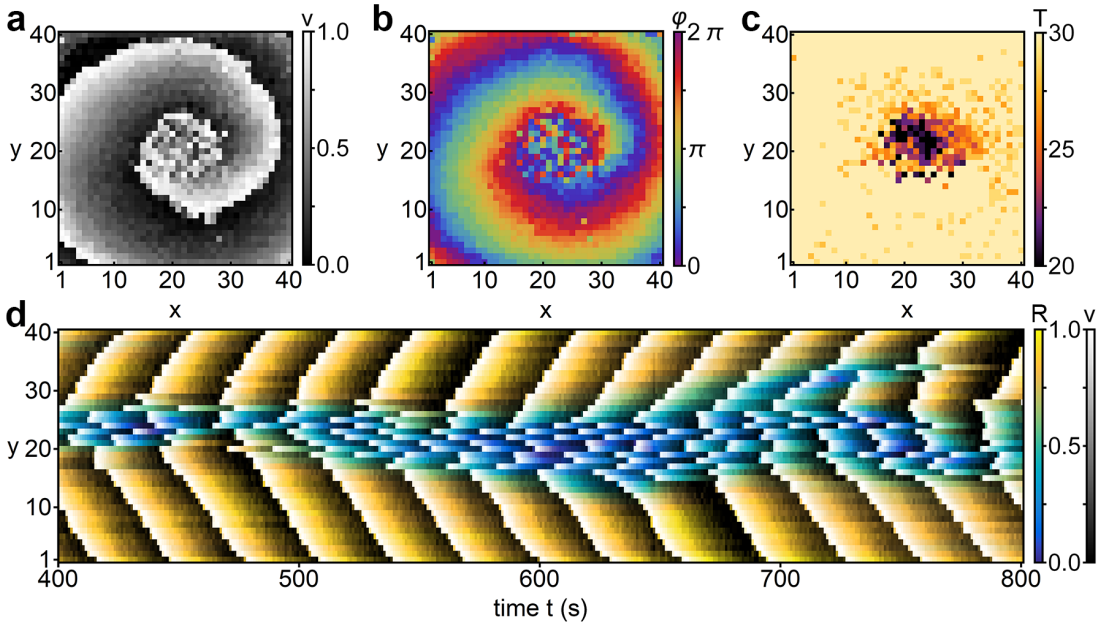

Figure 4.8 | Experimental observation of a spiral wave chimera state. (a) Spiral wave chimera in an array of $N = 1600$ photochemically coupled BZ oscillators. The gray value pattern v_i is from fluorescent light emitted by the reduced catalyst $Ru(dmbpy)_3^{2+}$. The spiral rotates with a period $T_{spiral} = 33\,s$ around the incoherent core consisting of approximately 40 phase-randomized oscillators. Image taken at $t = 700\,s$ after initiation. (b) Oscillator phases obtained from the gray values measured in (a). (c) Periods of the oscillators in (a) illustrating that oscillators in the spiral wave are approximately frequency synchronized in the rotating spiral wave, while the asynchronous core oscillators exhibit shorter periods. (d) Space-time plot of the spiral wave chimera from measurements along a cross section $x_{core}(t)$, that follows the core center during 14 rotational periods of the spiral. The coloration combines information from grayvalues v_i (a), which select the brightness, and the local order parameter R_i (4.43), which determines the color. Coupling parameters in (4.25) are: $K = 0.08$, $\kappa = 3.1$, $\tau = 2\,s$, $I_0 = 0.06\,mW\,cm^{-2}$, $\ell = 4$. Initial reactant concentrations: $[H_2SO_4]_0 = 0.77\,M$, $[NaBrO_3]_0 = 0.51\,M$, $[NaBr]_0 = 0.08\,M$, $[malonic\ acid]_0 = 0.16\,M$.

With the experimental setup described in section 4.2 and an informed choice of coupling parameters (section 4.3), we successfully confirmed the existence of spiral wave chimeras experimentally[334] (Fig. 4.8). The chemical oscillators for the experiment are selected from a reservoir of 2816 beads, whose period distribution has a mean of $(78.3 \pm 23.6)\,s$. Selecting suitable beads based on their periods from the interval $T \in [70, 98]\,s$, results in a narrow period distribution with a mean of $\langle T \rangle = (85.7 \pm 7.1)\,s$ and a width of $\delta T = 8.3\,\%$ relative to the mean period. Taken together the oscillators constitute a two-dimensional grid network consisting of $N = 40 \times 40 = 1600$ nodes.

The initial condition (4.40) is enforced with individual periodic forcing (4.29) for a duration of 200 s. On the two-dimensional grid this results in the feedback taking the shape of a rotating, triangular-shaped wave with one corner centered at $(x_0, y_0) = (20, 20)$. To guarantee entrainment, the forcing signal has a rectangular waveform and a period $T_{\text{forcing}} = 48\,\text{s}$ that is smaller than the lower bound of the selected period interval.

Directly afterwards, nonlocal photocoupling (4.25) between oscillators is initiated. During the first two periods the spiral wave formed while the core turned incoherent. Over the experiment, the size of the core fluctuated between 20 and 40 oscillators. A snapshot at $t = 700\,\text{s}$ of the fluorescence intensity emitted by the chemical beads and measured as grayvalues v_i by the camera is shown in figure 4.8a. To quantify synchronization with the local Kuramoto order parameter (4.43), oscillator phases φ_i (Fig. 4.8b) are calculated by linear interpolation between two consecutive peaks in the grayvalue time series (Fig. 4.5b,c) via equation (3.10). Grayvalues and phases clearly exhibit the distinctive incoherence in the core and the coherence of the spiral wave surrounding it. Both regions exhibit different mean periods, $T_{\text{spiral}} \neq T_{\text{core}}$, (Fig. 4.8c), which is another characteristic feature of chimera states[332].

While the snapshots depict the spatiotemporal pattern at a fixed instant in time, the temporal evolution is visualized with a kymograph or space-time plot (Fig. 4.8d). Here, we employ an enhanced kymograph, that simultaneously offers information on the spatial structure of the pattern as well as the local level of order (4.43). The grayvalues v_i, which encode the spatial details of the pattern, contribute to the brightness and the local Kuramoto order parameter R_i determines the color. This has the advantage, that the incoherent firing events in the core and the coherent rotating wave are resolved and colorized simultaneously. In addition, the kymograph is not based on a fixed cross section x_{core}, but tracks the current core center. This ensures that the object of interest, in this case the core, is not outside the cross section. This reveals that the spiral wave chimera shares the characteristic feature of spiral waves: The core region alternatingly emits waves in opposite directions. Eventually the motion of the spiral wave chimera leads to its termination. In the experiment the core collided with the boundary of the grid after lasting for 38 rotation periods.

The tip of a spiral wave in a reaction-diffusion system can be tracked by computing the intersection point of different iso-concentration lines[337] or the cross product of concentration gradients[338]. Due to the non-smooth, incoherent core, these approaches are not applicable to spiral wave chimeras. Instead the local order parameter R_i is utilized for reliable tracking. All oscillators i with $R_i \leq R_{\text{threshold}}$ are collected for $R_{\text{threshold}} = 0.4$. Then each node is assigned a weight $w_i = 1 - R_i/R_{\text{threshold}}$ that increases with declining order. Finally, the potentially multiple core positions are calculated as the weighted centroids $\boldsymbol{r}_{\text{core}} = \sum_i w_i \boldsymbol{i}$ of each simply-

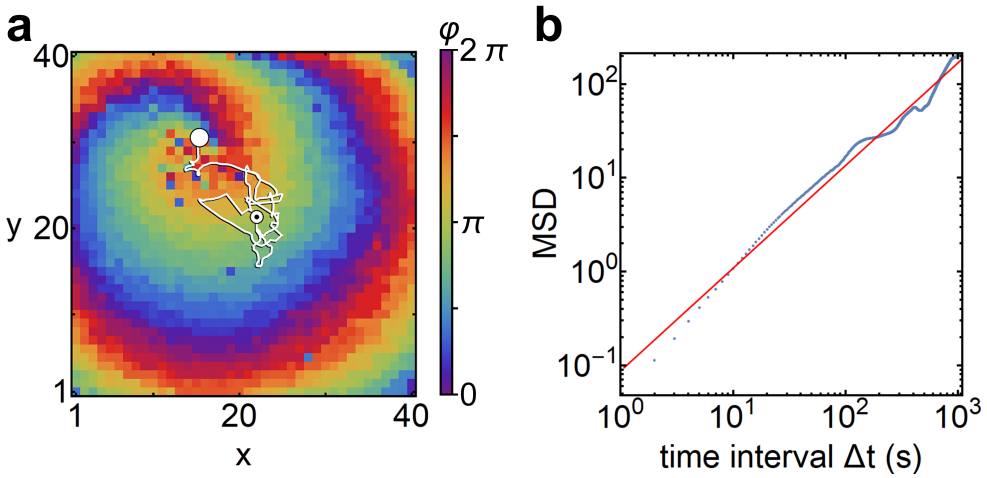

Figure 4.9 | Core trajectory. (a) Unlike a regular spiral wave, whose tip performs rigid rotation or meandering[335], the center of the incoherent core (Fig. 4.8) performs erratic motion as highlighted by the superimposed white line. The starting and end points are marked with a black-dotted and an unfilled circle, respectively. (b) In a logarithmic plot the mean-square displacement shows a roughly linear increase as a function of the measurement time interval Δt. The corresponding scaling exponent was determined from a linear fit (red) as 1.05, which is characteristic for erratic Brownian motion[336].

connected set of low-order oscillators. This method has proven robust against core size fluctuations and even works reliably in cases when a single core splits into many cores. The tracking algorithm is successfully employed (Fig. 4.9) to follow the core position of the experiment presented in figure 4.8. The starting point of the trajectory (white line in figure 4.9a) at $(x_0, y_0) = (20, 20)$ is marked with a white circle overlaid with a black dot. Instead of rigid rotation or meandering[339] the core of the chimera spiral wave traverses an irregular path. This random motion is quantified with the mean square displacement[336] (MSD), which is a measure for the erratic motion of individual particles. It is calculated from a single trajectory by averaging in time over all squared displacements,

$$\Delta r^2(\Delta t) = \Delta x^2(\Delta t) + \Delta y^2(\Delta t), \tag{4.45}$$

occurring for increasing time intervals Δt:

$$\mathrm{MSD}(\Delta t) = \langle \Delta r^2(\Delta t) \rangle_t = \frac{1}{N} \sum_{i=1}^{N} \Delta r_i^2(\Delta t). \tag{4.46}$$

Applied to the experimentally recorded core trajectory, this reveals a linearly increasing MSD (Fig. 4.9b). The corresponding scaling exponent is 1.05, which is an indicator of diffusive Brownian motion[336]. The random walk of the core is in agreement with previous observations in one[340,341] and two dimensions[245,311].

In the case of spiral wave chimeras, the random movement was suspected[311] to be a consequence of the neutral stability of spiral waves with regards to translational perturbations[339]. It is known that random forcing leads to erratic motion of spiral waves[342]. Furthermore a spiral wave is most vulnerable in the tip region[133], which is where the incoherent core of a spiral wave chimera is located at. Taken together, the random perturbations due to the incoherent core are likely to drive the random motion of the spiral wave chimera.

Beyond the experimental verification of spiral wave chimeras, we further investigate what patterns can emerge on an array of nonlocally delay-coupled oscillators (Figs. 4.10 and 4.11). Guided by the exploratory numerical simulations (Fig. 4.7), we successfully found representative examples for every distinct dynamical behavior in the chemical experiment.

At small values of time delay τ, three spiral patterns exist, that can be differentiated by the behavior of the core oscillators. In the order of increasing delay τ, first spiral wave chimeras appear whose oscillators are slower in the core than the spiral wave $T_{\text{core}} > T_{\text{spiral}}$ (Fig. 4.10a,b). The preliminary numerical simulations (Fig. 4.6) suggest, that this behavior is more pronounced for large coupling strength K, so in the experiment we choose a small time delay of $\tau = 1\,\text{s}$ with a larger $K = 0.15$ than previously (Fig. 4.8). The period heterogeneity is $T_0 = (54.8 \pm 1.4)\,\text{s}$. The slow core only consists of a small, but varying number of oscillators, $A_{\text{core}} = 2 - 10$ with $T_{\text{core}} = 49.2\,\text{s} > T_{\text{spiral}} = 31.3\,\text{s}$. The slow-down is due to the constant perturbations from the surrounding rotating wave, which effectively increase the illumination levels I_i, such that the periods T_i are prolonged. It drifts slowly on the grid until it eventually vanishes after collision with a boundary after 61 rotation periods.

In a small interval of time delay τ spiral waves exist, whose core oscillators are neither incoherent nor are their periods different from the surrounding spiral wave (Fig. 4.7 and Fig. 4.10e,f). They exist at the intersection point, where decreasing core periods $T_{\text{core}}(\tau)$ and rising spiral wave periods $T_{\text{spiral}}(\tau)$ match as the time delay τ is increased. In the experiment they were found for $K = 0.1$, $\kappa = 2.5$, $T_0 = (114.8 \pm 7.2)\,s$ and $\tau = 2\,\text{s}$.

The spiral wave chimera with a fast core $T_{\text{core}} < T_{\text{spiral}}$ (Fig. 4.8 and Fig. 4.10e,f) is the most prevalent representative in the experiments as its existence domain is the largest for small coupling strength K (Fig. 4.7). Besides the example previously discussed (Figs. 4.8 and 4.9), it was also observed for values of delay $\tau = 3\,\text{s}$ and $\tau = 5\,\text{s}$. Note that in all cases, the spiral wave chimera terminates by collision with a boundary. After its disappearance, global in-phase synchronization emerges. This verifies the characteristic coexistence[332] of the chimera state and in-phase synchronization.

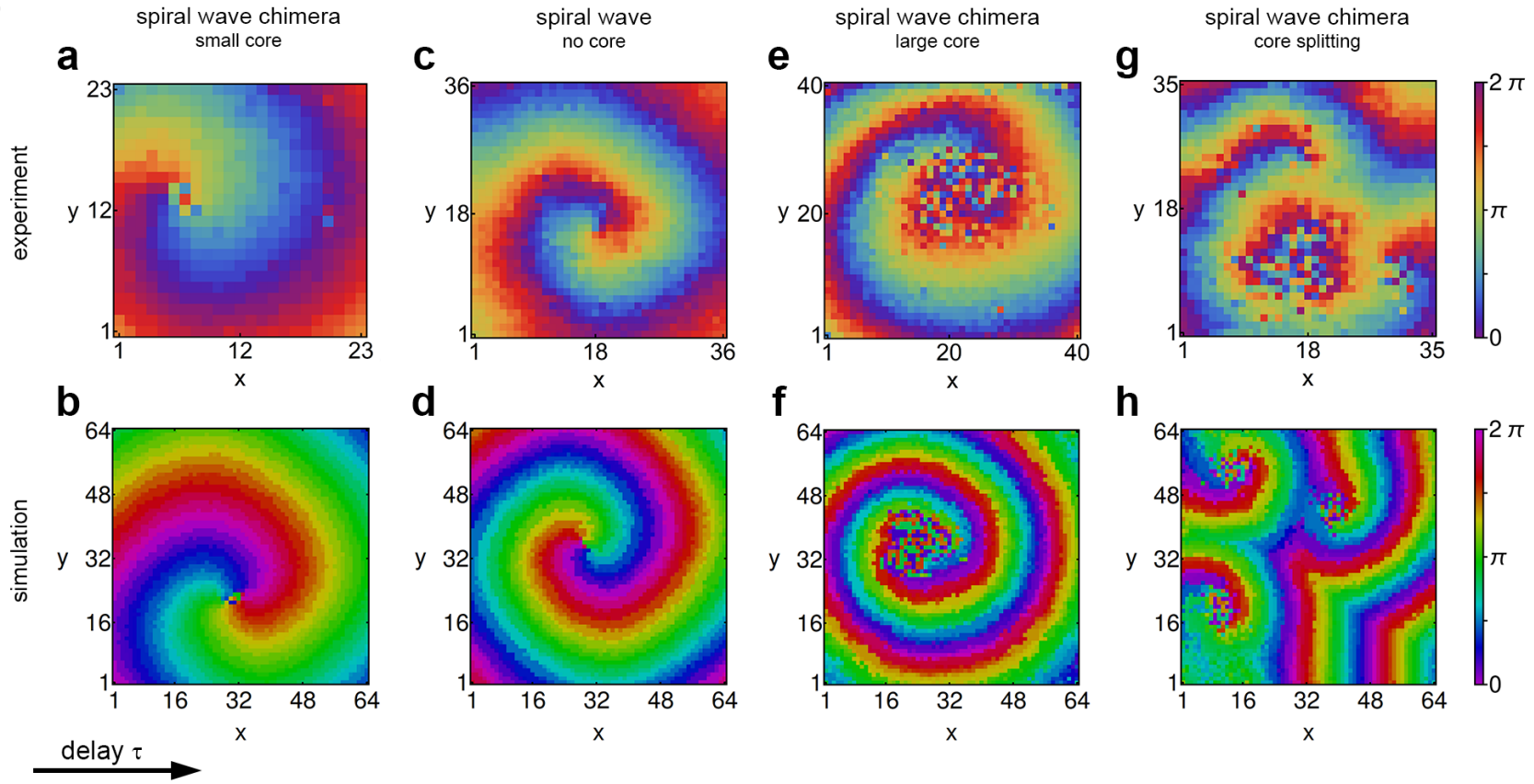

Figure 4.10 | Overview of patterns in nonlocally coupled oscillator arrays - Part I. For increasing values of time delay τ we find the following sequence of patterns in chemical experiments (top row) and in numerical simulations (bottom row): (a,b) Spiral wave chimeras with a slow core, (c,d) spiral waves with no core , (e,f) spiral wave chimeras with a fast core and (g,h) core splitting. The series continues (Fig. 4.11) on the next page.

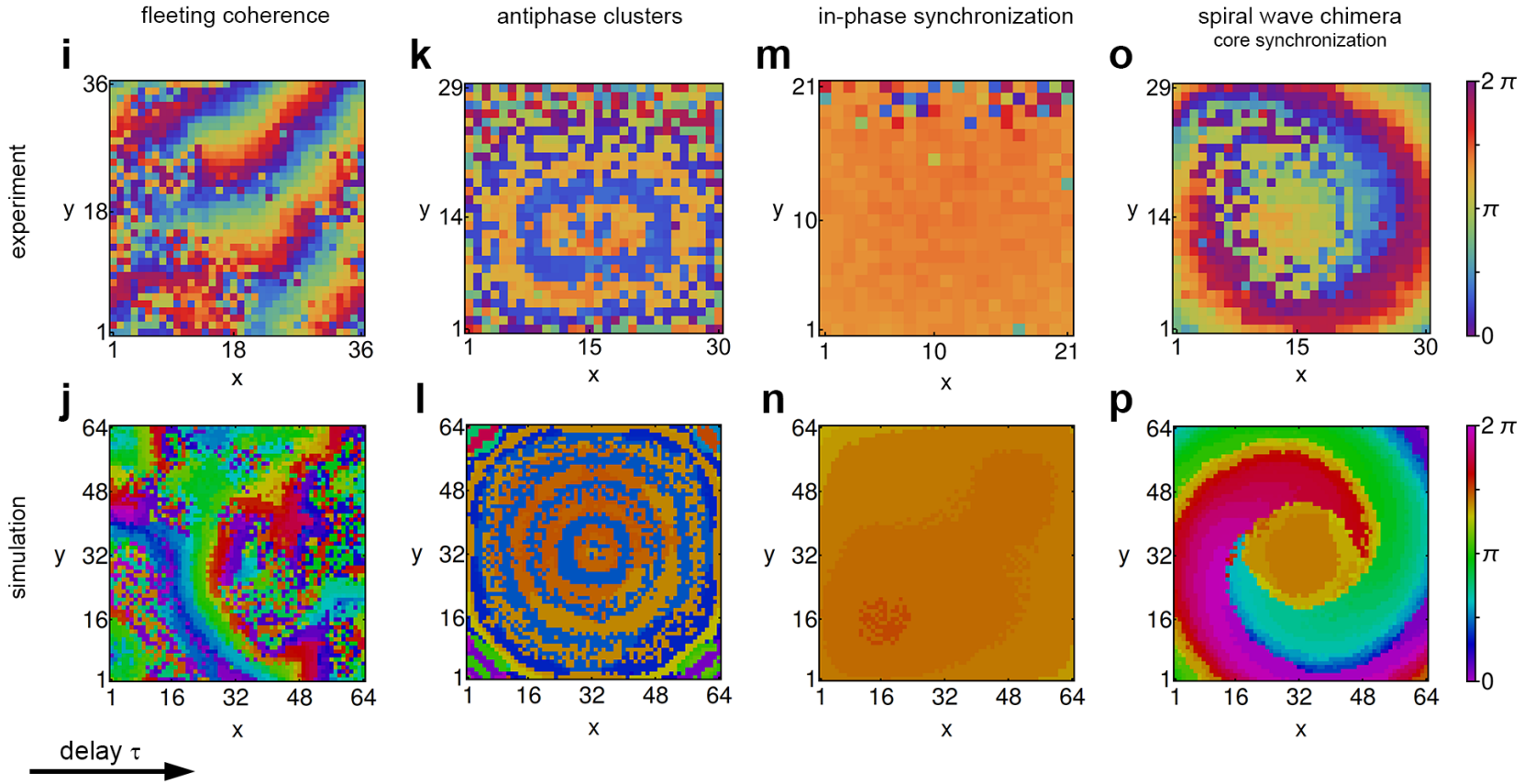

Figure 4.11 | Overview of patterns in nonlocally coupled oscillator arrays - Part II. Continuing from the previous page (Fig. 4.10), we find in chemical experiments (top row) and in numerical simulations (bottom row) for increasing values of time delay τ: (i,j) Fleeting coherence, (k,l) antiphase clusters, (m,n) an isochronous cluster and (o,p) spiral wave chimeras, whose fast core oscillators synchronize in-phase at the transition to in-phase synchronization. This sequence shows representative simulations analyzed in figure 4.7.

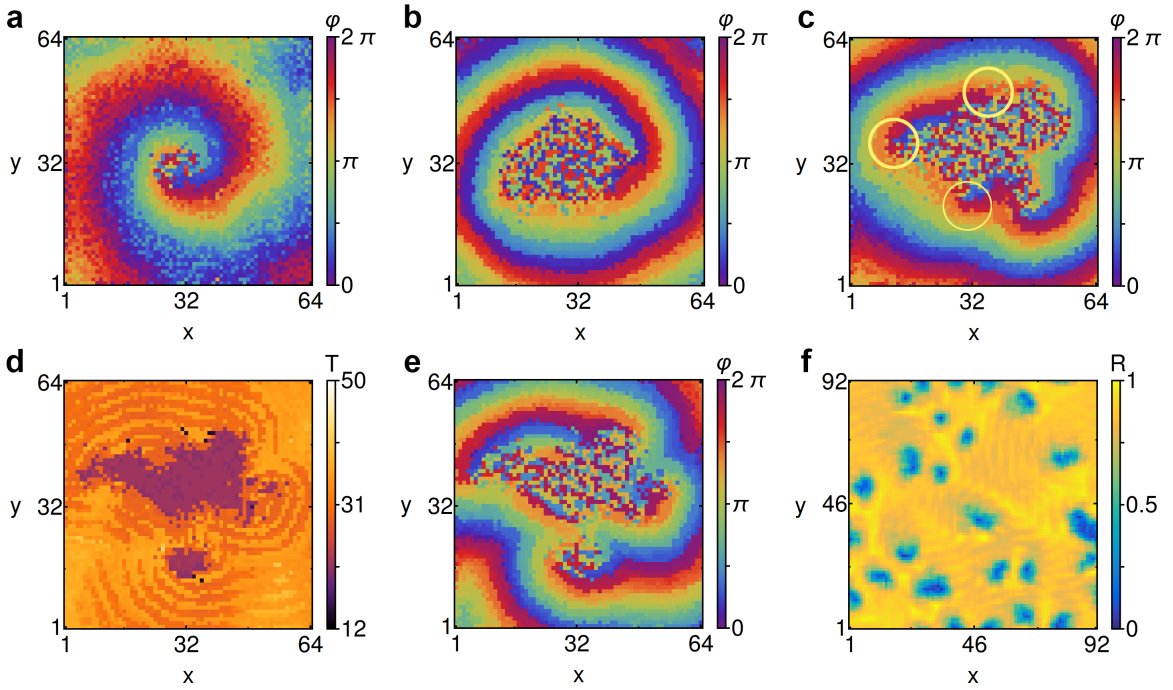

Figure 4.12 | Core Splitting. (a) $t = 4\,T_0$: An initially small incoherent core of a spiral wave chimera grows, until (b) at $t = 19\,T_0$ the core has more than tripled in circumference. (c) $t = 26\,T_0$: The spiral tip is so slow in completing a lap around the core, that it enables the high-frequency core to emit a new wave segment. This segment introduces two new spiral tips, which are highlighted with a thick yellow annulus in contrast to a thin annulus for the pre-existing tip. (d) $t = 31\,T_0$: Afterwards a part of the incoherent core synchronizes in frequency and phase to the surrounding oscillators, which divides the core into two parts. (e) $t = 31\,T_0$: At the end of the splitting event there are three tips rotating around two cores, which conserves the total topological charge in the system[38]. (f) $t = 140\,T_0$: In a larger grid with periodic boundary conditions (4.34), splitting events continue until merging events balance the number of cores. The final state resembles a vortex glass[343].

In the transition region between spiral wave chimeras and antiphase clusters, the core size A_{core} exhibits a pronounced increase (Fig. 4.7). Due to the increased core size, it takes longer for the spiral tip to complete a cycle around the core (Fig. 4.12a.b). This allows for the nucleation of a wave segment at the far side of the core relative to the current tip position (Fig. 4.12c). Note that the total topological charge Q (4.41) is conserved during the nucleation, because the open ends of the wave segment are equivalent to two new spiral tips with opposing chiralities, $Q_{\text{after}} = +1 - 1 + 1 = +1 = Q_{\text{before}}$. Shortly afterwards, a portion of the core oscillators frequency-locks to the surrounding spiral wave (Fig. 4.12d), such that the core fractures into two disjoint entities. In total the number of cores increased by one and the number of tips by two during the splitting event.

In later stages, further new cores nucleate via splitting while old existing ones can merge together or collide with boundaries. The number of cores eventually reaches a stationary size,

when the array is covered with the largest number of cores it can support simultaneously. The spatial core arrangement (Fig. 4.12f) does not exhibit long-range crystal-like order, but still retains the characteristic short-range order of an amorphous structure . A similar pattern observed with spiral waves in a reaction-diffusion system was termed vortex glass[343].
The observed behavior (Fig. 4.10g,h) is unlike similar spiral wave instabilities such as spiral breakup[344,345], where the wave speed depends on curvature in such a way that backfiring in the core region leads to turbulence. Also Kapral et al. observed a similar scenario[106] for spiral waves on a coupled map lattice. In their case chaotic dynamics, that are localized at the wave front, induce transversal wave instabilities[346].
For slightly larger values of delay the core expands too quickly to allow for splitting, but does not cover the entire array. The resulting pattern is a mixture of fleeting, intertwined coherent and incoherent domains (Fig. 4.11i,j).
At large enough time delay τ (Fig. 4.7), spiral patterns are superseded by antiphase $d = 2$ (Fig. 4.11k,l) and in-phase $d = 1$ clusters (Fig. 4.11m,n). The phase difference between oscillators constituting different clusters is $\Delta\varphi_d = 2\pi/d$. Their spatial arrangement depends sensitively on initial conditions. For an initial phase distribution in the shape of a target wave, the clusters arrange in approximate concentric circles (Fig. 4.11k,l), while for random initial conditions they are placed irregularly. The periods T_d of the clusters are linear functions of the time delay, $T_d(\tau) \sim d \cdot \tau$, whose slopes are given by the number of clusters d. Note that in-phase synchronization is very robust, since it even emerged in an experiment with very heterogeneous oscillators, whose mean period was $T = (75.3 \pm 21.5)\,\mathrm{s}$. This amounts to a spread of the period distribution that was 28.6 % relative to the mean period.
For large time delay τ, spiral wave chimeras emerge again (Fig. 4.7). Their core oscillators exhibit a faster oscillation cycle than the surrounding spiral wave $T_{\mathrm{core}} < T_{\mathrm{spiral}}$. However, they do not transition to antiphase clusters, but instead to in-phase synchronization. This transition involves the formation of in-phase synchronized patches inside of the core (Fig. 4.11o,p). These patches grow and push the wave rotating around them into the boundary where it annihilates. When the value of the time delay coincides with the unperturbed oscillation period, $\tau = T_0$, in-phase synchronization dominates with a period that is half of the time delay, $T(\tau) \sim 0.5\tau$.

The mechanism behind cluster formation and their periods can be understood from the phase-resetting character[87,347–349] of the particular BZ oscillators, but extends to general strongly coupled relaxation oscillators. In the absence of external perturbations, the phase φ of an oscillator can be defined in such a way that it increases uniformly (A.4) during an oscillation period (see appendix A.1). In response to a perturbation, the phase φ may be repulsed,

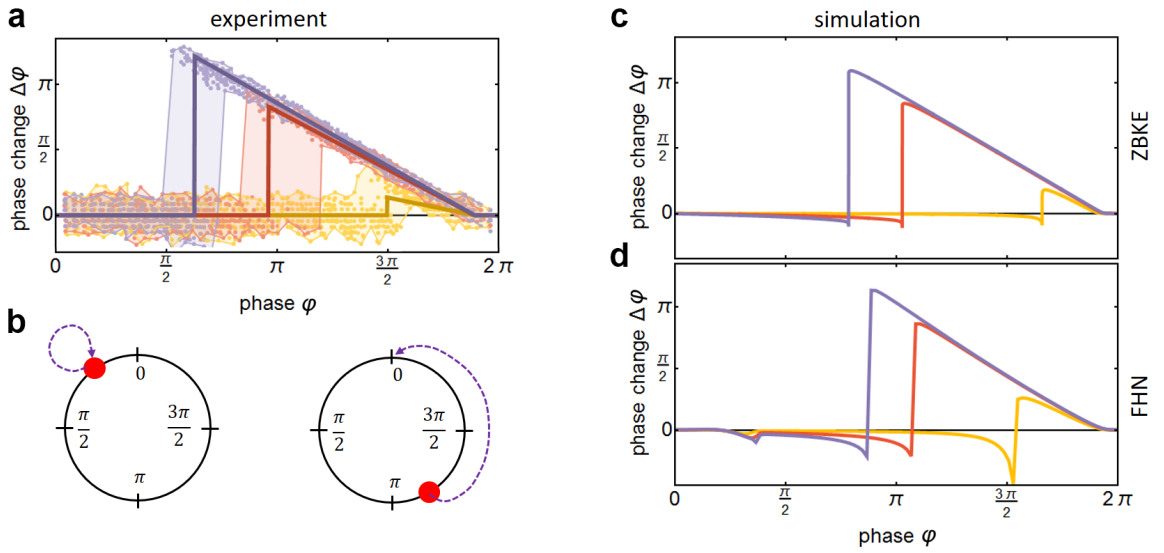

Figure 4.13 | Comparison of experimental and numerical phase response curves. (a) Simultaneous measurements (full circles) of the phase change $\Delta\varphi$ on a reservoir of oscillators at varying phases for different amplitudes I_p of the externally applied light perturbation: $0.09\,\mathrm{mW\,cm^{-2}}$ (yellow), $0.25\,\mathrm{mW\,cm^{-2}}$ (red) and $0.62\,\mathrm{mW\,cm^{-2}}$ (purple). The background intensity is $I_0 = 0.06\,\mathrm{mW\,cm^{-2}}$. Full lines are piecewise fits (4.48) to the experimental data. Shaded areas are bounds for all datapoints corresponding to a given perturbation amplitude. (b) Perturbations at early phases in the limit cycle lead to a vanishingly small phase recession $\Delta\varphi \lesssim 0$. Perturbations at a later stage induce a phase reset, such that the oscillation cycle restarts. (c) Numerically obtained PRCs for ZBKE oscillators (4.30) are in excellent agreement with the experimentally measured counterparts in (a). The results for three different perturbation amplitudes I_p are plotted: 0.2×10^{-3} (yellow), 2.5×10^{-3} (red) and 5.0×10^{-3} (purple). The background illumination intensity is $I_0 = 5.25\times10^{-4}$. (d) The phase response curve of a strongly perturbed FitzHugh-Nagumo oscillator (C.7) resembles its counterpart of the ZBKE oscillator in (c). The perturbation amplitudes I_p are 0.4, 1.5 and 2.0.

$\Delta\varphi < 0$, or advanced, $\Delta\varphi > 0$. It is possible to quantify the effect of a given perturbation by directly measuring the resulting period change from the unperturbed period T_0, $\Delta T = T_0 - T_p$, due to applied perturbations at various phases φ during the oscillation cycle. The period change ΔT is translated into a phase change $\Delta\varphi$,

$$\Delta\varphi = \frac{2\pi}{T_0}\Delta T, \tag{4.47}$$

which results in the phase response curve (PRC) $\Delta\varphi(\varphi)$. Measurements of the PRC for a short rectangular intensity perturbation $I_0 \to I_0 + I_p$ are shown in figure 4.13. Results from chemical experiments and simulations with the ZBKE model (4.30) are in excellent agreement. They show that a perturbation at the beginning of the oscillation cycle very slightly delays the phase $\Delta\varphi \lesssim 0$. At a certain critical transition point $\varphi^*(I_p)$, which depends

on the perturbation amplitude I_p, a discontinuous jump occurs. Beyond the jump point, perturbations reset the oscillation cycle by inducing an immediate new spike[87,350]. Fitting the experiments with a piecewise linear function,

$$\mathrm{PRC}(\varphi) = \begin{cases} 0 & ,\varphi < \varphi^*(I_p) \\ 2\pi + m \cdot \varphi & ,\varphi \geq \varphi^*(I_p) \end{cases} \tag{4.48}$$

reveals, that the PRC in the second part decays with a slope of $m = -1$, since the current phase φ changes by the remaining phase difference to 2π. For weak perturbations the fit is biased by varying jump points of heterogeneous chemical oscillators (Fig. 4.13a).
This behavior has also been observed in various biological settings, such as canine Purkinje fibers[351], galline and leporine cardiac sinoatrial pacemaker cells[352,353], interneurons responsible for the respiratory cycle in lamprey fish Lampetra fluviatilis[354], electrosensory pathway neurons in electric fish Eigenmannia[355], pyloric pacemaker neurons in lobsters Homarus Americanus[356] under electrical perturbation, circadian rhythm in Homo sapiens[357], algae Gonyaulax polyedra[358], fruit flies Drosophilia melanogaster[359] under light-stimulus.
Such discontinuous phase response curves were categorized as type zero by Winfree[87] and are characteristic for strongly perturbed oscillators. In contrast to weakly perturbed oscillators[213], the phase response curve does not scale linearly with the perturbation strength K,

$$\mathrm{PRC}(K, \varphi) \neq K \cdot \mathrm{PRC}(\varphi), \tag{4.49}$$

but changes its shape. In the case of BZ oscillators (Fig. 4.13), the jump point φ^* moves to smaller phases for larger perturbation strengths.

The shape of the PRC and its dependence on the perturbation strength (Fig. 4.13) are direct consequences of the underlying phase portrait (Fig. 4.14a). While an oscillator traverses the limit cycle in the ZBKE model (4.30), it moves with high speed during the excitation and extremely slowly during recovery , when it is on the left half of the attractor. A light perturbation $I \to I + \Delta I$ is equivalent to an additive offset on the current oscillator position. This offset is predominantly in the horizontal direction, because the light prefactor in the first equation of the ZBKE model is larger than in the second one, $1/0.11 > 2$. If the perturbation is small, the state returns after a brief excursion through a slow phase space region. Large perturbations push the oscillator beyond the black u-nullcline u_0 (Fig. 4.14a), such that they can not directly return without a large excursion in phase space. This explains why perturbations early in the limit cycle are of little effect. During the excitation, states very

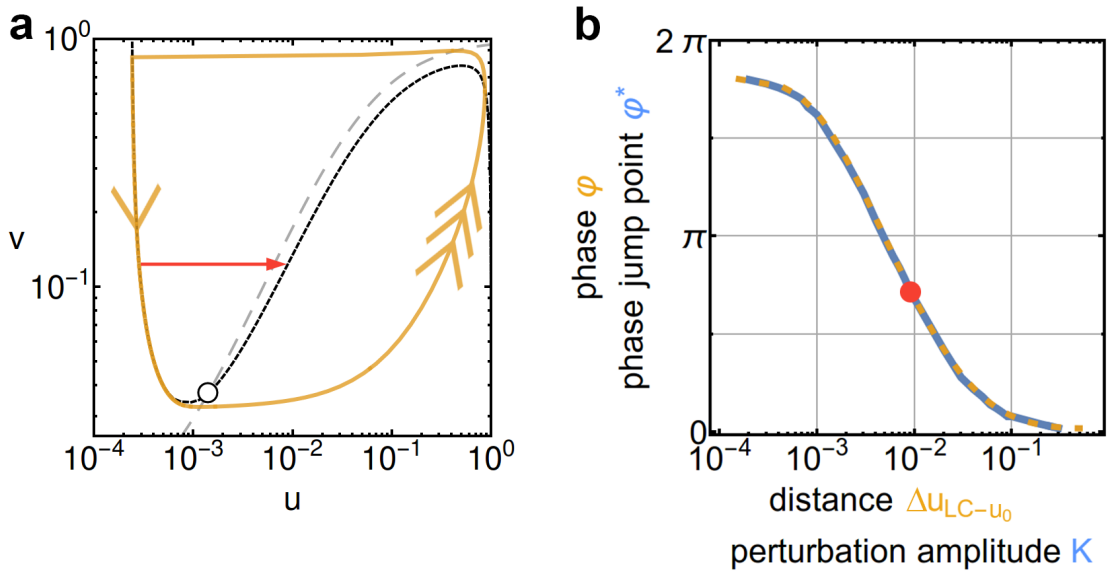

Figure 4.14 | Phase space dynamics underlying phase reset behavior. (a) The phase portrait of the ZBKE model (4.30) exhibits a stable limit cycle (yellow) around an unstable fixed point (unfilled circle) at the intersection of the gray, dashed v-nullcline $v_0(u)$ and black, dashed u-nullcline $u_0(u)$. Yellow arrowheads indicate the fast phase flow on the right part of the limit cycle and the vanishingly slow one on the left part. A perturbation in u-direction that induces a phase reset is indicated with a red arrow. (b) The distance $\Delta u_{\mathrm{LC}-u_0}$ between the limit cycle and the black u-nullcline u_0 at varying phases φ (orange, dashed) directly coincides with the phase jump point φ^* in PRCs for positive rectangular perturbations in u for different perturbation amplitudes (blue). The red dot corresponds to the position and size of the red arrow in (a).

quickly return to the right part of the limit cycle. Once the state reaches the slow, right half of limit cycle, perturbation-induced excursions are possible, but the distance from the limit cycle to the nullcline Δu_{LC-u_0} is very large for early phases. At later phases the distance Δu_{LC-u_0} decreases exponentially. Hence a smaller perturbation can more easily cause an excursion, which is equivalent to resetting the phase and initiating a new spike. This mechanism is reasonable, because the distance $\Delta u_{LC-u_0}(\varphi)$ as a function of phase φ along the limit cycle is identical to the phase jump point φ^* in PRCs for perturbations of different amplitudes in u-direction (Fig. 4.14b). Note that on a logarithmic scale the ZBKE model (4.30) resembles the FitzHugh Nagumo (FHN) model (C.7), which is the prototypical model for neuronal excitability type II[348]. Since the phase response curves of the ZBKE and FHN models agree very well (Fig. 4.13d), they are expected to give rise to similar patterns on a nonlocally coupled array of oscillators. Indeed, all behaviors discovered with the ZBKE model (Fig. 4.7) were successfully reproduced with the FHN model[334]. Furthermore, core splitting (Fig. 4.12) seems to be a behavior that is exclusively associated with type zero phase resetting, because it could not be reproduced in simulations with phase or Stuart-Landau[213] oscillators.

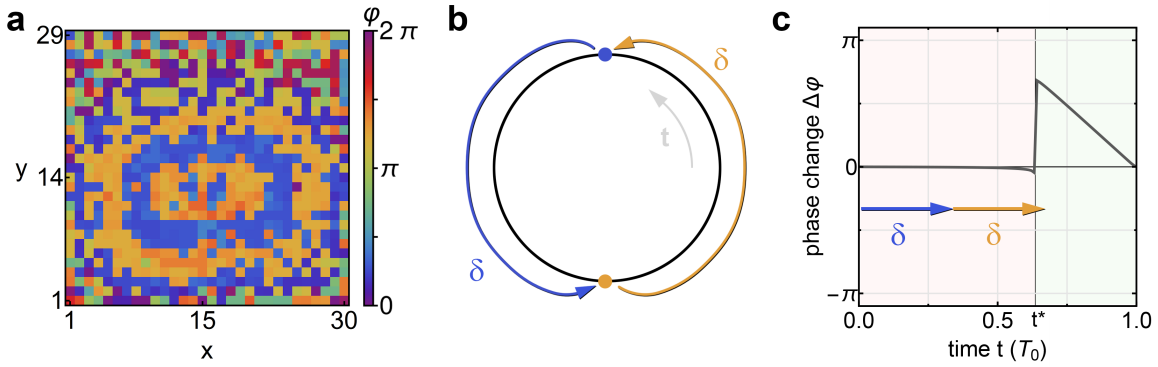

Figure 4.15 | Antiphase cluster states. (a) Experimental snapshot of an antiphase pattern with one group of oscillators at phase $\pi/2$ (blue) and the other $\Delta\varphi = \pi$ further at $3\pi/2$ (orange). Oscillators at the grid boundaries behave differently, because they have less nonlocal neighbors. (b) Schematic mechanism of antiphase patterns, where reciprocal perturbations arrive after a travel time $\delta = \Delta t_{\text{rise}} + \tau$. (c) The total period of the cluster state is the sum of travel times δ that is required to pass the jump point $t^* = \varphi^* T_0/2\pi$ in the PRC.

Antiphase patterns (Fig. 4.15a) and more generally d-cluster patterns are a direct consequence of strong, nonlocal coupling on an oscillator array. A strongly coupled oscillator responds to perturbations in one of two ways: It is either unresponsive or it fires. If a perturbation due to nonlocal coupling (4.25) is too small to cause a phase-reset, it is possible to either increase the coupling strength K or wait for a time Δt until the oscillator phase φ increased past its phase-reset point $\varphi^*(K)$ in order to successfully trigger a spike. In the case of an array of oscillators with random initial phases, one part of the population will fire while the other stays quiescent. However, given that the coupling strength K is sufficiently large, the unresponsive population will fire after a time interval of $\Delta t = \delta := \Delta t_{\text{rise}} + \tau$. This is the time duration for the perturbation from the group of the population that fired first to arrive. The time interval δ is composed of $\Delta t_{\text{rise}} \approx 1\,\text{s}$, which is the time required for a peak in the grayvalue time series to rise and the time delay τ in the coupling (4.25). Continuing in this fashion, the first group will fire again a time $\Delta t = \delta$ after the second group (Fig. 4.15b). Ultimately this mechanism determines the periods of the oscillators in the array to be

$$T_{\text{antiphase}}(\tau) = 2(\Delta t_{\text{rise}} + \tau) = 2\delta. \tag{4.50}$$

The existence of the antiphase clusters depends on the coupling strength K. It is required to be large enough, such that the accumulated travel times during one period exceed the jump point $t^* = \varphi^* T_0/2\pi$ after which a phase-reset is triggered: $2\delta \geq t^*(K)$ (Fig. 4.15c).
It is straightforward to generalize the mechanism behind antiphase clusters to d-clusters with positive integers $d \in \mathbb{N}^+$. A d-cluster may emerge, if the time delay τ and coupling

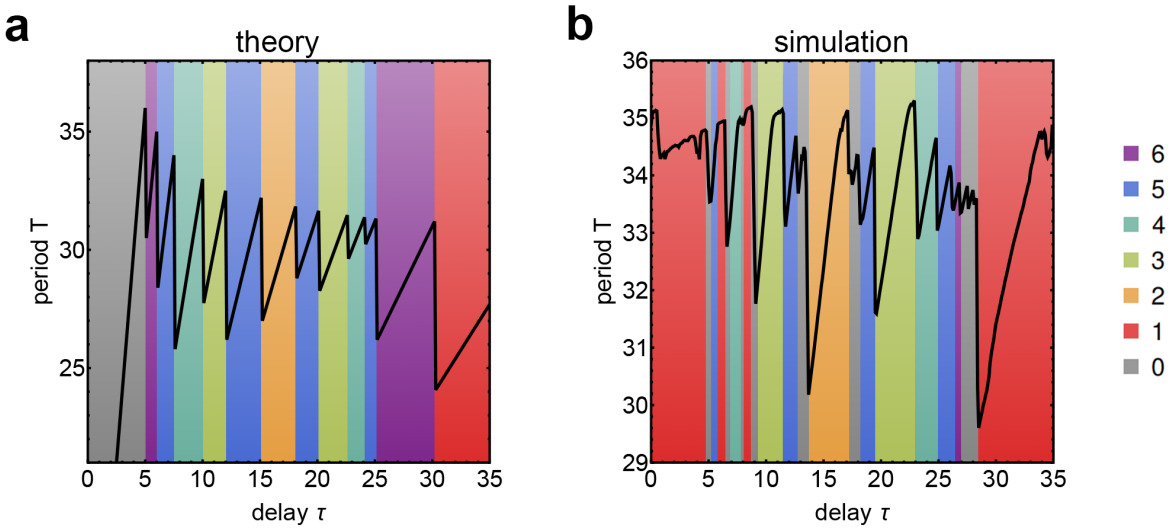

Figure 4.16 | d-Cluster states. (a) Theoretical prediction of periods (black line) and existence intervals (colored background) of d-clusters. At the beginning of each interval, the period drops sharply and then increases with a slope of $d/\Delta d$. The delay time τ is scaled, such that the jump point agrees with the value measured in simulations, $t^* = 30.2$. (b) Numerical simulations verify the sequence of clusters and the qualitative behavior of periods. Simulations are performed on an array of 64×64 oscillators with periodic boundary conditions. Each d-cluster state is identified with a localized version of (4.42). The coupling strength $K = 5.25 \times 10^{-5}$ was chosen small enough to allow for emergence of d-clusters with $d > 3$. The theoretical approach fails to predict the dynamics in the gray regions, which feature chimera spots and stripes, consisting of different d-cluster states. In addition the first region with wave synchronization up to $\tau = 5$ was missed. Both shortcomings are probably due to the negligence of oscillator heterogeneity and the phase-delaying part of the phase response curve (Fig. 4.13).

strength K give rise to a sequence of d perturbations, that exceed the jump point t^*, such that they obey: $d \cdot \delta \geq t^*(K)$. Of all possible clusters satisfying this condition, the d-cluster with the shortest firing sequence, $\min(d \cdot \delta)$, is established. This selection principle has an intuitive reason: Oscillators in d-clusters with a longer firing sequence get recruited to the fastest d-cluster over time.

In addition, it is possible that not all d oscillator clusters fire consecutively, but instead Δd clusters are skipped at each excitation. In the resulting d-cluster period $T_d(\tau)$, this can be accounted for by dividing over the number of omitted clusters:

$$T_d(\tau) = \frac{d}{\Delta d}(\Delta t_{\text{rise}} + \tau). \tag{4.51}$$

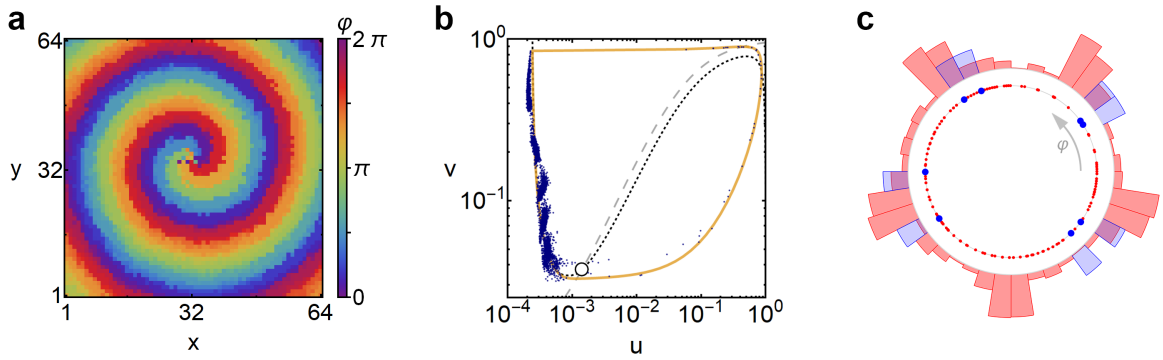

Figure 4.17 | Segmentation of the pattern in physical space and phase space. (a) Numerical simulation of a spiral wave chimera, where the phases in the spiral wave bunch together, such that the profile of the wave breaks into $d = 5$ clusters. (b) Also in the u-v phase space of concentrations five distinct groups of oscillators aggregate on the slow left part of the limit cycle. (c) The segmentation into five separate groups is clearly visible on a circular phase histogram of core (blue) and spiral wave oscillators (red). The core oscillators are attracted to the same segments, but can switch between them.

Following the same approach, the existence intervals for the clusters (Fig. 4.16a) can be computed. For $\Delta d = 1$, they assume a simple expression:

$$\frac{t^*}{d-1} < \tau + \Delta t_{\text{rise}} \leq \frac{t^*}{d}. \tag{4.52}$$

As shown in the comparison with numerical simulations (Fig. 4.16b), the sequence of d-cluster states can be correctly predicted as a function of time delay τ. This result is also in agreement with simulations of nonlocally coupled BZ oscillators on a ring[360]. Note that the above approach assumes global coupling between all oscillators. However, the two-dimensional nonlocal coupling kernel with a side length of $2\ell + 1 = 11$ takes into account 121 oscillators, which approximates global coupling.

Clustering also plays a role for the spiral pattern. The smooth wave profile divides into d consecutive segments. This occurs due to the same reason driving the d-cluster states. In experiments the segmentation is much less pronounced, since the jump points φ^* are more heterogeneous, than in the simulation (Fig. 4.13). Furthermore, the cluster mechanism also explains the core synchronization at large values of the delay (Fig. 4.11o,p), where the oscillators follow a period of period $T = 0.5(\tau + \Delta t_{\text{rise}})$. The delay history of the coupling (4.31), which encompasses nearly a complete period T_0, contains peaks from the oscillator itself and others at approximately half a period later. Over time all core oscillators share the same delay history. As the core grows, eventually all oscillators in the entire array are entrained and in-phase synchronized.

4.5 Short summary

We establish that photocoupled catalyst-loaded microparticles in Belousov-Zhabotinsky solution form a versatile experimental setup for experiments with relaxation oscillators on large networks exceeding $N = 1000$ nodes.
As a first example of the experimental capabilities we experimentally investigated and verified the spiral wave chimera[334] (Fig. 4.8), which was predicted by Kuramoto in 2002[271]. Besides verifying its existence, we also devised a core-tracking algorithm to characterize the erratic motion of the core (Fig. 4.9).
Taking the time delay τ as a bifurcation parameter, we explored the phase diagram of a two-dimensional array of nonlocally coupled oscillators numerically and experimentally (Figs. 4.7, 4.10 and 4.11). We discovered previously unreported patterns and transitions, such as spiral wave chimeras with a slow core (Fig. 4.10a,b), core splitting (Figs. 4.10g,h and 4.12) and core synchronization (Fig. 4.10o,p). Apart from spiral patterns, we also observed d-cluster states and described a mechanism that explains their emergence based on time delay τ and the type zero phase response curve (Fig. 4.15), that plays a role in neurobiology for strongly perturbed nerve cells[87].
Our findings are of significance beyond the chemical BZ oscillator (4.30), since they could be reproduced in the canonical model for nerve excitation, the FitzHugh Nagumo model (C.7). Thus we expect our findings might be of relevance to cardiac and cortical dynamics.

The experimental setup opens the door for a large number of future experiments. Some of which are outlined in the next section.

4.6 Future Directions

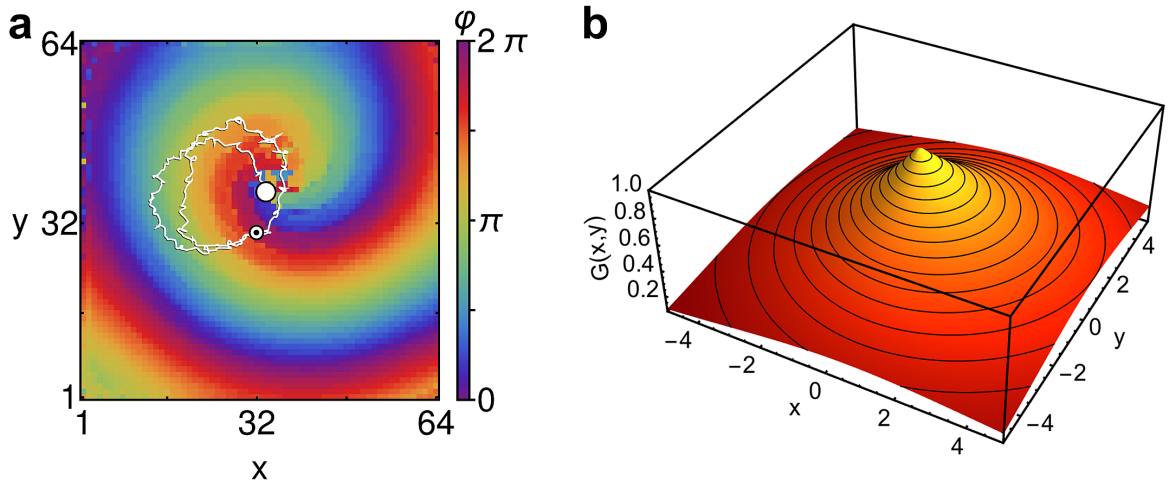

Figure 4.18 | Spiral Wave Chimera Control. (a) Spiral wave chimera after two laps on a forced circular trajectory (white). (b) Time-dependent nonlocal kernel with spatial asymmetry for orientation (4.53).

The experimental setup allows for a plethora of future experiments. Without further modifications of the experimental soft- or hardware, it would be possible to also do experiments on further chimera states in one, two and three dimensions, such as spots and scroll waves. Three dimensional grids would be limited to small systems, such as $10 \times 10 \times 10$ oscillators. Chimera scroll rings could be studied nonetheless in a reduced two-dimensional array by exploiting the azimuthal symmetry of the ring with reduced cylindrical coordinates.
On a one-dimensional ring different theoretically proposed control algorithms[302–305] can be implemented and tested. Furthermore control schemes for spiral wave chimeras could be devised by generalizing their counterparts in one dimension. For example it is possible to extend the asymmetric kernel in one dimension used previously[303] to two dimensions

$$G(r,\phi) = e^{-\alpha(\phi-\phi_0)r}, \tag{4.53}$$

$$\alpha(\phi-\phi_0) = \alpha_1 + \frac{1}{2}(\alpha_2-\alpha_1)(1+\cos(\phi-\phi_0)). \tag{4.54}$$

Here the asymmetric kernel is written in polar coordinates with an orientation angle ϕ_0, which can be externally manipulated to set the drift direction. The asymmetry of the kernel, $\alpha_2 - \alpha_1$, determines the speed of the drift. In figure 4.18 the orientation angle increases linearly in time, leading to two circular laps. Without control, the core location would perform a very slow Brownian motion around the array center.

Another possibility is testing those schemes that have proven successful in the control of ordinary spiral waves[125,166,167]. Further studies of spiral wave chimeras might reveal how and if they pin to spatial or parameter heterogeneities, like their regular counterparts[361,362]. Apart from chimera states, it would be interesting to verify that domains of large oscillator heterogeneity act as natural pacemakers[363].

One obstacle in the implementation of control algorithms will be the calculation of the instantaneous phase variable. In the current system, the phase is only known retrospectively, after the oscillator peaked again. One way around it, is to use a different order parameter[306], that is not derived from the instantaneous phase $\varphi(t)$.

Beyond regular grids, chimera states can also be investigated in complex networks, such as small world[364] and scale-free[286] networks. In addition connectomes known from biology, such as the hermaphrodite soil worm Caenorhabditis elegans[321] with 302 neurons, portions of fruit fly Drosophilia melanogaster connectome[365] with 380 neurons or coarse-grained macaque cortical network[366] can be implemented. In this venue it will be interesting to see how neuronal time-dependent connectivity as shaped by spike timing dependent plasticity[174] contributes to the natural rise of chimera states as it reinforces synchronized and desynchronized domains via potentiation and depression, respectively.

It seems feasible to experimentally verify the explosive synchronization transition[367] as well as symmetry cluster synchronization[202] by selecting nodes with an appropriate period distribution. Regarding the requirements of finding them, it is already possible to run experiments on arbitrary networks with selectable coupling strength and time delay. Furthermore appropriate oscillators can be drawn from the reservoir, such that the period distribution exhibits multiple peaks[213,368].

Apart from this, learning algorithms for artificial intelligence ranging from generations I-III featuring units with binary and smooth sigmoidal transfer functions up to spiking units[369] can be tested. The implementation of a XOR logic gate would serve as a first proof of concept. An additional benefit of the experiment in comparison to a simulation is the inherent heterogeneity, noise and aging in the experiment. Such obstacles would need to be overcome in a working real-world neural net, too. Especially the role of noise in learning[370] is an interesting venue as it could play a constructive role as in stochastic[371] and coherence resonance[372,373].

Changing the chemical BZ reagents appropriately allows for experiments with excitable instead of oscillatory units (Fig. C.2). This opens the possibility for an experimental study of bump states[239], thought to play an important role in short-term memory[374]. Coupling chemical oscillators together might also allow for chaotic units and possibly bistable elements.

Spreading excitation waves are also commonly observed in central pattern generators[209] (CPG) that determine the locomotion of invertebrate and vertebrate species, such as lamprey fish[375] and urodele amphibians[376]. Furthermore a CPG has been shown to successfully manage the motion of a robot[211] and adapt to external stimuli. This allows for the development of a "chemical brain", consisting of chemical micro-oscillators, that learns and controls the movement of a robot.

From a more general standpoint, it would be interesting to experimentally verify the curvature-induced propagation failure together with the accompanying generalized eikonal equation[198] on an network, where the front curvature κ is replaced by the node degree k: $\kappa \to k-2$.

The experimental setup also opens the possibility for the synchronization and spreading of waves in networks with time-dependent connectivities, as they are found in social contact[377] and travel networks[378]. In the latter cases, excitation waves are related to the dissemination of opinions[379] and the proliferation of infectious pathogens.

Reducing the bead distance on the acrylic glass plate allows for experiments with local diffusive coupling in addition to light-mediated nonlocal or global coupling. The interplay between both coupling schemes might lead to the emergence of interesting dynamics, which might resemble those in neuronal assemblies with nonlocal, biochemical synapses and local, electrical gap junctions[170,380].

Conclusion

In this thesis a number of self-organized patterns, that exhibit spatio-temporally periodic synchronized activity, are elucidated in numerical simulations and chemical experiments. Special focus is given to the propagation of excitation waves on different topologies.

In three spatial dimensions an unperturbed scroll ring far from any boundaries ordinarily either contracts and vanishes or undergoes a negative line tension instability that ends in Winfree turbulence. In chapter 2 we provide experimental and numerical evidence that a scroll ring with positive filament tension in spatial confinement does not only contract, but may also expand, which was previously associated with negative line tension exclusively. Beyond this unexpected finding, we also observe that boundary interaction can stabilize the ring radius for a long time, resulting in an effective autonomous pacemaker in a homogeneous medium without defects. To describe the experiments, we develop a semi-analytical kinematical model that explicitly takes the boundary interaction into account. It succeeds in accurately reproducing all numerical observations and illuminates the underlying mechanism of boundary-mediated stabilization in the experiment[162]. These findings are relevant to pathological scroll waves of electrical activity in the myocardium[36], which are naturally bounded by the spatial extent of the heart.

On a small network of relaxation oscillators, an excitation wave simply spreads from one node to its neighbors. Surprisingly the wave propagation is also bound by the symmetry properties of the network as elucidated in chapter 3. Those waves that spread on the network between symmetry clusters exclusively are found to be the generalization of target waves known from continuous active media. Both originate from the site of highest frequency in the system, known as the pacemaker. Their emitted waves spread while satisfying all symmetries of the underlying system, be it Euclidean symmetries or network automorphisms. Utilizing discrete chemical oscillators and numerical simulations we find that the domain of target wave synchronization in the space of coupling strength and oscillator mismatch resembles an Arnold tongue[217]. Besides the generalization of target waves, these findings might be of

relevance to assemblies of nerve cells, that support traveling cortical excitation waves[220] and neural central pattern generators that control rhythmic muscle movement[209].

The final chapter 4 details our experimental and numerical endeavors regarding the successful verification of spiral wave chimeras in a large array of nonlocally coupled chemical micro-oscillators. To this end we developed an experimental setup that consists of more than $N = 2500$ catalyst-loaded cation-exchange beads in Belousov-Zhabotinsky solution forming a reservoir of chemical relaxation oscillators. Each oscillator can be monitored via fluorescence and independently addressed with light illumination from a spatial light modulator. A self-built sieve machine facilitates the homogenization of the oscillator population in order to perform experiments on synchronization. This enabled us to construct a two-dimensional array of 40×40 oscillators to investigate the spiral wave chimera, predicted by Kuramoto in 2002[271]. Furthermore we elucidated the phase diagram of nonlocally delay-coupled oscillators on a two-dimensional grid. At the transition of spiral wave chimeras to incoherence, we found that relaxation oscillators exhibit a unique scenario, which involves the splitting of the incoherent core[334]. Further splitting events lead to the formation of a vortex glass consisting of chimera cores. In addition to spiral patterns, we also found d-cluster states. Taking into account the measured phase response curve of type zero[87] we devised a theoretical mechanism for the emergence of clusters in strongly coupled oscillators that we verified in numerical simulations. Our findings are of significance beyond chemical oscillators, since they apply to strongly coupled relaxation oscillators that are found in cardiac and cortical ensembles[239,353,359]. Apart from biological relevance, nonlocally coupled oscillators also play a role in physical systems, such as the photoelectrodissolution of doped silicon[248], arrays of opto-mechanical oscillators[230] and ultracold atoms[237] as well as metamaterials of superconducting quantum interference devices[234].

Appendix A

Dimension reduction of oscillators and oscillatory patterns

Detailed dynamical systems for real-world oscillators may contain such a large number of components, that they are difficult to analyze, see for example the MBM model of the BZ reaction[381] or detailed neural[382] or cardiac cell models[383]. While special methods, like adiabatic elimination and bath approximation (appendix C.2) or principal component analysis[384] can be applied to remove a number of components, the most elemental reduction is possible by exploiting the topological structure of the limit cycle: A closed circle embedded in a high-dimensional phase space[87,213,347].

The treatment of spatially coupled oscillators falls prey to the same problem, but further amplified. Their description is usually given in the framework of partial differential equations (PDE), which are infinite-dimensional due to the additional dependence on a continuous spatial variable. Discretizing a PDE via method of lines[158] yields a finite, but still large dimensional system. In the case of three spatial dimensions, the resulting dimension is: $d = n_x \times n_y \times n_z \times n_c$, where n_c is the number of components of the local dynamics and the other variables give the number of cells in each spatial directions. For the scroll ring dynamics (chapter 2), the dimension is on the order of 10^6.

A.1 Discrete oscillators

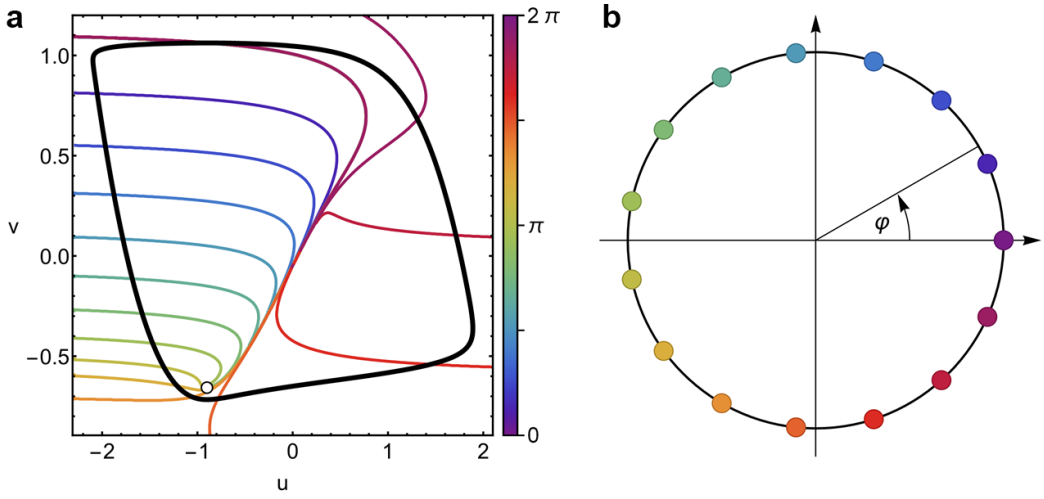

Figure A.1 | Phase reduction of a limit cycle. (a) In a planar dynamical system (C.7) a representative limit cycle Γ (black) is located around an unstable fixed point (unfilled circle). The velocity along Γ is not a constant as indicated by the non-equidistant colored isochrones indicate. The extension of the isochrones beyond Γ is calculated with the asymptotic phase. (b) With a suitable transformation, the non-uniform dynamics on Γ can be mapped to uniform motion on a topologically equivalent circle. Each point on the circle is parametrized by a phase ϕ, which follows (A.3)

Coupled discrete oscillators can be described with a system of coupled ordinary differential equations:

$$\frac{d}{dt}\boldsymbol{c}_i = \boldsymbol{f}_i(\boldsymbol{c}_i) + K\sum_{j=1}^{N}\boldsymbol{I}_{ij}(\boldsymbol{c}_i,\boldsymbol{c}_j). \tag{A.1}$$

Here the vectors $\boldsymbol{c}_i, \boldsymbol{c}_j \in \mathbb{R}^{n_c}$ are vectors of the dynamical variables with n_c components for each of the N coupled oscillators indexed by i, j. The dynamics of the coupled units may range from harmonic to relaxation oscillations and is given by the local dynamics $\boldsymbol{f}_i \in \mathbb{R}^{n_c}$. The oscillators interact with each other described by the scalar coupling strength $K \in \mathbb{R}$ multiplied with the interaction function $I_{ij} : \mathbb{R}^{n_c} \times \mathbb{R}^{n_c} \to \mathbb{R}^{n_c}$. The indices of $\boldsymbol{f}_i$ and $\boldsymbol{I}_{ij}$ reflect the possible heterogeneity of each node. First Winfree[12] and later Kuramoto[213] exploited the fact, that an uncoupled dynamical system,

$$\frac{d}{dt}\boldsymbol{c} = \boldsymbol{f}(\boldsymbol{c}) \tag{A.2}$$

showing time-periodic behavior $\boldsymbol{c}(t) = \boldsymbol{c}(t+T)$ must feature a limit cycle Γ embdedded in a high-dimensional phase space $\mathbb{R}^{n_c}$ that is topologically equivalent to a one-dimensional

ring embedded in two dimensions. While before the dynamic state was defined by the value of the dynamic variables $\{c_i\}_{i=1,\dots,n_c}$, the state along the one-dimensional manifold is given by the position on the circle or its phase φ (Fig. A.1). Points on the limit cycle are mapped directly to corresponding phase values, such that the phase grows linearly with constant angular frequency $\omega = 2\pi/T_0 \in \mathbb{R}$ in time[87,213]

$$\frac{d}{dt}\varphi = \omega \tag{A.3}$$

$$\implies \varphi_{\text{linear}}(t) = \omega t. \tag{A.4}$$

Here, the offset φ_0 is set to zero. This is also called the temporal phase definition[87]. Alternative phase definitions include the geometrical phase mapping[331], which takes into account the spatial position on the limit cycle:

$$\varphi_{\text{geometric}}(t) = \arctan\left(\frac{v(t)-v_0}{u(t)-u_0}\right). \tag{A.5}$$

Here (u_0, v_0) is a selectable reference point in phase space and arctan is the four-quadrant inverse tangent. The difficulty in applying this method successfully lies in determining a reference point, that remains inside the modified limit cycle in the presence of perturbations[385]. Another method employs the Hilbert transform H[386], to extend a single real-valued input $u(t)$ into a complex one $u(t) + \mathrm{i}H(u(t))$ and determine its phase:

$$H(u(t)) = \frac{1}{\pi}\fint_{-\infty}^{+\infty} \frac{u(\tilde{t})}{t-\tilde{t}}\, d\tilde{t} \tag{A.6}$$

$$\varphi_{\text{Hilbert}}(t) = \arctan\left(\frac{H(u(t))}{u(t)}\right). \tag{A.7}$$

However, the wave form $u(t)$ needs to be preprocessed, such that its zeroth Fourier mode vanishes[387]: $u(t) - u_0$. Otherwise if $u(t)$ is entirely positive, not all phase values $[0, 2\pi[$ are accessible. Since any frequency can be mapped from a time-dependent to a constant frequency by reparametrization

$$\omega(t) = \omega\big(t(s)\big) \,/\, \frac{ds}{dt} = \text{const}\,, \tag{A.8}$$

and due to its simplicity, we will choose (A.3) as the phase definition in what follows.
The phase corresponding to points $\boldsymbol{c}$ outside the limit cycle $\mathbb{R}^2 \setminus \Gamma$ can be calculated via the asymptotic phase $\varphi(\boldsymbol{c})$. It is defined via the phase corresponding to the point on the limit

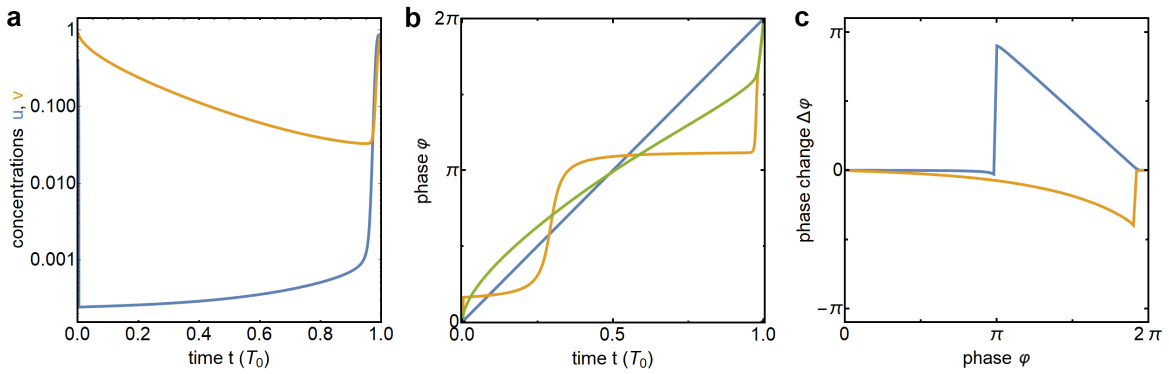

Figure A.2 | Phase definitions and dynamics. (a) Time series of dynamical variables during an unperturbed relaxation oscillation with period T_0 in a model for the BZ reaction (C.5). Both dynamical variables correspond to chemical concentrations. (b) Comparison of different time-phase mappings: linear (blue), geometric (yellow), Hilbert (green) (c) The impact of perturbations at phases φ in terms of resultant phase change $\Delta\varphi$ (A.9) along the limit cycle is quantified as phase response curves. Here the linear time-phase mapping (A.4) is employed. The perturbations are in the form of additive inputs $u \to u + \Delta u$ (blue) and $v \to v + \Delta v$ (yellow). While perturbations in u advance the phase by resetting it to zero, perturbations in v delay the phase.

cycle, that the trajectory reaches for $t \to \infty$ starting from state $\boldsymbol{c}$. This procedure allows for finding isochrones, lines of equal asymptotic phase $\varphi(\boldsymbol{c})$ in phase space (Fig. A.1).
Coupled oscillators continuously perturb each others phases by advancing or delaying each other. The phase shift $\Delta\varphi$ due to a perturbation is quantified with the phase response curve (PRC) $Q(\varphi)$. It can be calculated directly by measuring the perturbed period T_p in relation to the unperturbed period T_0:

$$\Delta\varphi = 2\pi\frac{T_0 - T_p}{T_0}. \tag{A.9}$$

An example for a PRC is shown in figure A.2c for the ZBKE model (C.5). Negative values of $\Delta\varphi$ stand for phase delays and positive values for phase advances. Note that there are opposing sign conventions in the literature for the PRC[388]. In addition the pulse-shape $P(\varphi)$ defines the perturbation magnitude that an oscillator imposes on its neighbors depending on its current phase φ. Combining these two aspects and accounting for heterogeneity of oscillators, leads to the evolution for a single oscillator coupled to its N neighbors:

$$\frac{d}{dt}\varphi_i = \omega_i + Q_i\left(\sum_{j=1}^{N} K_j P_j(\varphi_j), \varphi_i\right). \tag{A.10}$$

Analytical progress can be made under the assumption of identical coupling strength $K_j = K$, homogeneous transfer $P_j = P$ and response $Q_i = Q$ to perturbations as well as weak interaction, which means that the state never deviates far from the limit cycle, since the attracting local dynamics dominates over the coupling. This has two important implications: The total result of all perturbations can be expressed as their linear superposition, $Q(K, \varphi) = KQ(\varphi_i)$, and the effect of the perturbations evolve on such a slow time scale that their effect is negligible during a single oscillation. Instead the perturbations accumulate over many periods on a slow timescale. Taken together this simplifies equation A.10 to the Winfree model[12]:

$$\frac{d}{dt}\varphi_i = \omega_i + KQ(\varphi_i)\sum_{j=1}^{N} P(\varphi_j). \tag{A.11}$$

The effect of the accumulated perturbations over an oscillation cycle period can be accounted for by averaging over a period[213,221]:

$$\frac{d}{dt}\varphi_i = \omega_i + K\sum_{j=1}^{N}\frac{1}{2\pi}\int_0^{2\pi} Q(\varphi_i + \tilde{\varphi})P(\varphi_j + \tilde{\varphi})d\tilde{\varphi}. \tag{A.12}$$

Note that φ was replaced here with $\tilde{\varphi} \to \varphi$, such that it does not represent the instantaneous phase φ anymore, but the accumulated phase change $\tilde{\varphi}$, that slowly changes over many periods. Choosing the simplest Fourier series term for the 2π-periodic phase response curve $Q(\varphi) = -\sin(\varphi)$ and a delta-peak as pulse-shape $P(\varphi) = 2\pi\delta(\varphi)$ to counter the integral, model (A.12) becomes

$$\frac{d}{dt}\varphi_i = \omega_i + K\sum_{j=1}^{N}\sin(\varphi_j - \varphi_i). \tag{A.13}$$

This is the paradigmatic Kuramoto model[213], which is frequently employed for studying synchronization in large networks.

Alternatively, the same result can be derived via multiple scale analysis[389–391] starting from (A.1) and assuming a limit cycle solution. For this purpose, we exploit the two time scales of the problem. Introducing an additional slow time scale $t'' = \varepsilon t$ with a small scalar parameter $\varepsilon \in \mathbb{R}$ besides the original fast one $t' = t$. Variations on the slow time scale will only become relevant after a long time $t \to t''/\varepsilon$.

Thus, taking into account both time scales, an appropriate perturbation ansatz for the solution $\boldsymbol{c}_i$ of (A.1) is:

$$\boldsymbol{c}_i(t) = \sum_{n=0}^{\infty} \varepsilon^n \boldsymbol{C}_{i,n}(t',t'') \approx \boldsymbol{C}_{i,0}(t',t'') + \varepsilon \boldsymbol{C}_{i,1}(t',t''). \tag{A.14}$$

The total time derivative of equation A.1 is transformed via the chain rule, such that

$$\frac{d}{dt}\boldsymbol{c}_i(t) \approx \frac{\partial \boldsymbol{C}_{i,0}}{\partial t'} + \varepsilon \frac{\partial \boldsymbol{C}_{i,0}}{\partial t''} + \varepsilon \frac{\partial \boldsymbol{C}_{i,1}}{\partial t'}. \tag{A.15}$$

To incorporate the assumption of weak coupling, the coupling strength K is supposed to be of order ε: $K = \varepsilon$. Plugging in the ansatz (A.14) and applying Taylor expansion, the right hand side of (A.1) in up to first order of ε becomes

$$\boldsymbol{f}(\boldsymbol{c}_i) \approx \boldsymbol{f}\left(\boldsymbol{C}_{i,0} + \varepsilon \boldsymbol{C}_{i,1}\right) \approx \boldsymbol{f}(\boldsymbol{C}_{i,0}) + \varepsilon \underline{\underline{D\boldsymbol{f}}}(\boldsymbol{C}_{i,0})\boldsymbol{C}_{i,1}, \tag{A.16}$$

$$K \sum_{j=1}^{N} \boldsymbol{I}(\boldsymbol{c}_i, \boldsymbol{c}_j) \approx \varepsilon \sum_{j=1}^{N} \boldsymbol{I}\left(\boldsymbol{C}_{i,0} + \varepsilon \boldsymbol{C}_{i,1}, \boldsymbol{C}_{j,0} + \varepsilon \boldsymbol{C}_{j,1}\right) \approx \varepsilon \sum_{j=1}^{N} \boldsymbol{I}(\boldsymbol{C}_{i,0}, \boldsymbol{C}_{j,0}), \tag{A.17}$$

where $\underline{\underline{D\boldsymbol{f}}}$ is the Jacobian of the local dynamics $\boldsymbol{f}$. Overall the resulting equation reads

$$\frac{\partial \boldsymbol{C}_{i,0}}{\partial t'} + \varepsilon \frac{\partial \boldsymbol{C}_{i,0}}{\partial t''} + \varepsilon \frac{\partial \boldsymbol{C}_{i,1}}{\partial t'} = \boldsymbol{f}(\boldsymbol{C}_{i,0}) + \varepsilon \underline{\underline{D\boldsymbol{f}}}(\boldsymbol{C}_{i,0})\boldsymbol{C}_{i,1} + \varepsilon \sum_{j=1}^{N} \boldsymbol{I}(\boldsymbol{C}_{i,0}, \boldsymbol{C}_{j,0}). \tag{A.18}$$

Collecting terms by order of ε:

$$\varepsilon^0: \quad \frac{\partial \boldsymbol{C}_{i,0}}{\partial t'} = \boldsymbol{f}(\boldsymbol{C}_{i,0}) \tag{A.19}$$

$$\varepsilon^1: \quad \frac{\partial \boldsymbol{C}_{i,1}}{\partial t'} - \underline{\underline{D\boldsymbol{f}}}(\boldsymbol{C}_{i,0})\boldsymbol{C}_{i,1} = \sum_{j=1}^{N} \boldsymbol{I}(\boldsymbol{C}_{i,0}, \boldsymbol{C}_{j,0}) - \frac{\partial \boldsymbol{C}_{i,0}}{\partial t''} \tag{A.20}$$

As expected, the zeroth order (A.19) returns the original dynamical system, whose solution is the unperturbed limit cycle:

$$\boldsymbol{C}_{i,0}\left(t',t''\right) = \boldsymbol{c}_{i,\mathrm{LC}}\left(t' + \varphi_i\left(t''\right)\right). \tag{A.21}$$

In the solution the position on the limit cycle is given by the fast time t' together with a phase offset $\varphi_i(t'')$, which evolves on the slow time scale, but not on the fast one.

The expression for the first order in ε (A.20) is in the form of an inhomogeneous linear differential equation for $\boldsymbol{C}_{i,1}$ after insertion of (A.21),

$$\left(\frac{\partial}{\partial t'} - \underline{\underline{\boldsymbol{Df}}}\left(\boldsymbol{c}_{i,\mathrm{LC}}\right)\right)\boldsymbol{C}_{i,1} = \sum_{j=1}^{N} \boldsymbol{I}(\boldsymbol{c}_{i,\mathrm{LC}}, \boldsymbol{c}_{j,\mathrm{LC}}) - \boldsymbol{c}'_{i,\mathrm{LC}}\frac{d\varphi_i}{dt''}. \tag{A.22}$$

This relation can be formulated as a solvability condition determined by the Fredholm Alternative[392] [a] . In Dirac notation[394,395] the theorem can be formulated for a linear differential operator $\hat{\mathscr{L}}$ with vectors $|x\rangle$ and dual vectors $\langle x|$, describing the existence of a solution to the equation

$$\hat{\mathscr{L}}\,|x\rangle = |b\rangle\,. \tag{A.23}$$

A solution $|x\rangle$ to equation A.23 exists if and only if:

$$\langle x|b\rangle = 0, \tag{A.24}$$

where $\langle x|$ is the left eigenvector to the adjoint eigenvalue problem to the eigenvalue 0, also called response function:

$$\langle x|\,\hat{\mathscr{L}}^{\dagger} = 0. \tag{A.25}$$

Simply stated, (A.23) only has a solution if the inhomogeneity $|b\rangle$ is orthogonal to the kernel subspace of the adjoint operator $\hat{\mathscr{L}}^{\dagger}$, which is populated by the response functions $\langle x|$. Applied to (A.22) the scalar product of (A.24) evaluates to:

$$\frac{1}{T}\int_0^T \boldsymbol{Q}(t') \cdot \left[\sum_{j=1}^{N} \boldsymbol{I}\left(\boldsymbol{c}_{i,\mathrm{LC}}\left(t'\right), \boldsymbol{c}_{j,\mathrm{LC}}\left(t' - (\varphi_i - \varphi_j)\right)\right) - \boldsymbol{c}'_{i,\mathrm{LC}}\frac{d\varphi_i}{dt''}\right] dt = 0, \tag{A.26}$$

Note that the phase offset is shifted, $t' + \varphi \to t'$, such that oscillator i has a relative phase of zero at time $t = 0$. The response function of (A.22) is denoted $Q(t)$, which is identical to the phase response curve in case of weak perturbations[348]. Utilizing the normalization condition

[a] For finite vector spaces, the Fredholm Alternative is a corollary of the rank-nullity theorem[393]: $\dim \underline{\underline{A}} = \dim(\ker \underline{\underline{A}}) + \dim(\mathrm{im}\,\underline{\underline{A}})$. If the kernel space is empty then the operator is injective and surjective. Otherwise it is neither. The latter case applies for vanishing eigenvalues, since $\underline{\underline{A}}\,\boldsymbol{x} = 0\boldsymbol{x} = \boldsymbol{0}$. Consequently, a solution $\boldsymbol{x}$ to $\underline{\underline{A}}\,\boldsymbol{x} = \boldsymbol{b}$ is not guaranteed to exist.

from Malkin's theorem[396]

$$\frac{1}{T}\int_0^T \boldsymbol{Q}(t')\cdot\frac{d\boldsymbol{f}(\boldsymbol{c}_{i,\mathrm{LC}})}{dt'}dt = 1, \tag{A.27}$$

it is possible to derive the evolution equation for the slowly changing phase offset:

$$\frac{d}{dt}\varphi_i = \varepsilon\frac{1}{T}\int_0^T \boldsymbol{Q}(\tilde{t})\cdot\sum_{j=1}^{N}\boldsymbol{I}\left(\boldsymbol{c}_{\mathrm{LC}}(\tilde{t}),\boldsymbol{c}_{\mathrm{LC}}\left(\tilde{t}+(\varphi_j-\varphi_i)\right)\right)d\tilde{t}, \tag{A.28}$$

$$= \varepsilon\omega_i + \varepsilon\sum_{j\neq i}^{N} H(\varphi_j-\varphi_i). \tag{A.29}$$

Note that for identical oscillators the interaction function H results in the frequency deviation from the unperturbed oscillation: $H(\varphi_i-\varphi_i)=\omega_i$[348]. Replacing the periodic function $H(\varphi_j-\varphi_i)$ by its first Fourier mode $\sin(\varphi_j-\varphi_i)$ times a scalar factor K, it is possible to recover the Kuramoto model[213]:

$$\frac{d}{dt}\varphi_i = \omega_i + K\sum_{j=1}^{N}\sin(\varphi_j-\varphi_i). \tag{A.30}$$

The scaling factor ε was absorbed into the time variable $\varepsilon t\to t$, such that the dynamics occur on a slow time scale in agreement with (A.13).

The synchronization dynamics of the Kuramoto model can be readily analyzed with a mean field approach[213]. The mean field is given by the centroid of the oscillators in the complex plane

$$Re^{i\Psi} = \frac{1}{N}\sum_k e^{i\varphi_k} \qquad \text{with } R = \left|\frac{1}{N}\sum_k e^{i\varphi_k}\right|. \tag{A.31}$$

Plugging these expressions back into the Kuramoto model (A.30), leaves us with a mean-field equation:

$$\frac{d\varphi_i}{dt} = \omega_i + KR\sin(\Psi-\varphi_i) \tag{A.32}$$

This equation describes how a single oscillator is coupled to the effective remainder of the network, which is given by the Kuramoto order parameter R and its phase Ψ. This shows that a single oscillator is always attracted to the mean phase of the bulk, since the frequency decreases due to the coupling if the oscillator is ahead and the frequency increases in the opposite case. In addition, the more oscillators align, the stronger is the pull of the

bulk on single oscillators. However, since $\sin(\varphi)$ is bounded, oscillators with a frequency that exceeds the maximum pulling $K_{cr} = K/\Delta\omega$, can not be synchronized. The frequency difference $\Delta\omega = \omega_i - \omega_0$ is taken between the individual ω_i and bulk frequency ω_0. The latter is given as the arithmetic mean of the frequency distribution,

$$\omega_0 = \frac{1}{N}\sum_{i=1}^{N}\omega_i, \tag{A.33}$$

because the coupling function is odd. At a sufficiently high coupling strength oscillators may start firing in unison by undergoing different synchronization scenarios, such as quorum sensing[397], mobbing[398], discontinuous explosive synchronization[367,399] or the continuous Kuramoto phase transition [12,213,313,400,401].

A.2 Continuous oscillator fields

In the previous section, an oscillator was perturbed due to its coupling to other discrete oscillators. For continuous oscillator fields the interaction is incorporated as a diffusion term

$$\Delta_d \boldsymbol{c} = \sum_{i=1}^{d}\frac{d^2\boldsymbol{c}}{dx_i^2}, \tag{A.34}$$

which gives rise to a partial instead of an ordinary differential equation. In order to reduce the dimensionality for $d = 3$ dimensional vortex dynamics in reaction diffusion problems,

$$\frac{d}{dt}\boldsymbol{c} = \boldsymbol{f}(\boldsymbol{c}) + \underline{\underline{D}}\Delta_3\boldsymbol{c}, \qquad \text{with } \boldsymbol{c} = \boldsymbol{c}(x,y,z,t), \tag{A.35}$$

it is advantageous to focus on the dynamics of self-organized structures called filaments[402]. These are lines of phase singularities to which spiral-shaped solutions $\boldsymbol{c}_0(\boldsymbol{r},t) = \boldsymbol{c}_0(r,\theta,t)$ of the two-dimensional reaction diffusion equation

$$\frac{d}{dt}\boldsymbol{c} = \boldsymbol{f}(\boldsymbol{c}) + \underline{\underline{D}}\Delta_2\boldsymbol{c}, \qquad \text{with } \boldsymbol{c} = \boldsymbol{c}(x,y,t), \tag{A.36}$$

are attached. In a co-rotating frame of polar coordinates, $\tilde{\theta}(t) = \theta - \omega t$, the solutions $\boldsymbol{c}_0(\boldsymbol{r})$ are stationary and can be determined by solving the equivalent nonlinear eigenvalue problem

$$\left(\underline{\underline{D}}\Delta_2 + \omega\partial_\theta + \boldsymbol{f}(\cdot)\right)\boldsymbol{c}_0(r,\theta-\omega t) = \boldsymbol{0}. \tag{A.37}$$

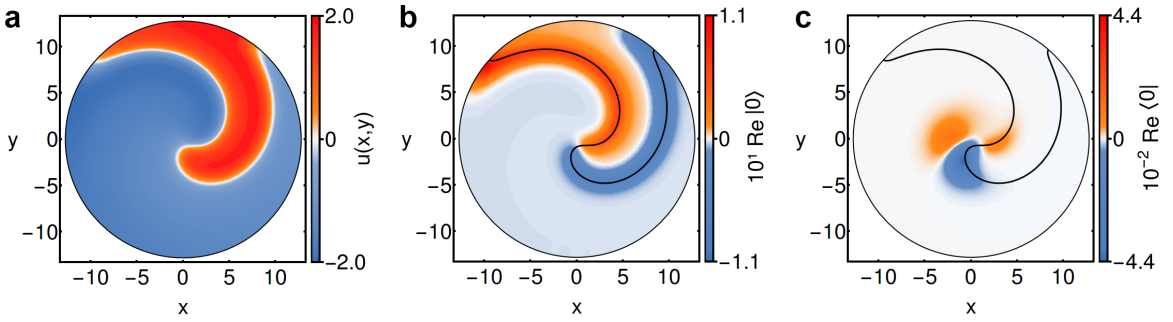

Figure A.3 | Goldstone modes and response functions of spiral waves. (a) The stationary u-concentration profile of a spiral wave simulated with the FHN model (C.7) on a circular domain enclosed by Neumann boundaries. (b) Real part of the rotational Goldstone mode $|0\rangle$. (c) Real part of the corresponding response function $\langle 0|$. It shows the spatial regions that are sensitive to perturbations, which will excite the Goldstone mode $|0\rangle$. The black contour line is for comparison. Simulation and mode determination is performed with DXSpiral[406].

Stability properties can be inferred from the corresponding linearized differential operator $\hat{\mathscr{L}}$. Its eigenvalue problem for general eigenvectors $|n\rangle$ reads:

$$\hat{\mathscr{L}}\,|n\rangle = \left(\underline{\underline{D}}\Delta_2 + \omega\partial_\theta + \underline{\underline{D\boldsymbol{f}}}(\boldsymbol{c}_0)\right)|n\rangle = (\mu + \mathrm{i}\omega_n)\,|n\rangle \tag{A.38}$$

$$\langle n|\,\hat{\mathscr{L}}^\dagger = \langle n|\left(\underline{\underline{D}}\Delta_2 - \omega\partial_\theta - \underline{\underline{D\boldsymbol{f}}}(\boldsymbol{c}_0)\right) = \langle n|\,(\nu - \mathrm{i}\omega_n) \tag{A.39}$$

Here the adjoint eigenvalue problem (A.39) is included as well. Note that the left $\langle n|$ and right eigenmodes $|m\rangle$ fulfill the orthogonality relation $\langle n|m\rangle = \delta_{nm}$.

From (A.37) it is apparent that we have to find the eigenvectors $\boldsymbol{c}_0(\boldsymbol{r})$ to the potentially degenerate eigenvalue $\lambda = 0$, which are called the Goldstone modes[206]. Perturbations in the form of these modes are shape-preserving and lead solely to translation and rotation of the spiral wave.

Due to the Euclidean symmetries of the infinite plane[339,403,404 b], there are three possible eigenmodes with a vanishing real part of the eigenvalue μ: one for rotation $\left(|0\rangle = \partial_\theta \boldsymbol{c}_0(\boldsymbol{r})\right)$ and two for translations $\left(|\pm 1\rangle = (\partial_x \pm i\partial_y)\boldsymbol{c}_0(\boldsymbol{r})\right)$. Note that in the non-rotating frame, the translational modes are the derivatives along the Euclidean basis vectors.

To gain further understanding of the role of response functions[132,133,407], let us consider a small perturbation $\varepsilon\boldsymbol{h}(\boldsymbol{c},\boldsymbol{r},t)$ on the two-dimensional spiral wave field $\boldsymbol{c}_0(\boldsymbol{r},t)$, which is a stable solution of (A.37). Since the perturbation is weak, it can only change the

[b] Here we limit ourselves to the special Euclidean group SE(2), which only contains rotation and translation symmetries. Reflection is excluded, since it would flip the chirality of the spiral pattern leading to a violation of topological charge conservation[38,405].

rotation frequency $\omega = \omega_0 + \varepsilon\omega_1$ and induce translational movement $\boldsymbol{v} = \varepsilon\boldsymbol{v}_1$ of the slightly perturbed concentration field $\boldsymbol{c} = \boldsymbol{c}_0 + \varepsilon\boldsymbol{c}_1$. In a frame that follows these rotations and translations, (A.36) together with the perturbation becomes

$$\begin{aligned}(\partial_t - (\omega_0 + \varepsilon\omega_1)\partial_\theta - \varepsilon\boldsymbol{v}_1 \cdot \nabla)(\boldsymbol{c}_0 + \varepsilon\boldsymbol{c}_1) \\ = \boldsymbol{f}(\boldsymbol{c}_0) + \varepsilon\underline{\underline{D\boldsymbol{f}}}(\boldsymbol{c}_0)\boldsymbol{c}_1 + \underline{\underline{D}}\Delta_2(\boldsymbol{c}_0 + \varepsilon\boldsymbol{c}_1) + \varepsilon\boldsymbol{h}\end{aligned} \tag{A.40}$$

On different scales we collect

$$\varepsilon^0: \quad (\partial_t - \omega_0\partial_\theta)\,\boldsymbol{c}_0 = \boldsymbol{f}(\boldsymbol{c}_0) + \underline{\underline{D}}\Delta_2\boldsymbol{c}_0 \tag{A.41}$$

$$\varepsilon^1: \quad \partial_t\boldsymbol{c}_1 - \omega_1\partial_\theta\boldsymbol{c}_0 - \boldsymbol{v}\cdot\nabla\boldsymbol{c}_0 = \hat{\mathscr{L}}\boldsymbol{c}_1 + \boldsymbol{h} \tag{A.42}$$

Noting that the stable spiral wave solution $\boldsymbol{c}_0$ is stationary in the co-rotating frame and thus $\partial_t\boldsymbol{c}_0 = \boldsymbol{0}$, (A.41) is identical to (A.37) and determines the unperturbed pattern $(\omega, \boldsymbol{c}_0)$. Since projections of response functions $\langle n|$ on $\boldsymbol{c}_1$ can be absorbed into $\boldsymbol{c}_0$, we can introduce a gauge condition[407], $\langle n|\boldsymbol{c}_1\rangle = 0$, such that $\langle n|\partial_t\boldsymbol{c}_1\rangle = 0$ and $\langle n|\hat{\mathscr{L}}\boldsymbol{c}_1\rangle = 0$. This relationship simplifies the evaluation of the Fredholm alternative of (A.42), which involves the projection on response functions:

$$\partial_t\phi \;\; = \varepsilon\omega_1 = -\varepsilon\,\langle 0|\boldsymbol{h}\rangle \tag{A.43}$$

$$\partial_t R_x = \varepsilon v_x \;\; = -\varepsilon\,\langle +|\boldsymbol{h}\rangle \tag{A.44}$$

$$\partial_t R_y = \varepsilon v_y \;\; = -\varepsilon\,\langle -|\boldsymbol{h}\rangle\,. \tag{A.45}$$

These are the equations of motion for a spiral wave under weak perturbations, such as a parameter gradient, advective fields or periodic forcing[408]. For the special case of a parameter step in an additive excitability threshold $\boldsymbol{h}(x,y,t) = \boldsymbol{e}_1\Delta p H(x - x_0)$, the theory predicts a stable spiral wave drifting in parallel to the step, which was confirmed experimentally as well[362]. The projection can be evaluated as[132]

$$\langle n|\boldsymbol{h}\rangle \propto \iint_{\mathbb{R}^2} \boldsymbol{Y}_n(\boldsymbol{r})\cdot\boldsymbol{h}(\boldsymbol{r})\;\, d^2\boldsymbol{r}, \tag{A.46}$$

where for clarity constant factors stemming from the transformation between fixed and co-rotating frame have been omitted. This shows that a perturbation $\boldsymbol{h}$ is most effective of inducing motion of the spatially unbounded spiral wave pattern $\boldsymbol{c}$, when it has a large overlap

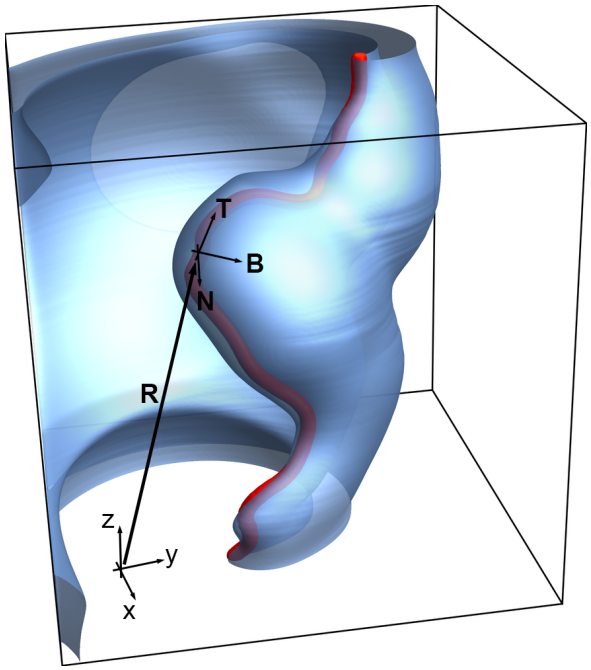

Figure A.4 | Frenet-Serret frame. A curved scroll wave with a twisted filament (red ribbon) simulated with the FHN model (C.7). Initial twist and torsion were initialized from a random walk in x and y directions as well as rotation phase φ_0. Frenet-Serret coordinate frame is locally attached to the curved filament to parametrize space (A.47).

integral with any of the response functions $\boldsymbol{Y}_n$, which are localized in the neighborhood of the spiral tip[133 c].

In order to make progress on the three-dimensional problem (A.35), we adopt from the differential geometry of space curves the curvilinear Frenet-Serret frame[410]. The filament curve can be described by a vector $\boldsymbol{R}(s)$, which is parametrized by its arclength s. To each point of the filament, a triad of orthonormal vectors, the tangent vector $\boldsymbol{T}(s) = \partial_s \boldsymbol{R}(s)$, the normal vector $\boldsymbol{N}(s) = \partial_{ss} \boldsymbol{R}(s)$ and the binormal vector $\boldsymbol{B}(s) = \boldsymbol{T}(s) \times \boldsymbol{N}(s)$, are attached locally. In addition this description naturally introduces the torsion $\tau(s) = -\partial_s \boldsymbol{B}(s) \cdot \boldsymbol{N}(s)$ and curvature $\kappa(s) = \partial_s \boldsymbol{T}(s) \cdot \boldsymbol{N}(s)$ of the filament. Globally, positions in space are parametrized with

$$\boldsymbol{r} = \boldsymbol{r}(s,p,q) = \boldsymbol{R}(s) + p\boldsymbol{B}(s) + q\boldsymbol{N}(s). \tag{A.47}$$

[c] Beyond the response functions, the entire spectrum of adjoint eigenmodes are localized at the spiral tip[409]. They are important in the case of unstable spiral waves as well as stable, confined spiral waves in bounded domains, where the continuous symmetries of the special Euclidean group SE(2) are broken.

Making use of the chain rule and the Frenet-Serret equations, the space and time derivatives in (A.35) can be expressed in the Frenet-Serret coordinates (Fig. A.4) [d]. Under the assumption that filament quantities vary on different spatial scales [118],

$$O(\varepsilon^{-1}):\ \boldsymbol{T}, \tag{A.48}$$

$$O(\varepsilon^{0}):\ \boldsymbol{N},\boldsymbol{B},\boldsymbol{c}_0,\boldsymbol{c}_{0,\theta},\boldsymbol{c}_{0,\theta\theta},\boldsymbol{c}_{0,p},\boldsymbol{c}_{0,q}, \tag{A.49}$$

$$O(\varepsilon^{1}):\ \tau,\phi_s,q,p,\boldsymbol{c}_{0,s}, \tag{A.50}$$

$$O(\varepsilon^{2}):\ \boldsymbol{c}_1,\boldsymbol{c}_{0,ss},\boldsymbol{R}_t,\boldsymbol{N}_t,\boldsymbol{B}_t,\phi_t,\phi_{ss},\tau_s,\kappa, \tag{A.51}$$

we can again apply multiple scale analysis in conjunction with the Fredholm alternative (A.24), but now in space instead of time. Here subscripted variables are shorthand for partial derivatives. The perturbation ansatz is given in the co-rotating frame and accounting for twist:

$$\boldsymbol{c}\approx\boldsymbol{c}_0+\boldsymbol{c}_1,\qquad \text{with}\quad \boldsymbol{c}=\boldsymbol{c}(s,p,q,t)=\boldsymbol{c}(r,\theta-\phi(s,t)-\omega t). \tag{A.52}$$

After simplifying $1-p\kappa\approx 1$, since the curvature is small, and linearizing the local dynamics $\boldsymbol{f}$, then up to order ε^2, equation A.35 in the corotating Frenet-Serret frames is:

$$\begin{aligned}\hat{\mathscr{L}}\boldsymbol{c}_1 :=& \left(\partial_t-\underline{\underline{D}}\Delta_2-\underline{\underline{Df}}(\boldsymbol{c}_0)\right)\boldsymbol{c}_1\\ =&\ \boldsymbol{f}(\boldsymbol{c}_0)+\underline{\underline{D}}\left(\partial_s(\phi_s+\tau)\partial_\theta\boldsymbol{c}_0+(\phi_s+\tau)^2\partial_{\theta\theta}\boldsymbol{c}_0+\kappa\partial_p\boldsymbol{c}_0\right)+\underline{\underline{D}}\Delta_2\boldsymbol{c}_0\\ &-(\phi_t-\omega)\,\partial_\theta\boldsymbol{c}_0+(\boldsymbol{R}_t+q\boldsymbol{N}_t+p\boldsymbol{B}_t)\cdot\boldsymbol{T}\ (\phi_s+\tau)\,\partial_\theta\boldsymbol{c}_0\\ &+\boldsymbol{R}_t\cdot\boldsymbol{N}\ \partial_p\boldsymbol{c}_0+\boldsymbol{R}_t\cdot\boldsymbol{B}\ \partial_q\boldsymbol{c}_0+\boldsymbol{N}_t\cdot\boldsymbol{B}\ \partial_\theta\boldsymbol{c}_0.\end{aligned} \tag{A.53}$$

This procedure decouples the spiral waves in each p-q plane , since their interaction in u_1 is on the scale ε^4. Introducing the twist [87], $w=\phi_s+\tau$, for brevity and collecting terms for

[d] Note that the coordinate system is degenerate in the case of a curve without curvature. This problem was remedied in recent work by Verschelde et al. [407,411], who replaced the Frenet-Serret frame with the Fermi-Walker frame, describing trajectories in curved space-time in general relativity [412], to prove a geodesic minimal principle [413] for filament evolution in anisotropic media.

different powers of ε results in:

$$\varepsilon^0: \quad \mathbf{0} = \boldsymbol{f}(\boldsymbol{c}_0) + \underline{\underline{D}}\Delta_2 \boldsymbol{c}_0 + \omega \partial_\theta \boldsymbol{c}_0, \tag{A.54}$$

$$\varepsilon^2: \hat{\mathscr{L}}\boldsymbol{c}_1 = w_s \underline{\underline{D}}\partial_\theta \boldsymbol{c}_0 + w^2 \underline{\underline{D}}\partial_{\theta\theta}\boldsymbol{c}_0 - \kappa \underline{\underline{D}}\partial_p \boldsymbol{c}_0 \tag{A.55}$$

$$- \phi_t \partial_\theta \boldsymbol{c}_0 + (\boldsymbol{R}_t + q\boldsymbol{N}_t + p\boldsymbol{B}_t)\cdot\boldsymbol{T}\, w\partial_\theta \boldsymbol{c}_0 \tag{A.56}$$

$$+ \boldsymbol{R}_t \cdot \boldsymbol{N}\, \partial_p \boldsymbol{c}_0 + \boldsymbol{R}_t \cdot \boldsymbol{B}\, \partial_q \boldsymbol{c}_0 + \boldsymbol{N}_t \cdot \boldsymbol{B}\, \partial_\theta \boldsymbol{c}_0 \tag{A.57}$$

$$=: |b\rangle\,. \tag{A.58}$$

In the lowest order (A.54), we recover (A.37), the nonlinear eigenvalue problem that determines the stationary pulse profile of a spiral wave in the corotating frame. For the equation in second order we invoke the Fredholm Alternative (A.24) for the rotational $\langle 0|$ and translational $\langle \pm|$ response functions. Due to the orthonormality relation between Goldstone modes and reponse functions, $\langle n|m\rangle = \delta_{nm}$, a number of terms in the solvability condition vanish. Furthermore, Biktashev showed, that products pairing rotational with translational modes and involving the diffusion matrix $\underline{\underline{D}}$, e.g. $\langle +|\underline{\underline{D}}0\rangle$, average to zero over one rotation period [120]. The remaining terms reveal the equations of motion for the filament [118,120]:

$$\phi_t = \boldsymbol{N}_t \cdot \boldsymbol{B} + \boldsymbol{R}_t \cdot \boldsymbol{T} w + \langle 0|\underline{\underline{D}}0\rangle\, w_s + \langle 0|\underline{\underline{D}}\partial_{\theta\theta}\boldsymbol{c}_0\rangle\, w^2, \tag{A.59}$$

$$\boldsymbol{R}_t = \langle +|\underline{\underline{D}}+\rangle\, \kappa \boldsymbol{N} + \langle -|\underline{\underline{D}}+\rangle\, \kappa \boldsymbol{B}. \tag{A.60}$$

For the simple case of a closed filament loop with no twist and constant curvature, projecting (A.60) into the loop plane, results in the equations for the evolution of ring radius R and drift along the symmetry axis $\boldsymbol{e}_z$:

$$\dot{R} = -\alpha/R, \tag{A.61}$$

$$\dot{z} = \beta/R. \tag{A.62}$$

Here $\alpha = \langle +|\underline{\underline{D}}+\rangle \in \mathbb{R}$ is called the filament tension, since the filament ring will compress for $\alpha > 0$ and expand for $\alpha < 0$ similar to the elastic properties of a stretched or compressed rubber-based material. The parameter $\beta = \langle -|\underline{\underline{D}}+\rangle \in \mathbb{R}$ gives the magnitude of the drift along the symmetry axis. The negative sign in the radius dynamics results from the radius R moving in opposite direction to the normal vector $\boldsymbol{N}$. Note that these equations are only strictly valid in the limit of small filament curvature κ and sufficiently far from system boundaries. An alternative derivation arises within a kinematic approach [414], which is based on the curvature induced motion of fronts.

In summary, the preceeding machinery allowed us to reduce a large problem on the order of 10^6 dimensions to a two-dimensional problem amenable to the standard theoretical tools of planar dynamical systems.

Appendix B

Implementations

B.1 Experimental setups

This section gives a chronological overview of the experimental setups and techniques developed and employed over the course of this thesis.

B.1.1 Setup I: Three-dimensional active medium

Spiral waves and scroll rings alike can be created by erasing a part of a planar wave[38]. To realize excitation waves in a spatially extended medium, we employ the Belousov-Zhabotinsky (BZ) reaction, which is well-established as a chemical oscillator (appendix C). Instead of exploiting sensitivities to externally applied fields like light (section B.1.2), it is possible to just shake the medium in order to completely erase excitation waves due to fluid mixing. Since a part of the original wave needs to remain in order to nucleate a scroll ring, there is a complementary part of the medium that consists of agarose hydrogel. The hydrogel matrix prevents hydrodynamic flows from occurring and thus preserves the structure of the excitation waves. The medium is prepared as follows:
A liquid- or gel layer with a height of 4 mm requires 25 ml of the following reaction solution: 14.5 ml of bidistilled H_2O (water), 8 ml 0.5 M H_2SO_4 (sulfuric acid), 1 ml 1 M $C_3H_4O_4$ (malonic acid or MA), 1 ml 1 M $NaBrO_3$ (sodium bromate), 0.5 ml 25 mM $(Fe(o-phen)_3)SO_4$ (ferroin) and in case of the gel layer 0.2 g $(C_{12}H_{18}O_9)_n$ (agarose).
The liquid layer is prepared by adding H_2O, H_2SO_4, $C_3H_4O_4$ and $NaBrO_3$ to an empty beaker with a volume of 50 ml. Before the solution for the gel layer receives the reagents, the agar must be cooked. To this end, only water with agarose and a magnetic stirrer is filled in another beaker of 50 ml. This mixture is brought to boil on a heating plate while stirred. Once the boiling point is reached after about 6 –7 min, the beaker is moved to an unheated

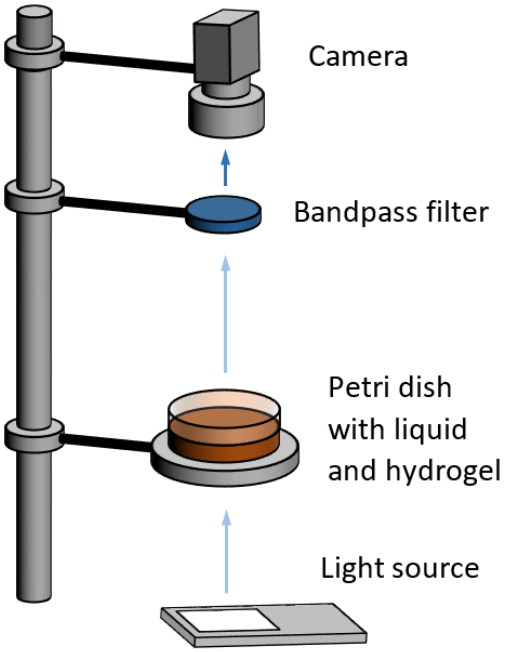

Figure B.1 | Setup I: Scroll ring formation and time evolution are monitored spectrophotometrically in a three-dimensional active medium. White light from a spatially homogeneous light source is absorbed depending on the oxidation state of the ferroin catalyst. This allows for the optical recording of chemical waves with a CCD camera.

plate for the solution to cool for 12 –13 min while gently stirred, but it is not to solidify. After this time, H_2SO_4, $C_3H_4O_4$, $NaBrO_3$ and ferroin are added with a pipette under rapid stirring. Adding the complete set of BZ reagents initiates the first chemical oscillation, which is visible as a periodic color change from red to blue. The first oscillation takes about 2 min, after which the solution in the beaker is transferred to a Petri dish. While the gel solidifies, ferroin is also added to the solution for the liquid layer while stirring strongly. It takes about 5 –7 min for solidification to finish, at which point the solution for the liquid layer is added on top of it in the Petri dish. This completes the preparation of the bipartite active medium. The procedure to generate a scroll ring starts with introducing a silver wire of high purity (99 % Ag) perpendicular to the gel-liquid interface for 15 –50 s. Because the silver wire perturbs the local ion balance via formation of AgBr, it initiates a small spherical excitation wave at the point of contact with the silver wire tip. About 20 s after its appearance, the medium is shaken manually to suppress wave formation in the liquid layer. Once the spherical wave in the gel layer reaches the desired initial radius R_0, shaking is suspended. This allows the wave to propagate into the now calm liquid layer and curl in, which nucleates the scroll ring. Note that the initial distance to the boundaries h_1 and h_2 (Fig. 2.4) is determined by the

used solution volumes of the gel and liquid layer. Caution has to be taken as to not shake the medium for too long, because phase waves will emerge after about 5 min that start from the radial Petri dish boundary and travel inwards. Their interaction with the spherical wave will disturb the circular shape of the scroll ring and can even prevent it from forming.
To observe the evolution of the scroll ring, the Petri dish containing the chemical bipartite medium is placed in a spectrophotometric setup (Fig. B.1). The Petri dish has to be placed perfectly in parallel to the ground to avoid inclined height gradients in the system. This is realized by a metal ring that sits on three small screws that can be adjusted in height to correct for inclinations. Before the observation begins, the active medium is sealed from outside oxygen, that is known to negatively affect the reaction[415], by very carefully placing a floating acrylic glass plate on the liquid layer and a plastic lid on the Petri dish. Convective temperature exchange is minimized by attaching a transparent plastic wrap to the bottom of the metal holding piece under the Petri dish. Furthermore, the entire setup is encased in a cardboard box.
With these precautions in place, the optical observation is performed by exploiting the difference in absorption spectra of the catalyst for different oxidation states. The white light from a spatially homogeneous light illuminator (Fiber-Lite PL-800) with light bulb (USHIO EKE/L 21 V, 150 W) gets absorbed strongly by the reduced form of the catalyst, but not by the oxidized form. The largest contrast is obtained for blue wavelengths (Fig. 2.3c), which is enhanced by a dichroic filter (Edmund Optics) that is light-transmissive for 400 –500 nm. The transmitted light-intensity is recorded in a spatially-resolved manner with a CCD camera (COHU 2122-1000), that relays the data to a framegrabber card (Data Translation 3155) to be saved as 8-bit grayvalue image files for later analysis (Fig. 2.5).

B.1.2 Setup II: Two- and three-dimensional active medium

It is possible to make the Belousov-Zhabotinsky reaction light sensitive[416] by utilizing the photosensitive catalyst ruthenium-tris-dimethylene-bipyridine ($Ru(dmbipy)_3^{2+}$)[126]. In addition the absorption spectra of the reduced, $Ru(dmbipy)_3^{2+}$, and the oxidized form, $Ru(dmbipy)_3^{3+}$, are sufficiently different to allow for spectrophotometric measurements (Fig. B.2). The oxidized form is approximately transparent to all visible wavelengths, while the reduced form absorbs blue wavelengths 400 –500 nm (Fig. B.3a).
To perturb excitation waves in a thick three-dimensional medium that absorbs light, large light intensities are required. These intensities can be achieved by tuning the projector (Casio XJ-A140V). As is shown in figure B.3, the projector natively emits blue, green and red light. In the experiment, we only require blue light. For this reason we remove the lenses and mirrors that inject the red and green beam into the output beam line. Furthermore, there is

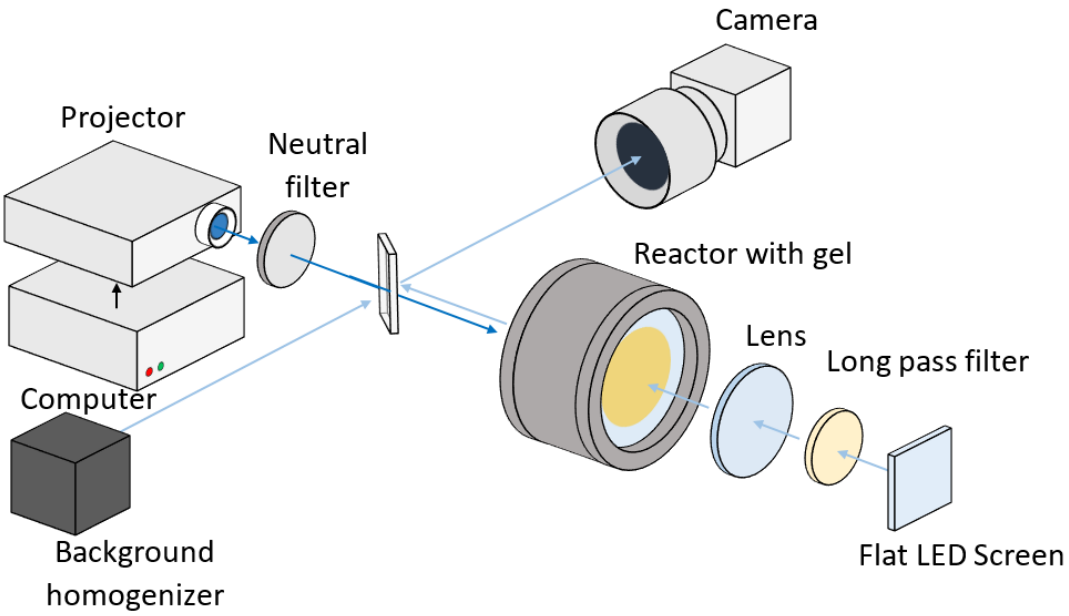

Figure B.2 | Setup II: Spectrophotometric setup for spiral wave control and scroll ring nucleation via light. The projector applies spatio-temporally varying light intensity for control (dark blue arrows) of chemical dynamics. The resulting patterns are observable due the absorption difference in the oxidation state with light (pale blue arrows) from a flat LED, which was repurposed from a cell phone. A hollow black cardboard box acts as a homogeneous background for the camera recording, because it does not reflect stray light.

no dedicated source for green light. Instead, blue light is transformed into green light via a fluorescent layer on the colorwheel. Unfortunately the colorwheel also functions as the internal clock of the projector, which stops operating without it. The solution is to remove the fluorescent coating and replace the lost mass in the form of copper disks to preserve the angular momentum. Another option is to extract the colorwheel and connect it to the projector mainboard from the outside.

Another challenge is the spatial light gradient over the area of a projected image. Initial experiments showed, that the native heterogeneous light negatively impacts the formation and lifetime of planar scroll rings.

The spatial light distribution of the projector is homogenized by first measuring the normalized sensitivity at every pixel of the camera chip $S_{\text{chip}}(x,y)$ by taking a snapshot of a cloud-free blue sky or the output of an Ulbricht sphere. This information allows us to correct for heterogeneities of the camera chip. Next we assign an image of constant brightness I_0 as the projector output. With the calibrated camera, we take a snapshot of the emitted projector light intensity $I_{\text{hetero}}(x,y)$ on a fluorescent screen. This allows us to compute a pixel-wise

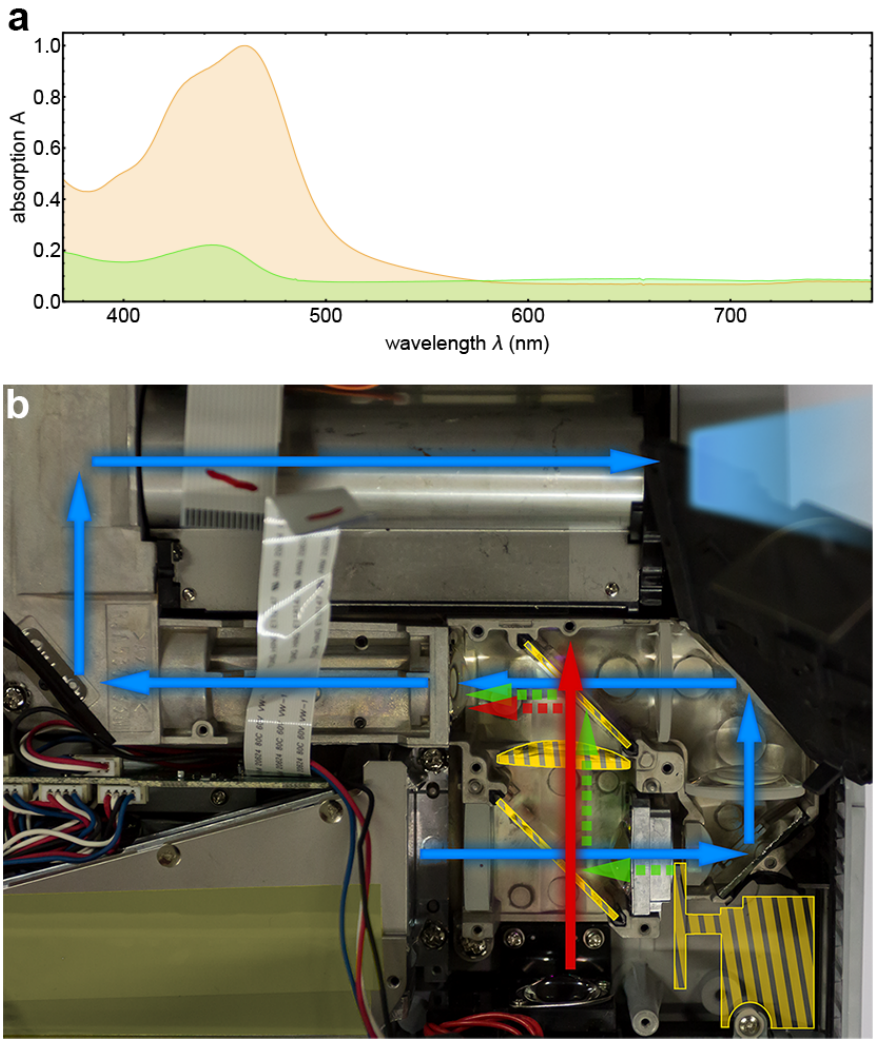

Figure B.3 | Control and observation by blue light. (a) Absorption spectra of the reduced (orange) and oxidized (green) form of the $Ru(dmbipy)_3^{2+}$ catalyst. Note that control and observation light can not be spectrally separated as both rely on the absorption peak at $\lambda = 450\,\text{nm}$. Thus the light distribution for spatio-temporal control is also visible on the camera image of the chemical pattern. (b) The projector (Casio XJ-A140V) is modified to emit a peak amount of blue, instead of red or green light. This is achieved by removing the optical elements, such as lenses, mirrors and the colorwheel (yellow dashed shapes) required for the red and green light to be passed into the main beamline.

multiplicative correction filter $F_{\text{correction}}$ for later use in experiments:

$$F_{\text{correction}}(x,y) = \frac{I_0}{I_{\text{hetero}}(x,y)} S_{\text{chip}}(x,y) \tag{B.1}$$

$$I_{\text{corrected}}(x,y) = I_{\text{hetero}}(x,y) \cdot F_{\text{correction}}(x,y). \tag{B.2}$$

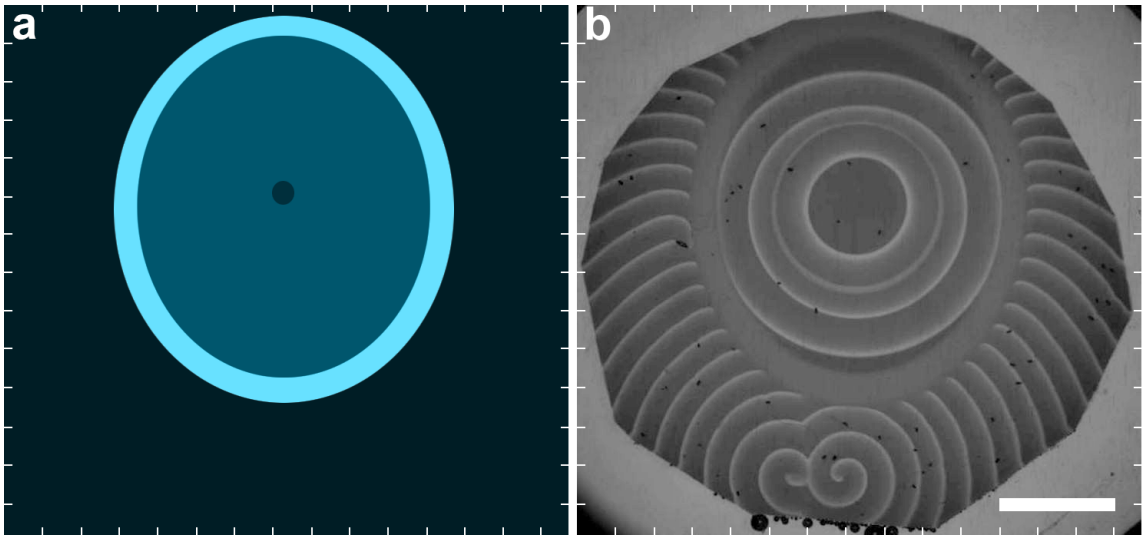

Figure B.4 | Light-mediated scroll ring initiation. (a) With the modified spatial light modulator, it is possible to emit a spatiotemporal light intensity $I(x,y,t)$ that allows for the formation of scroll rings. It consists of a bright boundary layer, that prevents waves from the outside to interact with the scroll ring, and a variable light intensity on the inside. (b) Inside the shielded area a scroll ring was nucleated, that periodically emits circular wavefronts. The white scale bar corresponds to 1 cm.

Scroll rings are initiated with a spatial light distribution $I(x,y)$ consisting of three concentric elliptic light regions stacked on top of each other (Fig. B.4a). The largest circle is very bright and prevents outside excitation waves, especially those coming from the hydrogel boundary, to interfere with the patterns on the inside. The next ellipse is less bright to support the propagation of excitation waves. The innermost circle is the darkest. In this region oscillations may occur spontaneously. Once this oscillation spreads into the excitable domain as an excitation wave, the innermost dark region is removed to prevent oscillations from interfering with the scroll ring. The upper part of the cylindrical excitation wave in the excitable domain is removed with a short burst of high light intensity. Here, the duration of the illumination is crucial. If it is too short the cylindrical wave is not perturbed, but if it is too long all waves are erased. The right duration of illumination finally leads to the successful nucleation of the scroll ring (Fig. B.4b).

In contrast to version I (section B.1.1), this versatile setup allows for creating scroll rings of large initial radii R_0, because interference from the boundaries is suppressed with light. In addition rings of both chiralities are possible by switching the brightness of the two inner elliptic regions. Furthermore any autocompletion patterns, like spirals[169] or multiple, interacting scroll waves or closed filaments with varying curvature, like ellipses, squares or heart-shaped loops can be realized by starting from a suitable initial condition and then removing the upper half of the wave structures with an intense short burst of light intensity.

B.1.3 Setup III: Discrete oscillators

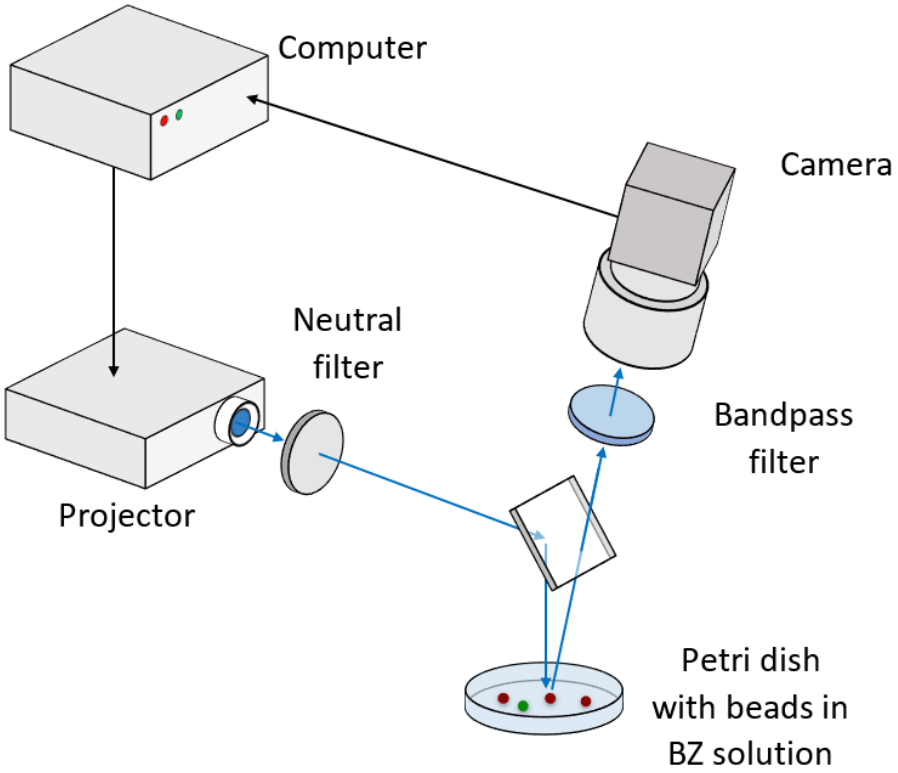

Figure B.5 | Setup III: Chemical oscillators in a Petri dish exhibit color changes depending on the phase in their oscillation cycle. The color information is recorded in grayscale by a CCD camera mounted under a slight angle to avoid reflections from the liquid surface. Note that the grayscale value is proportional to the scattered light intensity at bead surface. The grayscale information is fed back to a computer. The computer calculates the coupling signal (3.9), which is projected on each bead with a spatial light modulator (Toshiba TLP X20). The neutral filter allows for reducing the intensity of the projector without restraining the dynamic illumination range of the projector. The bandpass filter increases the contrast by blocking irrelevant wavelengths outside of 440 –460 nm.

This experimental setup (Fig. B.5) supports experiments on discrete chemical micro-oscillators that are connected by mutual light perturbations instead of diffusive coupling via mass exchange[244,245,417–419]. Discrete chemical oscillators are realized by placing cation-exchange beads (DOWEX SOW X4-200) soaked with the catalyst ruthenium-tris(bipyridine) ($Ru(bipy)_3$) in a Petri dish filled with BZ solution. Employed reagent concentrations are given in table C.1. Since the catalyst is confined to the bead locations, the BZ reaction can only occur at the bead sites. Each bead is a microporous sphere with a size of about 200 µm. When loaded with catalyst and soaked in water the diameter increases to about 300 µm. Resembling a solidified hydrogel[318] a bead features a tight polymer matrix with cavities and tunnels for exchange of molecules. The polymer matrix consists of long polystyrene chains that are

crosslinked with divinylbenzene[420]. It is important to note, that $Ru(bipy)_3$ is actually able to slowly leak from the beads, but at a very slow rate. After an hour, there is non-negligible loss of the catalyst to the surroundings. Hence, the duration of an experiment is limited to about half an hour, during which oscillation periods change about 10 %. This issue is resolved in version V (section B.1.5) with the introduction of additional dimethylene ligands in the complex catalyst.

As in previous experimental setups (sections B.1.1 and B.1.2) the chemical oscillation cycle can be monitored optically due to changes in the absorption spectra that follow the oxidation state of the catalyst. The absorption spectra of the $Ru(bipy)_3$ catalyst very closely resemble those of $Ru(dmbipy)_3^{2+}$ (Fig. B.3a). In contrast to the other setups, the grayvalues that are recorded by the CCD camera (Lumenera Infinity 2) are not related to changes in the transmitted light intensity, but are due to light scattered at the bead surfaces. The reason for this is that the camera views the beads under a small tilted angle to avoid bright reflections of the projector intensity from the water surface. In this reduced state of the catalyst incident light is absorbed, while in the oxidized state light can pass through the bead and scatter back from it. This light intensity is measured by the CCD camera as 8-bit grayvalues. To enhance the contrast, the measured grayvalues $v_{i,0}$ are normalized by the minimum $v_{i,\min}$ and maximum $v_{i,\max}$ from a running window over the last 100 s of the individual timeseries:

$$v_i(t) = \frac{v_{i,0}(t) - v_{i,\min}}{v_{i,\max} - v_{i,\min}}. \tag{B.3}$$

The resulting normalized grayvalues of each bead are used in an autonomously running MATLAB program to calculate the appropriate light perturbations to each oscillator based on the current state of all of its neighbors in the network (3.9). The feedback is applied with a projector (Toshiba TLP X20) with a dynamic range of 256 distinct light intensity values. Thus the feedback needs to be appropriately rescaled to fit in this range.

Note that the control and measurement light are not spectrally separated as in section B.1.2. To avoid artifacts in the recorded grayvalues, measurement and feedback are performed alternatingly in a duty cycle. The measurement duration is essentially given by the exposure time of the camera, which is about 1 s. After computing the new feedback values, which only takes a negligible amount of time, the feedback is applied for 2 s. Since the chemical oscillation period takes 40 –80 s, a duty cycle length of 3 s is too small to induce stroboscopic artifacts. This was also verified by varying the length of the duty cycle, which did not affect the experimental outcome.

One complication is that the beads are not spatially fixated in the Petri dish. This allows them to move around. The movement is caused by convective flows in the liquid layer due to the

produced reaction heat as well as the product CO_2 accumulating under the beads until there is enough to rise up and simultaneously push the bead to a different location. Experiments showed, that the convective flow can be suppressed by reducing the height of the liquid layer to 2.0 mm. However, this also worsens aging effects due to oxygen inflow through the open boundary with air.
The solution was to develop a tracking algorithm, that continuously updated the location of each bead for the projected image. For each bead, the position of its center of mass is detected with an image recognition program. The same procedure is repeated for the next camera snapshot. Then the algorithm compares the new positions to the old ones and pairs up those with the least distance. For not too large movement this algorithm works flawlessly. In the case of a collision between two beads the algorithm will fail. However, once two beads collide, they will also couple diffusively and thus corrupt the experiment either way.

B.1.4 Setup IV: Discrete oscillators

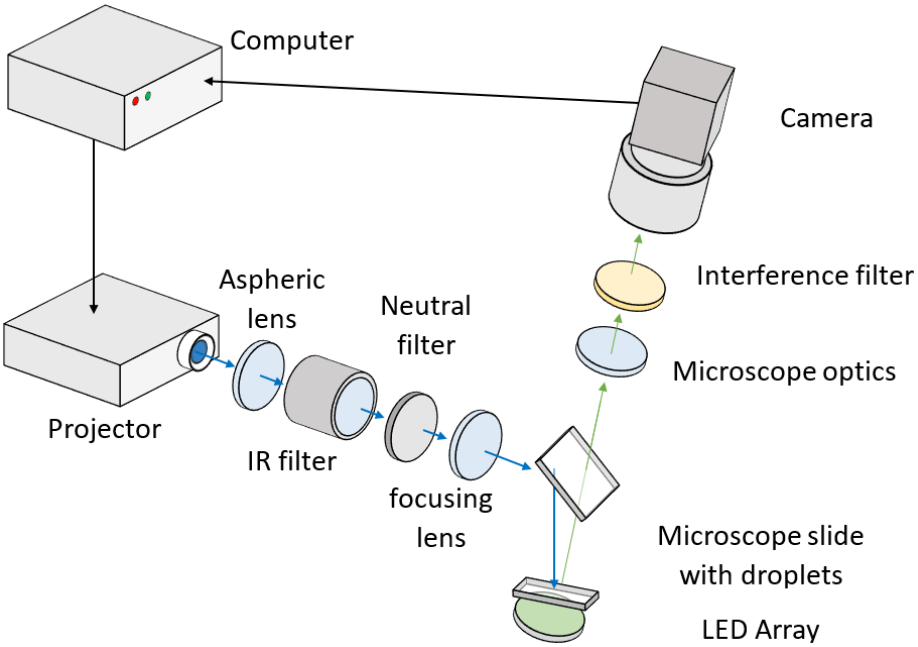

Figure B.6 | Setup IV: The projector (Acer P1120) provides optical feedback, that is focused by lenses at a microfluidic chamber holding BZ droplets on a microscope slide. A camera (QImaging Retiga 2000R), attached to a microscope (Zeiss Stemi 2000-C) mounted over the droplets, records the chemical oscillation states of the droplets as grayvalues due to changes in absorption spectra of the catalyst. Based on their arithmetic mean, the intensity of the global light feedback is adjusted.

In this variant, BZ droplets[421,422], instead of beads are used as discrete chemical micro-oscillators in spectrophotometric measurements (Fig. B.6). Droplets are micrometer-sized

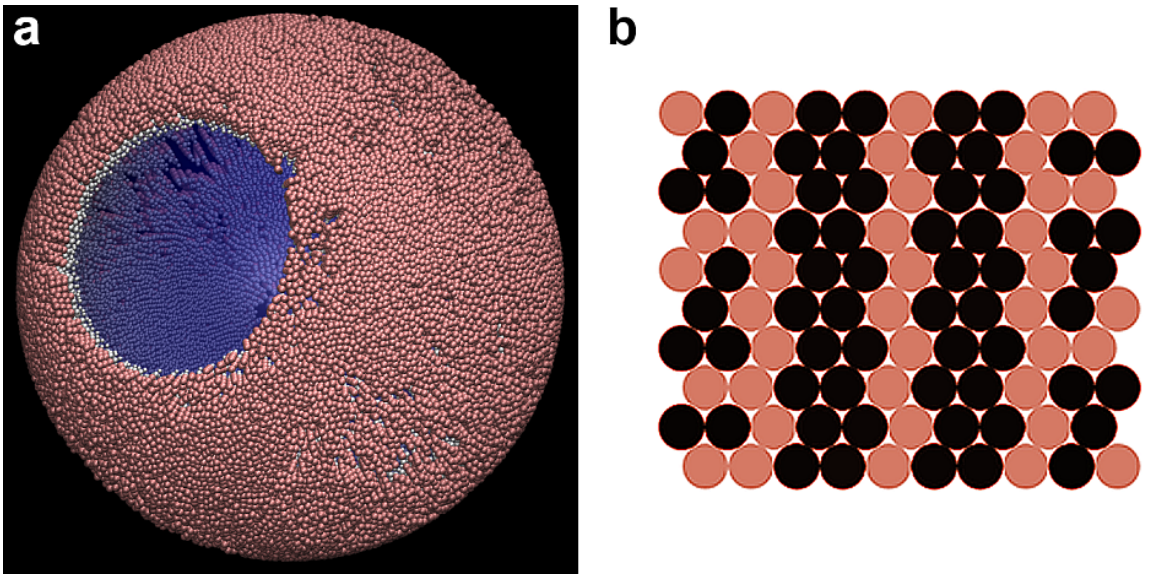

Figure B.7 | BZ Droplets. (a) The molecular arrangement in the membrane of a lipid monolayer micelle as positioned with packmol[423] and visualized with VMD[424]. Non-polar heads of the surfactant (red) are turned to the outside, while polar heads (white) are turned to the inside, where the BZ reaction (blue) occurs. (b) A hexagonal carpet of droplets as modeled with (C.6) exhibits a Turing pattern composed of droplets with high and low catalyst concentration.

objects with a diameter between 50 –300 µm. They contain a small volume of BZ solution, which is encased in a monolayer (Fig. B.7) of surfactants (Pico-Surf). These lipid vesicles resemble living cells, whose membrane is a lipid bilayer.

Once the BZ droplets are pumped into a rectangular region on a microfluidic chip, they form a close-packed hexagonal lattice that is immersed in oil (Fluorinert FC-40). The droplets can interact with each other, because non-polar chemical compounds can pass through the droplet membrane and diffuse through the oil phase. The most significant non-polar intermediate in the BZ reaction is bromine (Br_2). That explains why coupling through the oil-phase slows down chemical oscillations in the BZ reaction, because bromine can spontaneously decay to bromide (Br^-), which acts as the inhibitor in the BZ mechanism (see appendix C.1.3).

The BZ solution in the droplets contains a dual catalyst, consisting of ferroin as well as photosensitive $Ru(bipy)_3$. This allows for the spectral separation of control and observation light. While the oscillation cycle can be manipulated with light of 400 –500 nm (Fig. B.3a), it can simultaneously be observed at 500 –600 nm (Fig. 2.3c). However, an additional interference filter is also required to exclude fluorescence (Fig. 4.2c) of the $Ru(bipy)_3$ catalyst at large wavelength $\lambda > 550\,\text{nm}$.

In contrast to version III (section B.1.3), care has to be taken in order to not evaporate the droplets with illumination from the 200 W mercury lamp in the projector. For this purpose

an additional infrared filter, that consists of a water chamber, is included in the beam line that removes heat radiation with $\lambda > 1100\,\text{nm}$.
Note, that droplets can disappear over time. This is due to a sudden failure of structural integrity of the surfactant membrane, which results in the dissolution of the droplet. These spontaneously appearing defect sites in the regular hexagonal lattice lead to a drifting motion of all remaining droplets until the lattice finds a new state of minimum energy. Furthermore, the BZ reagents inside the droplets are consumed after about 100 oscillation periods. Since the membrane is impermeable for polar molecules, it is not possible to replenish them.
The oil phase is only permeable for inhibiting but not for activating species. As a consequence, Turing patterns prevalently emerge on hexagonal carpets of BZ droplets (Fig. B.7b). Depending on initial conditions they can take the shape of patches, stripes and spots. Introducing yet another source of inhibitory coupling via global illumination based on the mean grayvalue, leads to oscillating antiphase patterns, where direct neighbors never fire together. In addition, there are also mixed oscillatory and Turing patterns, where one set of oscillators ceases their activity, while the other oscillators continue to oscillate. Increasing the global feedback strength enlarges the domain of the mixed patterns.

B.1.5 Setup V: Discrete oscillators

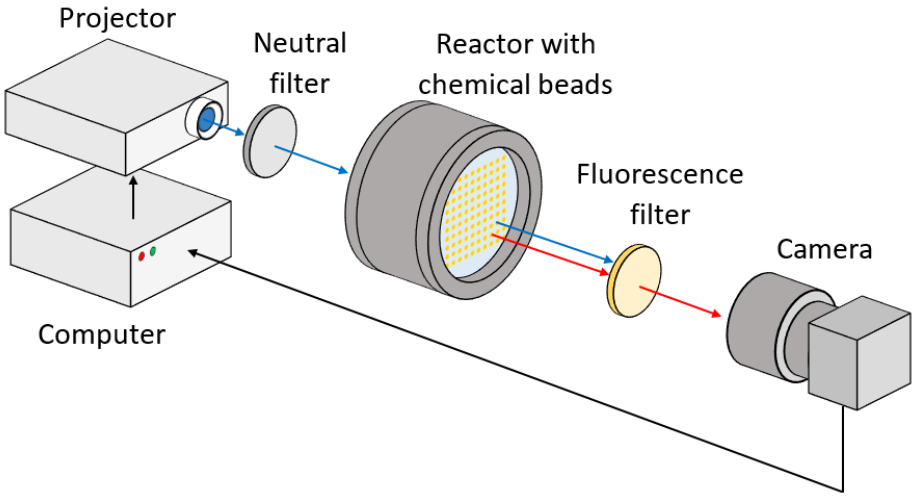

Figure B.8 | Setup V: A large reservoir of chemical micro-oscillators is fixated on an acrylic glass plate in an open thermostatted reactor[126]. During their oscillation cycles they emit fluorescence photons (red arrows), which are recorded as grayvalues with a hardware-triggered (NI-USB 6000) CMOS camera (Imaging Source DMK 23UX174) and a 50 mm objective. The values are sent to a computer to determine the projected light intensity I_i on oscillator i according to (4.24). This feedback (blue arrows) is applied to the oscillators with a spatial light modulator (Casio XJ-A140V).

Version V is specifically developed to support a large number of addressable oscillators and simultaneously allow for independent and individual control of every oscillator[334]. The setup only features a single optical axis due to the fact, that the ruthenium-tris(dimethylene-bipyridine) catalyst ($Ru(dmbipy)_3^{2+}$) absorbs light around $\lambda = 450\,nm$ and emits fluorescence photons for $\lambda > 600\,nm$. This allows for the spectral separation of control and observation light. An additional improvement over version III (section B.1.3), is the use of three additional dimethylene groups as ligands in the ruthenium based catalyst $Ru(dmbipy)_3^{2+}$[126]. They keep the catalyst sterically fixated in the bead polymer matrix, such that it can not leak. This greatly reduces aging effects. The spatial drifting problem is resolved as well by confining the location of all beads. Every bead is trapped within a well on the acrylic glass plate and sealed off under a silica hydrogel layer. The setup also relies on modifying the projector for high blue light intensities (Fig. B.3b). Since the cross section of each bead is very small (Fig. 4.4a), they require a bright light intensity for successful manipulation. Note that the setup also allows for experiments on continuous systems, as the bead plate can readily be exchanged with a plate holding a gel layer. In this case the observed grayscale images will be inverted in comparison to images from version II (section B.1.2). This is because the reduced form of the catalyst emits fluorescence photons, whereas in version II the oxidized form of the catalyst is transmissive for visible light.

Micro-oscillator preparation

It is known, that the size of the beads has an impact on the oscillation period[325], because reagent exchange with the surrounding solution scales with the bead surface area. Here, we employ a sieving procedure for bead size homogenization with a custom-built sieve machine (Fig. B.9a). Its components are a default laptop that hosts a frequency generator program. The output is fed to an amplifier (Phase Evolution RS4) and powered by a DC generator with 13 V (Statron, Model 3233). The amplifier is connected to a subwoofer speaker (SXCTRON, S8P12W, 12 inch membrane diameter, 200 W). Once turned on, the low-frequency vibration of the membrane (18 Hz) is transferred to the sieve tower that is fixated on the membrane by two-sided tape and crossed rubber bands. To reduce movement, the speaker is fitted to a wooden base and weighted with a heavy lead block. The sieve tower consists of a collection basin, three sieves of 10 cm diameter (Retsch) with mesh sizes, 106 µm, 112 µm and 125 µm, as well as a glass top. We employ three stages to reduce the load on the sieve in the middle, because if there are too many particles, they clog the sieve mesh. To increase the throughput of the sieving process, we also add glass beads of 1 mm diameter (Retsch) to each sieve. Their kinetic energy pushes the resin through the holes. After two hours of sieving, the beads are separated well by their diameters and are collected from the sieves. The quality of the sieving

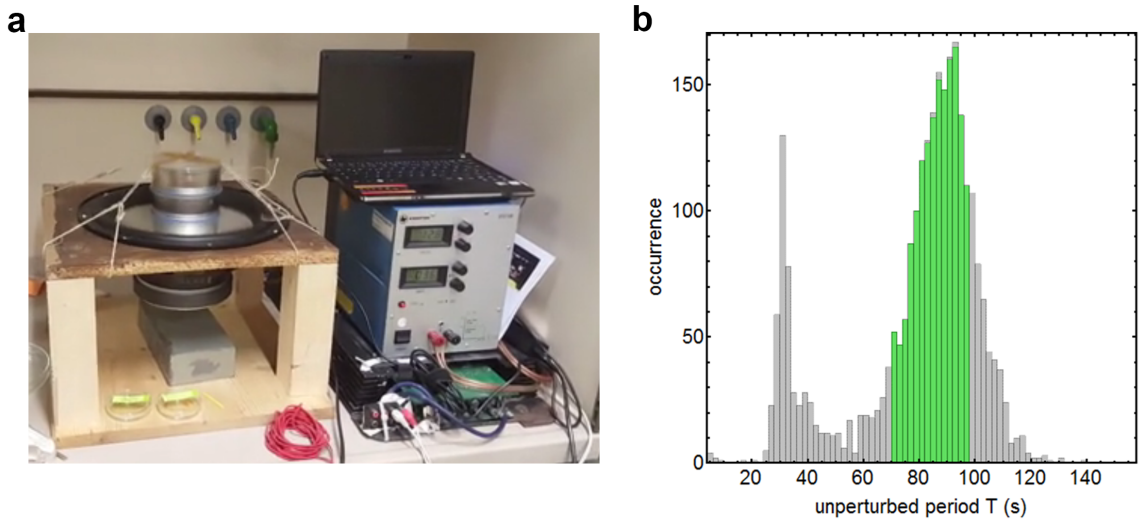

Figure B.9 | Size homogenization of micro-oscillators. (a) Photograph of the custom-built sieve machine. (b) The distribution shows the narrow period selection used for the experiment shown in figure 4.8. The tails of the distribution are due to oscillator beads with abnormal concentrations of catalyst and the second peak is due to double occupancy of some wells.

process is controlled by measuring the beads under a basic light field microscope (Motic SMZ-143 Series) with a mounted camera (ImagingSource DFK 21AUC03). The particles and their sizes are detected automatically employing OpenCV algorithms in Python. Sieved resin beads, $m_{\text{beads}} = 1.0\,\text{g}$ in $V_{H_2O} = 5\,\text{ml}$ H_2O, are mixed by a vortex mixer (Velp Scientifica) in a test tube with $V_{\text{cat}} = 15\,\text{ml}$ of $c_{\text{cat}} = 1.66\,\text{mM}$ Ru(dmbpy)_3^{2+} solution. The latter is slowly added with a pipette over a span of 10 minutes. Mixing continues autonomously for two days to achieve a homogeneous catalyst loading of 2.5×10^{-5} mol Ru(dmbpy)_3^{2+}/g resin on all beads. To achieve a desired catalyst load n_{load}, the required catalyst concentration c_{cat} can be calculated according to:

$$c_{\text{cat}}[\text{mM}] = n_{\text{load}}[10^{-6}\,\text{molg}^{-1}] \cdot \frac{m_{\text{beads}}[\text{g}]}{V_{H_2O} + V_{\text{cat}}[\text{ml}]}. \tag{B.4}$$

The outcome of this process is verified by color saturation measurements (Fig. 4.4b). Note that an overloading of beads with Ru(dmbipy)_3^{2+} leads to the decay of the catalyst. This can be inferred from exposure to ultraviolet light, to which the intact catalyst responds with fluorescence. Also the color of beads turns to pitch black, if there was too much catalyst loaded on them. The catalyst-loaded beads are placed on an acrylic glass plate with $64 \times 44 = 2816$ wells. The wells have a depth of 150 µm, a diameter of 200 µm, and a separation of 400 µm, covering an area of $3.8 \times 2.6\,\text{cm}^2$. To allow for distribution of the beads, the plate is coated with methanol or a water-surfactant (Titan X 0.05 %) mixture to

lower the surface tension. A fine brush is used to place a single bead in each well. For convenient placement, a CCD camera is mounted to a microscope so the placement progress can be viewed via a computer screen.
After three hours, the beads are sealed in their wells by applying liquid silica hydrogel with 20 shots from a spray bottle. Surfactant is added to the mixture, to reduce surface tension, which otherwise induces droplet formation from the sprayed mist. Note that spilling the liquid hydrogel over the plate would pull the beads out of the holes, that they were carefully placed in. Afterwards the hydrogel is allowed to solidify and dry for 30 minutes and the plate is stored in a mildly acidic solution.
On the next day, the plate, prepared with oscillator beads, is installed in the reactor. Catalyst-free BZ solution is pumped into the reactor to allow for the BZ reaction to occur, but only at the bead locations. From the array of chemical oscillators, we select oscillators based on their natural oscillation periods, as shown in Fig. B.9(b).

B.1.6 LabVIEW Control Program

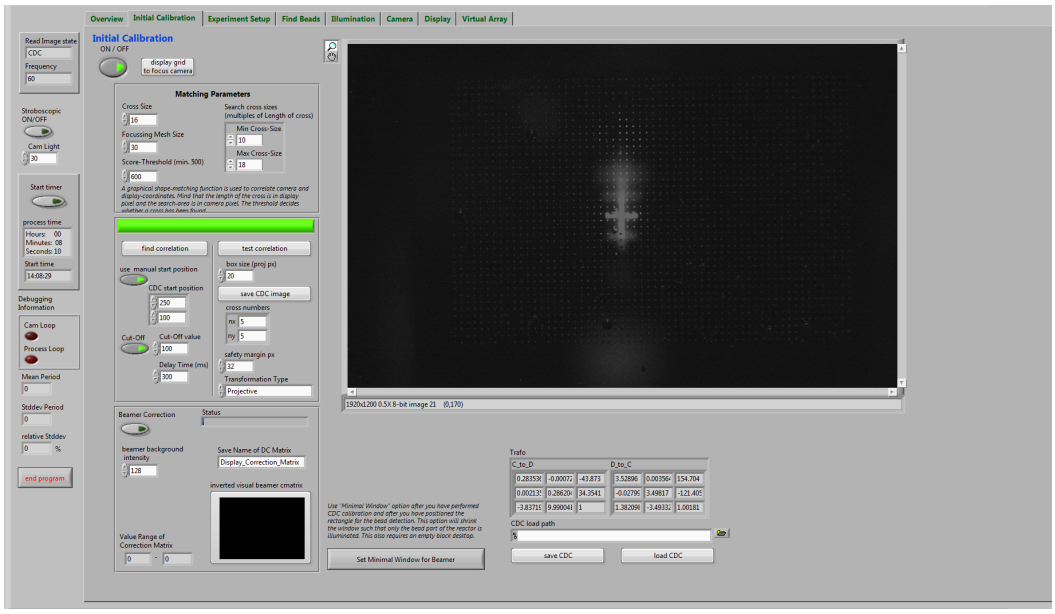

Figure B.10 | Camera display correlation. This routine projects 5×5 crosses subsequently at equally spaced positions on the reactor plane, that are recorded with the camera. If a cross is not found, it performs a random walk until it is sharp enough to be detected at a different location.

The program to control setups II and V is written in LabVIEW as it provides an intuitive user interface to the experimentalist. Its architecture follows an object-oriented approach to allow for the simple integration of future experiment routines.

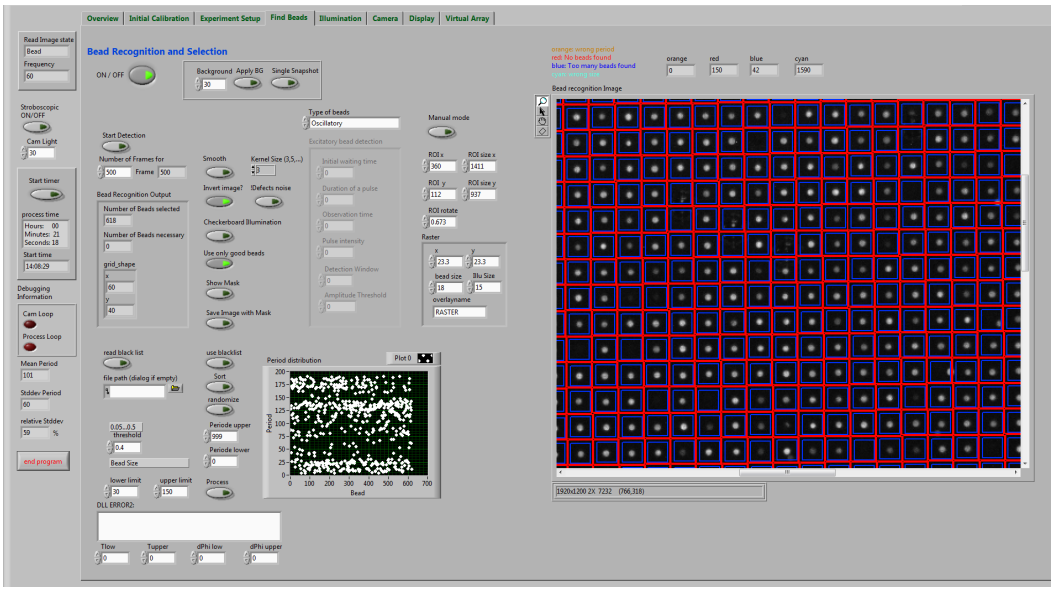

Figure B.11 | Bead detection and selection. The image shows the bead array on the acrylic glas plate overlaid with red and blue lines based on spatial information that was entered by the experimentalist. Only beads that are located inside blue boxes are accepted as valid oscillators. The scatter plot shows the periods of the currently selected oscillators.

Before any experiments can be performed, the setup needs to be initialized. It requires a mapping between coordinates on the virtual projector image and coordinates in the real-world that are observed with the camera. The mapping is used to correctly spatially address different locations on a continuous gel or individual nodes in a network. The spatial mapping is based on a homographic transformation[425], which corrects for perspective distortions. To find it, a number of white crosses are applied by the projector at different locations on the reactor plane (Fig. B.10). With an image recognition routine, these crosses are detected in the camera images. After all crosses were found, the matrix elements in the homographic transformation are computed employing a linear regression.

In the case of experiments with networks, the available beads must be located and characterized (Fig. B.11). Since each bead is located in a well on a rectangular grid, the dimensions of this grid in the camera image are required by the program to assign each oscillating pixel in the grid to a bead. Pixels without oscillations of sufficient amplitude are discarded. Beads are further filtered based on their size. Even after the mixing procedure there might be few very small or very large outliers that are left over. Also a single well may be occupied by two beads, which appears as a single large one. Furthermore the oscillation is tested for its relaxation character exhibiting a steep rise and a slow decay. False oscillations can occur that are due to pinned CO_2 bubbles periodically growing and bursting. Once all true oscillators in the reservoir have been identified, they can be further filtered based on the natural oscillation

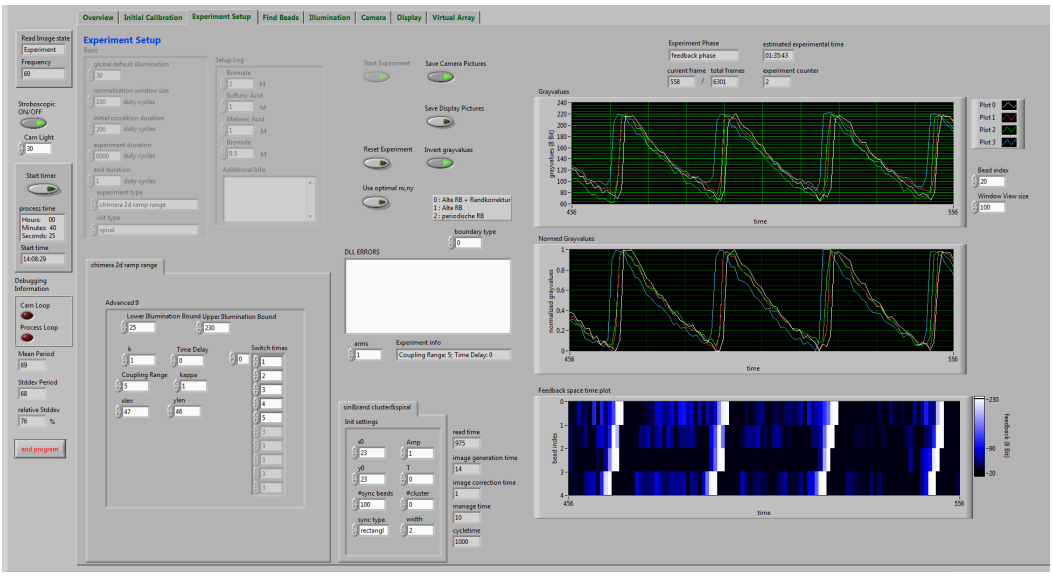

Figure B.12 | Experiment supervision. This frontpanel allows for selecting from a number of different types of network experiments and initial conditions. While the experiment runs, the live dynamics of a subset of all nodes as well as feedback applied to them is visualized.

periods for example to achieve a narrow or multi-peaked period distribution. Another option is to filter the beads by their responsiveness to light perturbations.

Once all suitable oscillators have been selected, they can be coupled into a desired network with a chosen coupling function (Fig. B.12). After an initial condition stage during which individual oscillator phases are entrained by local periodic feedback to show a desired starting condition, the coupling function takes over and continues autonomously until the preprogrammed experiment duration expires. Then all data is saved to binary files for later analysis and visualization. As a means of quickly exploring parameter space, it is also possible for the experimentalist to change coupling parameters like coupling strength K and time delay τ during the experiment. The effect of these changes can be followed in a live visualization of the oscillators.

Variations of this program were developed in LabVIEW and MATLAB to suit the requirements for experiments in the workgroups of Kenneth Showalter in Morgantown and Vladimir Vanag in Kaliningrad.

B.2 Numerical Implementations

Simulations of three-dimensional spatial domains of nonlinear PDEs (chapter 2) or nonlocally coupled equations in two dimensions (chapter 4) are computationally very expensive and take a long time.
For this reason a simple, but fast forward Euler integrator[158,426] is implemented. In order to discretize an autonomous continuous dynamical system,

$$\frac{d}{dt}\boldsymbol{c}(t) = \boldsymbol{f}\left(\boldsymbol{c}(t)\right) \tag{B.5}$$

with local dynamics $\boldsymbol{f}$ and a dynamical variable vector $\boldsymbol{c}(t)$, the time evolution is discretized into steps $t \to t_i = i\Delta t$ and the time derivative is replaced with a difference quotient. The shorthand notation $\boldsymbol{c}^{t+1} = \boldsymbol{c}(t_{i+1})$ is introduced here for clarity,

$$\frac{d}{dt}\boldsymbol{c}(t) \to \frac{\Delta \boldsymbol{c}}{\Delta t} = \frac{\boldsymbol{c}^{t+1} - \boldsymbol{c}^t}{t_{i+1} - t_i} = \boldsymbol{f}(\boldsymbol{c}^t) \leftarrow \boldsymbol{f}(\boldsymbol{c}(t)). \tag{B.6}$$

Solving now for $\boldsymbol{c}^{t+1}$ the forward Euler scheme is:

$$\boldsymbol{c}^{t+1} = \boldsymbol{c}^t + \Delta t\, \boldsymbol{f}(\boldsymbol{c}^t). \tag{B.7}$$

Note that the choice of the time index in the local dynamics gives rise to either the explicit Euler scheme for $\boldsymbol{c}^t$ or the unconditionally stable, implicit Euler scheme for $\boldsymbol{c}^{t+1}$ [158].
Introducing spatial coupling leads to a reaction diffusion equation:

$$\frac{\partial}{\partial t}\boldsymbol{c}(x,t) = \boldsymbol{f}(\boldsymbol{c}(x,t)) + \underline{\underline{D}}\frac{\partial^2}{\partial x^2}\boldsymbol{c}(x,t). \tag{B.8}$$

This PDE is translated into a set of coupled ODEs via the method of lines[158]. Discretizing space $x \to x_i = i\Delta x$ and replacing spatial derivatives with difference quotients yields:

$$\frac{\partial}{\partial t}\boldsymbol{c}_i(t) = \boldsymbol{f}(\boldsymbol{c}_i(t)) + \underline{\underline{D}}\frac{\boldsymbol{c}_{i+1}(t) - 2\boldsymbol{c}_i(t) + \boldsymbol{c}_{i-1}(t)}{\Delta x^2}. \tag{B.9}$$

In the final step this system of ODEs can be discretized in the same way as (B.5), yielding:

$$\boldsymbol{c}_i^{t+1} = \boldsymbol{c}_i^t + \Delta t\left(\boldsymbol{f}(\boldsymbol{c}_i^t) + \underline{\underline{D}}\frac{\boldsymbol{c}_{i+1}^t - 2\boldsymbol{c}_i^t + \boldsymbol{c}_{i-1}^t}{\Delta x^2}\right). \tag{B.10}$$

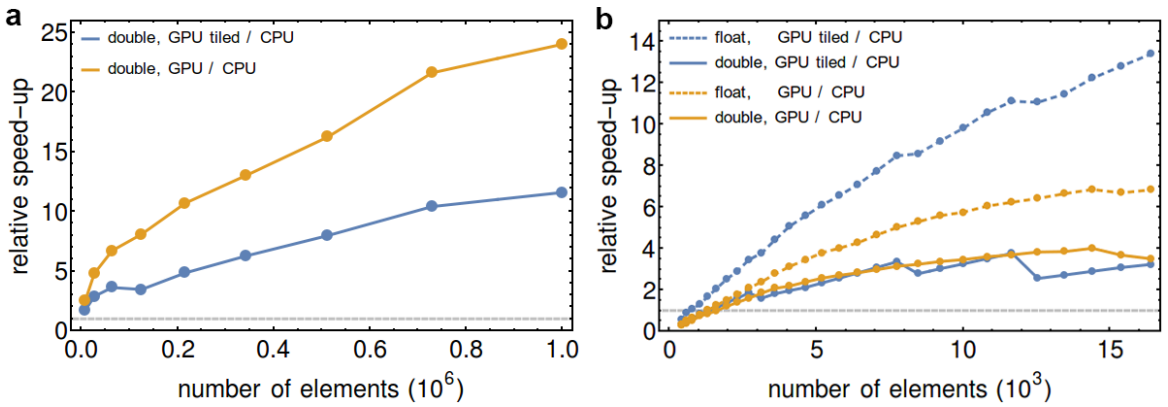

Figure B.13 | Runtime reduction due to GPU algorithm. (a) Comparison of runtimes on GPU vs CPU for the three-dimensional diffusion problem. Note that the tiling algorithm does not lead to an improvement, as the stencil size is too small. (b) Runtime comparison for nonlocally coupled systems. Here, the FHN model is used to portray the speedup for single and double precision. For the tiling algorithm to be effective in the case of double precision numbers, the hardware settings of the GPU, such as block size of concurrent threads must be tuned finely. For small problems the CPU version outperforms the GPU version, since it avoids the overhead of transferring data to the GPU. Used hardware in the test: (CPU) Intel i5-2500 4 cores @ 3.30 GHz, 8 GB RAM; (GPU) Nvidia GTX 970, CUDA 8.0, block size = 24^2 threads, 4 GB RAM

More accurate higher order methods as well as multi-step methods of the Runge-Kutta type, or predictor-corrector algorithms like Adams-Bashforth[158], take a longer computation time[a], but do not lead to qualitative differences with the Euler scheme once the time step Δt is small enough. This is due to the dissipative character of the local dynamics, which always attracts the trajectory back to the limit cycle or fixed points. Note that time-adaptive methods[158] can lead to a speed-up for a single oscillator. However, for a grid of coupled units, a speed-up is only achieved when all oscillators move in unison. In other cases, there is one oscillator, which will move in fast region of phase space and limit the time step to its smallest possible value. This results effectively in a non-adaptive method.

Even with the simple and fast Euler integrator, long simulations or parameter searches are prohibitively long. However, the numerical problem is very amenable to parallelization. The local dynamics and the coupling of each oscillator can be solved consecutively in such a way, that the calculations for each oscillator occur mostly independently. For a large number of oscillators, the large number of processors on a GPU[428] is perfect. CPU parallelization of 4 cores is already advantageous but ultimately can not compete with over a 1000 parallel cores of a GPU. For demanding computations presented in this thesis an Nvidia GTX 970 with 4 GB RAM was used. In the case of three-dimensional scroll rings a speed-up of factor 25 was

[a] One exception is the exponential time-differencing algorithm ETDRK4[427], which is also very fast for PDEs in three spatial dimensions. However, it is less effective for nonlocally coupled systems.

achieved and two-dimensional nonlocally coupled systems ran 2-4 times faster on the GPU in comparison to the CPU (Fig. B.13).

The code for computing spiral wave chimeras is available on public Git repository:
https://github.com/bzjan/Spiral_Wave_Chimera_Solver.git

B.2.1 CUDA Solver

For nonlocal coupling a speed up can be achieved by exploiting the shared memory of the GPU for faster access speeds. Whereas for the diffusion problem only a few nearest neighbors are used for the computation, in the case of nonlocal coupling, a large number of neighbors will be required. Thus many values will be reused multiple times. This fact can be exploited by preloading all values into the shared memory section of the GPU, which is known as tiling algorithm[429].

Algorithm B.1 | CUDA pseudocode for solving a reaction-diffusion equation. CUDA-specific syntax is highlighted in green. An introduction to the CUDA programming language can be found in the literature[428–430]. Here only a part of loading data from the host to the device memory (lines 1-5) is shown as well as the parallelized evaluation of local dynamics (lines 8-18) and coupling (lines 21-42) together with the function call (lines 45-54).

```
1  // transfer array to GPU
2  array_size = nx*ny*sizeof(double2);
3  cudaMalloc(&(d->c),array_size);
4  cudaMalloc(&(d->cnew),array_size);
5  cudaMemcpy(d->c,h.c,array_size,cudaMemcpyHostToDevice);
6
7
8  // local dynamics (FHN model)
9  __global__ void reaction(double2* c, double2* cnew, int len, double dt){
10 double ooeps=1.0/0.05;
11 double a=0.9;
12
13 int i = threadIdx.x + blockDim.x*blockIdx.x;
14 if(i<len){
15   cnew[i].x=c[i].x + dt*( ooeps*(c[i].x-1.0/3.0*c[i].x*c[i].x*c[i].x-c[i].y) );  // u
16   cnew[i].y=c[i].y + dt*( c[i].x + a );                                          // v
17 }
18 }
19
20
21 // spatial coupling
22 __global__ void diffusion(double2* c, double2* cnew, int nx, int ny, const double2 diffs){
23
24 int x = threadIdx.x + blockDim.x*blockIdx.x;
25 int y = threadIdx.y + blockDim.y*blockIdx.y;
26 if(x<nx && y<ny){
27   int idx = x + y*nx;
28
29   int left=idx-1;
30   int right=idx+1;
31   int top = idx + nx;
32   int bottom = idx - nx;
33
34   // Neumann BC
35   if(x==0) left++;
36   if(x==nx-1) right--;
37   if(y == ny-1) top -= nx;
38   if(y == 0) bottom += nx;
39
40   cnew[idx] += diffs*( c[left] + c[right] + c[top] + c[bottom] - 4.0*c[idx] );
41 }
42 }
43
44
45 // solve reaction diffusion equation
46 int warpsize=32;
47 dim3 nBlocks((ncomponents*n-1)/warpsize+1);
48 dim3 nThreads(warpsize);
49
50 for(int t=0; t<nsteps; t++){
51   reaction<<<nBlocks,nThreads>>>(d->c,d->cnew,nx*ny,dt);
52   coupling<<<nBlocks,nThreads>>>(d->c,d->cnew,nx,ny,diffcoeffs);
53   swapGPU(d->c,d->cnew);
54 }
```

Algorithm B.2 | CUDA pseudocode for long-range coupling via tiled[429] convolution. The algorithm consists of three steps. First, all threads in the block preload data that will later be needed for the coupling into shared memory for faster access (lines 15-22). The two-dimensional thread indices in the block are aligned with the positions in the input tile. However, the output tile is smaller than the input tile, since edge positions are filled with tile boundary values. Thus the convolution operation (lines 25-36) only uses a subset of the threads available. In the last part, the result is scaled appropriately and added on the output array (lines 39-41).

```
1  template <int maskRadius>
2  __global__ void nonlocal_delay_homo_tiled_zbke2k_2d(double2* input, double2* output, \
3    double2* input_delay, int width, int height, int o_tile_width,                      \
4    const double* __restrict__ M, const double2 coupleCoeff){
5
6  extern __shared__ double input_shared[];
7
8  int tx = threadIdx.x;
9  int ty = threadIdx.y;
10 int col_o = blockIdx.x*o_tile_width+tx;
11 int row_o = blockIdx.y*o_tile_width+ty;
12 int col_i = col_o-maskRadius;
13 int row_i = row_o-maskRadius;
14
15 int idx = col_i+row_i*width;
16 double output_temp{};
17 if((row_i>=0) && (row_i<height) && (col_i>=0) && (col_i<width)){
18   input_shared[tx+ty*blockDim.x] = input_delay[idx].y;
19 }else{
20   input_shared[tx+ty*blockDim.x] = 0.0;
21 }
22 __syncthreads();
23
24
25 if(ty<o_tile_width && tx < o_tile_width){
26   double ksum{};
27   int maskWidth=2*maskRadius+1;
28   double input0=input[row_o*width+col_o].y;
29   for(int i=0; i<maskWidth; i++){
30   for(int j=0; j<maskWidth; j++){
31     output_temp += M[j*maskWidth+i] * !!input_shared[i+tx+blockDim.x*(j+ty)] *      \
32        (input_shared[i+tx+blockDim.x*(j+ty)] - input0);
33   }}
34 }
35 __syncthreads();
36 }
37
38 if(row_o<height && col_o<width && tx<o_tile_width && ty<o_tile_width){
39   output[row_o*width+col_o] += couplecoeff*max(output_temp,-5.25e-4);
40 }
41 }
42
43
44 int maskWidth=2*maskRadius+1;
45 int o_TileWidth=blockWidth-maskWidth+1;
46 dim3 nBlocks((nx-1)/o_TileWidth+1,(ny-1)/o_TileWidth+1);
47 dim3 nThreads(blockWidth,blockWidth);
48 int mem_size=blockWidth*blockWidth*sizeof(double);
49
50 nonlocal_delay_tiled_2d<maskRadius><<<nBlocks,nThreads,mem_size>>>(d->c,            \
51   d->cnew,d->cdelay,nx,ny,o_TileWidth,d->mask,d->coupling_coeffs2);
52 }
```

Appendix C

Chemistry

C.1 Belousov-Zhabotinsky reaction

The Belousov-Zhabotinsky (BZ) reaction is the protoypical chemical oscillator[431–434]: Over the course of the reaction it exhibits periodic changes in the concentrations of intermittently produced and consumed chemical species.

C.1.1 History & Applications

Discovered serendipitously in 1951[43], it has been employed as an experimental proving ground for a variety of counter-intuitive mathematically predicted phenomena, such as deterministic chaos[435,436], chaos control[437], mixed-mode oscillations[438], collective synchronization[397], spiral wave and scroll wave dynamics and control[89,125,439,440], stochastic resonance[441,442], coherence resonance[443,444], Turing mechanism[312,445,446] and chimera states[244,245].

In addition a number of applications based on the BZ reaction were developed, i.e. chemical diodes[447], parallelized chemical computation[448–451], memory devices[452,453], image segmentation[454], quantitative chemical sensors[455], neuromorphic spike-timing dependent plasticity[25], autonomously moving agents[27,117,456], message encryption[457], biomimetic self-oscillating hydrogels, whose volume changes are entrained to the chemical oscillations[23]. They open the door for pistons in microfluidic devices, active metamaterials, peristaltic mass transport and models of organs, such as intestine, uterus and the heart, as well as actuators in soft robotics.

C.1.2 Apparent violation of the second law of thermodynamics

The reaction was initially dismissed[43,431] as impossible, since it apparently violated the second law of thermodynamics: $\Delta S \geq 0$; or equivalently from a chemical standpoint: $\Delta G \leq 0$[458]. Acceptance was not until after the work by Field, Körös and Noyes, who – in elucidating the underlying chemical mechanism – indeed showed that the oscillations did not violate the second law of thermodynamics[459–463]. The resolution of the paradox is that the oscillations occur not through the thermodynamic equilibrium but far from it. Thus the reaction enthalpy G decreases monotonically while periodically switching between a fast and a slow rate. Without external replenishment of reagents, the oscillations will eventually cease and the system will move towards thermodynamic equilibrium[33,431].

C.1.3 Reaction mechanism

The Belousov-Zhabotinsky reaction is the oxidation of an organic substrate (usually malonic acid, MA) in an acidic medium in the presence of a redox-catalyst (M_{red} / M_{ox})[433,460]. In the absence of a catalyst the net reaction,

$$3\,\mathrm{MA} + 2\,\mathrm{BrO_3^-} + 2\,\mathrm{H^+} \longrightarrow 2\,\mathrm{BrMA} + 3\,\mathrm{CO_2} + 4\,\mathrm{H_2O}, \tag{BZ}$$

is very slow even though its free enthalpy change is very large[433]. Introducing a catalyst into the system allows for a faster pathway and leads to the aforementioned concentration oscillations. The most complete reaction scheme to date involves 37 species in 48 elementary reactions[381]. However, the main mechanism[433,460] behind the oscillations can be reduced to a small subset and is depicted in figure C.1. The oscillation cycle can be divided into three distinct phases: A, B and C. In each phase a different set of chemical reactions takes the lead over the others. The protagonists are bromous acid ($HBrO_2$), bromide (Br^-) and the oxidized form of the metal catalyst M_{ox}. Starting with process B, we find that bromous acid reproduces autocatalytically

$$\mathrm{HBrO_2} + \mathrm{BrO_3^-} + 3\,\mathrm{H^+} + 2\,\mathrm{M_{ox}} \longrightarrow 2\,\mathrm{M_{red}} + 2\,\mathrm{HBrO_2} + \mathrm{H_2O}, \tag{AUTO}$$

where the presence of $HBrO_2$ promotes its own further increase. The resulting exponential growth is countered with decay via disproportionation:

$$2\,\mathrm{HBrO_2} \longrightarrow \mathrm{HOBr} + \mathrm{BrO_3^-} + \mathrm{H^+}. \tag{R7}$$

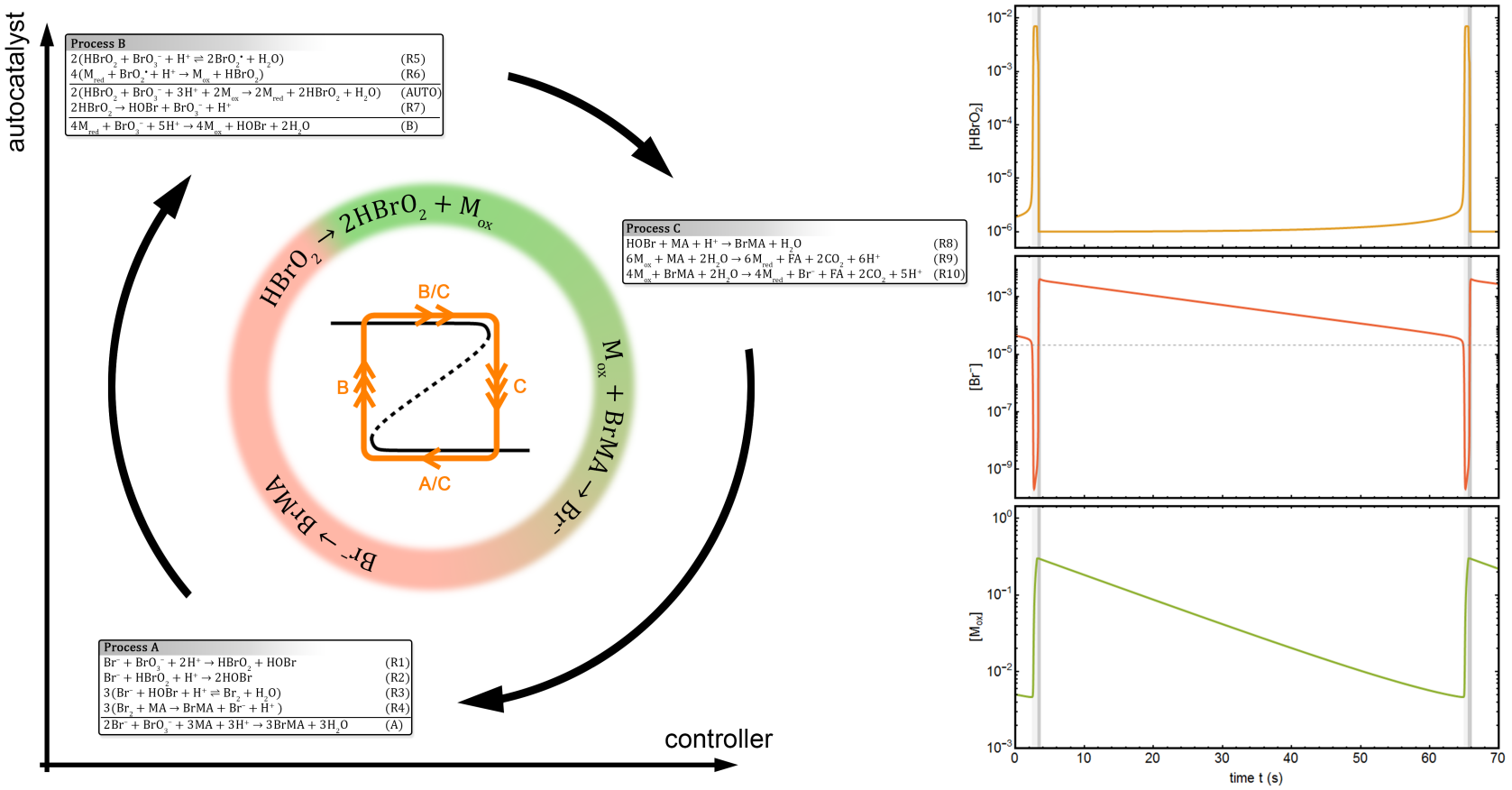

Figure C.1 | Mechanism of the BZ reaction. On the left the outer circle depicts the most important reactions grouped into 3 processes: A, B and C. The inner circle shows the production and consumption of the most relevant chemical species during different stages of the oscillation and the accompanying color changes of the reaction solution. At the center of the oscillations lies a sketch of the mechanism: An autocatalytic species shows bistability for certain values of a controller species. The controller species grows for large values of the autocatalyst and decays for small values. Thus driving the oscillations. The acronyms in the reactions stand for: malonic acid (MA=$CH_3(COOH)_2$), bromomalonic acid (BrMA=$BrCH(COOH)_2$) and formic acid (FA=HCOOH). On the right, time traces of the relevant species are obtained by simulations with the FKN model (C.1). During the majority of the oscillation cycle, process A dominates. Process B and C take over for a short amount of time (see gray shaded regions) after the bromide concentration falls below a critical value. While process A dominates, process C is at work as well, as can be inferred from the decaying oxidized catalyst concentration.

Once both processes balance out, $HBrO_2$ will reach a quasi-steady concentration. However, the reaction cycle does not end here, since the reduced form of the catalyst M_{red} in reaction (R6) gains an electron and thus attains its oxidized form M_{ox}. Even though M_{ox} does not directly compromise the autocatalytic production, it brings out the seeds for its future decline by providing the fuel for process C.
In its oxidized form, the catalyst M_{ox} is an electron donor, also known as an oxidizing agent. This allows M_{ox} to oxidize not only MA, the original organic substrate, but bromomalonic acid (BrMA) as well:

$$6\,M_{ox} + MA + 2\,H_2O \longrightarrow 6\,M_{red} + FA + 2\,CO_2 + 6\,H^+, \tag{R9}$$

$$4\,M_{ox} + BrMA + 2\,H_2O \longrightarrow 4\,M_{red} + Br^- + FA + 2\,CO_2 + 5\,H^+. \tag{R10}$$

Note that process C is not understood in its entirety[433], since MA and BrMA give rise to a large number of different radicals and organic acids. That is the reason why instead of giving a complete set of reactions, figure C.1 only shows the relevant reactions that are agreed upon in the literature[433,436,464]. The most important product of these reactions is bromide Br^-, the inhibitor.
Its role becomes clear during process A. In a series of reactions an excess Br^- concentration leads to the decomposition of different oxybromine species whose remainders ultimately react with MA to form new BrMA. Among these oxybromine species is the autocatalyst, $HBrO_2$, as well. Its concentration is kept in a low steady state since it is produced, but consumed as well. As long as Br^- is above a low critical concentration $[Br^-]_{cr}$, $HBrO_2$ autocatalysis will be suppressed. Only once enough of Br^- is consumed during the production of BrMA, Process B can start anew and initiate another cycle. Note that the reactions have been renumbered in comparison to the original FKN paper[460] for clarity.
In summary, process B describes the autocatalytic step or the positive feedback loop. Process C switches from high $HBrO_2$ to low $HBrO_2$ by seeding process A with Br^- which poisons the autocatalytic step. This completes the delayed negative feedback.
From the standpoint of nonlinear dynamics, the reason for the oscillations is very simple. The core principle of this mechanism can be identified as a switch between two coexisting, bistable branches of high and low $HBrO_2$ concentration. At high concentrations of the catalyst or the controlling species, the transition may only occur from high to low $HBrO_2$, while at small concentrations the transition occurs from low to high concentrations. This mechanism has been identified to lie at the heart of chemical oscillations[465] and was successfully employed to design new chemical oscillators[466,467].

C.1.4 Redox catalysts

As is evident from the oscillation mechanism, a suitable catalyst is required to receive an electron from one species (oxidation, R6) and later donate it to another (reduction, R9 and R10). Thereby forming Br^- from BrO_3^-. This kind of catalyst is called a redox-catalyst[468]. In addition the catalysts for the BZ reaction exhibit different colors depending on their oxidation state. This allows for simple visual recording of the concentration oscillations. Originally Belousov utilized the transition metal cerium, whose ions are colorless in the reduced state Ce(III) and appear yellow in the oxidized state Ce(IV)[43]. Another example is the transition metal complex ferroin, the cation of 1,10-(ortho)-phenanthroline ferrous sulfate or Fe(phen), which exhibits a strong contrast between red $(Fe(phen)^{3+})$ and blue $(Fe(phen)^{4+})$ colors during different phases of the oscillation cycle[43]. While the different oxidation states of manganese Mn(II) and Mn(III) also exhibit color changes between transparent and red, this catalyst is also employed in setups, where the oscillation state is tracked using magnetic resonance imaging (MRI)[469]. The oscillation cycle can also be tracked potentiometrically with concentration-specific electrodes[460], thermometrically[470], calorimetrically[471] or via chemiluminescence[472,473].

Among the BZ catalysts, the ruthenium-tris(2,2'-bipyridine) complex $(Ru(bipy)_3^{2+})$ or Rubipy stands out[434]. Besides allowing for spectrometrical measurements, this catalyst also introduces the possibility for control, since it is photo-sensitive[416]. After absorption of photons at $\lambda = 452\,\mathrm{nm}$, it turns from a weak reducing agent into a very strong one[452,474],

$$Ru(bipy)_3^{2+} + \hbar\omega \longrightarrow {}^*Ru(bipy)_3^{2+}. \tag{R-L1}$$

The transition to the long-lived excited state[474,475] allows the redox-catalyst to lend its electrons even more easily to other reagents and thus catalyze more reactions than in the ground state. It was shown that the previously unaccessible reaction,

$${}^*Ru(bipy)_3^{2+} + Ru(bipy)_3^{2+} + BrO_3^- + {}_3H^+ \longrightarrow HBrO_2 + 2\,Ru(bipy)_3^{3+} + H_2O, \tag{R-L2}$$

is the main benefactor of the stronger reducing agent[476]. Due to light illumination, the autocatalytic species $HBrO_2$ is produced as well as oxidized catalyst $Ru(bipy)_3^{3+}$ which leads to the delayed rise of the inhibitor Br^-. In summary light illumination has both, a direct excitatory and an indirect inhibitory effect on the oscillation cycle.

A later modification of the catalyst adds a dimethylene-group to each bipyridine ligand, which increases the spectrometric contrast and steric fixation in hydrogel polymer matrices[126] as well as in cation-exchange resin particles. Furthermore $Ru(bipy)_3^{2+}$ and $Ru(dmbipy)_3^{2+}$ emit

strong fluorescence intensity[477] at $\lambda > 600\,\text{nm}$ (Fig. 4.2c) that allows for robust tracking of the oscillation cycle (see chapter 4). Note that interfering chemiluminescence is suppressed at large concentration of $[H_2SO_4]$[478].
Due to its desirable photoredox properties, the Rubipy catalyst and its derivatives[474] are popular in fields beyond the Belousov-Zhabotinsky reaction, such as luminescent sensors[479,480], environmentally friendly catalysis[481,482], fuel cells[483], photovoltaics[484], light emitting diodes[485] as well as diagnostic[486] and therapeutic applications[487].

C.1.5 Parameter drift

Over the course of the BZ reaction, the amplitude and the period of oscillations change. The phenomenon is known as parameter drift or aging[346,488]. This introduces a difficulty absent from idealized numerical simulations. During the chemical reaction, reagents are converted into products. The rates of change of the concentrations are functions of the concentrations themselves, so they will change over time. However, even with an open system[126] that continuously feeds new reagents (BrO_3^-, MA) into the system and allows for escape of gaseous products, most notably CO_2, an aging effect can still be observed. This can be due to the catalyst slowly leaking from the system, as in version II (appendix B.1.2) and III (appendix B.1.3). After increasing the size of the ligands with three dimethylene groups, the catalyst molecule is fixated in the hydrogel or bead polymer matrix, which resolves this particular issue[126]. However, even with these precautions, there is still a non-vanishing parameter drift. This might be due to slow oxidative degradation of the photocatalyst[489,490] or the escape of gaseous intermediates such as Br_2.

C.1.6 Troubleshooting

There are a number of strategies to overcome the shortcomings of the BZ reaction. Different catalysts can be mixed resulting in what is called dual catalysts[434]. This way an experiment can feature the strong optical contrast of the ferroin catalyst with the photosensitivity of Rubipy catalysts. Another application is to combine absorption spectra of different catalysts for tunable spectrometric properties.
It was shown that the rate of parameter drift can be drastically reduced by replacing the hydrogen-donating acid (H_2SO_4 or HNO_3) with a protic ionic liquid[491,492].
Gaseous CO_2 presents itself as a major problem since it leads to the growth of numerous spherical inclusions that act as defect sites in solidified BZ gel systems. One remedy is to use cyclohexanedione (CHD) as a replacement for MA as the organic substrate, since it does not lead to CO_2 formation[493,494].

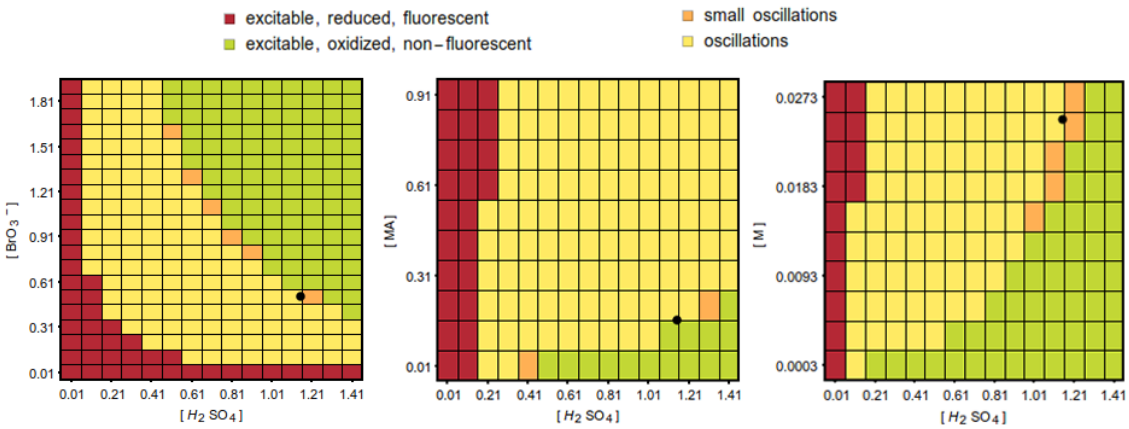

Figure C.2 | Concentration Space Overview. Figures show the dynamical state of the FKN model modified to account for light illumination in dependence of initial chemical reagent concentrations of H_2SO_4, $NaBrO_3$, MA and the metal catalyst M. States are automatically identified by checking for monotonous convergence to a fixed point and its value as well as for oscillations by evaluating the difference between the maximum and minimum concentration. The black dot is a reference point for comparison with initial concentrations of $[H_2SO_4]_0 = 1.1\,\text{M}$, $[NaBrO_3]_0 = 0.5\,\text{M}$, $[MA]_0 = 0.15\,\text{M}$ and $[M]_0 = 25\,\text{mM}$.

Mixing the BZ reagent with the correct concentrations does not lead to immediate oscillations. Usually it takes a few minutes up to an hour, before oscillations start. This time interval is known as the induction period[461], during which intermediate species are slowly built up for the ensuing oscillations. The induction period can be decreased by adding Br^- and BrMA to the initial reagent mixture[326].

To ensure reproducibility of experiments it is important to thoroughly remove any trace amounts of oxybromine species including Br_2 from reactor chambers that are to be used again. For one set of experiments, chemicals from only the same batch should be used. In addition the employed chemical reagents should be of analytical grade as they can contain impurities that perturb the reaction[495]. All BZ reagents can be obtained from chemical vendors. Variations of the standard reagents, e.g. the $Ru(dmbipy)_3^{2+}$ catalyst must be produced via repeated reflux and recrystallization[126,496,497] or microwave synthesis[498].

Finding the right concentrations for an excitable or oscillatory system can be accelerated with a quantitative numerical model of the BZ reaction (see FKN model (C.1)). Employing the rate constants compiled in table C.2, the behavior of the BZ system can be simulated for a range of initial reagent concentrations.

The effect of the different reagents on the dynamics of the BZ reaction can be seen in figure C.2. Increasing the sulfuric acid (H_2SO_4) concentration, and thereby the proton (H^+) concentration, leads to a transition from a stable fixed point through a Hopf bifurcation with consecutive Canard explosion[499,500] to a large stable limit cycle. Following another Hopf

bifurcation the fixed point becomes stable again, but this time it is located at large values of the oxidized catalyst. Perturbations to the fixed point at low oxidized catalyst concentration lead to a large phase space excursion, while perturbations to the fixed point at high oxidized catalyst concentrations do not. So only the fixed point at low oxidized catalyst corresponds to excitability. The result of increasing bromate concentration [BrO_3^-] is the same as increasing [H_2SO_4], while increasing [MA] or the total catalyst concentration has the opposite effect. Note that [H^+] is not linearly dependent on [H_2SO_4], but is based on the Hammett acidity function, whose values are given in the literature[501]. These diagrams can be used to tune concentrations of an experiment in order to find the desired dynamical behavior.

C.1.7 Chemical recipes

The concentrations for the different experiments described in this thesis are listed in table C.1 for reproducibility.

Table C.1 | Employed initial concentrations for the experiments. Note that the units of the catalyst depend on the type of the experiment. In experiments with continuous hydrogels, the concentration is given in mM, whereas with discrete particles, the unit is amount of catalyst in moles per mass of exchange resin in grams.

concentration experimental setup	scroll ring[162] version I	scroll ring[152] version II	network[217] version III	network[334] version V
$[H_2SO_4]_0$ (M)	0.16	0.39	0.78	0.77
$[NaBrO_3]_0$ (M)	0.04	0.2	0.48	0.51
$[NaBr]_0$ (M)	0	0.09	0.02	0.08
$[MA]_0$ (M)	0.04	0.17	0.08	0.16
$[M_{red} + M_{ox}]_0$	0.5 mM	4.5 mM	8.3×10^{-6} mol/g	2.5×10^{-5} mol/g
catalyst dynamics	$Fe(phen)_3^{2+}$ oscillatory	$Ru(dmbipy)_3^{2+}$ excitable	$Ru(bipy)_3^{2+}$ oscillatory	$Ru(dmbipy)_3^{2+}$ oscillatory

C.2 Overview of numerical models

The reaction mechanism by Field, Körös and Noyes[460] as detailed above contains 37 chemical species and 48 reaction steps. It can be translated into a system of first order differential equations, which are amenable to numerical simulation. The conversion involves standard techniques from reaction kinetics[458]: mass action law, adiabatic elimination, also known as quasi steady state approximation, and bath approximation, which assumes reactant species to be so abundantly available, that their concentration is constant. The resulting FKN model consists of seven coupled ordinary differential equations[460,464], which capture the dynamics of the BZ reaction semi-quantitatively:

$$\begin{aligned}
\dot{U} &= -k_2UW + k_1W - 2k_7U^2 - k_5U + k_{-5}R^2 + k_6SR,\\
\dot{V} &= -k_9V - k_{10}V + k_6SR,\\
\dot{W} &= -k_2UW - k_1W - k_3WP + k_{-3}O + k_4O + k_{10}V,\\
\dot{O} &= k_3WP - k_{-3}O - k_4O,\\
\dot{P} &= 2k_2UW + k_1W + k_7U^2 - k_3WP + k_{-3}O - k_8P,\\
\dot{R} &= 2k_5U - 2k_{-5}R^2 - k_6SR,\\
\dot{S} &= k_9V + k_9V - k_6SR.
\end{aligned} \tag{C.1}$$

The variables U, V, W, O, P, R, S stand for the concentrations of bromous acid ($HBrO_2$), oxidized catalyst (M_{ox}), bromide (Br^-), hypobromous acid (HOBr), bromine (Br_2), hypobromous acid radical ($BrO_2^\bullet$) and reduced catalyst (M_{red}), respectively. All k_i are reaction rate constants and their values are listed in table C.2. Note that the rate constants and variables have been renamed for consistency throughout this chapter.

Table C.2 | FKN model. Reaction rate constants of the FKN mechanism and their values[421]. Due to discrepancies in the literature[126,326,421,433] the following rate constants are selected, since they lead to agreement with experimental observations in the photosensitive BZ reaction[464]. The concentrations of bath reagents are absorbed into the rate constants.

rate constant	value	rate constant	value
k_1	$2\,\mathrm{M}^{-3}\mathrm{s}^{-1}[\mathrm{H^+}]_0^2[\mathrm{BrO_3^-}]_0$	k_{-5}	$2\times10^8\,\mathrm{M}^{-1}\mathrm{s}^{-1}$
k_2	$2\times10^6\,\mathrm{M}^{-2}\mathrm{s}^{-1}[\mathrm{H^+}]_0$	k_6	$5\times10^6\,\mathrm{M}^{-1}\mathrm{s}^{-1}$
k_3	$5\times10^9\,\mathrm{M}^{-2}\mathrm{s}^{-1}[\mathrm{H^+}]_0$	k_7	$3\times10^3\,\mathrm{M}^{-1}\mathrm{s}^{-1}$
k_{-3}	$10\,\mathrm{s}^{-1}$	k_8	$9.3\,\mathrm{M}^{-1}\mathrm{s}^{-1}[\mathrm{MA}]_0$
k_4	$29\,\mathrm{M}^{-1}\mathrm{s}^{-1}[\mathrm{MA}]_0$	k_9	$0.05\,\mathrm{M}^{-1}\mathrm{s}^{-1}[\mathrm{MA}]_0$
k_5	$42\,\mathrm{M}^{-2}\mathrm{s}^{-1}[\mathrm{H^+}]_0[\mathrm{BrO_3^-}]_0$	k_{10}	$1\,\mathrm{M}^{-1}\mathrm{s}^{-1}[\mathrm{BrMA}]_0$

An analysis of the involved time scales[502] reveals which chemical species may be adiabatically eliminated for further simplification. After taking into account that the total catalyst concentration is conserved and non-dimensionalization, the resulting qualitative model reads:

$$\begin{aligned} \dot{u} &= \frac{1}{\varepsilon_1}\left(-w(u-\mu)-u^2+u\right), \\ \dot{v} &= u-v, \\ \dot{w} &= \frac{1}{\varepsilon_2}(fv+\phi-w(u+\mu)). \end{aligned} \tag{C.2}$$

The remaining variables u, v, w stand for the dimensionless concentrations of $HBrO_2$, M_{ox} and Br^-. Conversion formulas for the parameters[434] are found in table C.3. Since the organic reaction pathways are not known in detail, the production of Br^- can be estimated with a stoichiometric factor f. This factor relates the number of produced moles of Br^- from a mole of consumed M_{ox}[433,463]. Note that this model is called the Modified Complete Oregonator[415], since it incorporates the effect of light exposure into the original Oregonator model[463]. Here, light illumination was thought to exclusively produce the inhibitor Br^- via

$$^*Ru(bipy)_3^{2+} + BrMA \longrightarrow Ru(bipy)_3^{3+} + Br^-. \tag{R-L3}$$

This reaction is accounted for as an additive bromide source term ϕ. However, the model neglects the excitatory impact of light[476], as described in reaction R-L2.
Adiabatically eliminating the inhibitor species w, leads to the two-component Oregonator model[463,502]:

$$\begin{aligned} \dot{u} &= \frac{1}{\varepsilon_1}\left(u(1-u)-\frac{u-\mu}{u+\mu}(fv+\phi)\right), \\ \dot{v} &= u-v. \end{aligned} \tag{C.3}$$

Table C.3 | Oregonator models. Conversion formulas[434] for parameters in (C.2) and (C.3). The same rate constants[464] as in table C.2 are employed. Majuscule and minuscule variables stand for concentrations with and without dimensions, respectively. Bath species are abbreviated as $A = [BrO_3^-]_0$ and $B = [BrMA]_0 = 0.1[MA]_0$[464] and $H = [H^+]_0$ (via Hammett acidity function[501]).

$u = \frac{2k_7}{k_5 A}U$	$v = \frac{k_7 k_{10} B}{(k_5 A)^2}V$	$w = \frac{k_2}{k_5 A}W$ $\quad \tau = k_{10}Bt$
$\varepsilon_1 = \frac{k_{10}B}{k_5 A}$	$\varepsilon_2 = \frac{2k_7 k_{10} B}{k_2 k_5 A}$	$\mu = \frac{2k_1 k_7}{k_2 k_5}$
$k_1 = 2\,\mathrm{M}^{-3}\mathrm{s}^{-1}H^2A$	$k_2 = 2\times 10^6\,\mathrm{M}^{-2}\mathrm{s}^{-1}H$	$k_5 = 42\,\mathrm{M}^{-2}\mathrm{s}^{-1}HA$
$k_7 = 3\times 10^3\,\mathrm{M}^{-1}\mathrm{s}^{-1}$	$k_{10} = 1\,\mathrm{M}^{-1}\mathrm{s}^{-1}B$	

Table C.4 | Rovinsky model. Rate constants and conversion formulas[154] for parameters in (C.4). Majuscule and minuscule variables stand for concentrations with and without dimensions, respectively. Bath species are abbreviated as $A = [BrO_3^-]_0$ and $B = [BrMA]_0 = 0.1[MA]_0$[464], $C = [M_{red}]_0 + [M_{ox}]_0$ and $H = [H^+]_0$ (via Hammett acidity function[501]).

$u = \frac{2k_4}{k_1 A} U$	$v = \frac{1}{C} V$	$\tau = \frac{(k_1 A)^2 H}{k_4 C} t$
$\varepsilon = \frac{k_1 A}{k_4 C}$	$\alpha = \frac{k_4 k_8 B}{(k_1 A H)^2}$	$\beta = \frac{2k_4 k_{13B}}{(k_1 A)^2 H}$
$\mu = \frac{2k_4 k_6}{k_1 k_5}$		
$k_1 = 10\,\mathrm{M}^{-2}\mathrm{s}^{-1}$	$k_4 = 1.7 \times 10^3\,\mathrm{M}^{-2}\mathrm{s}^{-1}$	$k_5 = 10^6\,\mathrm{M}^{-2}\mathrm{s}^{-1}$
$k_7 = 1.5\mathrm{M}^{-2}\mathrm{s}^{-1}$	$k_8 = 2 \times 10^{-6}\,\mathrm{Ms}^{-1}$	$k_{13} = 10^{-7}\,\mathrm{s}^{-1}$

Later Rovinsky and coworkers[154,503,504] devised another model (C.4) based on a slightly augmented FKN scheme that leads to semi-quantitative agreement between simulations and experiments in case of the ferroin-catalyzed BZ-reaction:

$$\begin{aligned} \dot{u} &= \frac{1}{\varepsilon}\left(u(1-u) - \frac{u-\mu}{u+\mu}\left(\beta + 2q\frac{\alpha v}{1-v}\right)\right), \\ \dot{v} &= \left(u - \frac{\alpha v}{1-v}\right). \end{aligned} \tag{C.4}$$

The variables u and v stand again for the concentrations of $HBrO_2$ and M_{ox}, in this case $Fe(phen)^{4+}$. Conversion formulas for the parameters[154] are found in table C.4. Note that the photosensitivity of the ferroin catalyst[416,505] is neglected. Instead the new parameter β accounts for the slow hydrolysis of BrMA into Br^-[504]. The other important change is the replacement of the oxidized catalyst v with the ratio $\alpha v/1-v$. This ratio results from adiabatic eliminations of organic species while taking the sum of reduced and oxized catalyst concentration as constant.

The ZBKE model by Zhabotinsky and Epstein[326] and its later refinements by Taylor and others[244,434] build on the Rovinsky model (C.4) but in addition take into account explicitly the concentration of the intermediate basic radical of bromous acid ($HBrO_2^+$). This species plays a role in process B during the radicalic oxidation of the catalyst:

$$\begin{aligned} BrO_2^\bullet + H^+ &\rightleftharpoons HBrO_2^+, \\ M_{red} + HBrO_2^+ &\rightleftharpoons M_{ox} + HBrO_2 \cdot \end{aligned}$$

Table C.5 | ZBKE model. Rate constants[262] and conversion formulas[326] for parameters in (C.5). Majuscule and minuscule variables stand for concentrations with and without dimensions, respectively. Bath species are abbreviated as $A = [\mathrm{BrO_3^-}]_0$ and $B = [\mathrm{BrMA}]_0 = 0.1[\mathrm{MA}]_0$[464], $C = [\mathrm{M_{red}}]_0 + [\mathrm{M_{ox}}]_0$ and $H = [\mathrm{H^+}]_0$ (via Hammett acidity function[501]).

$u = \frac{2k_4}{k_5 HA} U$	$v = \frac{1}{C} V$	$\tau = \frac{(k_5 HA)^2}{2k_4 C} t$	$\mu = \frac{2k_3 k_4}{k_2 k_5 H}$	$\gamma = \frac{k_{-5}}{k_6}$
$\varepsilon_1 = \frac{k_5 HA}{2k_4}$	$\varepsilon_2 = \frac{(k_5 HA)^2}{2k_4 k_6 C^2}$	$\varepsilon_3 = \frac{k_8}{k_{-7} HC}$	$\alpha = \frac{2k_4 k_7 k_8 B}{k_5^2 k_{-7} H^3 A^2}$	$\beta = \frac{2k_4^* k_9 B}{(k_5 HA)^2}$
$k_2 = 2.0 \times 10^6\,\mathrm{M^{-2}s^{-1}}$	$k_3 = 2\,\mathrm{M^{-2}s^{-1}}$	$k_4 = 3 \times 10^3\,\mathrm{M^{-1}s^{-1}}$		
$k_5 = 33\,\mathrm{M^{-2}s^{-1}}$	$k_{-5} = 4.2 \times 10^6\,\mathrm{M^{-1}s^{-1}}$	$k_6 = 4.0 \times 10^6\,\mathrm{M^{-1}s^{-1}}$		
$k_7 = 9.2 \times 10^{-1}\,\mathrm{M^{-1}s^{-1}}$	$k_8/k_{-7} = 2.5 \times 10^{-4}\,\mathrm{M^2}$	$k_9 = 3.3 \times 10^{-6}\,\mathrm{s^{-1}}$		

Its adiabatic elimination leads to a two-component model involving the activator u ($[\mathrm{HBrO_2}]$) and ox. catalyst v ($[\mathrm{Ru(dmbipy)_3^{3+}}]$):

$$\begin{aligned} \sigma_{ss} &= \frac{1}{4\gamma\varepsilon_2}\left(\sqrt{16\gamma u\varepsilon_2 + v^2 - 2v + 1} + v - 1\right), \\ \dot{u} &= \frac{1}{\varepsilon_1}\left(\phi + u(-1-u) - \frac{u-\mu}{u+\mu}\left(\beta + q\frac{\alpha v}{\varepsilon_3 + 1 - v}\right) + \gamma\varepsilon_2\sigma_{ss}^2 + (1-v)\sigma_{ss}\right), \\ \dot{v} &= 2\phi + (1-v)\sigma_{ss} - \frac{\alpha v}{\varepsilon_3 + 1 - v}. \end{aligned} \tag{C.5}$$

Parameter formulas[326] are listed in table C.5. Note that the oxidation of the catalyst $\mathrm{Ru(bipy)_3^{2+}}$ by radicals (reaction R6) is irreversible[434] in contrast to ferroin. This means the parameter δ in the original model[326] vanishes. For modelling cation-exchange particles loaded with BZ catalyst (chapters 3 and 4), the ZBKE model turned out to be superior over the Oregonator (C.3), because it allowed for a larger spread of periods. In the simulations the heterogeneity in periods was modeled by the stoichiometric parameter q.

For BZ nano- and microdroplets[421], Vanag developed a number of models[506,507], which are based on the original FKN mechanism. The model presented here is designed to explicitly account for non-polar $\mathrm{Br_2}$ molecules that are exchanged between the droplets through an oil phase. To this end, the disproportionation of $\mathrm{Br_2}$ is taken into account as well,

$$\mathrm{Br_2 + H_2O \longrightarrow Br^- + HOBr + H^+}\cdot$$

In addition the influence of the photosensitive catalyst $\mathrm{Ru(bipy)_3^{3+}}$ is incorporated. The light interaction is assumed[507] to have an exclusive inhibitory impact via reactions (R-L1)

and (R-L3). Also the decay of the excited state via fluorescent photon emission[328] is taken into account:

$$^{*}\mathrm{Ru(bipy)}_3^{2+} \longrightarrow \mathrm{Ru(bipy)}_3^{2+} + \hbar\omega. \tag{R-L4}$$

Instead of invoking the bath approximation, the periodic time-evolution of [BrMA] is explicity accounted for. The number of resulting differential equations are reduced by taking the total catalyst concentration $[\mathrm{M_{red}}] + [\mathrm{M_{ox}}]=\mathrm{C}$ to be constant and adiabatic eliminations of $\mathrm{HBrO^{\bullet}}$, HOBr and $^{*}\mathrm{M_{red}}$. Furthermore terms with the smallest contribution to the rate of change are eliminated[507]. However, as in all models presented before, the adiabatic elimination of $\mathrm{HBrO^{\bullet}}$ introduces a flaw in model: The autocatalytic production of $\mathrm{HBrO_2}$ (see R6) is not limited by the concentration of $\mathrm{M_{red}}$ anymore. To resolve this issue, the rate constant k_5 is made dependent on $\mathrm{M_{red}}$[506]:

$$k_5' = k_5 \frac{C-V}{C-V+S_{\min}}.$$

Here $S_{\min}$ is the smallest concentration of reduced catalyst during the oscillation cycle. For large V, $k_5' \to k_5$ but for small V, $k_5' \to 0$, which effectively stops the autocatalysis. The full model is:

$$\begin{aligned}
\dot{U} &= -k_1UW + k_2W - 2k_3U^2 + k_4U\frac{C-V}{C-V+S_{\min}},\\
\dot{V} &= 2k_4U\frac{C-V}{C-V+S_{\min}} - k_9BV - k_{10}V + \frac{C-V}{K_L/B+1}\phi,\\
\dot{W} &= -3k_1UW - 2k_2W - k_3U^2 + k_7P + k_9BV + \frac{C-V}{K_L/B+1}\phi,\\
\dot{P} &= 2k_1UW + k_2W + k_3U^2 - k_7P,\\
\dot{B} &= k_7P - k_9BV - k_{13}B.
\end{aligned} \tag{C.6}$$

The variables U, V, W, P, B represent the species $[\mathrm{HBrO_2}]$, $[\mathrm{M_{ox}}]$, $[\mathrm{Br^-}]$, $[\mathrm{Br_2}]$ and [BrMA] as in the FKN model (C.1). Values of rate constant are compiled in table C.6.

From the perspective of nonlinear dynamics, the chemical oscillations in the BZ system require bistability and a controller species that moves the system between both stable branches[465]. The bistability can be realized with a species that has a cubic nullcline. Both properties are found in the FitzHugh-Nagumo model, which is the paradigmatic model of neural dynamics[348]:

$$\begin{aligned}
\dot{u} &= \frac{1}{\varepsilon}\left(u - \frac{1}{3}u^3 - v\right) + \phi,\\
\dot{v} &= u + a.
\end{aligned} \tag{C.7}$$

Table C.6 | Vanag model. Rate constants[507] employed in (C.6). Majuscule and minuscule variables stand for concentrations with and without dimensions, respectively. Bath species are abbreviated as $A = [BrO_3^-]_0$, $M = [MA]_0$, $C = [M_{red}]_0 + [M_{ox}]_0$ and $H = [H^+]_0$ (via Hammett acidity function[501]).

$S_{min} = \sqrt{3k_r k_{10} C}/k_{red}$		
$k_1 = 2 \times 10^6\,\mathrm{M}^{-1}\mathrm{s}^{-1} H$	$k_2 = 2\,\mathrm{s}^{-1} H^2 A$	$k_3 = 3 \times 10^3\,\mathrm{M}^{-1}\mathrm{s}^{-1}$
$k_4 = 42\,\mathrm{s}^{-1} HA$	$k_7 = 29\,\mathrm{s}^{-1} M$	$k_9 = 20\,\mathrm{M}^{-1}\mathrm{s}^{-1}$
$k_{10} = 0.05\,\mathrm{s}^{-1} M$	$k_r = 2 \times 10^8\,\mathrm{M}^{-1}\mathrm{s}^{-1}$	$k_{red} = 5 \times 10^6\,\mathrm{M}^{-1}\mathrm{s}^{-1}$
$K_L = 0.05$		

In neural systems, u corresponds to the membrane voltage and v to the fast gating variable[432]. Model (C.7) features a supercritical Hopf bifurcation at $a = 1$ with a consecutive Canard. This captures the essential characteristic dynamics observed in BZ models (Eqs. C.1 to C.6). The time scale separation in the relaxation oscillations can be tuned via ε. The parameter ϕ is introduced additively in the activator variable u to mimic the excitatory effect of light illumination in the BZ reaction (R-L2). The different nature of the models is best illustrated with a depiction of the phase space (or a projection thereof in the u-v phase plane) and their respective phase response curves (PRC) in figure C.3.

Quantitative agreement between a model and an experiment is difficult to attain, as not all values of the rate constants are available with high precision[326,433]. In addition small temperature changes will lead to different rate constants due to the Arrhenius law[458]. Furthermore the purity of the employed reactants is not perfect and may contain impurities, such as trace amounts of halogens e.g. Br^- and Cl^-, which strongly influence the sensitive dynamic behavior of the BZ reaction[495].

For the ferroin-catalyzed BZ reaction, the Rovinsky model (C.4) gave semi-quantitative agreement with the experiments on spiral waves in continuous media[162] and the FKN model (C.1) yielded good results for a photosensitive BZ system with droplets[464]. The Oregonator models, (C.3) and (C.2), are very useful to qualitatively describe an excitable BZ system. The latest attempt in elucidating the role of light illumination in the BZ[476] showed that the ZBKE model (C.5) incorporates the excitatory and inhibitory influence of light correctly.

Besides the FKN model[461], extensive chemical models are available that take into account a wide range of concurrent reactions, such as the GTF model[508], which was later simplified via principal component analysis[509]. The most recent entry is the MBM model[381] with detailed dynamics for the organic subprocess. The above listing gives insight into finding reduced models of the BZ reaction and an overview of the models used in this thesis.

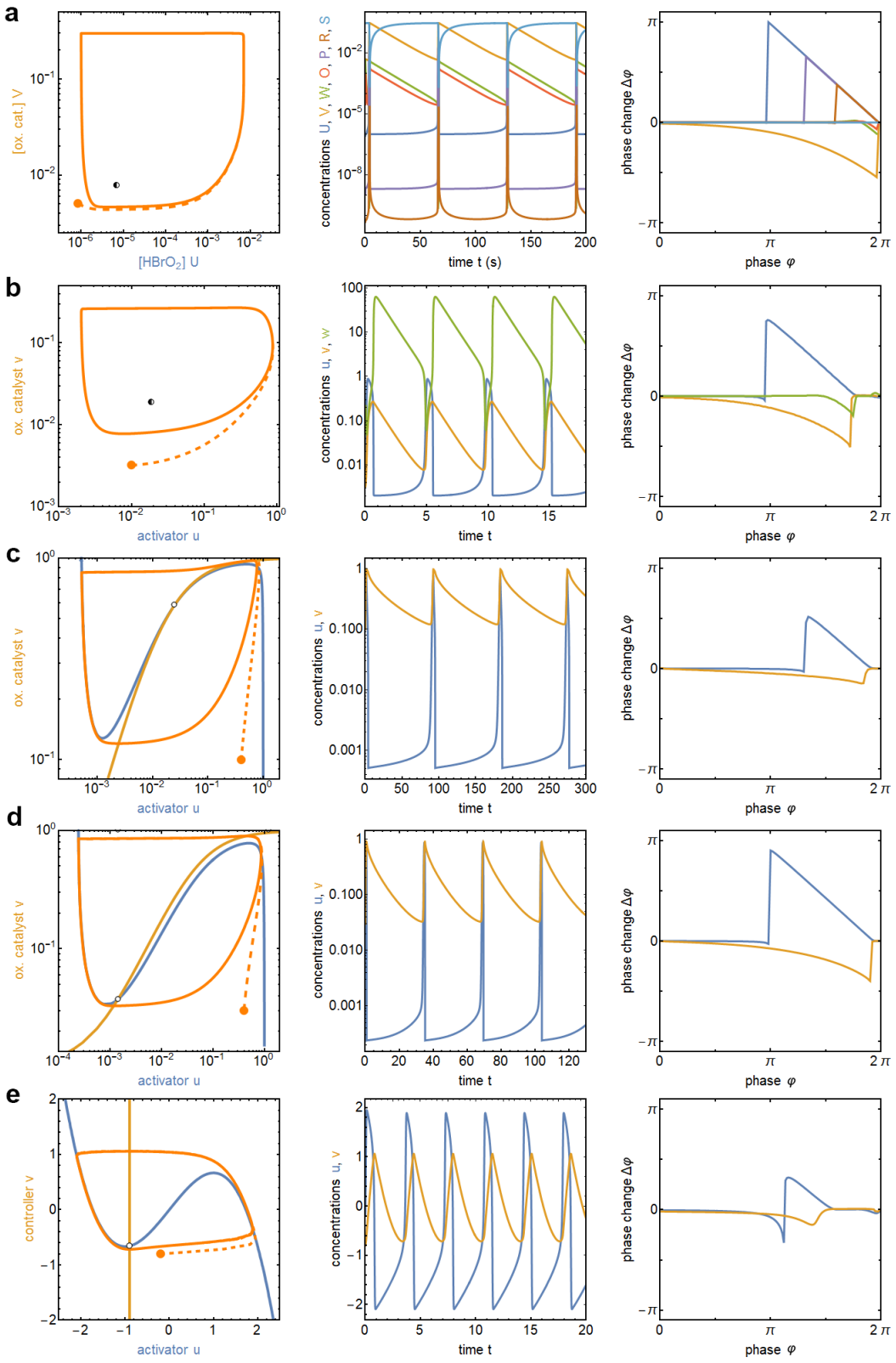

Figure C.3 | Model Overview. All models are compared via their limit cycle, time series and phase response curve. (a) FKN (C.1), (b) modified complete Oregonator (C.2), (c) Rovinsky (C.4), (d) ZBKE, (C.5) (e) FHN (C.7). The unfilled and half-filled markers in the limit cycle show the unstable nodes and saddle points, respectively. Note that all models show a phase-reset character for species that are identified as activators and a phase-delaying character with large negative contributions for inhibitory species.

References

[1] R. Clausius. Ueber verschiedene für die Anwendung bequeme Formen der Hauptgleichungen der mechanischen Wärmetheorie. *Ann. Phys.* **201**, 353 (1865)

[2] M. S. Rappé, S. A. Connon, K. L. Vergin, and S. J. Giovannoni. Cultivation of the ubiquitous SAR11 marine bacterioplankton clade. *Nature* **418**, 630 (2002)

[3] B. Würsig, W. Perrin, B. Würsig, and J. Thewissen, eds. Encyclopedia of Marine Mammals. Academic Press (2008)

[4] R. Danovaro, A. Dell'Anno, A. Pusceddu, C. Gambi, I. Heiner, and R. Møbjerg Kristensen. The first metazoa living in permanently anoxic conditions. *BMC Biol.* **8**, 30 (2010)

[5] A. Clarke, G. J. Morris, F. Fonseca, B. J. Murray, E. Acton, and H. C. Price. A Low Temperature Limit for Life on Earth. *PLOS ONE* **8**, e66207 (2013)

[6] G. Fiala and K. O. Stetter. Pyrococcus furiosus sp. nov. represents a novel genus of marine heterotrophic archaebacteria growing optimally at 100°C. *Arch. Microbiol.* **145**, 56 (1986)

[7] E. Schrödinger. What Is Life? The Physical Aspect of the Living Cell. Cambridge University Press (1944)

[8] J. D. Watson and F. H. C. Crick. Molecular Structure of Nucleic Acids: A Structure for Deoxyribose Nucleic Acid. *Nature* **171**, 737 (1953)

[9] P. Glansdorff and I. Prigogine. Thermodynamic Theory of Structure, Stability and Fluctuations. Wiley (1971)

[10] I. Prigogine. Time, Structure, and Fluctuations. *Science* **201**, 777 (1978)

[11] A. M. Turing. The chemical basis of morphogenesis. *Phil. Trans. R. Soc. Lond. B* **237**, 37 (1952)

[12] A. T. Winfree. Biological rhythms and the behavior of populations of coupled oscillators. *J. Theor. Biol.* **16**, 15 (1967)

[13] T. H. Maiman. Stimulated Optical Radiation in Ruby. *Nature* **187**, 493 (1960)

[14] H. Haken and H. Sauermann. Nonlinear interaction of laser modes. *Z. Physik* **173**, 261 (1963)

[15] H. Haken. Synergetics: Introduction and Advanced Topics. Springer (2004)

[16] W. Ebeling. Strukturbildung bei Irreversiblen Prozessen. Eine Einführung in die Theorie dissipativer Strukturen. Teubner (1976)

[17] G. Ertl. Reactions at Surfaces: From Atoms to Complexity (Nobel Lecture). *Angew. Chem., Int. Ed.* **47**, 3524 (2008)

[18] W. A. Zehring, D. A. Wheeler, P. Reddy, R. J. Konopka, C. P. Kyriacou, M. Rosbash, and J. C. Hall. P-element transformation with period locus DNA restores rhythmicity to mutant, arrhythmic drosophila melanogaster. *Cell* **39**, 369 (1984)

[19] L. B. Vosshall, J. L. Price, A. Sehgal, L. Saez, and M. W. Young. Block in nuclear localization of period protein by a second clock mutation, timeless. *Science* **263**, 1606 (1994)

[20] J. L. England. Statistical physics of self-replication. *J. Chem. Phys.* **139**, 121923 (2013)

[21] J. L. England. Dissipative adaptation in driven self-assembly. *Nat. Nanotechnol.* **10**, 919 (2015)

[22] J. M. Horowitz and J. L. England. Spontaneous fine-tuning to environment in many-species chemical reaction networks. *Proc. Natl. Acad. Sci. USA* **114**, 7565 (2017)

[23] Y. S. Kim, R. Tamate, A. M. Akimoto, and R. Yoshida. Recent developments in self-oscillating polymeric systems as smart materials: From polymers to bulk hydrogels. *Mater. Horiz.* **4**, 38 (2017)

[24] M. Wehner, R. L. Truby, D. J. Fitzgerald, B. Mosadegh, G. M. Whitesides, J. A. Lewis, and R. J. Wood. An integrated design and fabrication strategy for entirely soft, autonomous robots. *Nature* **536**, 451 (2016)

[25] H. Ke, M. R. Tinsley, A. Steele, F. Wang, and K. Showalter. Link weight evolution in a network of coupled chemical oscillators. *Phys. Rev. E* **89**, 052712 (2014)

[26] P. A. Merolla, et al. A million spiking-neuron integrated circuit with a scalable communication network and interface. *Science* **345**, 668 (2014)

[27] X. Lu, L. Ren, Q. Gao, Y. Zhao, S. Wang, J. Yang, and I. R. Epstein. Photophobic and phototropic movement of a self-oscillating gel. *Chem. Commun.* **49**, 7690 (2013)

[28] J. C. Nawroth, H. Lee, A. W. Feinberg, C. M. Ripplinger, M. L. McCain, A. Grosberg, J. O. Dabiri, and K. K. Parker. A tissue-engineered jellyfish with biomimetic propulsion. *Nat. Biotech.* **30**, 792 (2012)

[29] S.-J. Park, et al. Phototactic guidance of a tissue-engineered soft-robotic ray. *Science* **353**, 158 (2016)

[30] T. Patino, R. Mestre, and S. Sánchez. Miniaturized soft bio-hybrid robotics: A step forward into healthcare applications. *Lab Chip* **16**, 3626 (2016)

[31] M. S. Lundberg, J. T. Baldwin, and D. B. Buxton. Building a bioartificial heart: Obstacles and opportunities. *J. Thorac. Cardiovasc. Surg.* **153**, 748 (2017)

[32] A. N. Zaikin and A. M. Zhabotinsky. Concentration Wave Propagation in Two-dimensional Liquid-phase Self-oscillating System. *Nature* **225**, 535 (1970)

[33] I. R. Epstein and J. A. Pojman. An Introduction to Nonlinear Chemical Dynamics: Oscillations, Waves, Patterns, and Chaos: Oscillations, Waves, Patterns, and Chaos. Oxford University Press (1998)

[34] R. H. Clayton, E. A. Zhuchkova, and A. V. Panfilov. Phase singularities and filaments: Simplifying complexity in computational models of ventricular fibrillation. *Prog. Biophys. Mol. Biol.* **90**, 378 (2006)

[35] A. Karma. Physics of Cardiac Arrhythmogenesis. *Annu. Rev. Condens. Matter Phys.* **4**, 313 (2013)

[36] A. T. Winfree. Electrical turbulence in three-dimensional heart muscle. *Science* **266**, 1003 (1994)

[37] N. Joshi. Solitons. In "Encyclopedia of Nonlinear Science", Taylor & Francis Group (2006)

[38] A. S. Mikhailov. Foundations of Synergetics I: Distributed active systems. Springer (1990)

[39] A. L. Hodgkin and A. F. Huxley. A quantitative description of membrane current and its application to conduction and excitation in nerve. *J. Physiol.* **117**, 500 (1952)

[40] C. Koch. Biophysics of Computation: Information Processing in Single Neurons. Oxford University Press (2005)

[41] Y. Kuramoto. Reduction methods applied to non-locally coupled oscillator systems. In "Nonlinear Dynamics and Chaos: Where Do We Go from Here?", 209–227. CRC Press (2002)

[42] D. Kim, D. Browder, and M. Heiberg. Star Craft II. Blizzard Entertainment (2010)

[43] A. T. Winfree. The prehistory of the Belousov-Zhabotinsky oscillator. *J. Chem. Educ.* **61**, 661 (1984)

[44] P. G. Kevrekidis, D. J. Frantzeskakis, and R. Carretero-González. The Defocusing Nonlinear Schrödinger Equation: From Dark Solitons to Vortices and Vortex Rings. SIAM (2015)

[45] P.-J. Hsu, A. Finco, L. Schmidt, A. Kubetzka, K. von Bergmann, and R. Wiesendanger. Guiding Spin Spirals by Local Uniaxial Strain Relief. *Phys. Rev. Lett.* **116**, 017201 (2016)

[46] A. R. Verma. Spiral Growth on Carborundum Crystal Faces. *Nature* **167**, 939 (1951)

[47] A. A. Chernov. Formation of crystals in solutions. *Contemp. Phys.* **30**, 251 (1989)

[48] I. S. Aranson, A. R. Bishop, I. Daruka, and V. M. Vinokur. Ginzburg-Landau Theory of Spiral Surface Growth. *Phys. Rev. Lett.* **80**, 1770 (1998)

[49] I. Bischofberger, B. Ray, J. F. Morris, T. Lee, and S. R. Nagel. Airflows generated by an impacting drop. *Soft Matter* **12**, 3013 (2016)

[50] S. J. Haward, R. J. Poole, M. A. Alves, P. J. Oliveira, N. Goldenfeld, and A. Q. Shen. Tricritical spiral vortex instability in cross-slot flow. *Phys. Rev. E* **93**, 031101 (2016)

[51] E. Bodenschatz, J. R. de Bruyn, G. Ahlers, and D. S. Cannell. Transitions between patterns in thermal convection. *Phys. Rev. Lett.* **67**, 3078 (1991)

[52] M. Assenheimer and V. Steinberg. Transition between spiral and target states in Rayleigh–Bénard convection. *Nature* **367**, 345 (1994)

[53] S. V. Kiyashko, L. N. Korzinov, M. I. Rabinovich, and L. S. Tsimring. Rotating spirals in a Faraday experiment. *Phys. Rev. E* **54**, 5037 (1996)

[54] J. R. de Bruyn, B. C. Lewis, M. D. Shattuck, and H. L. Swinney. Spiral patterns in oscillated granular layers. *Phys. Rev. E* **63**, 041305 (2001)

[55] R. Wille. Kármán Vortex Streets. *Adv. Appl. Mech.* **6**, 273 (1960)

[56] D. Kondepudi and I. Prigogine. Modern Thermodynamics: From Heat Engines to Dissipative Structures. Wiley (2014)

[57] J. H. Rogers. The Giant Planet Jupiter. Cambridge University Press (1995)

[58] S. J. Bolton, et al. Jupiter's interior and deep atmosphere: The initial pole-to-pole passes with the Juno spacecraft. *Science* **356**, 821 (2017)

[59] C. C. Lin and F. H. Shu. On the Spiral Structure of Disk Galaxies. *Astrophys. J.* **140**, 646 (1964)

[60] B. P. Abbott, et al. Observation of Gravitational Waves from a Binary Black Hole Merger. *Phys. Rev. Lett.* **116**, 061102 (2016)

[61] B. P. Abbott, et al. Multi-messenger Observations of a Binary Neutron Star Merger. *Astrophys. J. Lett.* **848**, L12 (2017)

[62] N. Wiener and A. Rosenblueth. The mathematical formulation of the problem of conduction of impulses in a network of connected excitable elements, specifically in cardiac muscle. *Arch. Inst. Cardiol. Mex.* **16**, 205 (1946)

[63] M. A. Allessie, F. I. Bonke, and F. J. Schopman. Circus movement in rabbit atrial muscle as a mechanism of tachycardia. III. The "leading circle" concept: A new model of circus movement in cardiac tissue without the involvement of an anatomical obstacle. *Circ. Res.* **41**, 9 (1977)

[64] J. M. Davidenko, P. F. Kent, D. R. Chialvo, D. C. Michaels, and J. Jalife. Sustained vortex-like waves in normal isolated ventricular muscle. *Proc. Natl. Acad. Sci. USA* **87**, 8785 (1990)

[65] F. X. Witkowski, L. J. Leon, P. A. Penkoske, W. R. Giles, M. L. Spano, W. L. Ditto, and A. T. Winfree. Spatiotemporal evolution of ventricular fibrillation. *Nature* **392**, 78 (1998)

[66] S. Luther, et al. Low-energy control of electrical turbulence in the heart. *Nature* **475**, 235 (2011)

[67] G. Bub, L. Glass, N. G. Publicover, and A. Shrier. Bursting calcium rotors in cultured cardiac myocyte monolayers. *Proc. Natl. Acad. Sci. USA* **95**, 10283 (1998)

[68] S. Iravanian, Y. Nabutovsky, C.-R. Kong, S. Saha, N. Bursac, and L. Tung. Functional reentry in cultured monolayers of neonatal rat cardiac cells. *Am. J. Physiol. Heart Circ. Physiol.* **285**, H449 (2003)

[69] B. O. Bingen, et al. Light-induced termination of spiral wave arrhythmias by optogenetic engineering of atrial cardiomyocytes. *Cardiovasc. Res.* **104**, 194 (2014)

[70] R. A. B. Burton, A. Klimas, C. M. Ambrosi, J. Tomek, A. Corbett, E. Entcheva, and G. Bub. Optical control of excitation waves in cardiac tissue. *Nat. Photon.* **9**, 813 (2015)

[71] H. M. McNamara, H. Zhang, C. A. Werley, and A. E. Cohen. Optically Controlled Oscillators in an Engineered Bioelectric Tissue. *Phys. Rev. X* **6**, 031001 (2016)

[72] G. Kastberger, E. Schmelzer, and I. Kranner. Social Waves in Giant Honeybees Repel Hornets. *PLOS ONE* **3**, e3141 (2008)

[73] X. Huang, W. C. Troy, Q. Yang, H. Ma, C. R. Laing, S. J. Schiff, and J.-Y. Wu. Spiral Waves in Disinhibited Mammalian Neocortex. *J. Neurosci.* **24**, 9897 (2004)

[74] J. Lechleiter, S. Girard, E. Peralta, and D. Clapham. Spiral calcium wave propagation and annihilation in Xenopus laevis oocytes. *Science* **252**, 123 (1991)

[75] N. A. Gorelova and J. Bureš. Spiral waves of spreading depression in the isolated chicken retina. *J. Neurobiol.* **14**, 353 (1983)

[76] D. Taniguchi, S. Ishihara, T. Oonuki, M. Honda-Kitahara, K. Kaneko, and S. Sawai. Phase geometries of two-dimensional excitable waves govern self-organized morphodynamics of amoeboid cells. *Proc. Natl. Acad. Sci. USA* **110**, 5016 (2013)

[77] K. J. Tomchik and P. N. Devreotes. Adenosine 3',5'-monophosphate waves in Dictyostelium discoideum: A demonstration by isotope dilution–fluorography. *Science* **212**, 443 (1981)

[78] G. Seiden and S. Curland. The tongue as an excitable medium. *New J. Phys.* **17**, 033049 (2015)

[79] F. Macari, M. Landau, P. Cousin, B. Mevorah, S. Brenner, R. Panizzon, D. F. Schorderet, D. Hohl, and M. Huber. Mutation in the Gene for Connexin 30.3 in a Family with Erythrokeratodermia Variabilis. *Am. J. Hum. Genet.* **67**, 1296 (2000)

[80] A. J. Welsh, E. F. Greco, and F. H. Fenton. Dynamics of a human spiral wave. *Phys. Today* **70**, 78 (2017)

[81] R. D. Kirkton and N. Bursac. Engineering biosynthetic excitable tissues from unexcitable cells for electrophysiological and cell therapy studies. *Nat. Commun.* **2**, 300 (2011)

[82] W. J. E. P. Lammers. Circulating excitations and re-entry in the pregnant uterus. *Pflügers Arch. – Eur. J. Physiol.* **433**, 287 (1996)

[83] E. Pervolaraki and A. V. Holden. Spatiotemporal patterning of uterine excitation patterns in human labour. *BioSystems* **112**, 63 (2013)

[84] S. C. Müller, T. Mair, and O. Steinbock. Traveling waves in yeast extract and in cultures of Dictyostelium discoideum. *Biophys. Chem.* **72**, 37 (1998)

[85] J. T. Groves and J. Kuriyan. Molecular mechanisms in signal transduction at the membrane. *Nat. Struct. Mol. Biol.* **17**, 659 (2010)

[86] M. Gerhardt, M. Ecke, M. Walz, A. Stengl, C. Beta, and G. Gerisch. Actin and PIP3 waves in giant cells reveal the inherent length scale of an excited state. *J. Cell Sci.* **127**, 4507 (2014)

[87] A. T. Winfree. The Geometry of Biological Time. Springer (2001)

[88] N. Uchida and R. Golestanian. Synchronization and Collective Dynamics in a Carpet of Microfluidic Rotors. *Phys. Rev. Lett.* **104**, 178103 (2010)

[89] A. T. Winfree. Spiral Waves of Chemical Activity. *Science* **175**, 634 (1972)

[90] V. K. Vanag and I. R. Epstein. Inwardly Rotating Spiral Waves in a Reaction-Diffusion System. *Science* **294**, 835 (2001)

[91] M. Yoneyama, A. Fujii, and S. Maeda. Chemical oscillations in Ru(bpy)32+ Langmuir monolayers formed on Belousov-Zhabotinskii reaction solutions. *Physica D* **84**, 120 (1995)

[92] M. R. Tinsley, D. Collison, and K. Showalter. Propagating Precipitation Waves: Experiments and Modeling. *J. Phys. Chem. A* **117**, 12719 (2013)

[93] S. Jakubith, H. H. Rotermund, W. Engel, A. von Oertzen, and G. Ertl. Spatiotemporal concentration patterns in a surface reaction: Propagating and standing waves, rotating spirals, and turbulence. *Phys. Rev. Lett.* **65**, 3013 (1990)

[94] I. Krastev and M. T. M. Koper. Pattern formation during the electrodeposition of a silver-antimony alloy. *Physica A* **213**, 199 (1995)

[95] K. Agladze and O. Steinbock. Waves and Vortices of Rust on the Surface of Corroding Steel. *J. Phys. Chem. A* **104**, 9816 (2000)

[96] J. F. Nye and M. V. Berry. Dislocations in Wave Trains. *Proc. R. Soc. A* **336**, 165 (1974)

[97] P. Coullet, L. Gil, and F. Rocca. Optical vortices. *Opt. Commun.* **73**, 403 (1989)

[98] I. V. Basistiy, V. Y. Bazhenov, M. S. Soskin, and M. V. Vasnetsov. Optics of light beams with screw dislocations. *Opt. Commun.* **103**, 422 (1993)

[99] H. G. Pearlman and P. D. Ronney. Self-organized spiral and circular waves in premixed gas flames. *J. Chem. Phys.* **101**, 2632 (1994)

[100] P. Coullet and F. Plaza. Excitable Spiral Waves in Nematic Liquid Crystals. *Int. J. Bifurcat. Chaos* **04**, 1173 (1994)

[101] A. Martinez and I. I. Smalyukh. Light-driven dynamic Archimedes spirals and periodic oscillatory patterns of topological solitons in anisotropic soft matter. *Opt. Express* **23**, 4591 (2015)

[102] M. Schwabe, U. Konopka, P. Bandyopadhyay, and G. E. Morfill. Pattern Formation in a Complex Plasma in High Magnetic Fields. *Phys. Rev. Lett.* **106**, 215004 (2011)

[103] L. Dong, F. Liu, S. Liu, Y. He, and W. Fan. Observation of spiral pattern and spiral defect chaos in dielectric barrier discharge in argon/air at atmospheric pressure. *Phys. Rev. E* **72**, 046215 (2005)

[104] Y. Li, H. Li, Y. Zhu, M. Zhang, and J. Yang. Type of spiral wave with trapped ions. *Phys. Rev. E* **84**, 066212 (2011)

[105] R. Lauter, C. Brendel, S. J. M. Habraken, and F. Marquardt. Pattern phase diagram for two-dimensional arrays of coupled limit-cycle oscillators. *Phys. Rev. E* **92**, 012902 (2015)

[106] R. Kapral, R. Livi, G.-L. Oppo, and A. Politi. Dynamics of complex interfaces. *Phys. Rev. E* **49**, 2009 (1994)

[107] I. Aranson, M. Gitterman, and B. Y. Shapiro. Spiral fluxons and a characteristic frequency in two-dimensional Josephson junctions. *Phys. Rev. B* **52**, 12878 (1995)

[108] D. P. Zipes, J. Jalife, and W. G. Stevenson. Cardiac Electrophysiology: From Cell to Bedside. Elsevier (2017)

[109] T. Quail, A. Shrier, and L. Glass. Spatial Symmetry Breaking Determines Spiral Wave Chirality. *Phys. Rev. Lett.* **113**, 158101 (2014)

[110] V. Zykov, A. Krekhov, and E. Bodenschatz. Fast propagation regions cause self-sustained reentry in excitable media. *Proc. Natl. Acad. Sci. USA* **114**, 1281 (2017)

[111] A. T. Winfree and S. H. Strogatz. Singular filaments organize chemical waves in three dimensions: I. Geometrically simple waves. *Physica D* **8**, 35 (1983)

[112] A. Winfree and S. Strogatz. Singular filaments organize chemical waves in three dimensions II. Twisted waves. *Physica D* **9**, 65 (1983)

[113] A. Winfree and S. Strogatz. Singular filaments organize chemical waves in three dimensions: III. Knotted waves. *Physica D* **9**, 333 (1983)

[114] A. Winfree and S. Strogatz. Singular filaments organize chemical waves in three dimensions: IV. Wave taxonomy. *Physica D* **13**, 221 (1984)

[115] A. B. Medvinsky, A. V. Panfilov, and A. M. Pertsov. Properties of Rotating Waves in Three Dimensions. Scroll Rings in Myocard. In P. D. V. I. Krinsky, ed., "Self-Organization Autowaves and Structures Far from Equilibrium", 195–199. Springer (1984)

[116] A. T. Winfree. Scroll-Shaped Waves of Chemical Activity in Three Dimensions. *Science* **181**, 937 (1973)

[117] H. Kitahata, N. Yoshinaga, K. H. Nagai, and Y. Sumino. Spontaneous Motion of a Belousov–Zhabotinsky Reaction Droplet Coupled with a Spiral Wave. *Chem. Lett.* **41**, 1052 (2012)

[118] J. P. Keener. The dynamics of three-dimensional scroll waves in excitable media. *Physica D* **31**, 269 (1988)

[119] W. W. Mullins. Two-Dimensional Motion of Idealized Grain Boundaries. *J. Appl. Phys.* **27**, 900 (1956)

[120] V. N. Biktashev, A. V. Holden, and H. Zhang. Tension of Organizing Filaments of Scroll Waves. *Phil. Trans. R. Soc. Lond. A* **347**, 611 (1994)

[121] S. Alonso, F. Sagués, and A. S. Mikhailov. Taming Winfree Turbulence of Scroll Waves in Excitable Media. *Science* **299**, 1722 (2003)

[122] O. Steinbock, V. Zykov, and S. C. Müller. Control of spiral-wave dynamics in active media by periodic modulation of excitability. *Nature* **366**, 322 (1993)

[123] M. Markus, Z. Nagy-Ungvarai, and B. Hess. Phototaxis of Spiral Waves. *Science* **257**, 225 (1992)

[124] O. Steinbock and S. Müller. Chemical spiral rotation is controlled by light-induced artificial cores. *Physica A* **188**, 61 (1992)

[125] J. Schlesner, V. S. Zykov, H. Brandtstädter, I. Gerdes, and H. Engel. Efficient control of spiral wave location in an excitable medium with localized heterogeneities. *New J. Phys.* **10**, 015003 (2008)

[126] H. Brandtstädter, M. Braune, I. Schebesch, and H. Engel. Experimental study of the dynamics of spiral pairs in light-sensitive Belousov–Zhabotinskii media using an open-gel reactor. *Chem. Phys. Lett.* **323**, 145 (2000)

[127] M. Gómez-Gesteira, A. P. Muñuzuri, V. Pérez-Muñuzuri, and V. Pérez-Villar. Boundary-imposed spiral drift. *Phys. Rev. E* **53**, 5480 (1996)

[128] J. J. Tyson and J. P. Keener. Singular perturbation theory of traveling waves in excitable media (a review). *Physica D* **32**, 327 (1988)

[129] P. Foerster, S. C. Müller, and B. Hess. Curvature and Propagation Velocity of Chemical Waves. *Science* **241**, 685 (1988)

[130] D. Horváth, V. Petrov, S. K. Scott, and K. Showalter. Instabilities in propagating reaction-diffusion fronts. *J. Chem. Phys.* **98**, 6332 (1993)

[131] D. Margerit and D. Barkley. Large-excitability asymptotics for scroll waves in three-dimensional excitable media. *Phys. Rev. E* **66** (2002)

[132] V. Biktashev and A. Holden. Resonant Drift of Autowave Vortices in Two Dimensions and the Effects of Boundaries and Inhomogeneities. *Chaos* **5**, 575 (1995)

[133] I. V. Biktasheva and V. N. Biktashev. Wave-particle dualism of spiral waves dynamics. *Phys. Rev. E* **67**, 026221 (2003)

[134] V. N. Biktashev and I. V. Biktasheva. Dynamics of filaments of scroll waves. In "Engineering of Chemical Complexity II", 221–238. World Scientific (2014)

[135] T. Amemiya, P. Kettunen, S. Kádár, T. Yamaguchi, and K. Showalter. Formation and evolution of scroll waves in photosensitive excitable media. *Chaos* **8**, 872 (1998)

[136] T. Bánsági and O. Steinbock. Nucleation and Collapse of Scroll Rings in Excitable Media. *Phys. Rev. Lett.* **97**, 198301 (2006)

[137] T. Bánsági and O. Steinbock. Three-dimensional spiral waves in an excitable reaction system: Initiation and dynamics of scroll rings and scroll ring pairs. *Chaos* **18**, 026102 (2008)

[138] N. P. Das and S. Dutta. Interaction of scroll waves in an excitable medium: Reconnection and repulsion. *Phys. Rev. E* **91**, 030901 (2015)

[139] M. Vinson, S. Mironov, S. Mulvey, and A. Pertsov. Control of spatial orientation and lifetime of scroll rings in excitable media. *Nature* **386**, 477 (1997)

[140] C. Luengviriya, S. C. Müller, and M. J. B. Hauser. Reorientation of scroll rings in an advective field. *Phys. Rev. E* **77**, 015201 (2008)

[141] Z. Jiménez, B. Marts, and O. Steinbock. Pinned Scroll Rings in an Excitable System. *Phys. Rev. Lett.* **102** (2009)

[142] Z. A. Jiménez and O. Steinbock. Pinning of vortex rings and vortex networks in excitable systems. *Europhys. Lett.* **91**, 50002 (2010)

[143] S. Dutta and O. Steinbock. Topologically Mismatched Pinning of Scroll Waves. *J. Phys. Chem. Lett.* **2**, 945 (2011)

[144] S. C. Müller, T. Plesser, and B. Hess. Two-dimensional spectrophotometry and pseudo-color representation of chemical reaction patterns. *Sci. Nat.* **73**, 165 (1986)

[145] P. Ruoff. Excitability in a closed stirred Belousov-Zhabotinskii system. *Chem. Phys. Lett.* **90**, 76 (1982)

[146] A. Pertsov, M. Vinson, and S. C. Müller. Three-dimensional reconstruction of organizing centers in excitable chemical media. *Physica D* **63**, 233 (1993)

[147] Z. A. Jiménez and O. Steinbock. Stationary Vortex Loops Induced by Filament Interaction and Local Pinning in a Chemical Reaction-Diffusion System. *Phys. Rev. Lett.* **109** (2012)

[148] Z. A. Jiménez and O. Steinbock. Scroll wave filaments self-wrap around unexcitable heterogeneities. *Phys. Rev. E* **86**, 036205 (2012)

[149] T. Bánsági, Jr. and O. Steinbock. Negative filament tension of scroll rings in an excitable system. *Phys. Rev. E* **76**, 045202 (2007)

[150] P. J. Nandapurkar and A. T. Winfree. Dynamical stability of untwisted scroll rings in excitable media. *Physica D* **35**, 277 (1989)

[151] M. Courtemanche, W. Skaggs, and A. Winfree. Stable three-dimensional action potential circulation in the Fitzhugh-Nagumo model. *Physica D* **41**, 173 (1990)

[152] A. Azhand, J. F. Totz, and H. Engel. Three-dimensional autonomous pacemaker in the photosensitive Belousov-Zhabotinsky medium. *Europhys. Lett.* **108**, 10004 (2014)

[153] I. Aranson, L. Kramer, and A. Weber. On the interaction of spiral waves in non-equilibrium media. *Physica D* **53**, 376 (1991)

[154] R. R. Aliev and A. B. Rovinskii. Spiral waves in the homogeneous and inhomogeneous Belousov-Zhabotinskii reaction. *J. Phys. Chem.* **96**, 732 (1992)

[155] M.-A. Bray and J. P. Wikswo. Interaction Dynamics of a Pair of Vortex Filament Rings. *Phys. Rev. Lett.* **90**, 238303 (2003)

[156] F. Paul. Dreidimensionale Erregungswellen in oszillatorischen Medien. Diploma thesis, TU Berlin, Berlin (2011)

[157] D. A. Kulawiak. Über die Wechselwirkung rotierender dreidimensionaler Erregungswellen mit begrenzenden Neumann-Rändern. M.Sc. Thesis, TU Berlin (2014)

[158] Press, Teukolsky, Vetterling, and Flannery. Numerical Recipes: The Art of Scientific Computing. Cambridge University Press (2007)

[159] W. Skaggs, E. Lugosi, and E. Winfree. Stable vortex rings of excitation in neuroelectric media. *IEEE Trans. Circuits Syst.* **35**, 784 (1988)

[160] V. A. Davydov, A. S. Mikhailov, and V. S. Zykov. Kinematical Theory of Autowave Patterns in Excitable Media. In P. J. Engelbrecht, ed., "Nonlinear Waves in Active Media", 38–51. Springer (1989)

[161] A. Winfree. Stable Particle-Like Solutions to the Nonlinear Wave Equations of Three-Dimensional Excitable Media. *SIAM Rev.* **32**, 1 (1990)

[162] J. F. Totz, H. Engel, and O. Steinbock. Spatial confinement causes lifetime enhancement and expansion of vortex rings with positive filament tension. *New J. Phys.* **17**, 093043 (2015)

[163] V. Pérez-Muñuzuri, F. Sagués, and J. M. Sancho. Lifetime enhancement of scroll rings by spatiotemporal fluctuations. *Phys. Rev. E* **62**, 94 (2000)

[164] R.-M. Mantel and D. Barkley. Parametric forcing of scroll-wave patterns in three-dimensional excitable media. *Physica D* **149**, 107 (2001)

[165] S. Alonso, F. Sagués, and A. S. Mikhailov. Periodic forcing of scroll rings and control of Winfree turbulence in excitable media. *Chaos* **16**, 023124 (2006)

[166] V. Zykov and H. Engel. Feedback-mediated control of spiral waves. *Physica D* **199**, 243 (2004)

[167] V. Zykov, G. Bordiougov, H. Brandtstädter, I. Gerdes, and H. Engel. Global Control of Spiral Wave Dynamics in an Excitable Domain of Circular and Elliptical Shape. *Phys. Rev. Lett.* **92** (2004)

[168] I. Bakas and C. Sourdis. Dirichlet sigma models and mean curvature flow. *J. High Energy Phys.* **2007**, 057 (2007)

[169] K. I. Agladze, V. I. Krinsky, A. V. Panfilov, H. Linde, and L. Kuhnert. Three-dimensional vortex with a spiral filament in a chemically active medium. *Physica D* **39**, 38 (1989)

[170] E. R. Kandel, J. H. Schwartz, T. M. Jessell, S. A. Siegelbaum, and A. J. Hudspeth, eds. Principles of Neural Science. McGraw-Hill (2012)

[171] S. R. y Cajal. Nobel Lecture: The structure and connections of neurons (1906)

[172] F. de Castro, L. López-Mascaraque, and J. A. De Carlos. Cajal: Lessons on brain development. *Brain Res. Rev.* **55**, 481 (2007)

[173] D. O. Hebb. The Organization of Behavior: A Neuropsychological Theory. Wiley (1949)

[174] T. V. P. Bliss and T. Lømo. Long-lasting potentiation of synaptic transmission in the dentate area of the anaesthetized rabbit following stimulation of the perforant path. *J. Physiol.* **232**, 331 (1973)

[175] L. Carrillo-Reid, W. Yang, Y. Bando, D. S. Peterka, and R. Yuste. Imprinting and recalling cortical ensembles. *Science* **353**, 691 (2016)

[176] J.-H. Han, S. A. Kushner, A. P. Yiu, C. J. Cole, A. Matynia, R. A. Brown, R. L. Neve, J. F. Guzowski, A. J. Silva, and S. A. Josselyn. Neuronal Competition and Selection During Memory Formation. *Science* **316**, 457 (2007)

[177] A. J. Silva, Y. Zhou, T. Rogerson, J. Shobe, and J. Balaji. Molecular and Cellular Approaches to Memory Allocation in Neural Circuits. *Science* **326**, 391 (2009)

[178] L. J. Richards, T. J. Kilpatrick, and P. F. Bartlett. De novo generation of neuronal cells from the adult mouse brain. *Proc. Natl. Acad. Sci. USA* **89**, 8591 (1992)

[179] D. J. Jhaveri, A. Tedoldi, S. Hunt, R. Sullivan, N. R. Watts, J. M. Power, P. F. Bartlett, and P. Sah. Evidence for newly generated interneurons in the basolateral amygdala of adult mice. *Mol. Psychiatry* (2017)

[180] J. Fell and N. Axmacher. The role of phase synchronization in memory processes. *Nat. Rev. Neurosci.* **12**, 105 (2011)

[181] P. R. Roelfsema, A. K. Engel, P. König, and W. Singer. Visuomotor integration is associated with zero time-lag synchronization among cortical areas. *Nature* **385**, 157 (1997)

[182] E. Rodriguez, N. George, J.-P. Lachaux, J. Martinerie, B. Renault, and F. J. Varela. Perception's shadow: Long-distance synchronization of human brain activity. *Nature* **397**, 430 (1999)

[183] C. Hammond, H. Bergman, and P. Brown. Pathological synchronization in Parkinson's disease: Networks, models and treatments. *Trends Neurosci.* **30**, 357 (2007)

[184] J. J. Eggermont and L. E. Roberts. The neuroscience of tinnitus. *Trends Neurosci.* **27**, 676 (2004)

[185] P. A. Tass, I. Adamchic, H.-J. Freund, T. von Stackelberg, and C. Hauptmann. Counteracting tinnitus by acoustic coordinated reset neuromodulation. *Restor. Neurol. Neurosci.* **30**, 137 (2012)

[186] F. Mormann, K. Lehnertz, P. David, and C. E. Elger. Mean phase coherence as a measure for phase synchronization and its application to the EEG of epilepsy patients. *Physica D* **144**, 358 (2000)

[187] P. Jiruska, M. de Curtis, J. G. R. Jefferys, C. A. Schevon, S. J. Schiff, and K. Schindler. Synchronization and desynchronization in epilepsy: Controversies and hypotheses. *J. Physiol.* **591**, 787 (2013)

[188] N. Wiener. Nonlinear Problems in Random Theory. MIT Press (1958)

[189] A. Pikovsky, M. Rosenblum, and J. Kurths. Synchronization: A Universal Concept in Nonlinear Sciences. Cambridge University Press (2001)

[190] G. Buzsáki and A. Draguhn. Neuronal Oscillations in Cortical Networks. *Science* **304**, 1926 (2004)

[191] I. Fischer, R. Vicente, J. M. Buldú, M. Peil, C. R. Mirasso, M. C. Torrent, and J. García-Ojalvo. Zero-Lag Long-Range Synchronization via Dynamical Relaying. *Phys. Rev. Lett.* **97**, 123902 (2006)

[192] V. Flunkert, S. Yanchuk, T. Dahms, and E. Schöll. Synchronizing Distant Nodes: A Universal Classification of Networks. *Phys. Rev. Lett.* **105**, 254101 (2010)

[193] W. Klimesch, R. Freunberger, P. Sauseng, and W. Gruber. A short review of slow phase synchronization and memory: Evidence for control processes in different memory systems? *Brain Res.* **1235**, 31 (2008)

[194] V. Nicosia, M. Valencia, M. Chavez, A. Díaz-Guilera, and V. Latora. Remote Synchronization Reveals Network Symmetries and Functional Modules. *Phys. Rev. Lett.* **110**, 174102 (2013)

[195] H. Nakao and A. S. Mikhailov. Turing patterns in network-organized activator-inhibitor systems. *Nat. Phys.* **6**, 544 (2010)

[196] S. Hata, H. Nakao, and A. S. Mikhailov. Dispersal-induced destabilization of metapopulations and oscillatory Turing patterns in ecological networks. *Sci. Rep.* **4** (2014)

[197] H. Nakao and A. S. Mikhailov. Diffusion-induced instability and chaos in random oscillator networks. *Phys. Rev. E* **79**, 036214 (2009)

[198] N. E. Kouvaris, T. Isele, A. S. Mikhailov, and E. Schöll. Propagation failure of excitation waves on trees and random networks. *Europhys. Lett.* **106**, 68001 (2014)

[199] T. Isele, B. Hartung, P. Hövel, and E. Schöll. Excitation waves on a minimal small-world model. *Eur. Phys. J. B* **88**, 1 (2015)

[200] S. H. Strogatz. Exploring complex networks. *Nature* **410**, 268 (2001)

[201] D. Garlaschelli, F. Ruzzenenti, and R. Basosi. Complex Networks and Symmetry I: A Review. *Symmetry* **2**, 1683 (2010)

[202] L. M. Pecora, F. Sorrentino, A. M. Hagerstrom, T. E. Murphy, and R. Roy. Cluster synchronization and isolated desynchronization in complex networks with symmetries. *Nat. Commun.* **5**, 4079 (2014)

[203] L. M. Pecora and T. L. Carroll. Master Stability Functions for Synchronized Coupled Systems. *Phys. Rev. Lett.* **80**, 2109 (1998)

[204] L. Pecora, T. Carroll, G. Johnson, D. Mar, and K. S. Fink. Synchronization Stability in Coupled Oscillator Arrays: Solution for Arbitrary Configurations. *Int. J. Bifurc. Chaos* **10**, 273 (2000)

[205] W. Zou, D. V. Senthilkumar, R. Nagao, I. Z. Kiss, Y. Tang, A. Koseska, J. Duan, and J. Kurths. Restoration of rhythmicity in diffusively coupled dynamical networks. *Nat. Commun.* **6**, 7709 (2015)

[206] P. G. Kevrekidis and I. G. Kevrekidis. Wave of Translation. In "Encyclopedia of Nonlinear Science", 986–988. Taylor & Francis Group (2006)

[207] F. Sorrentino and L. Pecora. Approximate cluster synchronization in networks with symmetries and parameter mismatches. *Chaos* **26**, 094823 (2016)

[208] E. W. Dijkstra. A note on two problems in connexion with graphs. *Numer. Math.* **1**, 269 (1959)

[209] A. J. Ijspeert. Central pattern generators for locomotion control in animals and robots: A review. *Neural Netw.* **21**, 642 (2008)

[210] X. Wu and S. Ma. CPG-based control of serpentine locomotion of a snake-like robot. *Mechatronics* **20**, 326 (2010)

[211] S. Steingrube, M. Timme, F. Wörgötter, and P. Manoonpong. Self-organized adaptation of a simple neural circuit enables complex robot behaviour. *Nat. Phys.* **6**, 224 (2010)

[212] A. F. Taylor, M. R. Tinsley, and K. Showalter. Insights into collective cell behaviour from populations of coupled chemical oscillators. *Phys. Chem. Chem. Phys.* **31**, 20047 (2015)

[213] Y. Kuramoto. Chemical Oscillations, Waves, and Turbulence. Springer (1984)

[214] R. Olfati-Saber, J. A. Fax, and R. M. Murray. Consensus and Cooperation in Networked Multi-Agent Systems. *Proc. IEEE* **95**, 215 (2007)

[215] A.-L. Barabási and R. Albert. Emergence of Scaling in Random Networks. *Science* **286**, 509 (1999)

[216] A.-L. Barabási and E. Bonabeau. Scale-Free Networks. *Sci. Am.* **288**, 60 (2003)

[217] J. F. Totz, R. Snari, D. Yengi, M. R. Tinsley, H. Engel, and K. Showalter. Phase-lag synchronization in networks of coupled chemical oscillators. *Phys. Rev. E* **92**, 022819 (2015)

[218] M. Newman. Networks: An Introduction. Oxford University Press (2010)

[219] B. D. MacArthur and R. J. Sánchez-García. Spectral characteristics of network redundancy. *Phys. Rev. E* **80**, 026117 (2009)

[220] D. Rubino, K. A. Robbins, and N. G. Hatsopoulos. Propagating waves mediate information transfer in the motor cortex. *Nat. Neurosci.* **9**, 1549 (2006)

[221] M. J. Panaggio and D. M. Abrams. Chimera states: Coexistence of coherence and incoherence in networks of coupled oscillators. *Nonlinearity* **28**, R67 (2015)

[222] P. Ashwin, S. Coombes, and R. Nicks. Mathematical Frameworks for Oscillatory Network Dynamics in Neuroscience. *J. Math. Neurosci.* **6**, 1 (2016)

[223] D. M. Abrams and S. H. Strogatz. Chimera States for Coupled Oscillators. *Phys. Rev. Lett.* **93**, 174102 (2004)

[224] J. Hogan, A. R. Krauskopf, M. di Bernado, R. E. Wilson, H. M. Osinga, M. E. Homer, and A. R. Champneys, eds. Nonlinear Dynamics and Chaos: Where do we go from here? CRC Press (2002)

[225] E. Alvarez-Lacalle and B. Echebarria. Global coupling in excitable media provides a simplified description of mechanoelectrical feedback in cardiac tissue. *Phys. Rev. E* **79**, 031921 (2009)

[226] J. C. González-Avella, M. G. Cosenza, and M. San Miguel. Localized coherence in two interacting populations of social agents. *Physica A* **399**, 24 (2014)

[227] I. A. Shepelev, T. E. Vadivasova, A. V. Bukh, G. I. Strelkova, and V. S. Anishchenko. New type of chimera structures in a ring of bistable FitzHugh–Nagumo oscillators with nonlocal interaction. *Phys. Lett. A* **381**, 1398 (2017)

[228] M. Zhang, G. S. Wiederhecker, S. Manipatruni, A. Barnard, P. McEuen, and M. Lipson. Synchronization of Micromechanical Oscillators Using Light. *Phys. Rev. Lett.* **109**, 233906 (2012)

[229] M. Zhang, S. Shah, J. Cardenas, and M. Lipson. Synchronization and Phase Noise Reduction in Micromechanical Oscillator Arrays Coupled through Light. *Phys. Rev. Lett.* **115**, 163902 (2015)

[230] E. Gil-Santos, M. Labousse, C. Baker, A. Goetschy, W. Hease, C. Gomez, A. Lemaître, G. Leo, C. Ciuti, and I. Favero. Light-Mediated Cascaded Locking of Multiple Nano-Optomechanical Oscillators. *Phys. Rev. Lett.* **118**, 063605 (2017)

[231] M. Rohden, A. Sorge, M. Timme, and D. Witthaut. Self-Organized Synchronization in Decentralized Power Grids. *Phys. Rev. Lett.* **109**, 064101 (2012)

[232] M. Trepanier, D. Zhang, O. Mukhanov, and S. M. Anlage. Realization and Modeling of Metamaterials Made of rf Superconducting Quantum-Interference Devices. *Phys. Rev. X* **3**, 041029 (2013)

[233] N. Lazarides, G. Neofotistos, and G. P. Tsironis. Chimeras in SQUID metamaterials. *Phys. Rev. B* **91**, 054303 (2015)

[234] V. In and A. Palacios. Superconductive Quantum Interference Devices (SQUID). In "Symmetry in Complex Network Systems", 127–163. Springer (2018)

[235] S. Kaka, M. R. Pufall, W. H. Rippard, T. J. Silva, S. E. Russek, and J. A. Katine. Mutual phase-locking of microwave spin torque nano-oscillators. *Nature* **437**, 389 (2005)

[236] M. Zaks and A. Pikovsky. Chimeras and complex cluster states in arrays of spin-torque oscillators. *Sci. Rep.* **7**, 4648 (2017)

[237] H. W. Lau, J. Davidsen, and C. Simon. Chimera patterns in conservative systems and ultracold atoms with mediated nonlocal hopping. *arxiv* (2017)

[238] C. R. Laing and C. C. Chow. Stationary Bumps in Networks of Spiking Neurons. *Neural Comput.* **13**, 1473 (2001)

[239] C. R. Laing. Derivation of a neural field model from a network of theta neurons. *Phys. Rev. E* **90**, 010901 (2014)

[240] P. C. Bressloff and Z. P. Kilpatrick. Nonlocal Ginzburg-Landau equation for cortical pattern formation. *Phys. Rev. E* **78**, 041916 (2008)

[241] J. Viventi, et al. Flexible, foldable, actively multiplexed, high-density electrode array for mapping brain activity in vivo. *Nat. Neurosci.* **14**, 1599 (2011)

[242] R. G. Andrzejak, C. Rummel, F. Mormann, and K. Schindler. All together now: Analogies between chimera state collapses and epileptic seizures. *Sci. Rep.* **6**, 23000 (2016)

[243] R. Faubel, C. Westendorf, E. Bodenschatz, and G. Eichele. Cilia-based flow network in the brain ventricles. *Science* **353**, 176 (2016)

[244] M. R. Tinsley, S. Nkomo, and K. Showalter. Chimera and phase-cluster states in populations of coupled chemical oscillators. *Nat. Phys.* **8**, 662 (2012)

[245] S. Nkomo, M. R. Tinsley, and K. Showalter. Chimera States in Populations of Nonlocally Coupled Chemical Oscillators. *Phys. Rev. Lett.* **110**, 244102 (2013)

[246] M. Wickramasinghe and I. Z. Kiss. Spatially organized partial synchronization through the chimera mechanism in a network of electrochemical reactions. *Phys. Chem. Chem. Phys.* **16**, 18360 (2014)

[247] K. Schönleber, C. Zensen, A. Heinrich, and K. Krischer. Pattern formation during the oscillatory photoelectrodissolution of n-type silicon: Turbulence, clusters and chimeras. *New J. Phys.* **16**, 063024 (2014)

[248] L. Schmidt, K. Schönleber, K. Krischer, and V. García-Morales. Coexistence of synchrony and incoherence in oscillatory media under nonlinear global coupling. *Chaos* **24**, 013102 (2014)

[249] M. Patzauer, R. Hueck, A. Tosolini, K. Schönleber, and K. Krischer. Autonomous Oscillations and Pattern Formation with Zero External Resistance during Silicon Electrodissolution. *Electrochim. Acta* **246**, 315 (2017)

[250] P. Kumar, D. K. Verma, and P. Parmananda. Partially synchronized states in an ensemble of chemo-mechanical oscillators. *Phys. Lett. A* **381**, 2337 (2017)

[251] A. M. Hagerstrom, T. E. Murphy, R. Roy, P. Hövel, I. Omelchenko, and E. Schöll. Experimental observation of chimeras in coupled-map lattices. *Nat. Phys.* **8**, 658 (2012)

[252] J. D. Hart, K. Bansal, T. E. Murphy, and R. Roy. Experimental observation of chimera and cluster states in a minimal globally coupled network. *Chaos* **26**, 094801 (2016)

[253] E. A. Martens, S. Thutupalli, A. Fourrière, and O. Hallatschek. Chimera states in mechanical oscillator networks. *Proc. Natl. Acad. Sci. USA* **110**, 10563 (2013)

[254] T. Kapitaniak, P. Kuzma, J. Wojewoda, K. Czolczynski, and Y. Maistrenko. Imperfect chimera states for coupled pendula. *Sci. Rep.* **4**, 6379 (2014)

[255] J. Wojewoda, K. Czolczynski, Y. Maistrenko, and T. Kapitaniak. The smallest chimera state for coupled pendula. *Sci. Rep.* **6**, 34329 (2016)

[256] L. Larger, B. Penkovsky, and Y. Maistrenko. Virtual Chimera States for Delayed-Feedback Systems. *Phys. Rev. Lett.* **111**, 054103 (2013)

[257] L. Larger, B. Penkovsky, and Y. Maistrenko. Laser chimeras as a paradigm for multistable patterns in complex systems. *Nat. Commun.* **6**, 7752 (2015)

[258] F. Rossi, S. Ristori, N. Marchettini, and O. L. Pantani. Functionalized Clay Microparticles as Catalysts for Chemical Oscillators. *J. Phys. Chem. C* **118**, 24389 (2014)

[259] L. V. Gambuzza, A. Buscarino, S. Chessari, L. Fortuna, R. Meucci, and M. Frasca. Experimental investigation of chimera states with quiescent and synchronous domains in coupled electronic oscillators. *Phys. Rev. E* **90**, 032905 (2014)

[260] L. Q. English, A. Zampetaki, P. G. Kevrekidis, K. Skowronski, C. B. Fritz, and S. Abdoulkary. Analysis and observation of moving domain fronts in a ring of coupled electronic self-oscillators. *Chaos* **27**, 103125 (2017)

[261] D. R. Brumley, N. Bruot, J. Kotar, R. E. Goldstein, P. Cicuta, and M. Polin. Long-range interactions, wobbles, and phase defects in chains of model cilia. *Phys. Rev. Fluids* **1**, 081201 (2016)

[262] V. K. Vanag, L. Yang, M. Dolnik, A. M. Zhabotinsky, and I. R. Epstein. Oscillatory cluster patterns in a homogeneous chemical system with global feedback. *Nature* **406**, 389 (2000)

[263] P. Rupp, R. Richter, and I. Rehberg. Critical exponents of directed percolation measured in spatiotemporal intermittency. *Phys. Rev. E* **67**, 036209 (2003)

[264] L. Hall-Stoodley, J. W. Costerton, and P. Stoodley. Bacterial biofilms: From the Natural environment to infectious diseases. *Nat. Rev. Micro.* **2**, 95 (2004)

[265] S. Bayin. Mathematical Methods in Science and Engineering. Wiley (2006)

[266] Y. Kuramoto and S. Shima. Rotating Spirals without Phase Singularity in Reaction-Diffusion Systems. *Prog. Theor. Phys. Supplement* **150**, 115 (2003)

[267] S. Shima and Y. Kuramoto. Rotating spiral waves with phase-randomized core in nonlocally coupled oscillators. *Phys. Rev. E* **69**, 036213 (2004)

[268] V. Casagrande. Synchronization, Waves, and Turbulence in Systems of Interacting Chemical Oscillators. Ph.D. Thesis, TU Berlin, FHI (2006)

[269] M. Hazewinkel. Diffeomorphism. In "Encyclopaedia of Mathematics", Springer (2001)

[270] D. M. Abrams, R. Mirollo, S. H. Strogatz, and D. A. Wiley. Solvable Model for Chimera States of Coupled Oscillators. *Phys. Rev. Lett.* **101**, 084103 (2008)

[271] Y. Kuramoto and D. Battogtokh. Coexistence of Coherence and Incoherence in Nonlocally Coupled Phase Oscillators. *Nonlin. Phenom. Complex Syst.* **5**, 380 (2002)

[272] D. M. Abrams and S. H. Strogatz. Chimera States in a Ring of Nonlocally Coupled Oscillators. *Int. J. Bifurcat. Chaos* **16**, 21 (2006)

[273] O. E. Omel'chenko, Y. L. Maistrenko, and P. A. Tass. Chimera States: The Natural Link Between Coherence and Incoherence. *Phys. Rev. Lett.* **100**, 044105 (2008)

[274] O. E. Omel'chenko, M. Wolfrum, and Y. L. Maistrenko. Chimera states as chaotic spatiotemporal patterns. *Phys. Rev. E* **81**, 065201 (2010)

[275] I. Omelchenko, O. E. Omel'chenko, P. Hövel, and E. Schöll. When Nonlocal Coupling between Oscillators Becomes Stronger: Patched Synchrony or Multichimera States. *Phys. Rev. Lett.* **110**, 224101 (2013)

[276] R. G. Andrzejak, G. Ruzzene, and I. Malvestio. Generalized synchronization between chimera states. *Chaos* **27**, 053114 (2017)

[277] O. E. Omel'chenko, M. Wolfrum, S. Yanchuk, Y. L. Maistrenko, and O. Sudakov. Stationary patterns of coherence and incoherence in two-dimensional arrays of non-locally-coupled phase oscillators. *Phys. Rev. E* **85**, 036210 (2012)

[278] X. Tang, T. Yang, I. R. Epstein, Y. Liu, Y. Zhao, and Q. Gao. Novel type of chimera spiral waves arising from decoupling of a diffusible component. *J. Chem. Phys.* **141**, 024110 (2014)

[279] B.-W. Li and H. Dierckx. Spiral wave chimeras in locally coupled oscillator systems. *Phys. Rev. E* **93**, 020202 (2016)

[280] A. Schmidt, T. Kasimatis, J. Hizanidis, A. Provata, and P. Hövel. Chimera patterns in two-dimensional networks of coupled neurons. *Phys. Rev. E* **95**, 032224 (2017)

[281] M. Falcke and H. Engel. Influence of global coupling through the gas phase on the dynamics of CO oxidation on Pt(110). *Phys. Rev. E* **50**, 1353 (1994)

[282] Y. Maistrenko, O. Sudakov, O. Osiv, and V. Maistrenko. Chimera states in three dimensions. *New J. Phys.* **17**, 073037 (2015)

[283] H. W. Lau and J. Davidsen. Linked and knotted chimera filaments in oscillatory systems. *Phys. Rev. E* **94**, 010204 (2016)

[284] V. Maistrenko, O. Sudakov, O. Osiv, and Y. Maistrenko. Multiple scroll wave chimera states. *Eur. Phys. J. Spec. Top.* **226**, 1867 (2017)

[285] M. Shanahan. Metastable chimera states in community-structured oscillator networks. *Chaos* **20**, 013108 (2010)

[286] Y. Zhu, Z. Zheng, and J. Yang. Chimera states on complex networks. *Phys. Rev. E* **89**, 022914 (2014)

[287] P. Ashwin and O. Burylko. Weak chimeras in minimal networks of coupled phase oscillators. *Chaos* **25**, 013106 (2015)

[288] X. Jiang and D. M. Abrams. Symmetry-broken states on networks of coupled oscillators. *Phys. Rev. E* **93**, 052202 (2016)

[289] G. Ghoshal, A. P. Muñuzuri, and J. Pérez-Mercader. Emergence of a super-synchronized mobbing state in a large population of coupled chemical oscillators. *Sci. Rep.* **6**, 19186 (2016)

[290] J. Shena, J. Hizanidis, V. Kovanis, and G. P. Tsironis. Turbulent chimeras in large semiconductor laser arrays. *Sci. Rep.* **7**, 42116 (2017)

[291] A. Zakharova, M. Kapeller, and E. Schöll. Chimera Death: Symmetry Breaking in Dynamical Networks. *Phys. Rev. Lett.* **112**, 154101 (2014)

[292] A. Vüllings, J. Hizanidis, I. Omelchenko, and P. Hövel. Clustered chimera states in systems of type-I excitability. *New J. Phys.* **16**, 123039 (2014)

[293] I. Omelchenko, Y. Maistrenko, P. Hövel, and E. Schöll. Loss of Coherence in Dynamical Networks: Spatial Chaos and Chimera States. *Phys. Rev. Lett.* **106**, 234102 (2011)

[294] C. Gu, G. St-Yves, and J. Davidsen. Spiral Wave Chimeras in Complex Oscillatory and Chaotic Systems. *Phys. Rev. Lett.* **111**, 134101 (2013)

[295] G. C. Sethia, A. Sen, and F. M. Atay. Clustered Chimera States in Delay-Coupled Oscillator Systems. *Phys. Rev. Lett.* **100**, 144102 (2008)

[296] F. Böhm, A. Zakharova, E. Schöll, and K. Lüdge. Amplitude-phase coupling drives chimera states in globally coupled laser networks. *Phys. Rev. E* **91**, 040901 (2015)

[297] A. Zakharova, S. A. M. Loos, J. Siebert, A. Gjurchinovski, J. C. Claussen, and E. Schöll. Controlling Chimera Patterns in Networks: Interplay of Structure, Noise, and Delay. In "Control of Self-Organizing Nonlinear Systems", 3–23. Springer (2016)

[298] S. A. M. Loos, J. C. Claussen, E. Schöll, and A. Zakharova. Chimera patterns under the impact of noise. *Phys. Rev. E* **93**, 012209 (2016)

[299] V. Semenov, A. Zakharova, Y. Maistrenko, and E. Schöll. Delayed-feedback chimera states: Forced multiclusters and stochastic resonance. *Europhys. Lett.* **115**, 10005 (2016)

[300] N. Semenova, A. Zakharova, V. Anishchenko, and E. Schöll. Coherence-Resonance Chimeras in a Network of Excitable Elements. *Phys. Rev. Lett.* **117**, 014102 (2016)

[301] A. Buscarino, M. Frasca, L. V. Gambuzza, and P. Hövel. Chimera states in time-varying complex networks. *Phys. Rev. E* **91**, 022817 (2015)

[302] J. Sieber, O. E. Omel'chenko, and M. Wolfrum. Controlling Unstable Chaos: Stabilizing Chimera States by Feedback. *Phys. Rev. Lett.* **112**, 054102 (2014)

[303] C. Bick and E. A. Martens. Controlling chimeras. *New J. Phys.* **17**, 033030 (2015)

[304] I. Omelchenko, O. E. Omel'chenko, A. Zakharova, M. Wolfrum, and E. Schöll. Tweezers for Chimeras in Small Networks. *Phys. Rev. Lett.* **116**, 114101 (2016)

[305] T. Isele, J. Hizanidis, A. Provata, and P. Hövel. Controlling chimera states: The influence of excitable units. *Phys. Rev. E* **93**, 022217 (2016)

[306] F. P. Kemeth, S. W. Haugland, L. Schmidt, I. G. Kevrekidis, and K. Krischer. A classification scheme for chimera states. *Chaos* **26**, 094815 (2016)

[307] C. R. Laing. The dynamics of chimera states in heterogeneous Kuramoto networks. *Physica D* **238**, 1569 (2009)

[308] C. Laing. Chimeras in Two-Dimensional Domains: Heterogeneity and the Continuum Limit. *SIAM J. Appl. Dyn. Syst.* **16**, 974 (2017)

[309] E. Ott and T. M. Antonsen. Low dimensional behavior of large systems of globally coupled oscillators. *Chaos* **18**, 037113 (2008)

[310] D. Cohen, J. Neu, and R. Rosales. Rotating Spiral Wave Solutions of Reaction-Diffusion Equations. *SIAM J. Appl. Math.* **35**, 536 (1978)

[311] E. A. Martens, C. R. Laing, and S. H. Strogatz. Solvable Model of Spiral Wave Chimeras. *Phys. Rev. Lett.* **104**, 044101 (2010)

[312] N. Tompkins, N. Li, C. Girabawe, M. Heymann, G. B. Ermentrout, I. R. Epstein, and S. Fraden. Testing Turing's theory of morphogenesis in chemical cells. *Proc. Natl. Acad. Sci. USA* **111**, 4397 (2014)

[313] I. Z. Kiss, Y. Zhai, and J. L. Hudson. Emerging Coherence in a Population of Chemical Oscillators. *Science* **296**, 1676 (2002)

[314] D. K. Verma, H. Singh, P. Parmananda, A. Q. Contractor, and M. Rivera. Kuramoto transition in an ensemble of mercury beating heart systems. *Chaos* **25**, 064609 (2015)

[315] P. R. Buskohl, R. C. Kramb, and R. A. Vaia. Synchronicity in Composite Hydrogels: Belousov–Zhabotinsky (BZ) Active Nodes in Gelatin. *J. Phys. Chem. B* **119**, 3595 (2015)

[316] D. P. Rosin, D. Rontani, N. D. Haynes, E. Schöll, and D. J. Gauthier. Transient scaling and resurgence of chimera states in networks of Boolean phase oscillators. *Phys. Rev. E* **90**, 030902 (2014)

[317] M. R. Tinsley, A. F. Taylor, Z. Huang, and K. Showalter. Emergence of Collective Behavior in Groups of Excitable Catalyst-Loaded Particles: Spatiotemporal Dynamical Quorum Sensing. *Phys. Rev. Lett.* **102**, 158301 (2009)

[318] B. Neumann, Z. Nagy-Ungvarai, and S. Müller. Interaction between silica gel matrices and the Belousov-Zhabotinsky reaction. *Chem. Phys. Lett.* **211**, 36 (1993)

[319] D. J. Watts and S. H. Strogatz. Collective dynamics of 'small-world' networks. *Nature* **393**, 440 (1998)

[320] D. Witthaut and M. Timme. Braess's paradox in oscillator networks, desynchronization and power outage. *New J. Phys.* **14**, 083036 (2012)

[321] L. R. Varshney, B. L. Chen, E. Paniagua, D. H. Hall, and D. B. Chklovskii. Structural Properties of the Caenorhabditis elegans Neuronal Network. *PLOS Comput. Biol.* **7**, e1001066 (2011)

[322] T. A. Jarrell, Y. Wang, A. E. Bloniarz, C. A. Brittin, M. Xu, J. N. Thomson, D. G. Albertson, D. H. Hall, and S. W. Emmons. The Connectome of a Decision-Making Neural Network. *Science* **337**, 437 (2012)

[323] P. Hänggi and P. Jung. Colored Noise in Dynamical Systems. In I. Prigogine and S. A. Rice, eds., "Advances in Chemical Physics", 239–326. Wiley (1994)

[324] N. G. V. Kampen. Stochastic Processes in Physics and Chemistry. Elsevier (2011)

[325] K. Yoshikawa, R. Aihara, and K. Agladze. Size-Dependent Belousov-Zhabotinsky Oscillation in Small Beads. *J. Phys. Chem. A* **102**, 7649 (1998)

[326] A. M. Zhabotinsky, F. Buchholtz, A. B. Kiyatkin, and I. R. Epstein. Oscillations and waves in metal-ion-catalyzed bromate oscillating reactions in highly oxidized states. *J. Phys. Chem.* **97**, 7578 (1993)

[327] R. Toth, A. F. Taylor, and M. R. Tinsley. Collective Behavior of a Population of Chemically Coupled Oscillators. *J. Phys. Chem. B* **110**, 10170 (2006)

[328] S. Kádár, T. Amemiya, and K. Showalter. Reaction Mechanism for Light Sensitivity of the Ru(bpy)32+-Catalyzed Belousov-Zhabotinsky Reaction. *J. Phys. Chem. A* **101**, 8200 (1997)

[329] I. Omelchenko, A. Zakharova, P. Hövel, J. Siebert, and E. Schöll. Nonlinearity of local dynamics promotes multi-chimeras. *Chaos* **25**, 083104 (2015)

[330] I. Omelchenko, A. Provata, J. Hizanidis, E. Schöll, and P. Hövel. Robustness of chimera states for coupled FitzHugh-Nagumo oscillators. *Phys. Rev. E* **91**, 022917 (2015)

[331] M.-A. Bray and J. P. Wikswo. Use of topological charge to determine filament location and dynamics in a numerical model of scroll wave activity. *IEEE Trans. Biomed. Eng.* **49**, 1086 (2002)

[332] M. J. Panaggio and D. M. Abrams. Chimera states on the surface of a sphere. *Phys. Rev. E* **91**, 022909 (2015)

[333] A. A. Selivanov, J. Lehnert, T. Dahms, P. Hövel, A. L. Fradkov, and E. Schöll. Adaptive synchronization in delay-coupled networks of Stuart-Landau oscillators. *Phys. Rev. E* **85**, 016201 (2012)

[334] J. F. Totz, J. Rode, M. R. Tinsley, K. Showalter, and H. Engel. Spiral wave chimera states in large populations of coupled chemical oscillators. *Nat. Phys.* 1 (2017)

[335] A. T. Winfree. Varieties of spiral wave behavior: An experimentalist's approach to the theory of excitable media. *Chaos* **1**, 303 (1991)

[336] D. Frenkel and B. Smit. Understanding Molecular Simulation: From Algorithms to Applications. Academic Press (2001)

[337] D. Barkley, M. Kness, and L. S. Tuckerman. Spiral-wave dynamics in a simple model of excitable media: The transition from simple to compound rotation. *Phys. Rev. A* **42**, 2489 (1990)

[338] W. Jahnke, W. E. Skaggs, and A. T. Winfree. Chemical vortex dynamics in the Belousov-Zhabotinskii reaction and in the two-variable Oregonator model. *J. Phys. Chem.* **93**, 740 (1989)

[339] D. Barkley. Euclidean symmetry and the dynamics of rotating spiral waves. *Phys. Rev. Lett.* **72**, 164 (1994)

[340] M. Wolfrum and O. E. Omel'chenko. Chimera states are chaotic transients. *Phys. Rev. E* **84**, 015201 (2011)

[341] Y. L. Maistrenko, A. Vasylenko, O. Sudakov, R. Levchenko, and V. L. Maistrenko. Cascades of Multiheaded Chimera States for Coupled Phase Oscillators. *Int. J. Bifurcation Chaos* **24**, 1440014 (2014)

[342] I. Sendiña-Nadal, S. Alonso, V. Pérez-Muñuzuri, M. Gómez-Gesteira, V. Pérez-Villar, L. Ramírez-Piscina, J. Casademunt, J. M. Sancho, and F. Sagués. Brownian Motion of Spiral Waves Driven by Spatiotemporal Structured Noise. *Phys. Rev. Lett.* **84**, 2734 (2000)

[343] C. Brito, I. S. Aranson, and H. Chaté. Vortex Glass and Vortex Liquid in Oscillatory Media. *Phys. Rev. Lett.* **90**, 068301 (2003)

[344] M. Bär and M. Eiswirth. Turbulence due to spiral breakup in a continuous excitable medium. *Phys. Rev. E* **48**, R1635 (1993)

[345] M. Bär and L. Brusch. Breakup of spiral waves caused by radial dynamics: Eckhaus and finite wavenumber instabilities. *New J. Phys.* **6**, 5 (2004)

[346] Z. Nagy-Ungvarai and S. Müller. Characterization of Wave Front Instabilities in the Belousov-Zhabotinsky Raction: An Overview. *Int. J. Bifurc. Chaos* **04**, 1257 (1994)

[347] L. Glass and M. C. Mackey. From Clocks to Chaos: The Rhythms of Life. Princeton University Press (1988)

[348] E. M. Izhikevich. Dynamical Systems in Neuroscience. MIT Press (2007)

[349] N. W. Schultheiss, A. A. Prinz, and R. J. Butera. Phase Response Curves in Neuroscience: Theory, Experiment, and Analysis, volume 6. Springer (2011)

[350] L. Glass and A. T. Winfree. Discontinuities in phase-resetting experiments. *Am. J. Physiol. Regul. Integr. Comp. Physiol.* **246**, R251 (1984)

[351] J. Jalife and G. K. Moe. Effect of electrotonic potentials on pacemaker activity of canine Purkinje fibers in relation to parasystole. *Circ. Res.* **39**, 801 (1976)

[352] M. R. Guevara, A. Shrier, and L. Glass. Phase resetting of spontaneously beating embryonic ventricular heart cell aggregates. *Am. J. Physiol. Heart Circ. Physiol.* **251**, H1298 (1986)

[353] J. M. Anumonwo, M. Delmar, A. Vinet, D. C. Michaels, and J. Jalife. Phase resetting and entrainment of pacemaker activity in single sinus nodal cells. *Circ. Res.* **68**, 1138 (1991)

[354] D. F. Russell. Respiratory pattern generation in adult lampreys (Lampetra fluviatilis): Interneurons and burst resetting. *J. Comp. Physiol.* **158**, 91 (1986)

[355] R. Wessel. In vitro study of phase resetting and phase locking in a time-comparison circuit in the electric fish, Eigenmannia. *Biophys. J.* **69**, 1880 (1995)

[356] A. A. Prinz, V. Thirumalai, and E. Marder. The Functional Consequences of Changes in the Strength and Duration of Synaptic Inputs to Oscillatory Neurons. *J. Neurosci.* **23**, 943 (2003)

[357] S. B. S. Khalsa, M. E. Jewett, C. Cajochen, and C. A. Czeisler. A Phase Response Curve to Single Bright Light Pulses in Human Subjects. *J. Physiol.* **549**, 945 (2003)

[358] C. H. Johnson and J. W. Hastings. Circadian Phototransduction: Phase Resetting and Frequency of the Circadian Clock of Gonyaulax Cells in Red Light. *J. Biol. Rhythms* **4**, 417 (1989)

[359] V. Varma, N. Mukherjee, N. N. Kannan, and V. K. Sharma. Strong (Type 0) Phase Resetting of Activity-Rest Rhythm in Fruit Flies, Drosophila Melanogaster, at Low Temperature. *J. Biol. Rhythms* **28**, 380 (2013)

[360] J. Rode. Synchronization in Heterogeneous Networks - From Phase to Relaxation Oscillators. M.Sc. Thesis, TU Berlin (2016)

[361] J. F. Totz. Wechselwirkung spiralförmiger Erregungswellen mit kreisförmigen Heterogenitäten. B.Sc. thesis, TU Berlin, Berlin (2011)

[362] E. Nakouzi, J. F. Totz, Z. Zhang, O. Steinbock, and H. Engel. Hysteresis and drift of spiral waves near heterogeneities: From chemical experiments to cardiac simulations. *Phys. Rev. E* **93**, 022203 (2016)

[363] S. Alonso and M. Bär. Reentry Near the Percolation Threshold in a Heterogeneous Discrete Model for Cardiac Tissue. *Phys. Rev. Lett.* **110**, 158101 (2013)

[364] A. Rothkegel and K. Lehnertz. Irregular macroscopic dynamics due to chimera states in small-world networks of pulse-coupled oscillators. *New J. Phys.* **16**, 055006 (2014)

[365] S.-y. Takemura, et al. A visual motion detection circuit suggested by *Drosophila* connectomics. *Nature* **500**, 175 (2013)

[366] Y. Chen, S. Wang, C. C. Hilgetag, and C. Zhou. Features of spatial and functional segregation and integration of the primate connectome revealed by trade-off between wiring cost and efficiency. *PLOS Comput. Biol.* **13**, e1005776 (2017)

[367] S. Boccaletti, J. A. Almendral, S. Guan, I. Leyva, Z. Liu, I. Sendiña-Nadal, Z. Wang, and Y. Zou. Explosive transitions in complex networks' structure and dynamics: Percolation and synchronization. *Phys. Rep.* **660**, 1 (2016)

[368] B. Pietras, N. Deschle, and A. Daffertshofer. Equivalence of coupled networks and networks with multimodal frequency distributions: Conditions for the bimodal and trimodal case. *Phys. Rev. E* **94**, 052211 (2016)

[369] S. M. Bohte, J. N. Kok, and H. La Poutré. Error-backpropagation in temporally encoded networks of spiking neurons. *Neurocomputing* **48**, 17 (2002)

[370] R. Bates, O. Blyuss, and A. Zaikin. Stochastic resonance in an intracellular genetic perceptron. *Phys. Rev. E* **89**, 032716 (2014)

[371] L. Gammaitoni, P. Hänggi, P. Jung, and F. Marchesoni. Stochastic resonance. *Rev. Mod. Phys.* **70**, 223 (1998)

[372] H. Gang, T. Ditzinger, C. Z. Ning, and H. Haken. Stochastic resonance without external periodic force. *Phys. Rev. Lett.* **71**, 807 (1993)

[373] A. S. Pikovsky and J. Kurths. Coherence Resonance in a Noise-Driven Excitable System. *Phys. Rev. Lett.* **78**, 775 (1997)

[374] K. Wimmer, D. Q. Nykamp, C. Constantinidis, and A. Compte. Bump attractor dynamics in prefrontal cortex explains behavioral precision in spatial working memory. *Nat. Neurosci.* **17**, 431 (2014)

[375] A. H. Cohen and P. Wallén. The neuronal correlate of locomotion in fish. *Exp. Brain Res.* **41**, 11 (1980)

[376] I. Delvolvé, P. Branchereau, R. Dubuc, and J.-M. Cabelguen. Fictive Rhythmic Motor Patterns Induced by NMDA in an In Vitro Brain Stem–Spinal Cord Preparation From an Adult Urodele. *J. Neurophysiol.* **82**, 1074 (1999)

[377] M. Salathé, M. Kazandjieva, J. W. Lee, P. Levis, M. W. Feldman, and J. H. Jones. A high-resolution human contact network for infectious disease transmission. *Proc. Natl. Acad. Sci. USA* **107**, 22020 (2010)

[378] D. Brockmann and D. Helbing. The Hidden Geometry of Complex, Network-Driven Contagion Phenomena. *Science* **342**, 1337 (2013)

[379] T. W. Valente. Network Models of the Diffusion of Innovations. Hampton Press (1995)

[380] A. E. Pereda. Electrical synapses and their functional interactions with chemical synapses. *Nat. Rev. Neurosci.* **15**, 250 (2014)

[381] L. Hegedüs, M. Wittmann, Z. Noszticzius, S. Yan, A. Sirimungkala, H.-D. Försterling, and R. J. Field. HPLC analysis of complete BZ systems. Evolution of the chemical composition in cerium and ferroin catalysed batch oscillators: Experiments and model calculations. *Faraday Discuss.* **120**, 21 (2001)

[382] A. Erisir, D. Lau, B. Rudy, and C. S. Leonard. Function of Specific K+ Channels in Sustained High-Frequency Firing of Fast-Spiking Neocortical Interneurons. *J. Neurophysiol.* **82**, 2476 (1999)

[383] V. Iyer, R. Mazhari, and R. L. Winslow. A Computational Model of the Human Left-Ventricular Epicardial Myocyte. *Biophys. J.* **87**, 1507 (2004)

[384] S. Vajda and T. Turanyi. Principal component analysis for reducing the Edelson-Field-Noyes model of the Belousov-Zhabotinskii reaction. *J. Phys. Chem.* **90**, 1664 (1986)

[385] R. A. Gray, J. P. Wikswo, and N. F. Otani. Origin choice and petal loss in the flower garden of spiral wave tip trajectories. *Chaos* **19**, 033118 (2009)

[386] L. Cohen. Time-frequency Analysis. Prentice Hall (1995)

[387] N. E. Huang, Z. Shen, S. R. Long, M. C. Wu, H. H. Shih, Q. Zheng, N.-C. Yen, C. C. Tung, and H. H. Liu. The empirical mode decomposition and the Hilbert spectrum for nonlinear and non-stationary time series analysis. *Proc. R. Soc. A* **454**, 903 (1998)

[388] S. A. Oprisan. A Geometric Approach to Phase Resetting Estimation Based on Mapping Temporal to Geometric Phase. In "Phase Response Curves in Neuroscience: Theory, Experiment, and Analysis", 131–162. Springer (2011)

[389] J. K. Kevorkian and J. D. Cole. Multiple Scale and Singular Perturbation Methods. Springer (1996)

[390] C. M. Bender and S. A. Orszag. Advanced Mathematical Methods for Scientists and Engineers I: Asymptotic Methods and Perturbation Theory. Springer (1999)

[391] M. A. Schwemmer and T. J. Lewis. The Theory of Weakly Coupled Oscillators. In N. W. Schultheiss, A. A. Prinz, and R. J. Butera, eds., "Phase Response Curves in Neuroscience", 3–31. Springer (2012)

[392] R. Haberman. Applied Partial Differential Equations: With Fourier Series and Boundary Value Problems. Pearson (2013)

[393] K. Kuttler. Elementary Linear Algebra. Saylor Foundation (2012)

[394] P. A. M. Dirac. A new notation for quantum mechanics. *Math. Proc. Camb. Philos. Soc.* **35**, 416 (1939)

[395] G. Chacón, H. Rafeiro, and J. C. Vallejo. Functional Analysis: A Terse Introduction. de Gruyter (2016)

[396] F. C. Hoppensteadt and E. M. Izhikevich. Weakly Connected Neural Networks. Springer (1997)

[397] A. F. Taylor, M. R. Tinsley, F. Wang, Z. Huang, and K. Showalter. Dynamical Quorum Sensing and Synchronization in Large Populations of Chemical Oscillators. *Science* **323**, 614 (2009)

[398] S. Ghosh and S. Jalan. Emergence of Chimera in Multiplex Network. *Int. J. Bifurcation Chaos* **26**, 1650120 (2016)

[399] J. Gómez-Gardeñes, S. Gómez, A. Arenas, and Y. Moreno. Explosive Synchronization Transitions in Scale-Free Networks. *Phys. Rev. Lett.* **106**, 128701 (2011)

[400] Y. Kuramoto. Self-entrainment of a population of coupled non-linear oscillators. In "International Symposium on Mathematical Problems in Theoretical Physics", 420–422. Springer (1975)

[401] A. T. Winfree. On Emerging Coherence. *Science* **298**, 2336 (2002)

[402] A. T. Winfree. Two kinds of wave in an oscillating chemical solution. *Faraday Symp. Chem. Soc.* **9**, 38 (1974)

[403] B. Fiedler, B. Sandstede, A. Scheel, and C. Wulff. Bifurcation from Relative Equilibria of Noncompact Group Actions: Skew Products, Meanders, and Drifts. *Doc. Math. J. DMV* **1**, 479 (1996)

[404] R. B. Hoyle. Pattern Formation: An Introduction to Methods. Cambridge University Press (2006)

[405] N. D. Mermin. The topological theory of defects in ordered media. *Rev. Mod. Phys.* **51**, 591 (1979)

[406] D. Barkley, V. N. Biktashev, I. V. Biktasheva, G. V. Bordyugov, and A. J. Foulkes. DXSpiral: Code for studying spiral waves on a disk (2008)

[407] H. Dierckx, O. Bernus, and H. Verschelde. A geometric theory for scroll wave filaments in anisotropic excitable media. *Physica D* **238**, 941 (2009)

[408] I. V. Biktasheva, D. Barkley, V. N. Biktashev, and A. J. Foulkes. Computation of the drift velocity of spiral waves using response functions. *Phys. Rev. E* **81**, 066202 (2010)

[409] C. D. Marcotte and R. O. Grigoriev. Adjoint eigenfunctions of temporally recurrent single-spiral solutions in a simple model of atrial fibrillation. *Chaos* **26**, 093107 (2016)

[410] S. Dineen. Multivariate Calculus and Geometry. Springer (2014)

[411] H. Verschelde, H. Dierckx, and O. Bernus. Covariant Stringlike Dynamics of Scroll Wave Filaments in Anisotropic Cardiac Tissue. *Phys. Rev. Lett.* **99**, 168104 (2007)

[412] F. K. Manasse and C. W. Misner. Fermi Normal Coordinates and Some Basic Concepts in Differential Geometry. *J. Math. Phys* **4**, 735 (1963)

[413] M. Wellner, O. Berenfeld, J. Jalife, and A. M. Pertsov. Minimal principle for rotor filaments. *Proc. Natl. Acad. Sci. USA* **99**, 8015 (2002)

[414] A. S. Mikhailov. Three-dimensional kinematics. *Chaos* **5**, 673 (1995)

[415] H. J. Krug, L. Pohlmann, and L. Kuhnert. Analysis of the modified complete Oregonator accounting for oxygen sensitivity and photosensitivity of Belousov-Zhabotinskii systems. *J. Phys. Chem.* **94**, 4862 (1990)

[416] V. Gáspár, G. Basza, and M. T. Beck. The Influence of Visible Light on the Belousov-Zhabotinskii Oscillating Reactions applying Different Catalysts. *Z. Phys. Chem.* **264**, 43 (1983)

[417] H. Fukuda, H. Nagano, and S. Kai. Stochastic Synchronization in Two-Dimensional Coupled Lattice Oscillators in the Belousov–Zhabotinsky Reaction. *J. Phys. Soc. Jpn.* **72**, 487 (2003)

[418] T. Okano, A. Kitagawa, and K. Miyakawa. Array-enhanced coherence resonance and phase synchronization in a two-dimensional array of excitable chemical oscillators. *Phys. Rev. E* **76**, 046201 (2007)

[419] A. F. Taylor, P. Kapetanopoulos, B. J. Whitaker, R. Toth, L. Bull, and M. R. Tinsley. Clusters and Switchers in Globally Coupled Photochemical Oscillators. *Phys. Rev. Lett.* **100**, 214101 (2008)

[420] C. E. Carraher, Jr. Introduction to Polymer Chemistry. CRC Press (2017)

[421] M. Toiya, V. K. Vanag, and I. R. Epstein. Diffusively Coupled Chemical Oscillators in a Microfluidic Assembly. *Angew. Chem. Int. Ed.* **47**, 7753 (2008)

[422] M. Toiya, H. O. González-Ochoa, V. K. Vanag, S. Fraden, and I. R. Epstein. Synchronization of Chemical Micro-oscillators. *J. Phys. Chem. Lett.* **1**, 1241 (2010)

[423] L. Martínez, R. Andrade, E. G. Birgin, and J. M. Martínez. PACKMOL: A package for building initial configurations for molecular dynamics simulations. *J. Comput. Chem.* **30**, 2157 (2009)

[424] W. Humphrey, A. Dalke, and K. Schulten. VMD: Visual molecular dynamics. *J. Mol. Graph.* **14**, 33 (1996)

[425] E. Dubrofsky. Homography Estimation. M.Sc. Thesis, University of British Columbia, Vancouver (2009)

[426] S. H. Strogatz. Nonlinear Dynamics and Chaos: With Applications to Physics, Biology, Chemistry, and Engineering. Westview Press (2014)

[427] A.-K. Kassam and L. N. Trefethen. Fourth-Order Time-Stepping for Stiff PDEs. *SIAM J. Sci. Comput.* **26**, 1214 (2005)

[428] J. Sanders and E. Kandrot. CUDA by Example: An Introduction to General-Purpose GPU Programming. Addison-Wesley (2010)

[429] W.-m. Hwu. GPU Computing Gems Emerald Edition. Elsevier (2011)

[430] J. Cheng, M. Grossman, and T. McKercher. Professional CUDA C Programming. John Wiley & Sons (2014)

[431] R. J. Field and M. Burger, eds. Oscillations and Traveling Waves in Chemical Systems. Wiley (1985)

[432] J. J. Tyson. What Everyone Should Know About the Belousov-Zhabotinsky Reaction. In S. A. Levin, ed., "Frontiers in Mathematical Biology", 569–587. Springer (1994)

[433] A. F. Taylor. Mechanism and Phenomenology of an Oscillating Chemical Reaction. *Prog. React. Kinet. Mech.* **27**, 247 (2002)

[434] R. Toth and A. F. Taylor. The tris(2,2'-bipyridyl)ruthenium-catalysed Belousov–Zhabotinsky reaction. *Prog. React. Kinet. Mech.* **31**, 59 (2006)

[435] R. A. Schmitz, K. R. Graziani, and J. L. Hudson. Experimental evidence of chaotic states in the Belousov–Zhabotinskii reaction. *J. Chem. Phys.* **67**, 3040 (1977)

[436] R. J. Field. Chaos in the Belousov–Zhabotinsky reaction. *Mod. Phys. Lett. B* **29**, 1530015 (2015)

[437] V. Petrov, V. Gáspár, J. Masere, and K. Showalter. Controlling chaos in the Belousov—Zhabotinsky reaction. *Nature* **361**, 240 (1993)

[438] J. L. Hudson, M. Hart, and D. Marinko. An experimental study of multiple peak periodic and nonperiodic oscillations in the Belousov–Zhabotinskii reaction. *J. Chem. Phys.* **71**, 1601 (1979)

[439] A. T. Winfree. Rotating Chemical Reactions. *Sci. Am.* **230**, 82 (1974)

[440] O. Steinbock, J. Schütze, and S. C. Müller. Electric-field-induced drift and deformation of spiral waves in an excitable medium. *Phys. Rev. Lett.* **68**, 248 (1992)

[441] A. Guderian, G. Dechert, K.-P. Zeyer, and F. W. Schneider. Stochastic Resonance in Chemistry. 1. The Belousov-Zhabotinsky Reaction. *J. Phys. Chem.* **100**, 4437 (1996)

[442] S. Kádár, J. Wang, and K. Showalter. Noise-supported travelling waves in sub-excitable media. *Nature* **391**, 770 (1998)

[443] K. Miyakawa and H. Isikawa. Experimental observation of coherence resonance in an excitable chemical reaction system. *Phys. Rev. E* **66**, 046204 (2002)

[444] V. Beato, I. Sendiña-Nadal, I. Gerdes, and H. Engel. Coherence resonance in a chemical excitable system driven by coloured noise. *Phil. Trans. R. Soc. Lond. A* **366**, 381 (2008)

[445] V. Vanag and I. Epstein. Pattern Formation in a Tunable Medium: The Belousov-Zhabotinsky Reaction in an Aerosol OT Microemulsion. *Phys. Rev. Lett.* **87** (2001)

[446] T. Bánsági, V. K. Vanag, and I. R. Epstein. Tomography of Reaction-Diffusion Microemulsions Reveals Three-Dimensional Turing Patterns. *Science* **331**, 1309 (2011)

[447] K. Agladze, R. R. Aliev, T. Yamaguchi, and K. Yoshikawa. Chemical Diode. *J. Phys. Chem.* **100**, 13895 (1996)

[448] A. Adamatzky and B. D. L. Costello. Reaction–Diffusion Computing. In G. Rozenberg, T. Bäck, and J. N. Kok, eds., "Handbook of Natural Computing", 1897–1920. Springer (2012)

[449] J. Gorecki, K. Gizynski, J. Guzowski, J. N. Gorecka, P. Garstecki, G. Gruenert, and P. Dittrich. Chemical computing with reaction–diffusion processes. *Phil. Trans. R. Soc. A* **373**, 20140219 (2015)

[450] Y. Fang, V. V. Yashin, S. P. Levitan, and A. C. Balazs. Pattern recognition with "materials that compute". *Sci. Adv.* **2**, e1601114 (2016)

[451] A. L. Wang, J. M. Gold, N. Tompkins, M. Heymann, K. I. Harrington, and S. Fraden. Configurable NOR gate arrays from Belousov-Zhabotinsky micro-droplets. *Eur. Phys. J. ST* **225**, 211 (2016)

[452] L. Kuhnert. A new optical photochemical memory device in a light-sensitive chemical active medium. *Nature* **319**, 393 (1986)

[453] A. Kaminaga, V. K. Vanag, and I. R. Epstein. A Reaction–Diffusion Memory Device. *Angew. Chem. Int. Ed.* **45**, 3087 (2006)

[454] L. Kuhnert, K. I. Agladze, and V. I. Krinsky. Image processing using light-sensitive chemical waves. *Nature* **337**, 244 (1989)

[455] J. Ren, X. Zhang, J. Gao, and W. Yang. The application of oscillating chemical reactions to analytical determinations. *Cent. Eur. J. Chem.* **11**, 1023 (2013)

[456] N. J. Suematsu, Y. Mori, T. Amemiya, and S. Nakata. Oscillation of Speed of a Self-Propelled Belousov–Zhabotinsky Droplet. *J. Phys. Chem. Lett.* **7**, 3424 (2016)

[457] E. M. Bollt and M. Dolnik. Encoding information in chemical chaos by controlling symbolic dynamics. *Phys. Rev. E* **55**, 6404 (1997)

[458] D. A. McQuarrie and J. D. Simon. Physical Chemistry: A Molecular Approach. University Science Books (1997)

[459] R. M. Noyes, R. Field, and E. Koros. Oscillations in chemical systems. I. Detailed mechanism in a system showing temporal oscillations. *J. Am. Chem. Soc.* **94**, 1394 (1972)

[460] R. J. Field, E. Koros, and R. M. Noyes. Oscillations in chemical systems. II. Thorough analysis of temporal oscillation in the bromate-cerium-malonic acid system. *J. Am. Chem. Soc.* **94**, 8649 (1972)

[461] R. J. Field and R. M. Noyes. Oscillations in Chemical Systems III. Explanation of Spatial Band Propagation in the Belousov Reaction. *Nature* **237**, 390 (1972)

[462] R. J. Field and R. M. Noyes. Oscillations in chemical systems. IV. Limit cycle behavior in a model of a real chemical reaction. *J. Chem. Phys.* **60**, 1877 (1974)

[463] R. J. Field and R. M. Noyes. Oscillations in chemical systems. V. Quantitative explanation of band migration in the Belousov-Zhabotinskii reaction. *J. Am. Chem. Soc.* **96**, 2001 (1974)

[464] N. Li, N. Tompkins, H. Gonzalez-Ochoa, and S. Fraden. Tunable diffusive lateral inhibition in chemical cells. *Eur. Phys. J. E* **38** (2015)

[465] J. Boissonade and P. De Kepper. Transitions from bistability to limit cycle oscillations. Theoretical analysis and experimental evidence in an open chemical system. *J. Phys. Chem.* **84**, 501 (1980)

[466] P. De Kepper, I. R. Epstein, and K. Kustin. A systematically designed homogeneous oscillating reaction: The arsenite-iodate-chlorite system. *J. Am. Chem. Soc.* **103**, 2133 (1981)

[467] I. R. Epstein, K. Kustin, P. D. Kepper, and M. Orbán. Oscillating Chemical Reactions. *Sci. Am.* **248**, 112 (1983)

[468] P. W. Atkins and J. D. Paula. Atkins' Physical Chemistry. Oxford University Press (2002)

[469] A. Tzalmona, R. L. Armstrong, M. Menzinger, A. Cross, and C. Lemaire. Detection of chemical waves by magnetic resonance imaging. *Chem. Phys. Lett.* **174**, 199 (1990)

[470] U. Franck and W. Geiseler. Zur periodischen Reaktion von Malonsäure mit Kaliumbromat in Gegenwart von Cer-Ionen. *Sci. Nat.* **58**, 52 (1971)

[471] I. Lamprecht, B. Schaarschmidt, and T. Plesser. Heat production in oscillating chemical reactions: Three examples. *Thermochim. Acta* **112**, 95 (1987)

[472] F. Bolletta and V. Balzani. Oscillating chemiluminescence from the reduction of bromate by malonic acid catalyzed by tris(2,2'-bipyridine)ruthenium(II). *J. Am. Chem. Soc.* **104**, 4250 (1982)

[473] M. Iranifam, M. A. Segundo, J. L. M. Santos, J. L. F. C. Lima, and M. H. Sorouraddin. Oscillating chemiluminescence systems: State of the art. *Luminescence* **25**, 409 (2010)

[474] S. Campagna, F. Puntoriero, F. Nastasi, G. Bergamini, and V. Balzani. Photochemistry and Photophysics of Coordination Compounds: Ruthenium. In V. Balzani and S. Campagna, eds., "Photochemistry and Photophysics of Coordination Compounds I", 117–214. Springer (2007)

[475] D. W. Thompson, A. Ito, and T. J. Meyer. [Ru(bpy)32+* and other remarkable metal-to-ligand charge transfer (MLCT) excited states. *Pure Appl. Chem., PAC* **85**, 1257 (2013)

[476] L. Ren, B. Fan, Q. Gao, Y. Zhao, H. Luo, Y. Xia, X. Lu, and I. R. Epstein. Experimental, numerical, and mechanistic analysis of the nonmonotonic relationship between oscillatory frequency and photointensity for the photosensitive Belousov–Zhabotinsky oscillator. *Chaos* **25**, 064607 (2015)

[477] F. E. Lytle and D. M. Hercules. Luminescence of tris(2,2'-bipyridine)ruthenium(II) dichloride. *J. Am. Chem. Soc.* **91**, 253 (1969)

[478] F. Bolletta, L. Prodi, and N. Zaccheroni. Oscillating luminescence in the Belousov-Zhabotinsky reaction catalyzed by Ru(bpy)32+. *Inorg. Chim. Acta* **233**, 21 (1995)

[479] J. W. Dobrucki. Interaction of oxygen-sensitive luminescent probes Ru(phen)32+ and Ru(bipy)32+ with animal and plant cells in vitro: Mechanism of phototoxicity and conditions for non-invasive oxygen measurements. *J. Photochem. Photobiol. B* **65**, 136 (2001)

[480] G. Orellana and D. García-Fresnadillo. Environmental and Industrial Optosensing with Tailored Luminescent Ru(II) Polypyridyl Complexes. In "Optical Sensors", 309–357. Springer (2004)

[481] T. P. Yoon, M. A. Ischay, and J. Du. Visible light photocatalysis as a greener approach to photochemical synthesis. *Nat. Chem.* **2**, 527 (2010)

[482] C. K. Prier, D. A. Rankic, and D. W. C. MacMillan. Visible Light Photoredox Catalysis with Transition Metal Complexes: Applications in Organic Synthesis. *Chem. Rev.* **113**, 5322 (2013)

[483] S. Topcagic and S. D. Minteer. Development of a membraneless ethanol/oxygen biofuel cell. *Electrochim. Acta* **51**, 2168 (2006)

[484] M. K. Nazeeruddin, C. Klein, P. Liska, and M. Grätzel. Synthesis of novel ruthenium sensitizers and their application in dye-sensitized solar cells. *Coord. Chem. Rev.* **249**, 1460 (2005)

[485] F. G. Gao and A. J. Bard. Solid-State Organic Light-Emitting Diodes Based on Tris(2,2'-bipyridine)ruthenium(II) Complexes. *J. Am. Chem. Soc.* **122**, 7426 (2000)

[486] A. Ruggi, C. Beekman, D. Wasserberg, V. Subramaniam, D. N. Reinhoudt, F. W. B. van Leeuwen, and A. H. Velders. Dendritic Ruthenium(II)-Based Dyes Tuneable for Diagnostic or Therapeutic Applications. *Chem. Eur. J.* **17**, 464 (2011)

[487] K. T. Hufziger, F. S. Thowfeik, D. J. Charboneau, I. Nieto, W. G. Dougherty, W. S. Kassel, T. J. Dudley, E. J. Merino, E. T. Papish, and J. J. Paul. Ruthenium dihydroxybipyridine complexes are tumor activated prodrugs due to low pH and blue light induced ligand release. *J. Inorg. Biochem.* **130**, 103 (2014)

[488] C. Luengviriya, U. Storb, M. J. B. Hauser, and S. C. Müller. An elegant method to study an isolated spiral wave in a thin layer of a batch Belousov–Zhabotinsky reaction under oxygen-free conditions. *Phys. Chem. Chem. Phys.* **8**, 1425 (2006)

[489] P. K. Ghosh, B. S. Brunschwig, M. Chou, C. Creutz, and N. Sutin. Thermal and light-induced reduction of the ruthenium complex cation Ru(bpy)33+ in aqueous solution. *J. Am. Chem. Soc.* **106**, 4772 (1984)

[490] N. Bergman, A. Thapper, S. Styring, J. Bergquist, and D. Shevchenko. Quantitative determination of the Ru(bpy)32+ cation in photochemical reactions by matrix-assisted laser desorption/ionization time-of-flight mass spectrometry. *Anal. Methods* **6**, 8513 (2014)

[491] T. Ueki, M. Watanabe, and R. Yoshida. Belousov–Zhabotinsky Reaction in Protic Ionic Liquids. *Angew. Chem. Int. Ed.* **51**, 11991 (2012)

[492] T. Ueki, K. Matsukawa, T. Masuda, and R. Yoshida. Protic Ionic Liquids for the Belousov–Zhabotinsky Reaction: Aspects of the BZ Reaction in Protic Ionic Liquids and Its Use for the Autonomous Coil–Globule Oscillation of a Linear Polymer. *J. Phys. Chem. B* **121**, 4592 (2017)

[493] K. Kurin-Csörgei, I. Szalai, and E. Kőrös. The 1,4-cyclohexanedione-bromate-acid oscillatory system II. Chemical waves. *React. Kinet. Catal. Lett.* **54**, 217 (1995)

[494] K. Kurin-Csörgei, A. M. Zhabotinsky, M. Orbán, and I. R. Epstein. Bromate-1,4-Cyclohexanedione-Ferroin Gas-Free Oscillating Reaction. 1. Basic Features and Crossing Wave Patterns in a Reaction-Diffusion System without Gel. *J. Phys. Chem.* **100**, 5393 (1996)

[495] V. Gáspár and R. J. Field. Comment on "Simple KBrO3, H2SO4 Batch Oscillator". *J. Phys. Chem. A* **113**, 7979 (2009)

[496] R. A. Palmer and T. S. Piper. 2,2'-Bipyridine Complexes. I. Polarized Crystal Spectra of Tris (2,2'-bipyridine)copper(II), -nickel(II), -cobalt(II), -iron(II), and -ruthenium(II). *Inorg. Chem.* **5**, 864 (1966)

[497] I. Fujita and H. Kobayashi. Luminescence polarization of the tris(2,2'-bipyridine)ruthenium(II) complex. *Inorg. Chem.* **12**, 2758 (1973)

[498] X. Xiao, J. Sakamoto, M. Tanabe, S. Yamazaki, S. Yamabe, and T. Matsumura-Inoue. Microwave synthesis and electrospectrochemical study on ruthenium(II) polypyridine complexes. *J. Electroanal. Chem.* **527**, 33 (2002)

[499] E. Benoît, J. L. Callot, F. Diener, and M. Diener. Chasse au canard. *Collect. Math.* **32**, 37 (1981)

[500] J. Guckenheimer, K. Hoffman, and W. Weckesser. Numerical computation of canards. *Int. J. Bifurcation Chaos* **10**, 2669 (2000)

[501] E. B. Robertson and H. B. Dunford. The State of the Proton in Aqueous Sulfuric Acid. *J. Am. Chem. Soc.* **86**, 5080 (1964)

[502] J. J. Tyson. Scaling and reducing the Field-Koros-Noyes mechanism of the Belousov-Zhabotinskii reaction. *J. Phys. Chem.* **86**, 3006 (1982)

[503] A. B. Rovinskii and A. M. Zhabotinskii. Mechanism and mathematical model of the oscillating bromate-ferroin-bromomalonic acid reaction. *J. Phys. Chem.* **88**, 6081 (1984)

[504] A. B. Rovinskii. Spiral waves in a model of the ferroin catalyzed Belousov-Zhabotinskii reaction. *J. Phys. Chem.* **90**, 217 (1986)

[505] A. Belmonte and J.-M. Flesselles. Experimental Determination of the Dispersion Relation for Spiral Waves. *Phys. Rev. Lett.* **77**, 1174 (1996)

[506] A. Kaminaga, V. K. Vanag, and I. R. Epstein. "Black spots" in a surfactant-rich Belousov–Zhabotinsky reaction dispersed in a water-in-oil microemulsion system. *J. Chem. Phys.* **122**, 174706 (2005)

[507] V. K. Vanag and I. R. Epstein. A model for jumping and bubble waves in the Belousov–Zhabotinsky-aerosol OT system. *J. Chem. Phys.* **131**, 104512 (2009)

[508] L. Gyorgyi, T. Turanyi, and R. J. Field. Mechanistic details of the oscillatory Belousov-Zhabotinskii reaction. *J. Phys. Chem.* **94**, 7162 (1990)

[509] T. Turanyi, L. Gyorgyi, and R. J. Field. Analysis and simplification of the GTF model of the Belousov-Zhabotinskii reaction. *J. Phys. Chem.* **97**, 1931 (1993)